



**HAL**  
open science

# Design, Fabrication and Application of Polymeric Porous Media

Yajie Li

► **To cite this version:**

Yajie Li. Design, Fabrication and Application of Polymeric Porous Media. Mechanics of materials [physics.class-ph]. Ecole nationale supérieure d'arts et métiers - ENSAM; Tongji university (Shanghai, Chine), 2018. English. NNT : 2018ENAM0009 . tel-01760704

**HAL Id: tel-01760704**

**<https://pastel.hal.science/tel-01760704>**

Submitted on 6 Apr 2018

**HAL** is a multi-disciplinary open access archive for the deposit and dissemination of scientific research documents, whether they are published or not. The documents may come from teaching and research institutions in France or abroad, or from public or private research centers.

L'archive ouverte pluridisciplinaire **HAL**, est destinée au dépôt et à la diffusion de documents scientifiques de niveau recherche, publiés ou non, émanant des établissements d'enseignement et de recherche français ou étrangers, des laboratoires publics ou privés.

École doctorale n° 432 : Science des Métiers de l'ingénieur  
(et école partenaire cotutelle)

**Doctorat ParisTech**  
**T H È S E**

pour obtenir le grade de docteur délivré par

**l'École Nationale Supérieure d'Arts et Métiers**  
**Spécialité "Mécanique - Matériaux "**  
**And**  
**Tongji University**  
**Specialty "Material Science and Engineering"**

*présentée et soutenue publiquement par*

**Yajie LI**

le 09 Mars 2018 (09 March 2018)

**Design, Fabrication and Application of Polymeric Porous Media**

**Conception, Fabrication et Application de Milieux Poreux Polymériques**

Directeur de thèse : **Azita AHMADI**

Co-encadrement de la thèse : **Aziz OMARI and Hongting PU**

**Jury**

**M. Jie CHEN**, Professeur des Universités, Shanghai University

**M. Olivier ATTEIA**, Professeur des Universités, INP Bordeaux, ENSEGID

**M. Hongbin ZHANG**, Professeur des Universités, Shanghai Jiao Tong University

**Mme. Azita AHMADI**, Professeur des Universités, Arts et Métiers ParisTech

**M. Aziz OMARI**, Professeur à Bordeaux, INP/ENSCBP

**M. Hongting PU**, Professeur des Universités, Tongji University

**M. Henri BERTIN**, Directeur de Recherche CNRS, I2M

**M. Qiaolong YUAN**, Professeur des Universités, East China University of Science and Technology

Président

Rapporteur

Rapporteur

Examineur

Examineur

Examineur

Examineur

Examineur

## ABSTRACT

Due to the combination of the advantages of porous media and polymer materials, polymeric porous media possess the properties of controllable porous structure, easily modifiable surface properties, good chemical stability, etc., which make them applicable in a wide range of industrial fields, including adsorption, battery separator, catalyst carrier, filter, energy storage, etc. Although there exist various preparation methods, such as template technique, emulsion method, phase separation method, foaming process, electrospinning, top-down lithographic techniques, breath figure method, etc., the large-scale preparation of polymeric porous media with controllable pore structures and specified functions is still a long-term goal in this field, which is one of the core objectives of this thesis. Therefore, in the first part of the thesis, polymeric porous media are firstly designed based on the specific application requirements. Then the designed polymeric porous media are prepared by the combination of multilayer coextrusion and traditional preparation methods (template technique, phase separation method). This combined preparation method has integrated the advantages of the multilayer coextrusion (continuous process, economic pathway for large-scale fabrication, flexibility of the polymer species, and tunable layer structures) and the template/phase separation method (simple preparation process and tunable pore structure). Afterwards, the applications of the polymeric porous media in polycyclic aromatic hydrocarbons adsorption and lithium-ion battery separator have been investigated.

More importantly, in the second part of the thesis, numerical simulations of particle transport and deposition in porous media are carried out to explore the mechanisms that form the theoretical basis for the above applications (adsorption, separation, etc.). Transport and deposition of colloidal particles in porous media are of vital important in other applications such as aquifer remediation, fouling of surfaces, and therapeutic drug delivery. Therefore, it is quite worthy to have a thorough understanding of these processes as well as the dominant mechanisms involved. In this part, the microscale simulations of colloidal particle transport and deposition in porous media are achieved by a novel colloidal particle tracking model, called 3D-PTPO (Three-Dimensional Particle Tracking model by Python<sup>®</sup> and OpenFOAM<sup>®</sup>) code. The particles are considered as a mass point during transport in the flow and their volume is reconstructed when they are deposited. The main feature of the code is to take into account the modification of the pore structure and thus the flow streamlines due to deposit. Numerical simulations were firstly carried out in a capillary tube considered as an element of an idealized porous medium composed of capillaries of circular cross sections to revisit

the work of Lopez and co-authors by considering a more realistic 3D geometry and also to get the most relevant quantities by capturing the physics underlying the process. Then microscale simulation is approached by representing the elementary pore structure as a capillary tube with converging/diverging geometries (tapered pipe and venturi tube) to explore the influence of the pore geometry and the particle Péclet number (Pe) on particle deposition. Finally, the coupled effects of surface chemical heterogeneity and hydrodynamics on particle deposition in porous media were investigated in a three-dimensional capillary with periodically repeating chemically heterogeneous surfaces.

This thesis mainly includes the following aspects:

1) Multilayer polypropylene (PP)/polyethylene (PE) lithium-ion battery (LIB) separators were prepared via the combination of multilayer coextrusion (MC) and CaCO<sub>3</sub> template method (CTM). The as-prepared separators (referred to as MC-CTM PP/PE) exhibit higher porosity, higher ionic conductivity and better battery performance than the commercial trilayer separators (Celgard<sup>®</sup> 2325). Furthermore, the MC-CTM PP/PE not only possesses the effective thermal shutdown function, but also shows the strong thermal stability at high temperature (>160 °C). The thermal shutdown function of MC-CTM PP/PE can be adjusted widely in the temperature range from 127 °C to 165 °C, which is wider than the Celgard<sup>®</sup> 2325. The above competitive advantages which are brought from the convenient and cost-effective preparation method proposed in this work, make MC-CTM PP/PE a promising alternative to the commercialized trilayer LIB separators.

2) Multilayer PP/PE LIB separators (MC-TIPS PP/PE) with cellular-like submicron grade pore structure are efficiently fabricated by the combination of multilayer coextrusion and thermal induced phase separation (TIPS). In addition to the effective shutdown function, the as-prepared separator also exhibits a wider shutdown temperature window and stronger thermal stability than the Celgard<sup>®</sup> 2325, the dimensional shrinkage is negligible until 160 °C. Compared to the commercial separator, the MC-TIPS PP/PE has a higher porosity (54.6%) and electrolyte uptake (157%), leading to higher ionic conductivity (1.46 mS cm<sup>-1</sup>) and better battery performances. The above-mentioned significant characteristics make the MC-TIPS PP/PE a promising candidate high performance LIB separators.

3) Porous polystyrene (PS) membranes were prepared via the combination of multilayer coextrusion and CaCO<sub>3</sub> template method. Effects of etching time, CaCO<sub>3</sub> content, and the membrane thickness on the porous structures are investigated, which can be used to regulate and control the porous structure. To demonstrate the adsorption performance of porous PS membranes on PAH, pyrene is used as the model compound for polycyclic aromatic hydrocarbon. Compared with PS

solid membranes, porous PS membranes exhibit much higher adsorption performance on trace pyrene. The adsorption kinetics and isotherm of porous PS membranes respectively well fit the pseudo second-order kinetics and Freundlich isotherm model.

4) The transport and deposition of colloidal particles at the pore scale are simulated by 3D-PTPO code, using a Lagrangian method. This consists in the three-dimensional numerical modeling of the process of transport and deposition of colloidal particles in capillaries of a circular cross section. The velocity field obtained by solving the Stokes and continuity equations is superimposed to particles diffusion and particles are let to adsorb when they closely approach the solid wall. The particles are considered as a mass point during transport in the flow and their volumes are reconstructed when they are deposited, subsequently the flow velocity field is updated before a new particle is injected. The results show that both adsorption probability and surface coverage are decreasing functions of the particle's Péclet number. At low Péclet number values, when diffusion is dominant, the surface coverage approaches the Random Sequential Adsorption (RSA) value while at high Péclet number values, it drops drastically.

5) The microscale simulation of colloidal particle deposition in capillaries with converging/diverging geometries (tapered pipe and venturi tube) is approached by the improved 3D-PTPO code. The influence of the particle Péclet number (Pe) and the pore shape on the particle deposition was investigated. The results show that both deposition probability and surface coverage feature a plateau in the diffusion dominant regime (low Pe) and are decreasing functions of Pe in the convection dominant regime (high Pe). The results of the spatial density distribution of deposited particles show that, for the diffusion-dominant regime, the particle distribution is piston-like; while the distribution is more uniform for the convection-dominant regime. In addition, for the venturi tube with steep corners, the density of deposited particles is relatively low in the vicinity of the pore throat entrance and exit due to streamlines modification. The maximum dimensionless surface coverage  $\Gamma_{\text{final}}/\Gamma_{\text{RSA}}$  is studied as a function of Pe. The declining trend observed for high Pe is in good agreement with experimental and simulation results found in the literature.

6) The coupled effects of surface chemical heterogeneity and hydrodynamics on particle deposition in capillaries are investigated by the microscale simulation using the improved 3D-PTPO code. The porous medium is idealized as a bundle of capillaries and in this study, as an element of the bundle, i.e. a three-dimensional capillary with periodically repeating chemically heterogeneous surface (crosswise strips patterned and chess board patterned) is considered. The dependence of the deposition probability and dimensionless surface coverage ( $\Gamma/\Gamma_{\text{RSA}}$ ) on the frequency of the pitches

( $\lambda$ ), Pe and the reactive area fraction ( $\theta$ ), as well as the spatial density distribution of deposited particles were studied. The results indicate that particles tend to deposit at the leading and trailing edges of the favorable strips, and the deposition is more uniform along the patterned capillary compared to the homogeneous one. In addition, similar to the homogeneous capillary, the maximum dimensionless surface coverage  $\Gamma_{\text{final}}/\Gamma_{\text{RSA}}$  is a function of Pe. Besides, for the same  $\theta$ , the deposition probability is in a positive correlation with  $\lambda$ . Moreover, the overall deposition probability is increasing with  $\theta$ , which coincides well with the patchwise heterogeneity model.

In the last chapter, the general conclusions and perspectives of this thesis are discussed.

**Key Words:**

polymeric porous media, multilayer coextrusion, lithium-ion battery separator, PAH adsorption, microscale simulation, 3D-PTPO (three-dimensional particle tracking model by Python<sup>®</sup> and OpenFOAM<sup>®</sup>), particle transport and deposition

**Mots clés:**

milieux poreux polymériques, coextrusion multicouche, séparateur de batterie au lithium-ion, l'adsorption de PAH, simulation à l'échelle microscopique, 3D-PTPO (modèle tridimensionnel de suivi de particules par Python<sup>®</sup> et OpenFOAM<sup>®</sup>), transport et dépôt de particule

# CONTENTS

<b>ABSTRACT .....</b>	<b>I</b>
<b>CONTENTS .....</b>	<b>V</b>
<b>LIST OF FIGURES .....</b>	<b>VII</b>
<b>LIST OF TABLES .....</b>	<b>XII</b>
<b>CHAPTER 1 GENERAL INTRODUCTION .....</b>	<b>1</b>
1.1 CONTEXT AND OBJECTIVES OF THE PRESENT STUDY .....	1
1.2 ORGANIZATION OF THE THESIS .....	4
<b>CHAPTER 2 LITERATURE REVIEW .....</b>	<b>6</b>
2.1 DESIGN AND FABRICATION OF POLYMERIC POROUS MEDIA .....	6
2.2 TRANSPORT OF COLLOIDAL PARTICLES IN POROUS MEDIA .....	19
<b>PART I: PREPARATION OF POLYMERIC POROUS MEDIA FOR LITHIUM-ION BATTERY SEPARATORS AND WATER TREATMENT .....</b>	<b>44</b>
<b>CHAPTER 3 PREPARATION OF MULTILAYER POROUS POLYPROPYLENE/POLYETHYLENE LITHIUM-ION BATTERY SEPARATORS BY COMBINATION OF MULTILAYER COEXTRUSION AND TEMPLATE METHOD .....</b>	<b>44</b>
3.1 INTRODUCTION .....	44
3.2 EXPERIMENTAL SECTION .....	46
3.3 RESULTS AND DISCUSSION .....	50
3.4 CONCLUSIONS .....	59
<b>CHAPTER 4 PREPARATION OF MULTILAYER POROUS LITHIUM-ION BATTERY SEPARATORS BY COMBINATION OF MULTILAYER COEXTRUSION AND THERMAL INDUCED PHASE SEPARATION.....</b>	<b>60</b>
4.1 INTRODUCTION .....	60
4.2 EXPERIMENTAL SECTION .....	61
4.3 RESULTS AND DISCUSSION .....	64
4.4 CONCLUSIONS .....	71
<b>CHAPTER 5 PREPARATION OF POROUS POLYSTYRENE MEMBRANES VIA MULTILAYER COEXTRUSION AND ADSORPTION PERFORMANCE OF POLYCYCLIC AROMATIC HYDROCARBONS.....</b>	<b>72</b>

5.1 INTRODUCTION .....	72
5.2 EXPERIMENTAL SECTION.....	73
5.3 RESULTS AND DISCUSSION .....	75
5.4 CONCLUSIONS.....	86
<b>PART II : TRANSPORT OF COLLOIDAL PARTICLES IN POLYMERIC POROUS MEDIA :</b>	
<b>NUMERICAL MODELING.....</b>	<b>87</b>
<b>CHAPTER 6 COLLOIDAL PARTICLE DEPOSITION IN POROUS MEDIA IDEALIZED AS A BUNDLE OF CAPILLARIES.....</b>	<b>87</b>
6.1 INTRODUCTION .....	87
6.2 METHODOLOGY AND TOOLS .....	88
6.3 RESULTS AND DISCUSSION .....	90
6.4 CONCLUSIONS.....	95
<b>CHAPTER 7 THREE-DIMENSIONAL MICROSACLE SIMULATION OF COLLOIDAL PARTICLE TRANSPORT AND DEPOSITION IN MODEL POROUS MEDIA WITH CONVERGING/DIVERGING GEOMETRIES .....</b>	<b>96</b>
7.1 INTRODUCTION .....	96
7.2 NUMERICAL SIMULATIONS .....	98
7.3 RESULTS AND DISCUSSION .....	102
7.4 CONCLUSIONS.....	110
<b>CHAPTER 8 THREE-DIMENSIONAL MICROSACLE SIMULATION OF COLLOIDAL PARTICLE TRANSPORT AND DEPOSITION IN CHEMICALLY HETEROGENEOUS POROUS MEDIA .....</b>	<b>113</b>
8.1 INTRODUCTION .....	113
8.2 NUMERICAL SIMULATIONS .....	115
8.3 RESULTS AND DISCUSSION .....	119
8.4 CONCLUSIONS.....	128
<b>CHAPTER 9 CONCLUSIONS AND PERSPECTIVES .....</b>	<b>129</b>
<b>ACKNOWLEDGEMENT .....</b>	<b>132</b>
<b>REFERENCES .....</b>	<b>133</b>
<b>NOMENCLATURE.....</b>	<b>150</b>
RÉSUMÉ.....	155

## List of Figures

Figure 1.1 The summary of the classification of materials <sup>[3]</sup> .....	1
Figure 1.2 Illustration of representative natural and synthesized porous materials: (a) bamboo; (b) honeycomb; (c) alveolar tissue in mouse lung; (d) ordered macroporous polymer from direct templating; (e) porous aluminum; (f) porous silica <sup>[5]</sup> .....	2
Figure 2.1 Schematic illustration of different morphology of pores <sup>[18]</sup> .....	6
Figure 2.2 Illustration of pore surface, pore size, pore geometry, and framework structure of porous media <sup>[5]</sup> .....	7
Figure 2.3 Classification of porous media according to pore size <sup>[21]</sup> .....	7
Figure 2.4 Different pore configurations: (a) foams; (b) interconnected pore network; (c) powder compacts; (d) porous media produced from a powder with plate-like particles; (e) porous media consisting of fiber-shaped particles; (f) large pores connected by small pores; (g) both small pore networks and large pore networks <sup>[18]</sup> .....	8
Figure 2.5 Schematic illustration of fabrication of (a) spherical porous polymers, (b) tubular porous polymers, (c) ordered macroporous polymers <sup>[5]</sup> .....	10
Figure 2.6 Summary of removal conditions of various templates <sup>[5]</sup> .....	11
Figure 2.7 schematic representation of a binary phase diagram of a polymer solution <sup>[46]</sup> .....	13
Figure 2.8 Schematic representation for the change from conventional emulsion, through emulsion with the maximum packing fraction (74 vol%), to HIPE when increasing the volume fraction of internal phase <sup>[5]</sup> .....	14
Figure 2.9 Schematic representation of the problem <sup>[108]</sup> . (a) The small circle of radius a represents the moving sphere with a corresponding incoming impact parameter bin. The circle of radius b represents the fixed obstacle (a sphere or a cylinder). The empty circle represents the position of the suspended particle as it crosses the symmetry plane normal to the x-axis. The surface-to-surface separation $\xi$ and its minimum value $\xi_{\min}$ are also shown. (b) Representation of the conservation argument used to calculate the minimum separation. The unit vector in the radial direction $\mathbf{d}$ , the velocity components in the plane of motion, both far upstream ( $S_{\infty}$ ) and at the plane of symmetry ( $S_0$ ) are shown .....	25
Figure 2.10 Three filtration mechanisms of particle transport in porous media <sup>[132]</sup> .....	27
Figure 2.11 Key factors controlling engineered nanoparticle transport in porous media <sup>[144]</sup> .....	32
Figure 2.12 Schematic representation of the modeled surface charge heterogeneity. The square collector of height L consists of rectangular strips with alternate regions that are favorable	

(gray) and unfavorable (white) to deposition of widths $w$ and $b$ , respectively. The total width of a favorable and unfavorable strip gives the pitch, $p$ . The deposited spherical particles of diameter $d = 2a_p$ have their centers constrained to lie within the favorable strips [161]	39
Figure 2.13 Periodic surface patterns: (a) lengthwise strips, (b) crosswise strips, (c) patchwise pattern. Dark regions represent heterogeneous patches, light regions are the homogeneous surface. In each case the percent heterogeneous coverage is 50% [177]	40
Figure 2.14 Schematic of a patterned microchannel geometry with Poiseuille flow profile [188]	43
Figure 3.1 Preparation of MC-CTM PP/PE via the combination of multilayer coextrusion and $\text{CaCO}_3$ template method	48
Figure 3.2 (a) SEM image of the surface of the MC-CTM PP/PE. (b) SEM image of the cross-section (fractured in liquid nitrogen) of the MC-CTM PP/PE. (c) Optical microscope image of the MC-CTM PP/PE with multilayer structure (cross-section)	51
Figure 3.3 Stress-strain curve of MC-CTM PP/PE at room temperature	52
Figure 3.4 Arrhenius plots of ionic conductivity of MC-CTM PP/PE and Celgard <sup>®</sup> separator at elevated temperatures (from 30 to 80 °C)	53
Figure 3.5 (a) Thermal shrinkage of MC-CTM PP/PE and Celgard <sup>®</sup> 2325 as a function of heat treatment temperature; (b) photographs of MC-CTM PP/PE and Celgard <sup>®</sup> 2325 after heat treatment at different temperature for 0.5 h	54
Figure 3.6 (a) Impedance vs. temperature curves for cells containing different separators, commercial PE separator (SK Energy), commercial PP/PE/PP separator (Celgard <sup>®</sup> 2325), and MC-CTM PP/PE; (b) DSC curve of MC-CTM PP/PE	55
Figure 3.7 Chronoamperometry profiles of Li/electrolyte soaked separator/Li cells assembled with MC-CTM PP/PE and Celgard <sup>®</sup> separator by a step potential of 10 mV	56
Figure 3.8 Linear sweep voltammetry (LSV) curves of Li/electrolyte soaked separator/SS cells assembled with MC-CTM PP/PE and Celgard <sup>®</sup> separator with a scanning rate of $5 \text{ mV s}^{-1}$ over voltage range from 2 to 7 V	57
Figure 3.9 Electrochemical performances of MC-CTM PP/PE and Celgard <sup>®</sup> separator tested in Li/separator/LiFePO <sub>4</sub> configuration, (a) First discharge profiles at 0.2 C-rate, (b) Cycling performance at 0.2 C-rate, (c) C-rate behavior where the current densities are varied from 0.2 C to 2 C	59
Figure 4.1 Schematic illustration showing the preparation process of MC-TIPS PP/PE via the combination of multilayer coextrusion and thermal induced phase separation	62
Figure 4.2 (a) FESEM image and pore size distribution of the surface of MC-TIPS PP/PE; (b) FESEM image and pore size distribution of the cross-section of MC-TIPS PP/PE, fractured	

by liquid nitrogen; (c) Optical microscope image of the cross-sectional multilayer structure of MC-TIPS PP/PE .....	65
Figure 4.3 Stress-strain curve of MC-TIPS PP/PE at room temperature.....	66
Figure 4.4 Temperature dependence of ionic conductivity of MC-TIPS PP/PE and Celgard <sup>®</sup> separators .....	67
Figure 4.5 (a) Thermal shrinkage rate of MC-TIPS PP/PE and Celgard <sup>®</sup> 2325 as a function of heat treatment temperature; (b) photographs of MC-TIPS PP/PE and Celgard <sup>®</sup> 2325 after heat treatment at various temperatures for 0.5 h.....	68
Figure 4.6 (a) Impedance versus temperature curve for cells containing commercial PE separator (SK Energy), commercial PP/PE/PP separator (Celgard <sup>®</sup> 2325), and MC-TIPS PP/PE. (b) The DSC curve of MC-TIPS PP/PE .....	69
Figure 4.7 (a) Chronoamperometry profiles of LM/electrolyte soaked separator/LM cells assembled with MC-TIPS PP/PE and Celgard <sup>®</sup> separator by a step potential of 10 mV. (b) LSV curves of LM/electrolyte soaked separator/SS cells assembled with MC-TIPS PP/PE and Celgard <sup>®</sup> separator with a scanning rate of 5 mV s <sup>-1</sup> over voltage range from 2 to 6 V .....	70
Figure 4.8 Battery performances of MC-TIPS PP/PE and Celgard <sup>®</sup> separator tested in Li/separator/LiFePO <sub>4</sub> configuration. (a) Cycling performance at 0.2 C-rate and (b) C-rate behavior where the current densities ranging from 0.2 C to 2 C .....	71
Figure 5.1 (a) Schematic representation of the two-component multilayer coextrusion system, (b) Preparation of porous PS membranes via the combination of multilayer coextrusion and CaCO <sub>3</sub> template method .....	74
Figure 5.2 Optical microscope images (reflection mode) of the cross-section of LDPE/PS(CaCO <sub>3</sub> ) coextrusion films with multilayer structure, (a) 16 layers, (b) 32 layers, and (c) 64 layers.....	76
Figure 5.3 Optical microscope images (transmission mode) of PS(CaCO <sub>3</sub> ) membranes (40 wt% CaCO <sub>3</sub> ), (a) blended by the twin-screw extruder followed by compression molding, (b) prepared via multilayer coextrusion.....	76
Figure 5.4 Digital photographs of single layer PS(CaCO <sub>3</sub> ) membranes (a) before and (b) after etched in 15 wt% HCl solution for 48 h .....	77
Figure 5.5 SEM images of the frozen brittle fracture surface of porous PS membranes (40 wt% CaCO <sub>3</sub> , etched for 48 h) with different thickness, (a) 20 μm, (b) 10 μm, (c) 5 μm. ....	78
Figure 5.6 SEM images of the surface of polystyrene membranes with different etching time (in 15 wt% HCl solution), (a) before etching, (b) etched for 24 h, (c) etched for 48 h.....	78

Figure 5.7 Etching (in 15 wt% HCl solution) kinetics of CaCO <sub>3</sub> in the membranes (40 wt% CaCO <sub>3</sub> in the membranes, thickness 5 μm) .....	79
Figure 5.8 SEM images of the frozen brittle fracture surface of PS membranes with different CaCO <sub>3</sub> contents after etched in 15 wt% HCl solution for 48 h, (a) 20 wt% CaCO <sub>3</sub> , (b) 40 wt% CaCO <sub>3</sub> .....	79
Figure 5.9 (a) Fluorescence spectra of pyrene in aqueous solution after adsorbed by porous PS membranes (6 <sup>#</sup> ) for 12 h; (b) effects of the amount of porous PS membranes (6 <sup>#</sup> ) on the residual concentration of pyrene solution, which can be calculated according to the fluorescence intensity of the solution at 370 nm; the initial concentration of pyrene solution is 130 ppb.....	81
Figure 5.10 Fluorescence spectra of pyrene in aqueous solution after adsorbed for different time by (a) 1 <sup>#</sup> membranes, (b) 2 <sup>#</sup> membranes, (c) 3 <sup>#</sup> membranes, (d) 4 <sup>#</sup> membranes, (e) 5 <sup>#</sup> membranes, and (f) 6 <sup>#</sup> membranes; (g) Adsorption kinetics of pyrene in aqueous solution by membranes from 1 <sup>#</sup> to 6 <sup>#</sup> with 0.8 g L <sup>-1</sup> membranes in the solution, which can be calculated according to the fluorescence intensity of the solution at 370 nm, the initial concentration of pyrene solution is 130 ppb.....	83
Figure 5.11 (a) First-order rates for the adsorption of pyrene by membrane 1 <sup>#</sup> and 6 <sup>#</sup> ; (b) Second-order rates for the adsorption of pyrene by membrane 1 <sup>#</sup> and 6 <sup>#</sup> PS membranes; the initial concentration of pyrene is 0.13 mg L <sup>-1</sup> .....	84
Figure 5.12 Adsorption isotherm for the adsorption of pyrene by porous PS membranes (6 <sup>#</sup> ); (b) the values of lnQ <sub>eq</sub> against lnC <sub>eq</sub> based on Freundlich isotherm model; (c) the linear dependence of C <sub>eq</sub> /Q <sub>eq</sub> on C <sub>eq</sub> based on Langmuir isotherm model.....	85
Figure 6.1 Variation of deposition probability versus the number of injected particles for different Péclet numbers .....	91
Figure 6.2 Variation of $\Gamma/\Gamma_{RSA}$ versus the Péclet number .....	92
Figure 6.3 Visual illustration of adsorbed particles for two different Péclet numbers after the injection of 3000 particles (A) Pe=0.0015 and (B) Pe=150 .....	92
Figure 6.4 Variation of porosity values versus N at different Pe .....	93
Figure 6.5 Variation of permeability reduction versus N at various Pe (A); Hydrodynamic thickness $\delta/2r_p$ of the deposited layer versus Pe (B) <sup>[17]</sup> .....	94
Figure 7.1 Geometry and meshing of the two configurations considered: (a) tapered pipe; (b) venturi tube .....	99
Figure 7.2 Sketches of possible particle trajectories: (a) flow through; (b) approaching a deposited particle (in blue) and bouncing back to the bulk flow (in red); (c) deposited on the wall.....	102

Figure 7.3 Variation of deposition probability versus N at different Pe for the tapered pipe .... 104

Figure 7.4 (a) Spatial distribution of the density of deposited particles along the z coordinate at different N for Pe=0.0019; (b) 3D sectional view of the tapered pipe at N=200; (c) 3D sectional view of the tapered pipe at N=30000 (the flow occurs from left to right)..... 106

Figure 7.5 (a) Spatial distribution of the density of deposited particles along the z coordinate at different N for Pe=190; (b) 3D sectional view of the tapered pipe at N=200; (c) 3D sectional view of the tapered pipe at N=15000 (Pe=190, the flow occurred from left to right)..... 106

Figure 7.6 Streamline profiles in the tapered pipe without (a) and with (b) deposited particles (Pe=1.9)..... 106

Figure 7.7 Spatial distribution of the density of deposited particles along the z coordinate at different N for Pe=0.0014 ..... 107

Figure 7.8 Initial streamlines distribution in the venturi pipe at Pe=1.4 and Re=0.48×10<sup>-4</sup> ..... 108

Figure 7.9 Variation of dimensionless surface coverage  $\Gamma/\Gamma_{RSA}$  versus N at different Pe ..... 110

Figure 7.10 Variation of  $\Gamma_{final}/\Gamma_{RSA}$  versus Péclet number: (a) venturi tube; (b) tapered pipe; (c) capillary tube; (d) parallel planes of Lopez *et al* <sup>[17]</sup>; (e) experimental results of Veerapen *et al* <sup>[274]</sup> ..... 110

Figure 8.1 Surface heterogeneity is modeled as alternate bands (patches) of attractive and repulsive regions on the capillary wall to facilitate systematic continuum type evaluation: (a): Crosswise strips patterned; (b): Chess board patterned. Bright bands (patches) represent positively charged regions, blue bands (patches) represent negatively charged regions, and the particles are positively charged ..... 116

Figure 8.2 Sketches of possible particle trajectories: (a) flowing through the capillary; (b) approaching a deposited particle (in grey line) and bouncing back to the bulk flow (in orange line); (c) approaching repulsive regions (positively charged) on the capillary wall (in grey line) and bouncing back to the bulk flow (in green line); (d) approaching attractive regions (negatively charged) and depositing on the wall..... 119

Figure 8.3 (a) Spatial density distribution of the deposited particles versus the z coordinate at N=2000, Pe=0.0015 for both heterogeneous ( $\lambda=5$  and  $\theta=0.5$ ) and homogeneous capillary; (b) schematic representation of particle behavior near the boundaries between the favorable and unfavorable strips<sup>[280]</sup>. 3D sectional view of the heterogeneous (c) and homogeneous (d) capillary (the red small geometries represent the deposited particles; the flow occurred from left to right) ..... 120

Figure 8.4 Variation of deposition probability versus the number of injected particles (N) for heterogeneous (with different  $\lambda$ ) and homogeneous capillaries. (Pe=0.0015)..... 122

Figure 8.5 (a) Determination of the calculation method of the dimensionless surface coverage for heterogeneous capillary, the dotted line stands for the homogeneous capillary. (Pe=0.0015); (b) Variation of the dimensionless surface coverage versus N for heterogeneous capillary with different  $\lambda$ . The inset plot represents the overall particle deposition probability versus  $\lambda$  with N=5000 (Pe=0.0015)..... 123

Figure 8.6 Variation of dimensionless surface coverage  $\Gamma/\Gamma_{RSA}$ . (a)  $\Gamma/\Gamma_{RSA}$  versus N at different Pe; (b)  $\Gamma_{Max}/\Gamma_{RSA}$  as a function of Pe. ( $\lambda=5$  and  $\theta=0.5$  for the heterogeneous capillary)... 124

Figure 8.7 (a). 3D sectional view (left: crosswise strips patterned), (right: chess board patterned) of the heterogeneous capillary with deposited particles ; (b) variation of dimensionless surface coverage  $\Gamma/\Gamma_{RSA}$  versus N for crosswise strips patterned and chess board patterned capillaries. For both cases,  $\theta=0.5$ , pitch length=3  $\mu\text{m}$  and Pe=0.0015 ..... 126

Figure 8.8 (a) 3D sectional view of the heterogeneous capillary with deposited particles,  $\lambda=5$ , Pe=0.0015,  $\theta$  is ranging from 20% to 100%; (b) variation of the number of deposited particles (n) versus the number of injected particles (N) with different  $\theta$ ; (c) the dependence of the effective collector efficiency ( $\eta_{effective}/\eta_f$ ) on  $\theta$ . ( $\lambda=5$ , Pe=0.0015, N=10000)..... 127

## List of Tables

Table 2.1 Existing models for particle deposition in porous media <sup>[138]</sup> ..... 30

Table 3.1 Physical properties of MC-CTM PP/PE and Celgard<sup>®</sup> 2325 ..... 51

Table 4.1 Physical properties of MC-TIPS PP/PE and Celgard<sup>®</sup> 2325 ..... 66

Table 5.1 Regulation and controlling of the porosity of PS membranes ..... 80

Table 6.1 Detailed parameters of the simulation ..... 90

Table 7.1 Parameters used for simulations ..... 102

Table 8.1 Parameters used for simulations ..... 117

# Chapter 1 General Introduction

## 1.1 Context and objectives of the present study

Materials can be divided into dense materials and porous materials according to their density. Figure 1.1 shows a summary of the classification of materials. The study of porous material is an important branch of material science, which plays a significant role in our scientific research and industrial production. Each porous medium is typically composed of a solid skeleton and a void space, which is usually filled with at least one type of fluid (liquid or gas) <sup>[1-3]</sup>. There are many examples of natural (hollow bamboo, honeycomb, and alveoli in the lungs) and man-made porous materials (macroporous polymer, porous aluminum, and porous silica), as shown in Figure 1.2 <sup>[4,5]</sup>. Polymeric porous medium is one of the most important components of organic porous materials, which is the main object of this thesis. Polymeric porous medium (porous polymer) has the combined advantages of porous media and polymer materials. It possesses high porosity, abundant microporous structure and low density. The various preparation methods, controllable pore structure and easily modified surface properties make the polymeric porous media promising materials in a wide range of application fields including adsorption, battery separator, filter, energy storage, catalyst carrier, and biomedical science <sup>[5]</sup>. Therefore, it is quite interesting and worthy to study the new function of polymeric porous media and to develop a novel preparation method for this widely-used material.

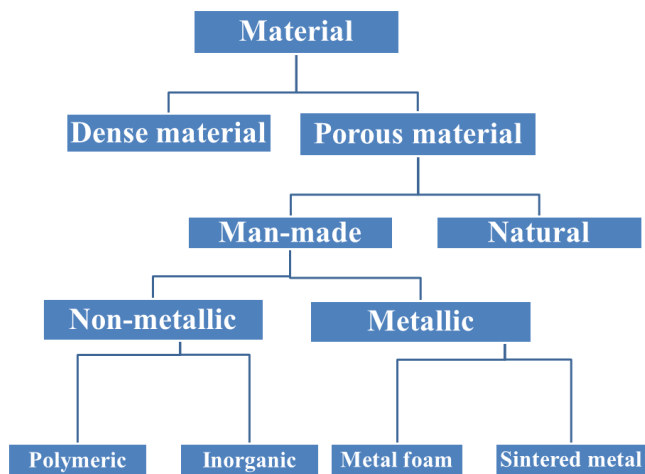


Figure 1.1 The summary of the classification of materials <sup>[3]</sup>

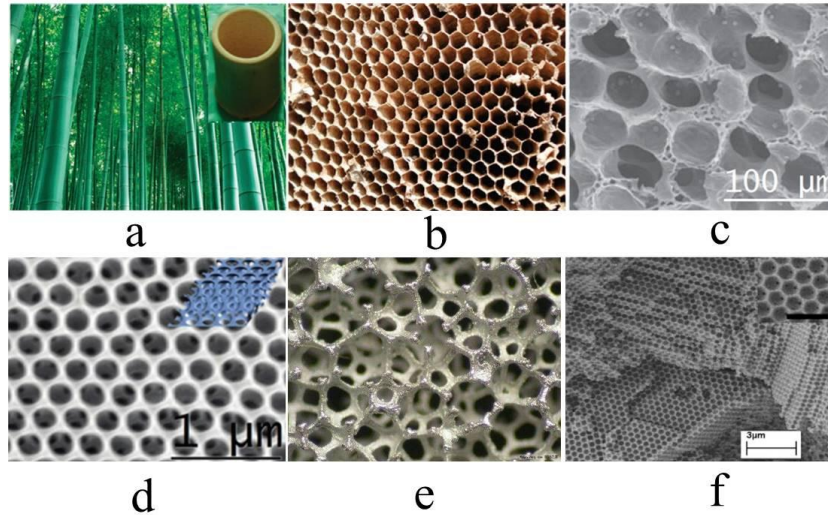


Figure 1.2 Illustration of representative natural and synthesized porous materials: (a) bamboo; (b) honeycomb; (c) alveolar tissue in mouse lung; (d) ordered macroporous polymer from direct templating; (e) porous aluminum; (f) porous silica <sup>[5]</sup>

Prior to the preparation and realization, the functions and the structures of polymeric porous media should be designed. The foremost aspect to consider is the main functions that we would like to realize in the media, which lead to specific application properties. Secondly, we need to determine the key factors that are directly related to the desired function, such as the pore geometry, pore size and the matrix porosity of the materials. Thirdly, based on the above considerations, the experimental scheme needs to be designed to prepare the polymeric porous media. Although various preparation methods exist, such as template technique, emulsion method, phase separation method, foaming process, electrospinning, top-down lithographic techniques, breath figure method, etc., the large-scale preparation of polymeric porous media with controllable pore structures and specified functions is still a long-term goal in this field, which is one of the core objectives of this thesis. A new approach, forced assembly multilayer coextrusion, has been used to economically and efficiently produce polymers of multilayers with individual layer thickness varying from micron to nanoscale. This advanced polymer processing technique has many advantages including continuous process, economic pathway for large-scale fabrication, flexibility of the polymer species, and the capability to produce tunable layer structures. Therefore, in the part I of this thesis, polymeric porous media are designed based on the specific application requirements and prepared by the combination of multilayer coextrusion and traditional preparation methods (template technique, phase separation method). This approach combines the advantages of the multilayer coextrusion and the template/phase separation method (simple preparation process and tunable pore structure). Afterwards, the applications of the polymeric porous media in PAHs adsorption and lithium-ion battery separator have been investigated.

More importantly, the basic mechanism of the above application processes (PAHs adsorption process or lithium-ion transport through separator) is based on the particle transport and deposition in porous media. Thus it is essential to have a thorough understanding of particle transport and deposition processes in porous media as well as the dominant mechanisms involved. In addition, transport and deposition of colloidal particles in porous media is of vital importance to other engineering and industrial applications <sup>[6]</sup>, such as particle-facilitated contaminants transport <sup>[7]</sup>, water purification <sup>[8]</sup>, wastewater treatment <sup>[9]</sup>, or artificial recharge of the aquifers <sup>[10]</sup>. In order to comprehend colloidal particle transport mechanisms in porous media, computational fluid dynamics (CFD) numerical simulations have been carried out to visualize and analyze the flow field <sup>[11]</sup>. Taking water filtration as an example, numerical techniques could be used to model the transport and dispersion of contaminants within a fluid <sup>[12]</sup>. Basically, there are two fundamental theoretical basis to study the transport of colloidal particles in porous media, classified as Eulerian and Lagrangian methods <sup>[13, 14]</sup>. The Eulerian method describes what happens at a fixed point in space, while the Lagrangian method implies a coordinate system moving along with the flow <sup>[15]</sup>. Pore geometries are often simplified into one or two dimensions to reduce the time consumption of the numerical simulations. However, this simplification restricts the particle motion and reduces the accuracy of the results. Therefore, it is necessary to improve the simulation model to enable three-dimensional simulations in more realistic geometries <sup>[16]</sup>. Moreover, particle transport and deposition in heterogeneous porous media have been an area of intense investigation recently. So far, there are few reported works on the combined effects of hydrodynamics and surface heterogeneity on colloidal particle deposition in porous media. Hence, it is necessary to better understand the mechanisms responsible for these phenomena, which is one of the objectives of the present work.

The objective of the part II of this thesis is the three-dimensional microscale simulation of colloidal particles transport and deposition in both homogeneous and heterogeneous porous media by means of CFD tools using the Lagrangian method in order to get the most relevant quantities by capturing the physics underlying the process. In order to perform the simulation, a novel colloid particle tracking model, namely 3D-PTPO (Three-dimensional particle tracking model by Python<sup>®</sup> and OpenFOAM<sup>®</sup>) code using Lagrangian method is developed in the present study. The major content of the part II of this thesis could be summarized as: firstly, particle deposition behavior is investigated on a homogeneous cylinder in order to revisit the previous work of Lopez et al. <sup>[17]</sup> by considering a more realistic 3D geometry. Indeed their work was limited to a particular geometry restricted to a slot-like geometry unlikely to be encountered in real porous media. In addition, it is necessary to validate the fundamental transport properties during the simulation, since the initial

validation part of the model development (involving deposition onto homogeneous collectors) was important for the following simulations of particle transport and deposition in the subsequent more complex pore geometries. Secondly, the three-dimensional numerical modeling of the process of particle transport and deposition in a more complex pore geometry (tapered pipe or venturi tube) of a circular cross section is carried out to explore the influence of pore geometry on the flow field as well as on the particle transport and deposition properties. Thirdly, the 3D-PTPO model is improved by incorporating surface chemical heterogeneity. The combined effects of the surface heterogeneity and hydrodynamics on the particle deposition behavior are investigated.

## 1.2 Organization of the thesis

The content of this thesis has been subdivided into the following nine chapters:

In Chapter 1, the general overview of the current research topic, the objectives of the thesis, as well as the outline have been explained.

In Chapter 2, firstly, a thorough review of existing work on polymeric porous media has been presented, including the evolution, the detailed preparation methods, as well as the applications. Secondly, particle transport and deposition in porous media has been reviewed. The transport and deposition mechanisms, the research methods, as well as the previous work are all illustrated in details. Particularly, reviews of particle deposition onto homogeneous/heterogeneous substrates have been summarized respectively.

In Chapter 3, a facile and continuous method to prepare porous multilayer polypropylene (PP)/polyethylene (PE) membranes via multilayer coextrusion and  $\text{CaCO}_3$  template method is proposed. The physical and electrochemical properties of the separators for lithium-ion batteries (LIBs) have been investigated and compared with the commercial separators.

In Chapter 4, multilayer PP/PE LIB separators with cellular-like submicron grade pore structure are efficiently fabricated by the combination of multilayer coextrusion and thermal induced phase separation (TIPS). The physical and electrochemical properties of the separators have been investigated and compared with the commercial separators.

In Chapter 5, a convenient and continuous method to prepare porous polystyrene (PS) membranes via multilayer coextrusion and template method is proposed. To investigate the

adsorption performance of porous PS membranes on PAHs, pyrene is used as the model compound for polycyclic aromatic hydrocarbon.

In Chapter 6, the particle transport and deposition onto a homogenous porous medium composed of a bundle of capillaries of a circular cross section has been carried out to validate the fundamental transport properties, which is important for the following simulations of particle transport and deposition in complex porous media.

In Chapter 7, the particle transport and deposition in homogenous porous media with converging/diverging geometries (tapered pipe and venturi tube) is investigated by the three-dimensional microscale simulation. The influence of the pore geometry and particle Péclet number ( $Pe$ ) on the particle deposition is explored.

In Chapter 8, the particle transport and deposition onto capillaries with periodically repeating chemical heterogeneous surfaces (crosswise strips patterned and chess board patterned) is investigated by the three-dimensional microscale simulation. The dependence of the deposition probability, dimensionless surface coverage ( $\Gamma/\Gamma_{RSA}$ ) on the frequency of the pitches ( $\lambda$ ), particle Péclet number ( $Pe$ ) and the favorable area fraction ( $\theta$ ), as well as the spatial density distribution of deposited particles have been studied.

In Chapter 9, major conclusions from each chapter are summarized and the perspectives for the future work are discussed.

## Chapter 2 Literature Review

### 2.1 Design and fabrication of polymeric porous media

#### 2.1.1 Polymeric porous media

Porous media are defined as solids containing pores. Normally, porous media have the porosity of 0.2-0.95. Pores are classified into two types: closed pores which are isolated from the outside and open pores which connect to the outside of the media. Especially, penetrating pores are a kind of open pores which possess at least two openings located on two sides of the porous media. The different morphology of pores are illustrated schematically in Figure 2.1. Open pores are required for most industrial applications such as filters, carriers for catalysts and bioreactors. This thesis mainly focuses on open pores. Introducing open pores in media, or to say producing open porous media, changes media properties. The decreased density and the increased specific surface area are the two essential changes, which can generate beneficial properties including permeability, filtration effects, as well as the thermal/acoustic insulation capabilities <sup>[18]</sup>.

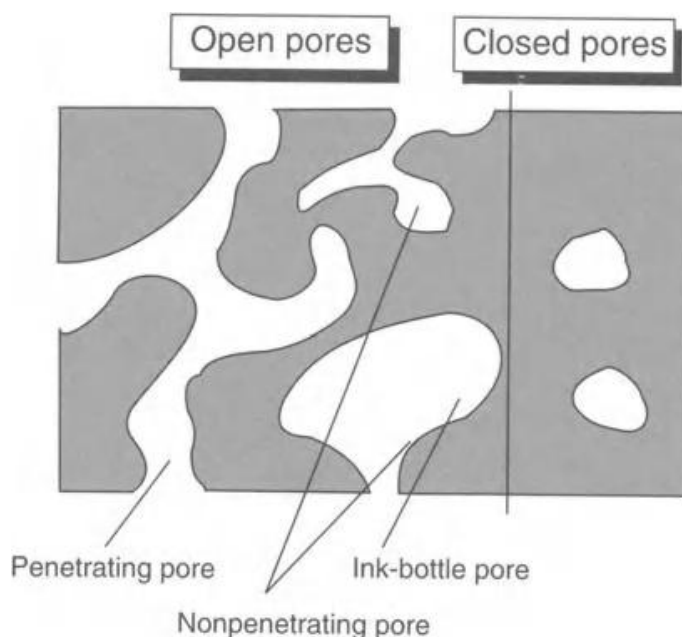


Figure 2.1 Schematic illustration of different morphology of pores <sup>[18]</sup>

There are several significant structural characteristics of porous media including pore size, pore geometry, pore surface functionality, and framework structure such as topology, composition, and functionality <sup>[5]</sup>, as is shown in Figure 2.2. Surface area is a very important parameter that is

employed to evaluate the pore structure; generally, pores with a smaller size contribute predominantly to the generation of materials with high surface area. Pore geometry includes tubular, spherical, and network-type morphologies that can be either assembled into ordered arrays or disorders. In addition to the physical structures, the functionalities of the pore surface and the framework are also important <sup>[19]</sup>, which can be engineered by post-modification processes or through the use of functional monomers <sup>[20]</sup>.

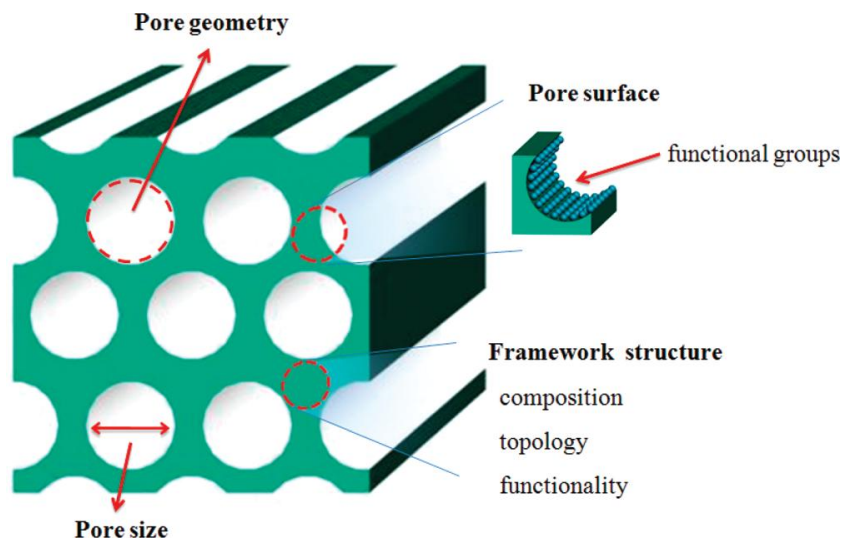


Figure 2.2 Illustration of pore surface, pore size, pore geometry, and framework structure of porous media <sup>[5]</sup>

Porous media can be classified by the above structural characteristics such as pore size, pore geometries and framework materials:

According to the International Union of Pure and Applied Chemistry (IUPAC) recommendation, the classification of porous media by pore size is shown in Figure 2.3 <sup>[21]</sup>. Macroporous media are defined as media with pore size larger than 50 nm in diameter, mesoporous media with pore size in the range of 2-50 nm, and microporous media with pore size smaller than 2 nm <sup>[22]</sup>.

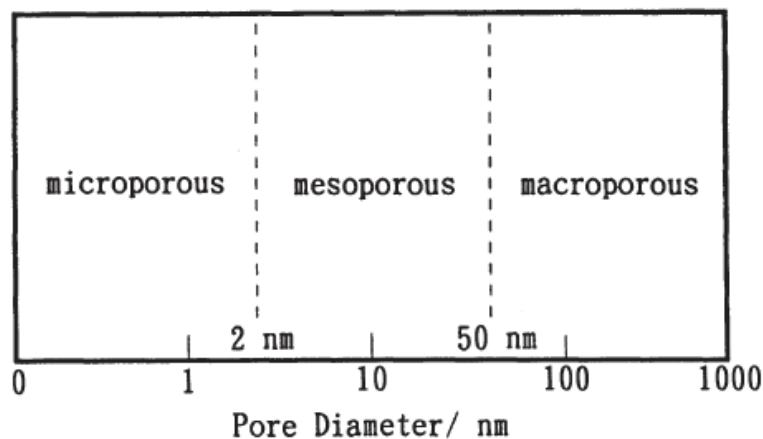


Figure 2.3 Classification of porous media according to pore size <sup>[21]</sup>

Porous media can also be classified by the pore geometries. Figure 2.4 illustrates the different kinds of pore geometries. Most porous media are foams with the open porosity ranging from 0.7 to 0.95. This configuration can be produced by bubbling the ceramic slurry or by using a large amount of pore forming agent. (Figure 2.4a) An interconnected pore network can be observed in porous glasses produced by a leaching technique that results in the spinodal decomposition, pores are homogenous in both size and shape (Figure 2.4b). Powder compacts have the geometry of opening pores between particles and the pore shape is angular fundamentally. (Figure 2.4c) Porous media produced from a powder with plate-like particles possess the geometry of opening pores between plates (Figure 2.4d). Porous media built up by fiber-shaped particles have the geometry of opening pores between fibers. (Figure 2.4e) Sintered porous materials with pore forming agents possess the configuration of large pores connected by small pores (Figure 2.4f). Porous media consisting of porous particles have the configuration of both small pore networks and large pore networks (Figure 2.4g) <sup>[18]</sup>.

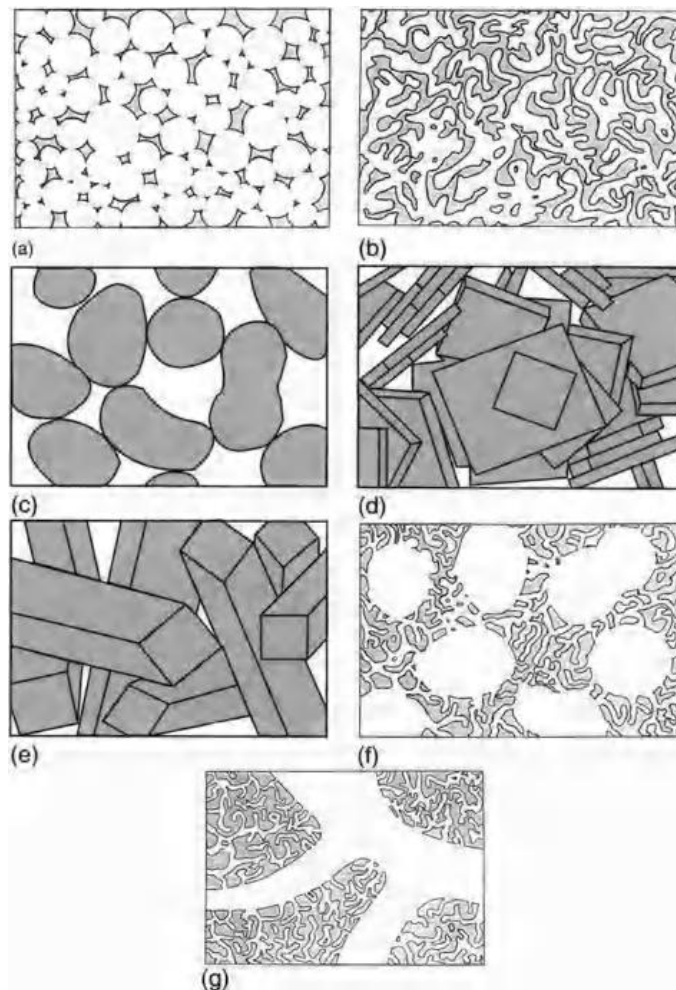


Figure 2.4 Different pore configurations: (a) foams; (b) interconnected pore network; (c) powder compacts; (d) porous media produced from a powder with plate-like particles; (e) porous media consisting of fiber-shaped particles; (f) large pores connected by small pores; (g) both small pore networks and large pore networks <sup>[18]</sup>

More importantly, classification based on the framework materials is of vital importance in the application of porous media. Depending on the desired properties such as mechanical strength, chemical stability and high-temperature resistance, materials are selected for porous solid including paper, polymer, metal, glass, and ceramic. Polymeric porous media especially have received an increased level of research interest due to their potential to merge the properties of both porous materials and polymers <sup>[23]</sup>. Firstly, porous polymers have the advantages of high surface area and well-defined porosity <sup>[24]</sup>. Secondly, the porous polymers possess good processability, which generates obvious advantages in many applications fields <sup>[25]</sup>. Thirdly, the diversity of preparation routes facilitates the construction and design of numerous porous polymers <sup>[26]</sup>. Finally, the polymeric frameworks are composed of light elements due to their organic nature, which provides a weight advantage in many applications <sup>[27]</sup>.

Polymeric porous media have been synthesized <sup>[28]</sup> by incorporating monomers into well-known step growth and chain-growth polymerization processes to provide cross-links between propagating polymer chains since the early 1960s, resulting in three-dimensional network materials. In the late 1980s, the copolymerization strategy and the use of discrete molecular porogens were combined to create molecularly imprinted polymers. These materials have been extensively investigated in sensing and catalysis applications <sup>[29]</sup>. Besides, it is often too fast and difficult to control the polymerization/cross-linking kinetics, yielding the macro-pores rather than the micro-pores. In the late 1990s, attempts were made <sup>[29]</sup> to synthesize microporous organic polymer materials from monomers. Slower bond-forming reactions were adapted to promote the formation of pores that closely match the potential guest molecules dimension <sup>[28, 29]</sup>. The ability to control the structure of pores and incorporate desired functionalities into the material has benefited from the great strides being made in the preparation of polymeric porous media by various preparation methods, as summarized in the following chapter.

### 2.1.2 Preparation methods

The past several years have witnessed an expansion of various methods directed at preparing polymeric porous media, including direct templating, block copolymer self-assembly, and direct synthesis methodologies. These techniques have been developed mainly based on the properties of the raw materials and the targeted applications. Polymeric porous media prepared by different techniques possess different characteristics, such as average pore size, porosity, and mechanical properties <sup>[30]</sup>. Hereafter, the preparation methods will be introduced in details.

### 2.1.2.1 Direct templating method

Direct templating method is a simple and versatile approach for the direct replication of the inverse structure of the preformed templates with stable morphology <sup>[5]</sup>. A large number of polymeric porous media have been successfully prepared by direct templating method, including individual spherical porous polymers from solid spherical nanoparticle templates (Figure 2.5a), tubular porous polymers from tubular porous templates (Figure 2.5b), and ordered macroporous polymers from colloidal crystal templates (Figure 2.5c) <sup>[5]</sup>.

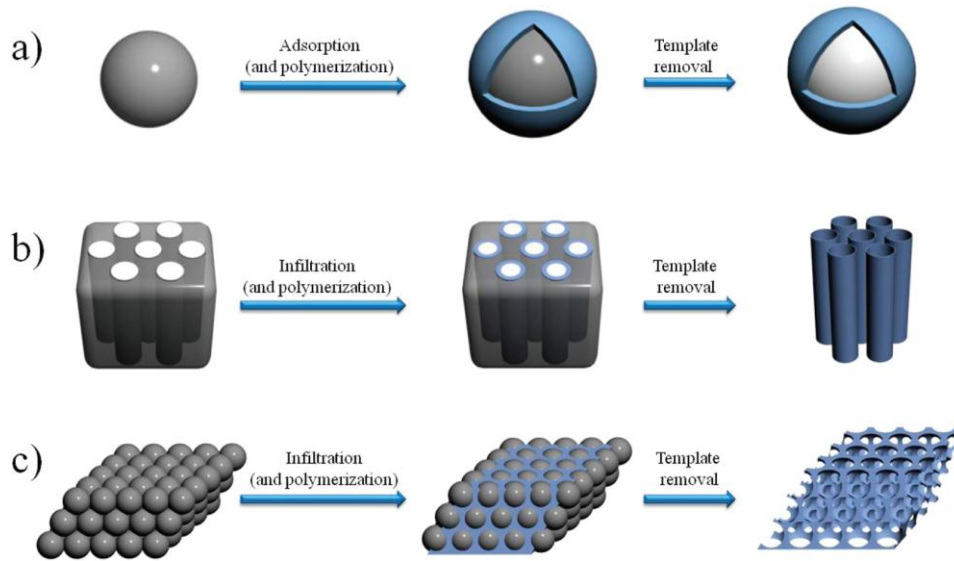


Figure 2.5 Schematic illustration of fabrication of (a) spherical porous polymers, (b) tubular porous polymers, (c) ordered macroporous polymers <sup>[5]</sup>

There are several requirements for the successful preparation of polymeric porous media by direct templating method. Firstly, in order to realize a faithful replication of the template, the surface properties of the templates should be compatible with the raw materials selected for the polymeric framework. Secondly, the templates should have well-defined structures. In this way, one can tune the predetermined porous structures of polymer replicas by a rational choice of templates. Thirdly, after templating the templates should be easily removed. Figure 2.6 outlines the template removal conditions employed for various templates <sup>[5]</sup>. Finally, the polymeric walls should provide the ability to incorporate designable functionalities for targeted applications <sup>[5]</sup>.



solvent accumulated in isolated zones forming either two distinct phases or two bicontinuous phases. Finally, the removal of the solvent phase left the final porous structure <sup>[36]</sup>. The phase separation process is determined by the kinetic and thermodynamic parameters, such as the chemical potentials and diffusivities of the individual components. The key to understand the formation mechanism of pore structure is the identification and description of the phase separation process <sup>[38]</sup>. Normally, phase separation methods can be classified into four main methods: precipitation by cooling, called thermally induced phase separation (TIPS) <sup>[39]</sup>; precipitation in a non-solvent (typically water), called nonsolvent-induced phase separation (NIPS) <sup>[40]</sup>; precipitation by absorption of non-solvent (water) from the vapor phase, called vapor induced phase separation (VIPS) <sup>[41]</sup>; and solvent evaporation-induced phase separation (EIPS) <sup>[42]</sup>.

Thermally induced phase separation (TIPS) technique is currently receiving much attention in industrial applications for the production of polymeric porous media. The TIPS process is applicable to a wide range of polymers <sup>[43]</sup>, allow greater flexibility, higher reproducibility, and effective control of the final pore size of porous polymer <sup>[44]</sup>. In principle, TIPS is based on a rule that a polymer is miscible with a diluent at high temperature, but demixes at low temperature. A typical TIPS process begins by dissolving a polymer in a diluent to form a homogeneous solution at an elevated temperature, which is cast or extruded into a desired shape. Then, a cooling bath is employed to induce a phase separation (e.g. liquid-liquid, solid-liquid, liquid-solid, or solid-solid demixing) <sup>[45]</sup> based on the changes in thermal energy, the de-mixing of a homogeneous polymer solution was induced into a multi-phase system <sup>[46]</sup>. Figure 2.7 presented a typical temperature composition phase diagram for a binary polymer-solvent system with an upper critical solution temperature. When the temperature of a solution is above the binodal curve, the polymer solution is homogeneous. A polymer-rich phase and a solvent-rich phase coexist in a solution in the L-L demixing region <sup>[47]</sup>. The maximum point is the critical point of the system, at which both the binodal and the spinodal curves merge <sup>[46]</sup>. The porous morphology of the resulting porous polymer can be controlled by the balance of various parameters <sup>[43]</sup>: the cooling depth, cooling rate, polymer type, polymer concentration, diluent composition and the presence of additives <sup>[48]</sup>.

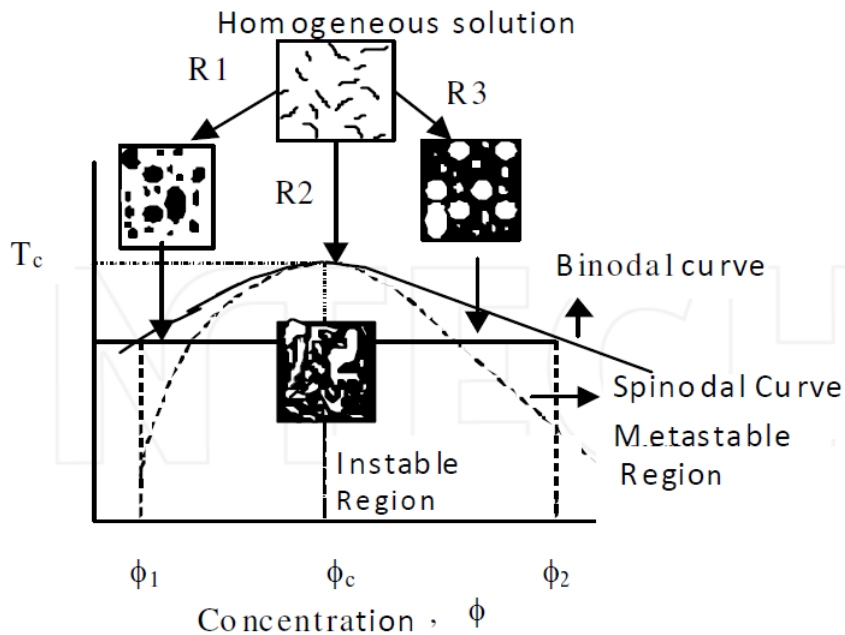


Figure 2.7 schematic representation of a binary phase diagram of a polymer solution <sup>[46]</sup>

Currently, the TIPS process has been applied to several polymers, including polypropylene (PP) <sup>[49]</sup>, polystyrene (PS) <sup>[50]</sup>, and poly(vinylidene fluoride) (PVDF) <sup>[51]</sup>. Recently, hydrophilic materials of cellulose acetate (CA) <sup>[45]</sup>, cellulose acetate butyrate (CAB), and polyacrylonitrile (PAN) <sup>[52]</sup> were used for the fabrication of polymeric porous media <sup>[53]</sup>.

Many researches have been carried out by this method. For example, Cheng et al. <sup>[54]</sup> employed TIPS to fabricate PVDF/polysulfone blend separators that showed the maximum electrolyte uptake of 129.76%. It is promising to develop new kinds of porous separators via TIPS for LIBs. Matsuyama et al. <sup>[50]</sup> achieved the first hydrophilic CA hollow fiber membrane using TIPS by liquid-liquid phase separation, and demonstrated that the membrane possess isotropic pore structure without the formation of macrovoids. Fu et al. <sup>[55]</sup> studied the effect of preparation conditions on the outer surface roughness of CAB hollow fiber membranes prepared via NIPS and TIPS. <sup>[53]</sup> Cui et al. <sup>[56]</sup> prepared porous PVDF via TIPS, the ionic conductivity of corresponding polymer electrolyte reached the standard of practical application for polymer electrolyte, which suggests that microporous PVDF prepared by the TIPS can be used as matrix of polymer electrolyte.

### 2.1.2.3 High internal phase emulsion polymerization

High internal phase emulsion (HIPE) polymerization approaches have been applied to the preparation of polymeric porous media. When the volume fraction of the internal phase in a conventional emulsion (Figure 2.8a) is above 74%, which is the maximum packing fraction of

uniform spherical droplets (Figure 2.8b), the droplets deform to create polyhedra, and the dispersed phase is surrounded by a thin film of the continuous phase, this conformation is called a HIPE (Figure 2.8c). Polymerization of the continuous phase containing monomers, such as styrene, and cross-linkers, such as DVB, will lock in the HIPE structure, leading to the formation of a porous polymer, called polyHIPE <sup>[5]</sup>.

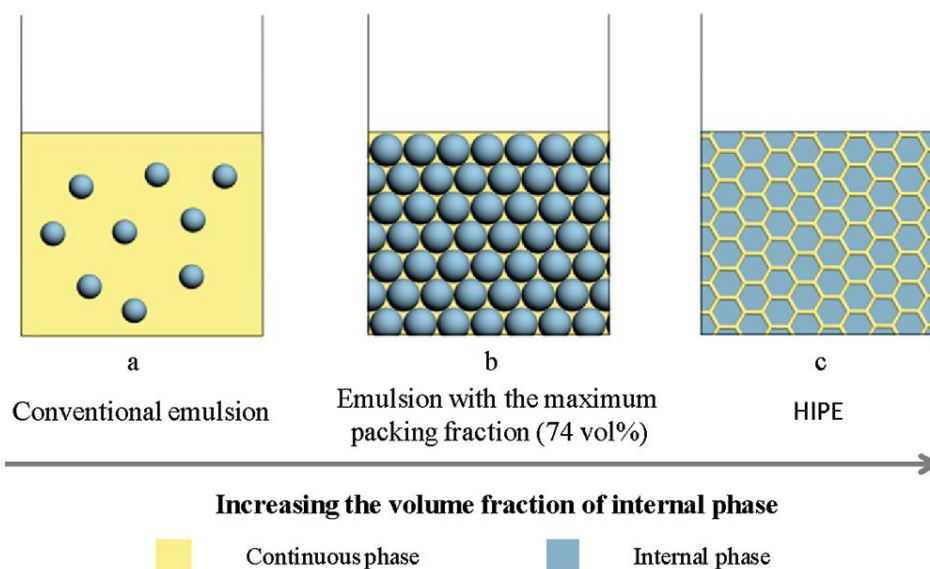


Figure 2.8 Schematic representation for the change from conventional emulsion, through emulsion with the maximum packing fraction (74 vol%), to HIPE when increasing the volume fraction of internal phase <sup>[5]</sup>

#### 2.1.2.4 Extrusion-stretching method

Extrusion-stretching method usually utilized to prepare porous polymeric membranes/fibers from either filled or unfilled semi-crystalline polymers. This process comprises two consecutive steps: firstly, an oriented film is produced by melt-extrusion process. After solidifying, the film is stretched in either parallel or perpendicular direction to the original orientation of the polymer crystallites. For filled systems, the second stretching results in partial removal of the solid fillers, yielding a porous structure <sup>[30]</sup>. For unfilled systems, the second stretching deforms the crystalline structure of the film and produces slit-like pores. Generally, porous membranes/fibers prepared by this technique have relatively poor tear strength along the orientation direction.

#### 2.1.2.5 Block copolymer self-assembly method

Generally, the self-assembly process can occur either in a pure block copolymer (BCP) or in a composite of BCP. There are two distinguishable roles for BCPs in the preparation of polymeric porous media. One is that BCPs serve as the source of the framework for the porous polymers. The other is that BCPs serve as the pore template followed by removal of the BCP to generate the pores.

In this regard, there are several diverse mechanisms for pore formation. The pores can be derived from (1) removal of additional components from a self-assembled composite containing a BCP; (2) selective etching of constituent block from a pure self-assembled BCP; (3) physical reconstruction of the morphology of the self-assembled BCPs; and (4) selective cross-linking of dynamic self-assembled BCP vesicles in solution to obtain hollow structured polymers <sup>[5, 57]</sup>.

#### 2.1.2.6 Breath figures method

Breath figures method (BFs) is commonly used to prepare honeycomb patterned porous polymeric media by casting a polymer solution from a volatile solvent under high humidity. Compared to other methods, BFs does not require high-tech equipment such as mask aligners and post-removal treatment. As a consequence, BFs has drawn increased attention for use as dust-free coatings, sensors, biomaterials, and separation membranes <sup>[5]</sup>. Many researches have been carried out by this method. For example, Barrow et al. <sup>[58]</sup> observed the process of droplets formation on the surface of polymer solution via high speed microphotographic apparatus. Size and number of water droplets on the solution surface increased with increasing exposure time to a humid atmosphere. Park et al. <sup>[59]</sup> reported the fabrication of PS film with hierarchically ordered porous structure by breath figures. The hierarchical ordering of aqueous droplets on polymer solution is realized by the imposition of physical confinement via various shaped gratings, ordered structure can be tuned by dissolving a bit of surfactant in the polymer solution. Pitois and Francois <sup>[60]</sup> observed the formation process of water droplets by lightscattering experiments, and they found that the evolution with time of the mean droplet radius by a power law with an exponent of 1/3.

In summary, the preparation of polymeric porous media has already become and will continue to become a thriving area of research. Despite significant progress have been achieved on the preparation of polymeric porous media, each methods have advantages and limitations. The common problem is that the production process of the above methods are relatively cumbersome, which clearly decreases the production efficiency and increase the cost. Thus A long-term goal for the preparation of porous polymers remains development of simple and scalable procedures for construction of porous polymers <sup>[5]</sup>. It is essential to find new methods which can optimize the excellent porous structure without sacrificing the high efficiency and low-cost. The multilayer coextrusion represents an advanced polymer processing technique, which is capable of economically and efficiently producing polymer materials of multilayers with individual layer thickness varying from micron to nanoscale. The multilayer coextrusion has many advantages including continuous process, economic pathway for large-scale fabrication, flexibility of the polymer species, and tunable

layer structures <sup>[61]</sup>. In the present study, a novel strategy is proposed to prepare polymeric porous media with tunable porous structure via multilayer coextrusion combined with the template method and the TIPS method, which is a highly efficient pathway for large-scale fabrication of polymeric porous media. Moreover, this method is applicable to any melt-processable polymer in principle.

### 2.1.3 Applications

Porous polymers can be used in a wide range of application fields such as adsorption materials, filtration/separation materials, gas storage and separation materials, battery separators, encapsulation agents for controlled release of drugs, catalysts, sensors, and electrode materials for energy storage. <sup>[5]</sup> In this thesis, we mainly focus on the application as adsorption materials and Li-ion battery separators.

#### 2.1.3.1 Lithium-ion batteries separators

Lithium-ion batteries (LIBs) are the preferred power source for most portable electronics due to their higher energy density, longer cycle life, higher operational voltage and no memory effect as compared to NiMH and NiCd systems <sup>[62]</sup>. A typical LIB consists of a positive electrode (composed of a thin layer of powdered metal oxide mounted on aluminum foil), a negative electrode (formed from a thin layer of powdered graphite or certain other carbons mounted on a copper foil), a porous membrane soaked in LiPF<sub>6</sub> dissolved in a mixture of organic solvents <sup>[62]</sup>. The porous membrane is often called as the separator, which is a crucial component for the LIBs. The essential function of LIB separator is to prevent electronic contact, while enabling ionic transport between the negative and positive electrodes. In addition, separator should improve the performance and ensure the safety of LIB application. An ideal separator used in LIBs should own the following features: (1) Electronic insulator to prevent an electric short circuit; (2) Excellent wettability to liquid electrolytes to obtain high lithium ion conductivity; (3) High thermal stability at increased temperature; (4) Mechanical and chemical stability; (5) Other appropriate properties, like thickness, resistance, etc <sup>[63]</sup>.

Many methods have been developed to improve separator's mechanical strength, thermal stability, porosity and electrochemical performance. For example, Ye et al. <sup>[64]</sup> prepared three-dimensional PANI/PI composites via electrospinning and in situ polymerization. Chen et al. <sup>[65]</sup> fabricated (PVDF-HFP)/PI double-components nanofiber membrane via electrospinning, followed by thermal calendaring. The process enhances the mechanical property via fusing the PVDF-HFP component which has lower melting temperature <sup>[66]</sup>.

With the coming out and development of all kinds of electronics, the application range of LIBs expands gradually. The improvements in safety of LIBs are more important than any time, especially in the newly growing application fields such as electric vehicles and aerospace systems<sup>[67]</sup>. Separator ‘shutdown’ function is a useful strategy for safety protection of LIBs by preventing thermal runaway reactions. Compared to the single layer separators, polypropylene (PP) /polyethylene (PE) multilayer separators are expected to provide wider shutdown window by combining the lower melting temperature of PE with the high melting temperature strength of PP<sup>[68]</sup>. The traditional method of preparing such multilayer separators is bonding the pre-stretched microporous monolayer membranes into the multilayer membranes by calendaring, adhesion or welding, and then stretched to obtain the required thickness and porosity<sup>[69]</sup>, which will enhance the mechanical strength but decrease the production efficiency. Moreover, the separators will suffer significant shrinkage at high temperature due to the residual stresses induced during the stretching process, hereby a potential internal shorting of the cell could occur<sup>[70]</sup>. During the past decades, various modifications have been devoted to improve the dimensional thermos-stability of separator including the surface dip-coating of organic polymers or inorganic oxides<sup>[71]</sup>, and chemically surface grafting<sup>[72]</sup>. However, the coated layers were easily to fall off when the separator is bent or scratched during the battery assembly process. Besides, most of the above approaches focused on modifying or reinforcing the existing separators<sup>[73]</sup>, which makes the manufacturing process more complicated and the separators more expensive. Thus it is essential to propose new solutions that can optimize the thermal stability, shutdown property and electrochemical performance without sacrificing the convenient and cost-effective preparation process. The multilayer coextrusion (MC) represents an advanced polymer processing technique that capable of economically and continuously producing multilayer polymers<sup>[74]</sup>. Template method and thermal induced phase separation (TIPS) are widely used manufacturing processes for polymeric porous media with well-controlled and uniform pore structure, high porosity, and good modifiability [Jun-li Shi\_2013]. To the best of our knowledge, no studies have been reported on the combination of the above methods with multilayer coextrusion to prepare multilayer porous separators. Thus in the present study, a novel strategy is proposed to prepare the multilayer LIBs separators comprising alternated layers of microporous PP and PE layers via the above combination.

### 2.1.3.2 Adsorption materials

Nowadays, environmental problems have become a global concern because of their impact on public health<sup>[75]</sup>. Various toxic chemicals such as dyes, polluted oil, heavy metals and polycyclic aromatic hydrocarbons (PAHs), are continuously discharged into the environment as industrial waste,

causing water, and soil pollutants. These chemicals are recalcitrant and persistent in nature, have low solubility in water but highly lipophilic <sup>[76]</sup>.

Dyes are widely used as coloring agents in many industries such as textile, cosmetics, paper, leather, plastics and coating industry. They occur in wastewater in substantial quantities and cause serious environmental problems due to the resistance to degradation. The removal of dyes from aqueous environment has been widely studied and numerous methods such as membrane filtration, adsorption, coagulation, chemical oxidation and electrochemical treatment have been developed. Among these methods, the adsorption technique is especially attractive because of its high efficiency, simplicity of design, and ease of operation <sup>[75]</sup>. Oil spill is a risk during the processes of oil being explored, transported, stored and used, which causes significant and serious environmental damage. The common cleanup methods include in situ burning, oil booms, bioremediation, oil dispersants, and oil sorbents. Among these methods, the application of oil sorbents has proven to be an effective and economical means of solving the problem. Researchers have developed a great deal of materials (inorganic mineral products, organic natural products, and synthetic organic products) as the adsorbents to concentrate, transfer, and adsorb spilled oils<sup>[77]</sup>.

Polycyclic aromatic hydrocarbons (PAHs) belong to a class of chemicals that contain two or more fused benzene rings, which are carcinogenic, teratogenic, mutagenic and difficult to be biodegraded. They are formed during the incomplete combustion of coal, oil, gas, wood, garbage, or other organic substances, such as tobacco <sup>[78]</sup>. In recognition of their toxicity and high mobility, the World Health Organization (WHO) has recommended a limit for PAH in drinking water. The European Environmental Agency (EEA) has also included these compounds in its list of priority pollutants to be monitored in industrial effluents <sup>[76]</sup>. In recent years, various techniques have been employed for the removal of PAHs from wastewaters including biological method, advanced oxidation process and adsorption. Since PAHs have certain toxic effects on microbial and the period of biological treatment is relatively long, the application of biological method is limited. Although advanced oxidation process is fast, it is also limited by easy formation of more toxic products <sup>[79]</sup>. Adsorption is a physical separation process in which certain compounds of a fluid phase are transferred to the surface of a solid adsorbent as a result of the influence of Van der Waals forces <sup>[76]</sup>. Adsorption method is nowadays considered effective for removing persistent organic pollutants and is regarded superior to other techniques, due to its low cost, simplicity of design, high efficiency, ease of operation and ability to treat a selection of PAHs in variety of concentrated forms. Moreover, it removes the complete PAH molecule unlike certain methods which destroy the molecule and leave harmful residues.

Extensive research has been conducted using various adsorbents to adsorb PAHs in contaminated water. Zhang et al. <sup>[80]</sup> explored an effective adsorption of phenanthrene and a natural geosorbent in single and binary solute systems. An et al. <sup>[81]</sup> investigated the adsorption of phenanthrene onto fly ash, which showed stepwise pattern, and solution chemistry such as pH and organic matter played an important role in the distribution of phenanthrene in fly ash-water system. Tang et al. <sup>[82]</sup> employed hexadecyltrimethylammoniumbromide modified fibric peat in adsorption of PAHs such as naphthalene, phenanthrene and pyrene. The hydrophobic fibric peat received improved adsorption rate and adsorption capacity for PAHs <sup>[79]</sup>.

The adsorption method is particularly appealing when the adsorbent is low-priced and could be mass produced <sup>[83]</sup>. According to the similar compatible principle, adsorbents with aromatic ring are comparatively suitable materials for PAHs adsorption. In our previous work, it is found that porous PS bulk materials via high internal phase emulsion polymerization are good candidates to deal with PAHs contamination in water <sup>[84]</sup>. Among the porous adsorption media, the porous membranes are preferable over bulk and powder materials since they possess higher contact area with water and are much easier to be separated from wastewaters. Currently, the porous membranes can be fabricated through numerous methods, including foaming process <sup>[85]</sup>, phase separation method <sup>[86]</sup>, electrospinning <sup>[87]</sup>, top-down lithographic techniques <sup>[88]</sup>, breath figure method <sup>[89]</sup>, template technique, and extrusion spinning process for hollow fiber membranes <sup>[90]</sup>. Among the above methods, the template technique has attracted much attention due to its relatively simple preparation process and tunable pore structure. With the help of the template method, the extrusion-blown molding seems a highly efficient way for the large-scale fabrication of porous membranes. However, the extrusion-blown molding is not suitable for the preparation of brittle PS or particle-embedded polymer membranes. In the present study, a novel strategy is proposed to prepare porous PS membranes with tunable porous structure via multilayer coextrusion combined with the template method, which is a highly efficient pathway for large-scale fabrication of porous PS membranes. The potential application of the porous PS membranes in adsorbing PAHs is explored preliminarily. Pyrene, a representative PAH with medium molecular weight and moderate solubility in water, is selected as the model compound to explore the adsorption performance of the porous PS membranes on PAHs. The related adsorption kinetics and isotherms of the porous PS are also discussed <sup>[78]</sup>.

## 2.2 Transport of colloidal particles in porous media

### 2.2.1 Background and overview

The basic mechanism of the above application processes (PAHs adsorption, Li-ion transport) is based on particle transport and deposition in porous media. Thus it is essential to have a thorough understanding of these processes as well as the dominant mechanisms involved. Moreover, colloidal particle transport and deposition processes in porous media are of great technological and industrial interest for over half a century since they are critical to many other applications ranging from drinking water treatment to drug delivery <sup>[3]</sup>. Accordingly, significant research efforts have been focused on the understanding of particle transport and deposition phenomena, as well as the related theories and mechanisms <sup>[91]</sup>. This chapter aims to summarize the extensive relevant works on particle transport and deposition in porous media, including both experimental researches <sup>[92] [93] [94]</sup> and numerical studies <sup>[95-97]</sup>. Furthermore, reviews of particle transport and deposition onto homogeneous and heterogeneous substrates will also be summarized.

In the past decades, numerous experiments of particle transport and deposition in porous media have been carried out to investigate the key factors that influence particle transport and deposition processes, including particle surface properties, flow field profiles, particle dispersion concentrations, and the geometry of the porous media. These researches contributed to a better understanding of particle transport in porous media under flow <sup>[6]</sup>, and they are helpful in the construction of mathematical models <sup>[98]</sup> for numerical simulation. For example, A. Scozzari et al. <sup>[6]</sup> studied the deposition kinetics of the suspended particles in two saturated granular porous media by performing pulse <sup>[92]</sup> and step-input <sup>[99]</sup> injections, under Darcy flow conditions by establishing breakthrough curves (BTC) The results of the two injection methods were compared to analyze their effects on particle deposition rates in laboratory columns. Yoon et al. <sup>[94]</sup> used laser-induced fluorescence for particle tracking in a translucent porous medium to examine the behavior of a dilute suspension of negatively charged, micron-sized particles. The fate of moving particles as a function of pore fluid velocity and bead surface roughness was observed at both the macroscopic and microscopic levels. In order to directly visualize particle movement in a complex pore space, Ghidaglia et al. <sup>[100]</sup> created an optically transparent medium to study particle transport. Wan et al. <sup>[101]</sup> used photochemically etched glass plates to simulate a porous medium. Similar work could also be seen in the literature <sup>[101, 102]</sup>.

Impinging jet flow or parallel-plate cells are commonly used to experimentally investigate colloids deposition mechanisms <sup>[103-105]</sup>. 1D column experiments using polystyrene Latex particles are the most commonly performed in porous media, owing to their simplicity giving output data in the form of Breakthrough curves (BTC) <sup>[106]</sup>. An Eulerian approach may be adopted to interpret experimental data <sup>[107]</sup>. Risbud and Drazer <sup>[108]</sup> have explored the transport of non-Brownian particles

around a spherical or a cylindrical collector in Stokes regime by focusing on the distribution of particles. Unni and Yang <sup>[105]</sup> have experimentally investigated colloid deposition in a parallel-plate flow cell by means of direct videomicroscopic observation. In filtration, the porous medium is usually assumed to be composed of unit bed elements containing cylindrical cells. For example, Chang et al. <sup>[109]</sup> investigated the deposition of Brownian particles in model parabolic constricted/hyperbolic constricted/sinusoidal constricted tubes.

Generally speaking, experimental studies can supply macroscopic results but with little exhaustive information, such as the particle trajectories and particle deposition and distribution in the whole domain due to the limited number of positioning measurement points. As an alternative, numerical simulations with detailed mathematical models, which are based on computational fluid dynamics (CFD) analysis, have aroused a great deal of interest for many researchers as they can precisely track particles at all locations and observe particle transport and deposition process in full-scale. According to the scale hierarchy, numerical simulations can be divided into macro-scale simulations and micro-scale (pore-scale) simulations. Macro-scale simulations could be obtained from the homogenization procedure <sup>[95]</sup> in order to describe large spatial domains, and are also adopted to ignore the complicated micro-porous structures. While macroscopic simulations could hardly be used to explore the mechanism of the adhesion process <sup>[98]</sup>. Besides, the macroscopic behaviors of flow and transport are controlled by microscopic mechanisms <sup>[110]</sup> Micro-scale simulations, with the advent of advanced algorithms and parallel computing, have become attractive tools to explore the average microscopic mechanisms and uncover the averaged macroscopic behavior by solving simultaneously the Stokes or Navier-Stokes equations and the advection-diffusion equation, which are the underlying governing equations for flow and transport in porous media respectively. The micro-scale models can simulate a variety of situations, such as bacteria in biofilms. Moreover, modification of fluid properties and boundary conditions is much easier during computer simulations than in experiments <sup>[111]</sup>. Extensive work has been done in the area of particle transport and deposition in porous media by means of microscale simulation.

For example, Boccardo et al <sup>[95]</sup> have numerically investigated the deposition of colloidal particles in 2D porous media composed of grains of regular and irregular shapes. They found that the Brownian attachment efficiency (to be defined below) deviates appreciably from the case of single collector. Coutelieis et al. <sup>[112]</sup> have considered flow and deposition in a stochastically constructed spherical grain assemblage by focusing on the dependence of capture efficiency and found that the well-known sphere-in-cell model remains applicable provided that the right porous medium properties are taken into account. Sefrioui et al. <sup>[113]</sup> studied the transport of solid colloidal particles

in presence of surface roughness and particle/pore physicochemical interactions by a “one fluid” approach. Lopez et al. <sup>[17]</sup> investigated the deposition kinetics of spherical colloidal particles in dilute regime through a pore consisting of two parallel plates. Sirivithayapakorn et al. <sup>[114]</sup> used micromodels to explore the mechanisms of transport of colloid particles of various sizes and they investigated factors that would influence the colloid transport in porous media. Bradford et al. <sup>[115]</sup> proposed a modeling framework to study the controlling mechanisms of colloid particle retention and release in porous media. Their work provided valuable and profound insight on the understanding of particle tracking process and mechanisms in porous media.

## 2.2.2 Particle transport and deposition mechanisms

Knowledge of the mechanisms governing colloidal particle transport and deposition in porous media is of great importance in several natural and engineered processes. Thus it is significant to investigate the dominant mechanisms and to develop a comprehensive understanding of the deposition processes <sup>[116]</sup>. Generally, the process of particle deposition can be divided into the following two steps: transport and attachment. During the first step, the particles are transported from the bulk of the fluid to the collector surface by diffusive and/or convective transport, and the collection efficiency is denoted by  $\eta_0$ . During the second step the particles are adsorbed on the collector surface, which is caused by the sorption process between the collector wall and the particles, and the attachment efficiency is denoted by  $\alpha$ . The product of the above two efficiencies gives the total collection efficiency,  $\eta = \eta_0\alpha$  (see below), which includes both the transport and the attachment of the particles <sup>[117]</sup>.

### 2.2.2.1 Diffusive transport and Brownian state

Diffusive transport occurs due to the Brownian motion of colloidal particles arising from the random collision of molecules of the surrounding fluid <sup>[118]</sup>. The trajectory of a colloidal particle could be obtained by tracking the movements of the colloidal particle undergoing Brownian motion at the usual experimental timescale intervals, the results show that the trajectory is not a mathematically smooth curve, and the apparent velocity of a Brownian particle derived from the trajectory could not reflect the real velocity of the particle. Therefore, the mean-square displacement is generally used to describe the motion of Brownian particles <sup>[117]</sup>.

The bulk diffusion coefficient for an isolated sphere in an infinite medium is given by the Stokes Einstein expression as:

$$D = \frac{k_B T}{6\pi \mu a_p} \quad (2-1)$$

where  $k_B$  is the Boltzmann constant,  $T$  is the absolute temperature,  $a_p$  is the particle radius and  $\mu$  is the dynamic viscosity. The thermal energy term  $k_B T$  represents the extent of molecular collisions, and the particle size and viscosity are two main factors that affect the diffusion process. Diffusion is inversely proportional to the particle size and the dynamic viscosity of the suspending fluid <sup>[99, 116]</sup>. As Equation (2-1) suggests, diffusion decreases as particle size becomes larger for a given value of viscosity but is the dominant mode of transport for “point like” particles. It is important to note that hydrodynamic interactions effect diffusive particle transport near the collector surface just like it does for convection <sup>[119-121]</sup>. Hence, it experiences increased resistance near the wall as it tries to squeeze the fluid molecules out of the thin space during its course of vibration. One can also obtain an approximate estimate of the system-size correction by using the Stokes-Einstein relation for the diffusion coefficient with either stick or slip boundary conditions <sup>[122]</sup>:

$$D \approx \begin{cases} \frac{k_B T}{6\pi \mu R} \text{(stick)} \\ \frac{k_B T}{4\pi \mu R} \text{(slip)} \end{cases} \quad (2-2)$$

where  $R$  is the hydrodynamic radius of the particle.

### 2.2.2.2 Convective transport and hydrodynamic interactions

Hydrodynamic factors such as flow field profiles, the distributions of hydraulic gradient and hydraulic conductivity contribute to particle convective transport. For Brownian particles, apart from the Brownian motion, colloidal particles suspended in a fluid are usually considered to flow along the streamlines with the same velocity as the fluid. In most colloidal deposition systems, the particles are usually assumed to be much smaller than the collector, so the flow field is only disturbed by the particles when the particles are deposited or very close to the surface wall <sup>[116, 123, 124]</sup>.

Based on the finite element method, a new mathematical model has been developed by Jin et al. <sup>[91]</sup> to study the overall influence of hydrodynamics on particle deposition on spherical collectors. Their work indicates that the particle deposition is highly influenced by the hydrodynamic effects. Early models, such as those presented in the works of Levich <sup>[125]</sup> and of Happel <sup>[126]</sup>, are developed for a single collector. However, the flow field around each collector could be influenced by the neighboring collectors and, as a result, particle transport and deposition process will also be affected.

Boccardo et al. <sup>[95]</sup> studied the effect of the irregularity of the collectors and the presence of multiple collectors. Consideration of hydrodynamic contributions to particle deposition may help to explain discrepancies between model-based expectations and experimental outcomes.

Risbud et al <sup>[108]</sup> investigated the suspended particle trajectory as it moves past a sphere/cylinder driven by a constant external force/a uniform velocity field in the limit of infinite Péclet number and zero Reynolds number. They derived an expression for the minimum particle-obstacle separation attained during the motion as a function of the incoming impact parameter, as is shown in Figure 2.9. The minimum distance between the particle and obstacle surfaces dictates the relevance of short-range non-hydrodynamic interactions such as van der Waals forces, surface roughness and so on. The scaling relation derived for small  $\text{Pe}$  shows that during the motion of a particle past a distribution of periodic or random obstacles, extremely small surface-to-surface separations would be common. This highlights the impact that short-range non-hydrodynamic interactions could have in the effective motion of suspended particles.

The frequency at which particles in the aqueous phase come into contact with the solid phase/ the “collector” is defined as collection efficiency  $\eta$ . One of the most commonly used formulas for  $\eta$  is derived from Rajagopalan and Tien’s Lagrangian trajectory analysis <sup>[14]</sup> within Happel’s sphere-in-cell porous media model <sup>[127]</sup>, which is written as <sup>[128]</sup>:

$$\eta = \frac{I}{\pi a_c^2 U C_0} \quad (2-3)$$

where  $I$  is the overall rate at which particles strike the collector,  $a_c$  is the radius of the collector,  $U$  is the approach velocity of the fluid, and  $C_0$  is the number concentration of particles in the fluid approaching the collector. The Péclet number ( $\text{Pe}$ ) is a dimensionless number that is relevant for the study of transport phenomena of colloidal dispersions. Here, it is defined to be the ratio of the rate of advection to the rate of particle’s diffusion:

$$\text{Pe} = \frac{\bar{u} a_p}{D} \quad (2-4)$$

where  $\bar{u}$  is the average convection velocity along the mean flow axis,  $a_p$  is the radius of the particles. In the case of multiple neighboring collectors, the collection efficiency  $\eta$  is defined as <sup>[129]</sup>:

$$\eta = 4\text{Pe}^{-2/3} A_s^{1/3} \quad (2-5)$$

where  $\eta$  is the diffusional collection (collection by Brownian motion),  $Pe$  is the Péclet number,  $T$  is the absolute temperature, and  $A_s$  is Happel's flow parameter [129]:

$$A_s = \frac{2(1-p^5)}{w}$$

$$\begin{cases} p=(1-\varepsilon)^{1/3} \\ w=2-3p+3p^5-2p^6 \end{cases} \quad (2-6)$$

where  $\varepsilon$  is the porosity.

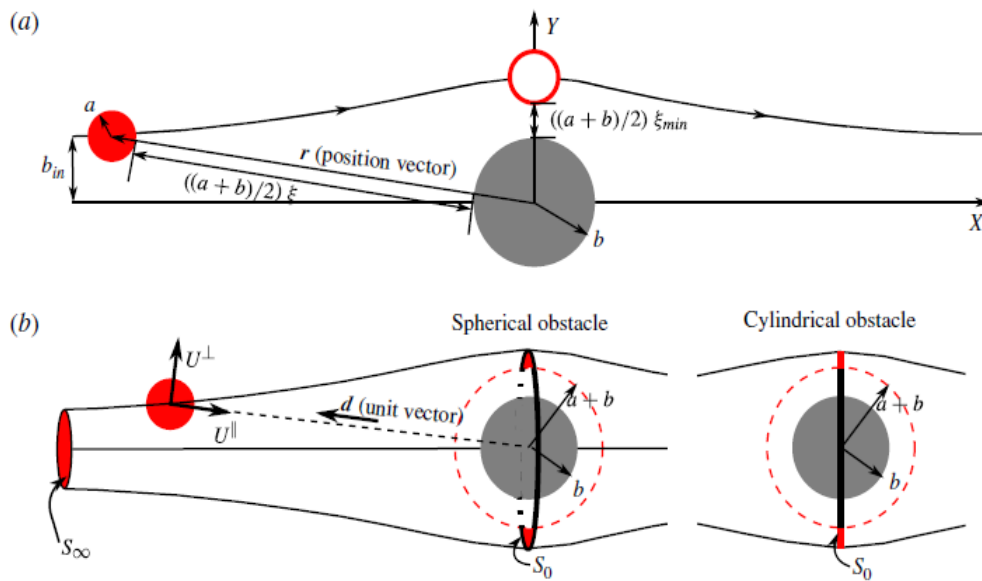


Figure 2.9 Schematic representation of the problem [108]. (a) The small circle of radius  $a$  represents the moving sphere with a corresponding incoming impact parameter  $b_{in}$ . The circle of radius  $b$  represents the fixed obstacle (a sphere or a cylinder). The empty circle represents the position of the suspended particle as it crosses the symmetry plane normal to the  $x$ -axis. The surface-to-surface separation  $\xi$  and its minimum value  $\xi_{min}$  are also shown. (b) Representation of the conservation argument used to calculate the minimum separation. The unit vector in the radial direction  $d$ , the velocity components in the plane of motion, both far upstream ( $S_\infty$ ) and at the plane of symmetry ( $S_0$ ) are shown

### 2.2.2.3 Extended DLVO theory

The process of particle deposition can be divided into the following two steps: convection to the collector and adsorption (capability of a solid substance to attract to its surface molecules of a gas or solution with which it is in contact) due to the particle/collector interaction. Such a potential which origin is the physical-chemical interaction, which is usually calculated from DLVO theory that include electrical double layer, van der Waals, and sometimes short range Born interactions [13].

According to different influence range, VDW and EDL are called long-range forces (up to 100 nm from the surface) and the dominant forces controlling the attachment and detachment of particles<sup>[107]</sup>, while the Born repulsion force is called short-range force (being dominant only within 5 nm from the surface) which drops very sharply with the distance. In general, the interaction contains two minimums and one energy barrier. When particle and collector are of opposite charges or when salt concentration is very high, the potential is purely attractive, which is usually called favorable deposition. The particle deposition rate is one of the most significant parameters in studies of particles deposition onto collector surfaces and it is necessary to express this rate in a dimensionless form<sup>[13]</sup>. For the isolated collector, the collector efficiency ( $\eta$ ) is commonly evaluated through the product of the attachment efficiency ( $\alpha$ ) and the dimensionless transport rate ( $\eta_0$ )<sup>[130]</sup>. The definition of collection efficiency ( $\eta$ ) could refer to equation (2-3)<sup>[128]</sup>. Therefore in the case of favorable deposition, the attachment efficiency is approximately 1, and the deposition rate is equal to the transport rate.

### 2.2.3 A review of colloidal particle transport and deposition in homogenous porous media

#### 2.2.3.1 Mathematical models, theoretical frameworks

The mathematical modeling of particle transport and deposition in homogenous porous media usually comprises the following three parts: (1) transport process in the liquid phase due to hydrodynamic dispersion and convection, (2) transfer between the liquid phase and the solid phase (due to attachment and detachment), (3) inactivation, grazing or death<sup>[124]</sup>. Particle transport in saturated porous media is usually described by the advection dispersion-sorption (ADS) equations<sup>[131]</sup>. There are various forms of ADS equations, for example, a simplified form for one-dimensional particle transport in a homogeneous porous medium is:

$$\varepsilon \frac{\partial c}{\partial t} + \rho_b \frac{\partial s}{\partial t} = \varepsilon D \frac{\partial^2 c}{\partial x^2} - v_D \frac{\partial c}{\partial x} + R_w \varepsilon - R_s \rho_b s \quad (2-7)$$

where  $s$  is the adsorbed mass per unit mass of the solid phase,  $c$  is the free particle mass concentration at a distance  $x$  and time  $t$ ,  $D$  is the hydrodynamic dispersion coefficient,  $v_D$  is the Darcy velocity,  $\varepsilon$  is the porosity,  $\rho_b$  is the dry bulk density of the porous medium,  $R_w$  and  $R_s$  are the decay or inactivation rates for particles in the liquid and solid phase, respectively<sup>[124]</sup>. . The equation above

is usually completed by the equilibrium equation stating that the variation of  $s$  arises from adsorption and desorption:

$$\rho_b \frac{\partial s}{\partial t} = \varepsilon k_a c - \rho k_d s \quad (2-8)$$

where  $k_a$  and  $k_d$  are the first order kinetic attachment and detachment rates, respectively. It is important to note that although the particle filtration processes occur at a microscopic level, the attachment and detachment rates are determined at the macroscopic scale <sup>[124]</sup>.

Classical Filtration Theory (CFT), corresponding to the case of  $k_d = 0$  in the Eq. (2-8), was the first theory developed to predict the particle attachment coefficient and the CFT attachment coefficient is based on the surface properties of both the porous medium and the particles. The particle sorption (the process in which one substance takes up or holds another) or “filtration” process in porous media may be governed by three primary mechanisms, as is shown in Figure 2.10: (1) surface filtration (the sizes of particles are larger than the pore sizes of the porous media), (2) straining filtration (the sizes of particles are not much smaller than the pore sizes), and (3) physico-chemical filtration (the sizes of particles are smaller than the pore sizes by several orders of magnitude) <sup>[132]</sup>.

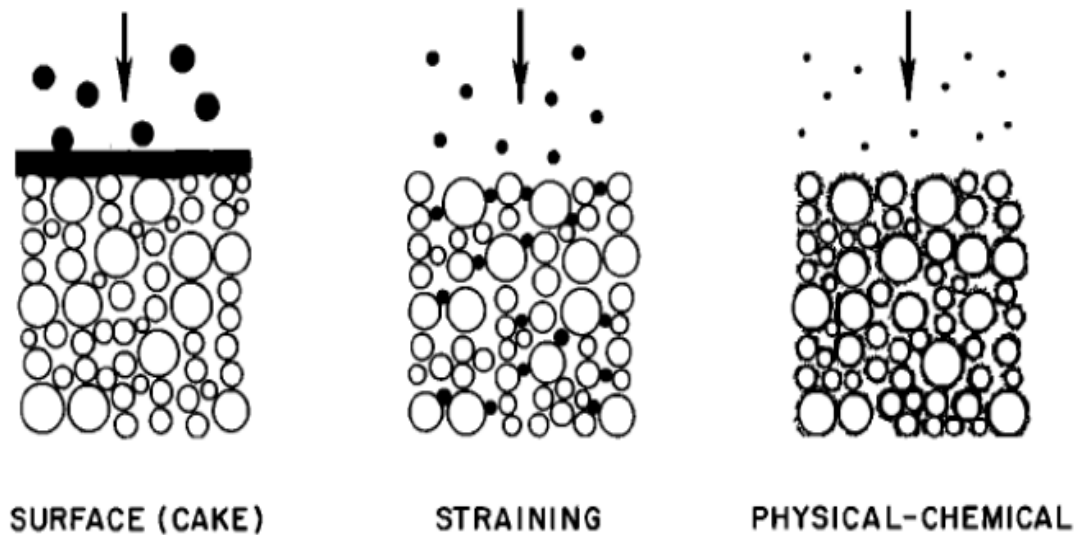


Figure 2.10 Three filtration mechanisms of particle transport in porous media <sup>[132]</sup>

The way to obtain the “collector efficiency” is firstly proposed by Yao et al. <sup>[13]</sup> This efficiency describes how particles interact with an isolated grain “collector” within a porous medium. In the classical CFT, the deposition efficiency is represented by the deposition efficiency of a unit collector (an isolated solid grain) since the porous medium is assumed to be represented by an assemblage of

perfect spherical solid grains (collectors). Generally, the colloid deposition efficiency is typically governed by the superposition of three mechanisms: interception, sedimentation (or gravitation forces), and diffusion. The introduction of CFT sparked several decades of research at the pore, macroscopic, and field scales to develop predictive capabilities and have comprehensive understanding of colloidal particle transport and deposition in porous media <sup>[13]</sup>. Nevertheless, many studies have reported that the classical CFT can only describe particle transport under very limited conditions <sup>[131]</sup>. For example, this theory is suitable for clean-bed filtration with no substantial energy barrier between the particles and targeted surfaces <sup>[91]</sup>.

When there are deposited particles on the surfaces, the hydrodynamic shadowing effect could not be ignored. The possibility to induce structure in layers of colloid particles by using the hydrodynamic blocking effect is investigated both experimentally and by using Monte Carlo simulations. The results indicate that the shadow length scales with the Pe with an exponent less than one due to attractive particle-surface interactions. The reduced particle density behind particles in the flow direction promises the possibility to selectively deposit particles in these locations after reducing the hydrodynamic screening of the surface. Simulations show that it is indeed possible to self-assemble particle pairs by performing consecutive depositions under different flow conditions on the same surface. The surface exclusion behind deposited particles is increase with the Pe. To model the data we used a simple expression of the shadow length  $L_s$  as a function of Pe, given by <sup>[133]</sup>

$$L_s = A_h Pe^n + L_{s0} \quad (2-9)$$

where  $L_{s0} = 9$  corresponds to the experimentally determined distance for the pair correlation function to reach unity in the direction perpendicular to the flow. A best fit was achieved for an exponent  $n = 0.87 \pm 0.1$  and  $A_h = 0.7$ .

### 2.2.3.2 Review of previous work and latest progress

Based on the above mathematical models, theoretical frameworks and classical researches, a great number of studies have been carried out to further investigate the colloidal particle transport and deposition in homogenous porous media during the past two decades. According to the research objective, these works could be divided into the following three parts:

#### 1. Investigation or improvement of modelling of deposition mechanisms

During the past decades, many researchers have focused on the investigation or improvement of modelling of the deposition mechanisms. Gianluca Boccardo and et al. <sup>[95]</sup> improved the current

understanding of particle transport and deposition in porous media by means of detailed CFD simulations. The results show that the interactions between close collectors result in behaviors that are different from the theory developed by Happel and co-workers <sup>[134]</sup>. Hasan Khan et al. <sup>[135]</sup> investigated the porous media damage and particle retention mechanisms under different conditions (particle size/pore size) by means of experimental and simulation methods. The results indicate that the retention mechanism for small particles is surface interaction dependant, while for large particle straining is dominant. Lopez et al. <sup>[17]</sup> carried out micro-scale numerical simulations of colloidal particles deposition onto the surface of a simple pore geometry consisting of two parallel planar surfaces. They investigated the deposition kinetics of colloidal spheres from dilute dispersions flowing through the pore. The results show that both the surface coverage  $\Gamma$  and the equivalent hydrodynamic thickness of the deposit,  $\delta_h$ , feature a definite plateau at low Pe (a dimensionless number defined to be the ratio of the rate of advection to the rate of particle's diffusion), and both are decreasing functions at high Pe. In addition, the dimensionless maximum surface coverage was shown to follow a power law given by  $Pe^{-1/3}$ , where the Péclet number was calculated on the basis of the flow velocity at a distance of 3 particle radii from the pore wall.

In the presence of an energy barrier, Johnson et al. <sup>[136]</sup> proposed a mechanistic description of colloid retention in porous media by means of a particle trajectory model. The results indicate that colloid retention in porous media with an energy barrier may occur via two mechanisms: wedging within grain to grain contacts and retention in flow stagnation zones. Both mechanisms were sensitive to colloid surface interaction forces such as the energy barrier height and secondary energy minimum depth. Civan et al. <sup>[137]</sup> presented a systematic formulation of the appropriate rate equations for the pore-surface and pore-throat particulate deposition and removal processes during flow through porous media. The exploration results offered many meaningful revisions for generalized applications. Although there are several transport models with respect to particle retention (the act of retaining or something retained) as is shown in Table 2.1, but neither Langmuir adsorption/desorption nor colloid filtration models could fully capture particle retention mechanisms under various types of flowing conditions. Zhang et al. <sup>[138]</sup> proposed an independent two-site model for nanoparticles deposition each of a given energy barrier. Numerous critical features of the widely different sets of experimental data are captured by this model, suggesting that its assumptions are addressing important phenomena. Moreover, the finite capacities in the two-site model provide some insight into the maximum nanoparticle retention concentration in porous media which is significant in nanoparticle applications in the oilfield .

Table 2.1 Existing models for particle deposition in porous media <sup>[138]</sup>

Model	Deposition term	Fitting parameters
Colloid filtration model	$\frac{\rho_b}{\phi} \frac{\partial s}{\partial t} = k_{dep} c \quad k_{dep} = \frac{3(1-\phi)}{2d_c} v \alpha \eta_0$	$\alpha$
Filtration model with site blocking	$\frac{\rho_b}{\phi} \frac{\partial s}{\partial t} = k_{dep} \left(1 - \frac{s}{s_{max}}\right) c$	$\alpha, s_{max}$
Filtration model with detachment	$\frac{\rho_b}{\phi} \frac{\partial s}{\partial t} = k_{dep} c - \frac{\rho_b}{\phi} k_{det} s$	$\alpha, k_{det}$
Kinetic Langmuir model	$\frac{\rho_b}{\phi} \frac{\partial s}{\partial t} = k_{\alpha} \left(1 - \frac{s}{s_{max}}\right) c - \frac{\rho_b}{\phi} k_d s$	$k_{\alpha}, k_d, s_{max}$

## 2. Exploration of the key influence factors of particle deposition

Numerous works have been carried out to explore the key factors that influence the particle transport and deposition in homogeneous porous media. For instance, Ahfir et al. <sup>[139]</sup> investigated the effects of porous media grain size distribution (GSD) on the transport and deposition of polydisperse suspended particles. The results indicate that both the deposition kinetics and the longitudinal hydrodynamic dispersion coefficients are influenced by the porous media grain size distribution. Moreover, the filtration efficiency is increasing with the uniformity coefficient of the porous medium grain size distribution. Large grain size distribution leads to narrow pores, which

also enhances the deposition of the particles by straining. Lin et al. <sup>[140]</sup> studied the dynamics of asphaltene deposition in porous media using microfluidic devices. Koullapis et al. <sup>[141]</sup> investigated the deposition of inhaled aerosol particles, and assess the effects of inlet flow conditions, particle size, electrostatic charge, and flowrate. The conclusions could be summarized as: the effect of inlet velocity profile dissipates quickly as a result of the complex geometry (realistic human upper airways geometry), and the deposition fraction of particles is increased with flow rate due to greater inertial impaction, especially for bigger particles ( $>2.5 \mu\text{m}$ ). Moreover, the effect of charge is more significant for smaller particles. Becker et al. <sup>[142]</sup> quantified the coupled effects of physical and chemical factors on the release behavior of polymer-coated magnetite nanoparticles in water-saturated quartz sand. The multi-dimensional multispecies transport simulator (SEAWAT) combined with experimental observations were employed. The results conclusively demonstrated that the introduction of de-ionized water into the flow lead to lower pore-water ionic strength and lower attractive forces, which will contribute to particle detachment. Park et al. <sup>[143]</sup> investigated the release of Engineered Nano Materials (ENMs) and their environmental behavior in aqueous porous media. Influencing factors including physicochemical properties, solution chemistry, soil hydraulic properties, and soil matrices have also been studied. The results indicate that ENMs are transported readily under ‘unfavorable’ conditions: surface functionalization, surface physical modifications, high pH, low ionic strength, and high flow velocity. Wang et al <sup>[144]</sup> provided an introductory overview of the key factors controlling the fate and transport of Engineered Nano Particles (ENP) fate and transport in porous media. The main factors that influence ENP transport could be categorized into three groups, as is shown in Figure 2.11.

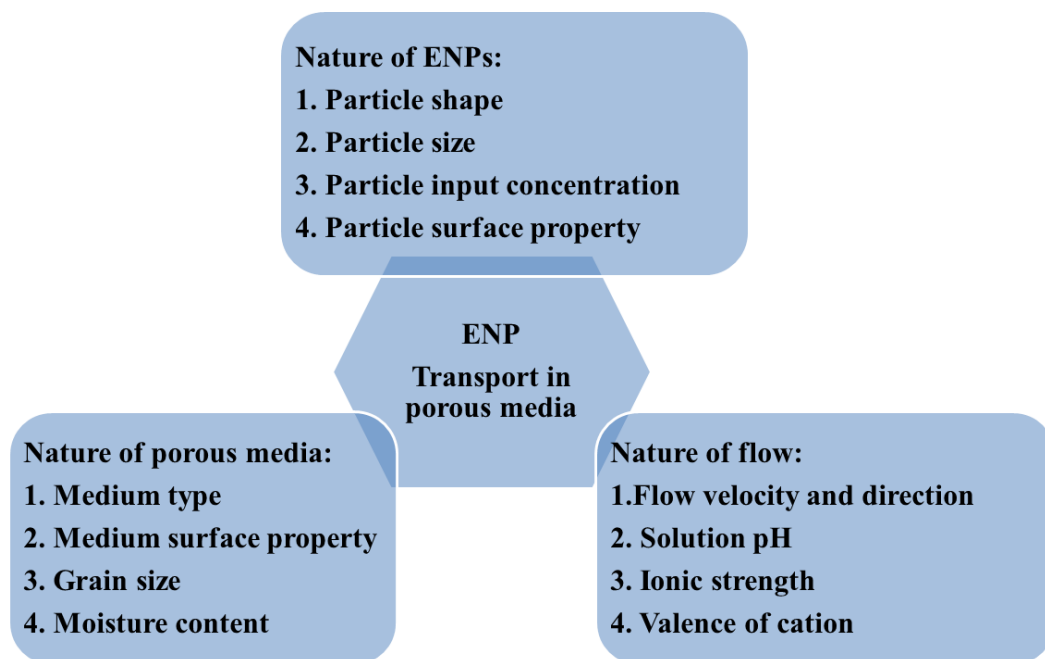


Figure 2.11 Key factors controlling engineered nanoparticle transport in porous media <sup>[144]</sup>

Li et al. <sup>[145]</sup> directly observed the colloid deposition environments in Porous Media (PM) in the absence of an energy barrier by means of light microscopy, Magnetic Resonance Imaging (MRI), and X-ray MicroTomography (XMT). The results demonstrated that the deposited concentrations decreased log-linearly with increasing transport distances. Buret et al. <sup>[146]</sup> carried out a laboratory study of oil-in-water emulsion flow in porous media to investigate the mechanisms of oil-droplet retention and its effect on permeability. The results demonstrate that at the Random Sequential Adsorption (RSA) limit, the induced permeability loss is significant even at high pore-size/droplet size ratio. In the considered Pe range, the permeability loss decreases according to a power law similar to that relating maximum surface coverage in Pe with an exponent of  $-1/3$ . Li et al. <sup>[147]</sup> also directly observed the colloid deposition environments in porous media in presence of an energy barrier by means of the XMT technique. The results indicate that the deposited concentrations decreased nonmonotonically with increasing transport distances, and in presence of an energy barrier, colloid deposition at grain-to-grain contacts is dominated. Sefrioui et al. <sup>[113]</sup> simulated the transport of a solid colloidal particle in presence of surface roughness and particle/pore physicochemical interactions, the simulation was carried out at the pore scale by adopting a “one fluid” approach. They found that the existence of surface roughness is a necessary but not sufficient condition for particles retention, and the residence time is increased with the ionic strength since particle/pore surface becomes less repulsive with higher ionic strength. Ahmadi et al. <sup>[148]</sup> investigated the colloids deposition and re-entrainment in presence of a rough surface, as well as the influence of physicochemical and hydrodynamic conditions. They present firstly experiments on retention and release of colloids in a porous medium and come up to the following conclusions: for given hydrodynamic conditions and suspension chemistry, the colloids deposition process is “piston-like” and the deposited layer at the end of the process is a monolayer. After the deposition step, when the porous medium is flushed by pure water at increasing Pe, the cumulative fraction of removed colloids increases until all already deposited particles are recovered.

### 3. Development of novel models or codes to solve specific and realistic problems

Since most real conditions are more complex and diverse, it is necessary to develop specific models or codes to solve specific problems. Taghavy et al. <sup>[149]</sup> developed and implemented the one-dimensional hybrid Eulerian-Lagrangian particle (HELP-1D) transport simulator to explore coupled particle aggregation and transport processes. The results indicate that when environmental conditions promote particle-particle interactions, neglecting aggregation effects can lead to under- or

over-estimation of nanoparticle mobility. Tosco et al. <sup>[150]</sup> developed a novel MNM1D code (Micro-and Nanoparticle transport Model in porous Media) to simulate colloid deposition and release in saturated porous media during transients ionic strength. The good agreement between MNM1D and the other models (well-established software, namely Hydrus-1D and Stanmod) demonstrate that this novel code could be used for the simulation of colloidal transport in groundwater under transient hydrochemical conditions. Later, Bianco et al. <sup>[16]</sup> proposed an improved modeling approach MNM3D (Micro and Nanoparticle transport Model in 3D geometries) to simulate engineered nanoparticles injection and transport in three-dimensional (3D) porous space. This simulation is based on the modified advection-dispersion-deposition equations accounting for the coupled influence of flow velocity and ionic strength on particle transport. Furthermore, MNM3D can also be applied to more realistic cases, with complex geometries and boundary conditions. Katzourakis et al. <sup>[151]</sup> developed a conceptual mathematical model to describe the cotransport of viruses and colloids in 3D water saturated, homogeneous porous media with uniform flow. The results illustrate the good agreement between the experimental data (collected by Syngouna and Chrysikopoulos) <sup>[152]</sup> and results from this model. This novel model captures most of the physicochemical processes during virus and colloid cotransport in porous media. Moreover, the results indicate that the interactions between suspended virus and colloid particles can significantly affect virus transport in porous media. Hoepfner et al. <sup>[153]</sup> presented a new investigative tool to better understand asphaltene behavior. The results indicate that the governing factor controlling the magnitude of asphaltene deposition is the concentration of insoluble asphaltenes present in a crude oilprecipitant mixture. Moreover, the deposit is significantly thicker at the inlet than at the outlet. Su et al. <sup>[154]</sup> developed an algorithm named RIGID (spherical particle and geometry interaction detection) to detect particle interactions with an arbitrarily complex wall in the framework of soft-sphere model and applied it to simulations of dense gas-particle flows in complex geometries. Three test cases have been carried out, (single particle collision with a complex geometry/bubble fluidized bed/immersed tube fluidized bed) and the results indicate that RIGID can be used to detect particle-wall contact in an arbitrarily complex geometry since particle contacts with any geometry are in fact a combination of the three basic types of contact tested in their work (plane/convex edge/convex vertex with single particle contact).

Apart from the above three main aspects, the investigation of the spatial distribution of deposited particles have also attracted considerable attention. Indeed, the understanding of the particle distribution regularities could help us to obtain the desired distribution of deposited particles, which could be used in many practical applications, including the optimization of inhalation therapeutic strategies to target drugs to desired lung regions <sup>[155]</sup>. There are relatively few researches that have

been carried out to clarify the particle deposition distribution in porous media. For example, Kusaka et al. <sup>[156]</sup> explored latex particle deposits on a cylindrical collector in a microfluidic chamber by means of an in-situ observation method. The results demonstrated that the deposits morphology generated at a single collector surface in a microfluidic chamber is highly dependant on particle size and flow rate. For lower Péclet numbers (Pe), particles deposit is mainly uniform except at the rear where particles do not attach. For higher Pe, deposits adopt a columnar morphology at the collector stagnation point. For smaller particles, the distribution is uniform with lower Pe, while it is anisotropic for higher Pe. For bigger particles, the distribution is anisotropic for all cases with different Pe, and the particles deposit at the rear. Ahfir et al. <sup>[139]</sup> explored the coupled effects of porous medium's grain size distribution and hydrodynamic forces on transport and deposition of suspended particles by performing transport experiments in a column of 62 cm in length using the step-input injection technique. The results show that the retention is non-uniformly distributed in the porous media, the deposition is more obvious at the entrance, while decreases with depth. Moreover, the retention decreases with increasing flow velocity. Li et al. <sup>[157]</sup> reported the two-dimensional simulation of the motion and deposition of micro- or nano-scaled particles transported by a fluid traversing three different kinds of square pores. The flow fields are numerically simulated by means of Lattice Boltzmann Method (LBM). The results show that the dispersion of particles in the three different square pore structures are very different, and vary with Stokes number (defined as the ratio of the characteristic time of a particle to a characteristic time of the flow or of an obstacle) for the same square pore even the Reynolds numbers are the same. In addition, the number and the position of deposited particles are analyzed. It is shown that the deposition characteristics of each wall are mainly influenced by Stokes number, Reynolds number and the pore structure.

### 2.2.3.3 Limitations and inspirations for the current work

The above research works have provided valuable and profound insight on the understanding of particle transport and deposition process in homogeneous porous media, and improved and enriched the theoretical frameworks in this field, which are of great importance for the current work. However, most of the above investigations are valid only for clean-bed filtration (before any significant deposition of particles on the collector occurs). Particle deposition and filtration are intrinsically transient processes, since deposited material changes both the geometry of the interstitial spaces of the filter (porous medium) and the nature of the collector surfaces, therefore affecting the deposition of other colloidal particles. Nevertheless, due to the complexity of the topic, it is usually modelled under steady state conditions, assuming that the deposited particles suddenly “disappear” after contacting the filter medium (clean bed filtration theory). This assumption is valid at the initial stage

of the phenomenon, while when the number of deposited particles increases to a certain value, the influence of deposited particles cannot be neglected. Until now, few works have consider the volume of the deposited particles. Thus in the present study, in order to take the volume occupied by the deposited particles into account, the geometry of the pores was reconstructed and the flow field was updated once particles were deposited. <sup>[137]</sup>

In addition, in most of the above-mentioned studies, simulations were simplified into one or two dimensions to reduce the calculation time. However, this simplification restricts the particle motion, and reduced the accuracy of the results since most real porous media are three-dimensional. Therefore, it is necessary to improve the simulation model by enabling three-dimensional simulation <sup>[16]</sup>. To the author's knowledge, few simulation tools are available in the literature to explore the three-dimensional spatial distribution of deposited particles in microchannel while taking the influence of deposited particles into account. Consequently, in the present study, a novel 3D-PTPO (Three-dimensional particle tracking model by Python<sup>®</sup> and OpenFOAM<sup>®</sup>) code developed in I2M laboratory is proposed to investigate the relationship between particle distribution profiles and Péclet number, as well as the geometry of porous media. In addition, the transport and deposition behavior of colloid particle in porous media and the variations of several key parameters (surface coverage, porosity, permeability, etc.) versus  $Pe$  are also investigated. The validity of the numerical code has been demonstrated via comparing results with other studies and theories. Furthermore, modifications could be easily made to adjust the code to further applications, e.g. to simulate the multi-layer particle deposition by introducing attractive particle-particle interaction, to realize the functionalization of a certain region in porous media, etc.

## 2.2.4 A review of colloidal particle transport and deposition in heterogeneous porous media

### 2.2.4.1 Research background mathematical models

The discussions in the previous sections of this chapter focus on particle transport and deposition onto homogeneous surfaces. However, almost all natural porous media exhibit both physical and chemical heterogeneities. Artificial porous media are sometimes geometrically and chemically simpler, while heterogeneity still exists in most of their wall surfaces <sup>[158]</sup>. Particle transport and deposition in heterogeneous porous media have been an area of intense investigation. This is because when particles under flow approach such heterogeneously patterned surfaces, they exhibit various

adhesion characteristics and dynamic signatures according to their different physico-chemical properties including charge, shape and size. A thorough understanding of the above processes and dominated mechanisms is significant for the development of separation, adsorption and emerging sensing technologies at the micro- and nano-scales <sup>[116, 159]</sup>.

For chemical surface heterogeneities (patches) much larger than the colloidal particles, the patchwise heterogeneity model provides an accurate description of particle deposition rates on heterogeneous surfaces. For example, the two-patch charge model has been successfully applied to describe colloidal transport and deposition in chemically heterogeneous porous media. These studies demonstrated that colloid deposition rate is directly proportional to the degree of porous medium chemical heterogeneity <sup>[160]</sup>. While for size of surface heterogeneities much smaller than the colloidal particles, the patchwise heterogeneity models may not be well-suited as some deposition is always predicted if any region of the surface is favorable <sup>[161]</sup>.

In order to develop more realistic models for particle deposition onto heterogeneous porous media, and have a systematic understanding of the above process and mechanisms, extensive research has been done during the past two decades in the area of both experimental and theoretical studies, dealing with surface chemical/physical heterogeneity at macroscopic or microscopic scales, as described below <sup>[162]</sup>. Here, it should be define that, according to the sources of heterogeneity, surface heterogeneity can be divided into two categories: physical heterogeneity and chemical heterogeneity. The former one is usually due to surface roughness and the latter one is usually attributed to the non-uniform distribution of charged species <sup>[116]</sup>. Besides, surface heterogeneity can be classified in terms of scale as either macroscopic or microscopic.

#### 2.2.4.2 Physical and chemical heterogeneity

##### 1. Physical heterogeneity

Physical heterogeneity has far-reaching effects on particle deposition, and often allows to explain the disagreement between the measurements of interaction force made by means of atomic force microscopy or electrophoretic mobility at small Debye lengths (a measure of a charge carrier's net electrostatic effect in solution and how far its electrostatic effect persists) and the predictions obtained from the classical DLVO theory <sup>[159]</sup>. In the presence of physical heterogeneity (surface roughness), the closest distance between two surfaces are usually shifted, the interaction potential between smooth surfaces is more difficult to calculate, and the adhesion of small particles through an increase in the contact area (for particles of appropriate size) will also be enhanced <sup>[158]</sup>.

During the past decades, works targeting to study the impact of the physical heterogeneities on the interaction energies and particle deposition are numerous. For example, Suresh et al. <sup>[163]</sup> investigated the reduced energy barrier to particle deposition in presence of surface heterogeneity compared to a smooth surface. Later on, Zhao et al. <sup>[164]</sup> explored the depletion interaction potential for both ordered and disordered physical heterogeneities, and the self-assembly of rough platelets were modelled. Wang et al. <sup>[165]</sup> explored the adsorption of polyethylene (PE) with different chain lengths on nanoscale protrusions-patterned graphite surfaces by means of molecular dynamics simulations. The results indicate that the order parameter, the adsorption energy, and the normalized surface-chain contacting pair number all decreased with the size of the protrusion. Bradford et al. <sup>[115]</sup> explored the determination of fundamental parameters and controlling mechanisms of colloid retention and release on surfaces of porous media by modelling at the representative elementary volume (REV) scale. The results indicate that the nanoscale roughness produced localized primary minimum interactions that control long-term retention. Microscopic roughness play a dominant role in colloid retention under low ionic strength and high hydrodynamic conditions, especially for larger colloids. Phenrat et al. <sup>[166]</sup> evaluated the effect of porous media heterogeneity and the dispersion properties in heterogeneous porous media within a 2D cell. The results indicate that polymer modified Nanoscale Zero Valent Iron (NZVI) are mostly deposited in regions where fluid shear is insufficient to prevent NZVI agglomeration and deposition .

## 2. Chemical heterogeneity

Chemically heterogeneous surfaces are ubiquitous in natural and engineered systems. They are considered to be an important influencing factor to colloid transport in porous media. Chemical heterogeneity may occur on natural colloids or solid surfaces as a result of constituent minerals, chemical imperfections, coatings, and adsorption of different ions, organics, and clay particles <sup>[161]</sup>. This chemical variability results in heterogeneous surface charges that are randomly distributed with various length scales and arbitrary geometrical shapes <sup>[161]</sup>.

During the past two decades, particle deposition onto chemically heterogeneous surfaces have been extensively investigated <sup>[161, 167]</sup>. For example, Elimelech et al. <sup>[168]</sup> investigated the influence of microscopic charge heterogeneity on colloid deposition behavior under dynamic flow conditions, they compared the deposition rate onto the micropatterned surfaces to the deposition rate based on the patch mode. The results show that the colloid deposition kinetics is well-fitted by patch model for low Pe and moderate- to high- Ionic Strength (IS) conditions. However, deviations are observed for high Pe and/or low IS. The results are attributed to the interplay between hydrodynamic and

electrostatic double layer interactions and are explained by a phenomenon called the “hydrodynamic bump”. Bradford et al. <sup>[169]</sup> developed an improved approach to predict resisting torque ( $T_A$ ) to removal of adsorbed particles in chemically heterogeneous porous media and use this approach to determine meaningful estimates of fraction of the solid surface area that contributes to colloid immobilization ( $S_f^*$ ) under saturated conditions at the representative elementary area (REA) scale. The results indicate that the colloid attachment depend on solution ionic strength, the colloid radius, the Young’s modulus ( $E$ ), the amount of chemical heterogeneity ( $P_+$ ), and the Darcy velocity ( $v_D$ ). Duffadar et al. <sup>[170]</sup> Develop a computational model to predict the dynamic adhesion behavior of micrometer-scale particles in a low  $Re$  flow over planar surfaces with nanoscale electrostatic heterogeneity (randomly distributed “patches”). The results indicate that the ionic strength of flowing solution determines the extent of the electrostatic interactions and can be used to tune selectively the dynamic adhesion behavior. Chatterjee et al. <sup>[171]</sup> analyzed particle deposition on Janus and patchy collectors numerically. The results indicate that particles tend to deposit at the edges of the favorable strips and this preferential accumulation varies along the tangential position due to the nonuniform nature of the collector. Zhang et al. <sup>[172]</sup> investigated and simulated the transport and retention of Multi-Walled Carbon NanoTubes (MWCNTs) in chemically heterogeneous porous media with different mass ratios of Quartz Sand (QS) and Goethite coated Quartz Sand (GQS) by means of the HYDRUS-1D code 55. The results indicate that MWCNT retention in chemically heterogeneous porous media was controlled mainly by roughness. The mass fraction and surface area of chemical heterogeneity also played an important secondary role. Rizwan et al. <sup>[161]</sup> experimentally created well defined charge-heterogeneous surfaces by employing soft lithographic techniques. They also studied the deposition of model colloidal particles onto such substrates under a no flow (or quiescent) condition, this research is mainly focusing on the surface coverage and deposit morphologies obtained after a long time. Moreover, they presented a simple mathematical description of particle deposition on the created rectangular (striped) surface features by means of the Monte-Carlo-type simulation technique, as is shown in Figure 2.12, and the results are compared with the experiments. The results indicate that particles tend to preferentially deposit at the edges of the favorable strips, while the extent of this bias can be controlled by varying the distance between consecutive favorable strips as well as the particle size relative to the strip width. In addition, simple binary probability distribution-based Monte Carlo RSA deposition model adequately predicts the deposit structure, particularly the periodicity of the underlying patterns on the substrate. Lin et al. <sup>[173]</sup> studied the transport of uncoated AgNPs in geochemically heterogeneous porous media composed of silica glass beads (GB) modified with partial coverage of iron oxide and compared to that in porous media

composed of unmodified GB. The results demonstrated a linear correlation between the average nanoparticle affinity for collector and the composition of FeO.

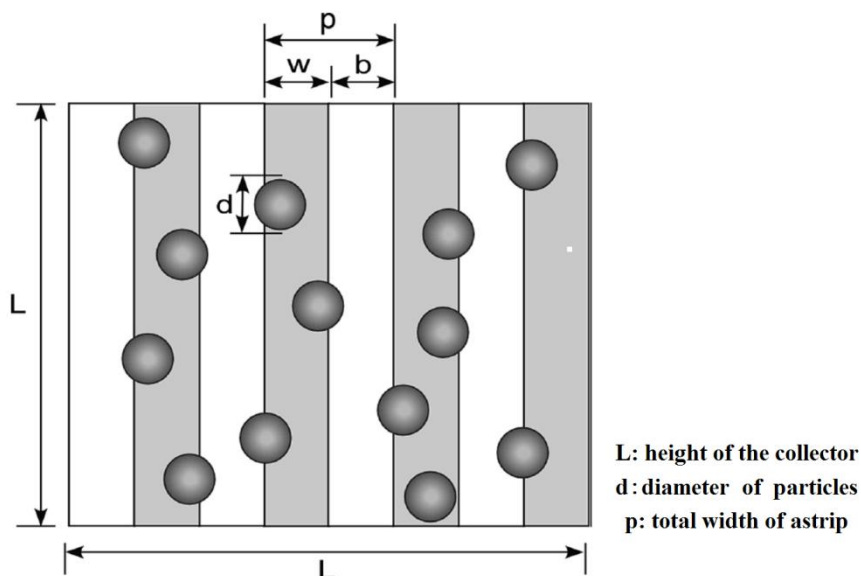


Figure 2.12 Schematic representation of the modeled surface charge heterogeneity. The square collector of height  $L$  consists of rectangular strips with alternate regions that are favorable (gray) and unfavorable (white) to deposition of widths  $w$  and  $b$ , respectively. The total width of a favorable and unfavorable strip gives the pitch,  $p$ . The deposited spherical particles of diameter  $d = 2a_p$  have their centers constrained to lie within the favorable strips <sup>[161]</sup>

### 2.2.4.3 Macroscale and microscale heterogeneity

#### 1. Macroscale heterogeneity

For macroscopic scale heterogeneous patches, isolated patches are assumed to be significantly larger than the particles, and the interactions at patch boundaries can be neglected. Several direct and indirect observations have successfully demonstrated the presence of such macroscopic heterogeneities on solid surfaces <sup>[160]</sup>. For these systems, the attachment rate is directly related to the favorable surface fraction of the collectors, which can be predicted by the patchwise model developed by Johnson et al. <sup>[174]</sup>. In this model, two types of surface charge are defined on the collector surface and the surface area fraction occupied by one type of surface charge is evaluated using a two site averaging process.

Pham et al. <sup>[175]</sup> numerically explored the transport and kinetics of nanoparticles migrating through the pore space between unconsolidated packed spheres and through consolidated Berea sandstone by means of lattice Boltzmann method with Lagrangian particle tracking. The surface charge heterogeneity was distributed according to different patterns, designated as Entry, Exit, Strips, and Mixture patterns for beds packed with spheres. The results indicate that the particle breakthrough

curves do not reach a plateau before complete saturation under the effect of surface blocking. Surface saturation also improves particle propagation due to the surface blocking mechanism. Recently, Pham et al. <sup>[176]</sup> investigated the effect of spatial distribution of the porous matrix surface heterogeneity on particle deposition. It is found that the pattern effect is controlled by the attachment rate constant, the particle size, and the fraction of surface that is favorable to deposition. Chen et al. <sup>[160]</sup> investigated the role of spatial distribution of porous medium patchwise chemical heterogeneity in colloid transport in heterogeneous packed columns. Although the spatial distribution of the modified and unmodified sands was varied, the total extent of mean chemical heterogeneity in the entire column was fixed at 10% favorable surface fraction. The results indicate that particle deposition rate and transport behavior is independent of the spatial distribution of porous media chemical heterogeneity, and dependent of the mean value of chemical heterogeneity. Erickson et al. <sup>[177]</sup> examined the electroosmotically driven flow through a microchannel exhibiting a periodically repeating patchwise heterogeneous surface pattern with the microfluidics-based finite element code. In this study, the electroosmotically driven flow through a slit microchannel (i.e., a channel formed between two parallel plates) exhibiting one of the three periodically repeating heterogeneous surface patterns shown in Figure 2.13. The results indicate the existence of distinct three-dimensional flow structures that, depending on the degree of heterogeneity, vary from a weak circulation perpendicular to the applied electric field to a fully circulatory flow system.

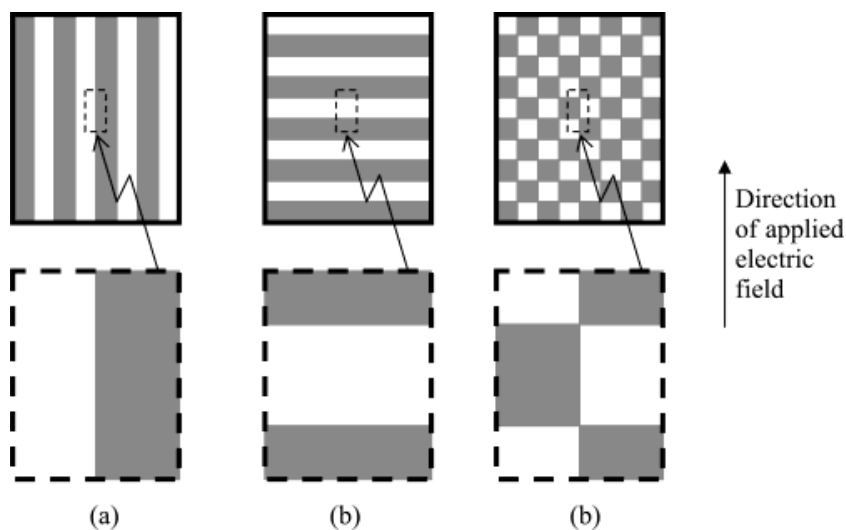


Figure 2.13 Periodic surface patterns: (a) lengthwise strips, (b) crosswise strips, (c) patchwise pattern. Dark regions represent heterogeneous patches, light regions are the homogeneous surface. In each case the percent heterogeneous coverage is 50% <sup>[177]</sup>

## 2. Microscale heterogeneity

In the case of microscopic heterogeneity, the size of surface patches is much smaller than the particles. For these systems, the size and number of microscopic-scaled heterogeneities have great influences on the parameters including the interaction energy, the zeta potential, and the attachment efficiency <sup>[178]</sup>. A variety of theoretical studies and surface integration techniques have been developed and utilized to investigate the effects of microscopic physical and/or chemical heterogeneity on colloid attachment and transport <sup>[179]</sup>. For example, Duffadar and Davis <sup>[162]</sup> developed grid-surface integration to calculate DLVO interaction energy between a colloid and chemically heterogeneous surface <sup>[180]</sup>. The Grid Surface Integration (GSI) technique utilizes known solutions for particle interactions between two parallel plates to compute the interaction between particles and a heterogeneously patterned surface. The GSI technique calculates the total interaction energy on the particle by summing the contribution on each of the discretized surface elements over the entire particle surface <sup>[179]</sup>. Duffadar et al. <sup>[158]</sup> explored the impact of random chemical heterogeneity on pairwise interactions and dynamic adhesion, exemplified by the capture of particles on heterogeneous planar surfaces by means of the GSI. The results indicate that for heterogeneity-dominated cases, high ionic strength pairwise interactions are more attractive than predicted by DLVO, and adhesion threshold depends on Debye length. Furthermore, Duffadar and Davis <sup>[162]</sup> also explored the interaction of a micrometer-scale spherical silica particle with a nanotextured heterogeneously charged surface. The results indicate that the spatial fluctuations in the local surface density of the deposited patches are responsible of the dynamic adhesion phenomena observed experimentally, including particle capture on a net-repulsive surface. Bradford et al. <sup>[179]</sup> developed a simplified model to account for the influence of microscopic chemical heterogeneity on colloid adhesive parameters for continuum models. The results indicate that the probability density functions (PDFs) of colloid adhesive parameters at the representative elementary area (REA) scale sensitive to the size of the colloid and the heterogeneity, the charge and number of grid cells, and the ionic strength. Furthermore, Shen et al. <sup>[180]</sup> examined the attachment/detachment of negatively charged microparticles onto/from a negative planar surface carrying positively charged square patches of different sizes by means of surface element integration technique. Their results indicate that a critical patch size is needed to attach a particle at a given ionic strength.

#### 2.2.4.4 Limitations and inspirations for the current work

As discussed above, several experimental and simulation studies dealing with colloidal particle deposition onto planar heterogeneous surfaces have been reported. However, there is still a paucity of rigorous models of colloidal particle deposition onto heterogeneous substrates in other geometries, such as microchannels and spherical collectors <sup>[120]</sup>. Especially, transport of particles suspended in a

carrier fluid in the micropores is central to numerous microfluidic and nanofluidic systems including Lab-On-Chip (LOC) systems, porous media flows, and membrane separations. Adamczyk et al. <sup>[181]</sup> investigated particle transport and deposition in narrow homogeneous cylindrical channels almost four decades back. Since then, fundamental concepts of particle transport has been used in various microfluidic applications. Waghmare et al. <sup>[182]</sup> discussed the transport of microbead suspension in rectangular capillaries. Fridjonsson et al. <sup>[183]</sup> investigated the transport of fluids with colloidal suspensions in a bifurcated capillary system by NMR microscopy and CFD simulations. Waghmare et al. <sup>[184]</sup> have also explored the transport of cells through buffer solution in microchannels for immunoassay based sensing devices. Saadatmand et al. <sup>[185]</sup> focussed on blood transport in a capillary tube to investigate mixing in biomedical microdevices and microcirculation. Several other similar applications for particle transport in micro and nano channels can be found in literature <sup>[186, 187]</sup>. Although, numerous investigations have been performed to analyze transport in these microfluidic and nanofluidic systems, there is no significant theoretical model which predicts particle transport in microchannels considering the effects of surface heterogeneities for evaluating particle capture. Hence, in order to facilitate tractable evaluation of particle transport and deposition under the influence of such surfaces, a technique must be devised to systematically define the heterogeneity. Chatterjee et al. <sup>[188]</sup> have investigated the particle transport in patchy heterogeneous cylindrical microchannels. The schematic representation of patchy microchannel with micropatterned surface charge distribution is indicated in Figure 2.14. The surface heterogeneity is modeled as alternate bands of attractive and repulsive regions on the channel wall to facilitate systematic continuum type evaluation. The results indicate that particles tend to collect at the leading edge of the favorable sections, the extent of this deposition could be controlled by changing Péclet number. Higher Pe resulted in a more uniform deposition along the length of the channel due to the particles being convected with the fluid. This study provides a comprehensive theoretical analysis of how the transport of such suspended particles is affected in these microchannels due to the heterogeneities on the microchannel walls. While in their model, they considered neutrally buoyant particles to ensure 2D symmetry, which would not be the case in all practical situations.

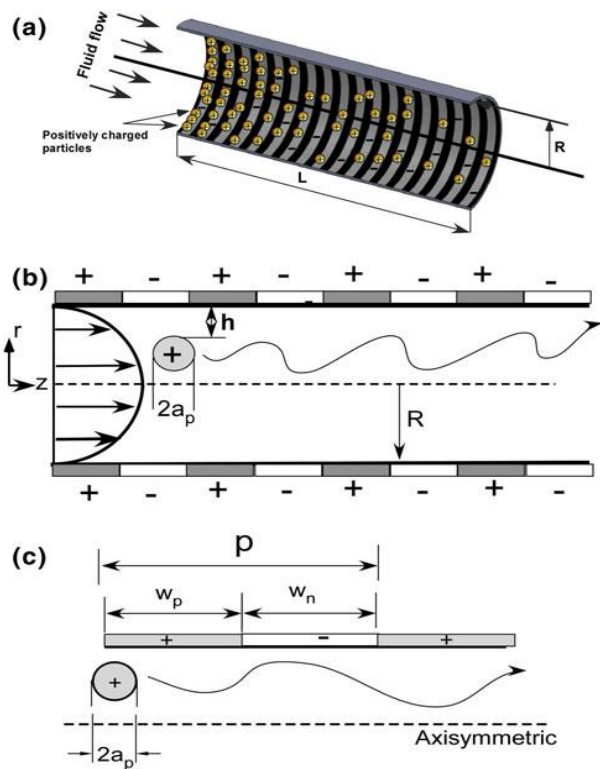


Figure 2.14 Schematic of a patterned microchannel geometry with Poiseuille flow profile <sup>[188]</sup>

Hence, 3D simulations must be performed once again to develop a complete picture of particle transport in a microchannel. This is also one of the objectives of the present work.

# **Part I: Preparation of Polymeric Porous Media for Lithium-Ion Battery Battery Separators and Water Treatment**

## **Chapter 3 Preparation of Multilayer Porous**

### **Polypropylene/Polyethylene Lithium-Ion Battery Separators by Combination of Multilayer Coextrusion and Template Method**

#### **3.1 Introduction**

Lithium-ion batteries (LIBs) have been predominantly used in portable consumer electronics due to their high specific energy density, long cycle life, and lack of memory effect <sup>[189]</sup>. Furthermore, LIBs are also regarded as one of the most promising power sources for electric vehicles and aerospace systems <sup>[190]</sup>. However, improvements in safety are still urgently required for full acceptance of LIBs in these newly growing application fields. The presence of the combustible electrolyte, as well as the oxidizing agent (lithium oxide cathodes) makes LIBs susceptible to fires and explosions <sup>[70]</sup>. Once LIBs are subjected to extreme conditions such as short-circuiting, overcharging, and high-temperature thermal impacting, exothermic chemical reactions are initiated between the electrodes and the electrolyte, which will raise the internal pressure and temperature of the battery <sup>[191]</sup>. The increased temperature accelerates these reactions and releases heat rapidly through the dangerous positive feedback mechanism which will lead to thermal runaway, cell cracking, fire or even explosion <sup>[192]</sup>. During the past two decades, there were more than 100 battery-related air incidents involving fire, extreme heat, or explosion according to the Federal Aviation Administration (FAA) <sup>[70]</sup>. To prevent catastrophic thermal failure in LIBs, plenty of strategies including temperature-sensitive electrode materials, positive temperature-coefficient electrodes, and thermal shutdown electrode <sup>[193, 194]</sup> have been proposed as a self-activating protection mechanism to prevent LIBs from thermal runaway. While the above methods often involve in either difficult material synthesis or complicated electrode processing, which make them inconvenient for battery application. Besides, the thick coating layers of the electrodes would decrease the energy density of the batteries and hinder their practical use in batteries. From the viewpoint of industrial application, thermal shutdown separator is therefore the most attractive means for safety protection of LIBs since it can overcome the above defects <sup>[194]</sup>.

Shutdown separators rely on a phase change mechanism to limit ionic transport via formation of an ion-impermeable layer between the electrodes [62]. Shutdown separators typically consist of polypropylene (PP)/polyethylene (PE) bilayer or PP/PE/PP trilayer structure. In such kind of laminated separators, PE with the lower melting point serves as shutdown agent while PP with the higher melting point serves as mechanical support [195]. Once the internal temperature rises up to the melting point of PE, the PE layer is softened and melted to close off the inner pores and thereby preventing ionic conduction and terminating the electrochemical reaction [70]. The majority of the commercial bilayer or trilayer separators are made by laminating different functional layers together by calendaring, adhesion, or welding. The traditional method of making such bilayer or trilayer separators comprises the procedure of making the microporous reinforcing layer and shutdown layer by the stretching process, bonding the above microporous layers alternately into the bilayer or trilayer membranes. Afterwards, the bilayer or trilayer membranes were stretched to the bilayer or trilayer battery separator with required thickness and porosity [69]. In addition, other methods to fabricate the multilayer separators have been reported in patent literatures. For example, Tabatabaei et al. investigated the fabrication of microporous polypropylene/high density polyethylene/polypropylene trilayer membranes as well as monolayer films using the cast extrusion followed by stretching. The results indicate that the tensile properties and the puncture resistance were evaluated. Besides, the trilayer membranes showed a lower permeability than the monolayer membranes due to the presence of the interface [196]. Callahan et al. described a multilayer separator fabrication process including the steps of preparing a film precursor by blown film extrusion, annealing the film precursor and stretching the annealed film precursor to form the microporous membrane. The above methods can produce multilayer separators with thermal shutdown function, and most of which include the stretching process and obviously enhance the mechanical strength of separators. Nevertheless, the quite cumbersome production process clearly decreases the production efficiency. Furthermore, the stretching process has high requirements for the equipment, which will increase the production cost. More importantly, these separators will suffer significant shrinkage from rather limited temperature range, with an onset for shrinkage around 100 °C because of the residual stresses induced during the stretching process of the separators and the difference in density between the crystalline and amorphous phases of the separator materials, hereby a potential internal shorting of the cell could occur [197].

To improve the thermal stability of the current polyolefin separators, various surface modification approaches have been devoted to minimize the shrinkage of separators. For example, the dip-coating of some organic polymers or inorganic oxides with excellent thermal stability onto

the surface of the polyolefin separators has been extensively studied <sup>[198]</sup> . Although layer coated separator shows significantly improved thermal stability, the coated layer are easy to fall off when the separator is bent or scratched during the battery assembly process <sup>[199]</sup>. Moreover, the dip-coating method also generates inevitable negative effects, such as the seriously blocked porous structure, unmodified inner pores of separators, as well as the significantly increased thickness <sup>[197]</sup> , which is unfavorable for the cell electrochemical performance. Besides, constructing the heat-resistant skeleton can also solve the thermal shrinkage issues, such as cellulose based composite nonwoven separator <sup>[200]</sup>, porous polyether imide separator <sup>[201]</sup>, and polymethyl methacrylate colloidal particles-embedded poly(ethylene terephthalate) composite nonwoven separator <sup>[202]</sup>. Even though the above-mentioned separators exhibit improved thermal stability, the complicated manufacturing process makes the separators more expensive <sup>[67]</sup> . It is essential to find new methods which can optimize the thermal stability, shutdown property and electrochemical performance of polyolefin separators without sacrificing their excellent microporous structure and low-cost.

In this chapter, a novel strategy is proposed to prepare multilayer LIB separators comprising alternated layers of microporous PP layer and PE layer via multilayer coextrusion combined with CaCO<sub>3</sub> template method. This approach combines the advantages of the multilayer coextrusion (continuous process, economic pathway for large-scale fabrication, and tunable layer structures) and the template method (simple preparation process and tunable pore structure). A key improvement of this approach is that the porous structure is formed by the template method instead of the stretching process, which is beneficial for the thermal stability. Compared to the commercial bilayer or trilayer separators, the dimensional shrinkage of these multilayer membranes may be reduced. More significantly, this approach is quite convenient and efficient, avoid the traditional bilayer or trilayer cumbersome processes during the production process. Moreover, this method is applicable to any melt-processable polymer in addition to PP and PE.

## 3.2 Experimental section

### 3.2.1 Materials

Polypropylene (PP, V30G) and polyethylene (PE, Q210) resin (injection and extrusion grade) were purchased from Sinopec Shanghai Petrochemical Co.. CaCO<sub>3</sub> particles (diameter 0.1 μm) were purchased from Changxing Huayang Sujia Co.. Hydrochloric acid (AR, 36.0-38.0%) was purchased from Sinopharm Chem. Reagent Co.. Isopropyl dioleic (dioctylphosphate) titanate (TMC 101) was

obtained from Tianchang Green Chem. Additive Factory. Cationic dyeing agent (turquoise blue X-GB) was purchased from Guangzhou Rongqing Chem. Products Co.. The commercialized PP/PE/PP separator (Celgard<sup>®</sup> 2325) and commercialized PE separator (SK Energy) were selected as the control sample. Prior to the processing, PP, PE, and CaCO<sub>3</sub> particles were dried separately at 70 °C for 48 h in vacuum oven to remove any humidity which may have been adsorbed during storage.

### 3.2.2 Preparation of multilayer porous PP/PE membranes

The multilayer porous PP/PE membrane was prepared by the combination of multilayer coextrusion and CaCO<sub>3</sub> template method. The preparation steps are as follows, (1) Preparation of PP (CaCO<sub>3</sub>) and PE (CaCO<sub>3</sub>) masterbatches. Prior to the multilayer coextrusion, CaCO<sub>3</sub> particles were pre-dispersed in PP or PE resins with TMC 101 as the dispersing agent. CaCO<sub>3</sub> particles and PP (or PE) resins with the mass ratio of 66: 34 were mixed and put into the twin-screw extruder to prepare PP (CaCO<sub>3</sub>) or PE (CaCO<sub>3</sub>) masterbatches. (2) Preparation of porous multilayer PP/PE membranes. The schematic representation of the lab self-designed multilayer coextrusion equipment has been reported in our previous studies [203]. The preparation principle of porous multilayer membranes through the joint of multilayer coextrusion and CaCO<sub>3</sub> template method is shown in Figure 3.1. In the layer multiplier, the layered composites were sliced vertically, spread horizontally and recombined sequentially, then an assembly of n layer multipliers could produce a tape with 2<sup>(n+1)</sup> layers [204]. In this study, the value of n is selected as 1, therefore the layer of the produced membranes is 4. Afterwards, the multilayer membranes were soaked into diluted hydrochloric acid solution (15 wt%) for 6 h, then the membranes were washed to remove the excess acid and dried at 60 °C for 24 h in vacuum. The obtained PP/PE multilayer separator was referred to as MC-CTM PP/PE.

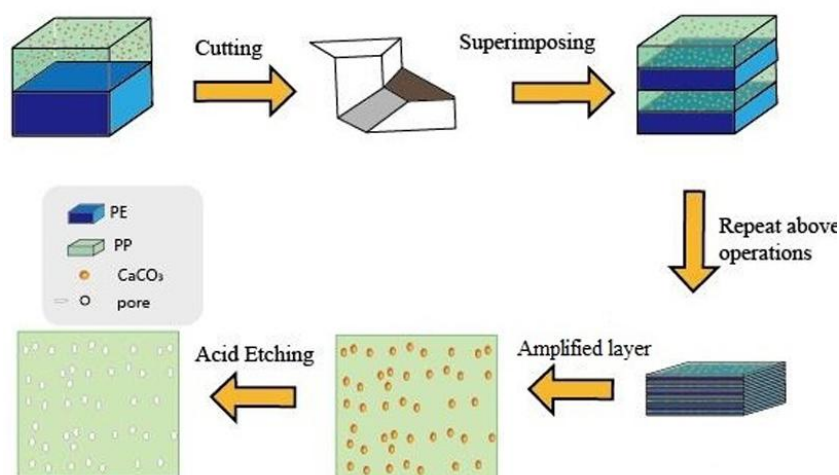


Figure 3.1 Preparation of MC-CTM PP/PE via the combination of multilayer coextrusion and CaCO<sub>3</sub> template method

### 3.2.3 Characterization

The surface and the fractured surfaces of the porous membranes were observed on Field Emission Scanning Electron Microscopy (FESEM, Philips XL30FEG). Thermal gravimetric analysis (TGA) was performed on a Netzsch STA 449 C thermogravimetric analyzer with a heating rate of 20 °C min<sup>-1</sup> from ambient temperature to 1000 °C under the air flow. Differential scanning calorimetry (DSC) measurement was made with STA 449 F3 Jupiter Netzsch using a heating rate of 5 °C min<sup>-1</sup>. Fourier transform infrared spectroscopy (FTIR) (Thermofisher Nicolet IS5) was utilized to check whether CaCO<sub>3</sub> templates could be etched by hydrochloric acid or not. The optical microscope (Nanjing Kell Instrument Co., KEL-XMT-3100) was used to observe the multilayer configuration of layer-by-layer structure of the coextrusion membranes. Tensile strength was measured on WDT30 Universal Material Testing Machine (Kailiqiang Machinery Co.) according to ASTM D882-09, where the stretching rate was 50 mm min<sup>-1</sup>.

The thickness of the separators was measured using an electronic thickness gauges, test for 8 times to obtain the average values. The porosity ( $\varepsilon$ ) of the porous membranes was determined by n-butanol soaking method, in which the weight of the membranes was measured before and after soaking in n-butanol for 2 h at room temperature, and calculated using the following equation,

$$\varepsilon(\%) = \frac{W - W_0}{\rho_L \times V_0} \times 100\% \quad (3-1)$$

where  $W$  and  $W_0$  are the weight of n-butanol soaked membrane and dry membrane respectively,  $\rho_L$  is the density of n-butanol, and  $V_0$  is the geometric volume of the membranes<sup>[64]</sup>. The electrolyte uptake (EU) was determined by the weight change of the membrane before and after absorbing the liquid electrolyte, and calculated by following equation,

$$EU(\%) = \frac{W_a - W_b}{W_b} \times 100\% \quad (3-2)$$

where  $W_b$  and  $W_a$  are the weight of membranes before and after soaking in the electrolyte, respectively<sup>[64]</sup>. Then the soaked membrane was put into an airtight container for 48 h, and the same calculation method as EU was adopted to measure its electrolyte retention (ER) after 48 h. The

porosity, electrolyte uptake and electrolyte retention of the separator was obtained as the average of the values determined in five measurements.

The thermal dimensional stability of the membranes at enhanced temperature was investigated by treating them at different temperatures for 0.5 h, the thermal shrinkage rate was determined by calculate the dimensional change (area based,  $3 \times 3 \text{ cm}^2$  square) before and after the heat treatment using the following equation,

$$\text{Shrinkage}(\%) = \frac{S_0 - S}{S_0} \times 100\% \quad (3-3)$$

where  $S_0$  and  $S$  are area of the membrane before and after thermal treatment, respectively <sup>[195]</sup>

The electrochemical properties of the separators were determined by CHI 604B electrochemical workstation (CH Instruments Inc). The cells (2025-type coin) were assembled by sandwiching the separators between anode and cathode materials in an argon-filled glove box (Lab 2000, Etelux) with water and oxygen content lower than 0.1 ppm. The ionic conductivity was measured by the electrochemical impedance spectroscopy (EIS) via sandwiching the separator between two stainless steel electrodes (SS). Impedance spectra were recorded over a frequency range from 1 Hz to 105 Hz with the AC amplitude of 5 mV under open circuit potential condition. The ionic conductivity ( $\sigma$ ) was calculated using equation (3-4),

$$\sigma = \frac{d}{A \cdot R_b} \quad (3-4)$$

where  $R_b$  is the bulk impedance,  $d$  and  $A$  are the thickness and contact area between the separator and electrodes, respectively <sup>[205]</sup>. The electrochemical stability was determined by the liner sweep voltammetry (LSV) measurements with the scanning rate of  $5 \text{ mV s}^{-1}$  over voltage range from 2 to 7 V, using stainless steel and lithium metal as the working and counter electrodes, respectively <sup>[206]</sup>. The lithium ion transference number was calculated from the chronoamperometry profile with the step potential of 10 mV via sandwiching the separator between two lithium metal electrodes. Test of battery performance of the membranes was conducted by assembling the unit cell via sandwiching the separator between a  $\text{LiFePO}_4$  cathode ( $\text{LiFePO}_4/\text{Acetylene black}/\text{PVDF}=80/10/10$ , w/w/t) and a lithium metal anode wetted by the liquid electrolyte <sup>[207]</sup>. The discharge capacity, cycle performance, and rate performance of cells were measured on a multichannel battery tester (LANHE, LAND 2001A, Wuhan, China) in the voltage window of 2.0-4.2 V at ambient condition. The charge and discharge cycling test was performed at a current density of 0.2 C for 50 cycles, and the C-rate capability measurements were performed at the current rates of 0.2 to 2 C.

### 3.3 Results and discussion

The surface and the cross-sectional morphologies of the MC-CTM PP/PE are shown in Figure 3.2a and 3.2b. According to SEM images, the membrane exhibits abundant three-dimensional spherical porous structure. The typical pore size is sub-micrometer scale with certain uniformity. The abundant porous structure is essential in absorbing more electrolytes, which allows the transport of lithium ions and results in high ionic conductivity and lithium ion transference number. Moreover, the sub-micron pore size makes the membrane hopeful to be used as a critical part in terms of avoiding self-discharge and internal short circuits to improve the safety property <sup>[208]</sup>. In addition, CaCO<sub>3</sub> particles could rarely be observed, which indicates that the majority of the templates have been etched. The cross-sectional multilayer configurations of the MC-CTM PP/PE can be observed from optical microscope image, as shown in Figure 3.2c. Alternated PP layers (brighter slabs) and PE layers (darker slabs) are clearly visible. In order to facilitate the distinction, the color masterbatch was mixed with PE layer. All the layers are parallel and continuous along the coextrusion directions. The average thickness of every layer is approximately 6  $\mu\text{m}$ , and the total thickness of the separators is around 25  $\mu\text{m}$ .

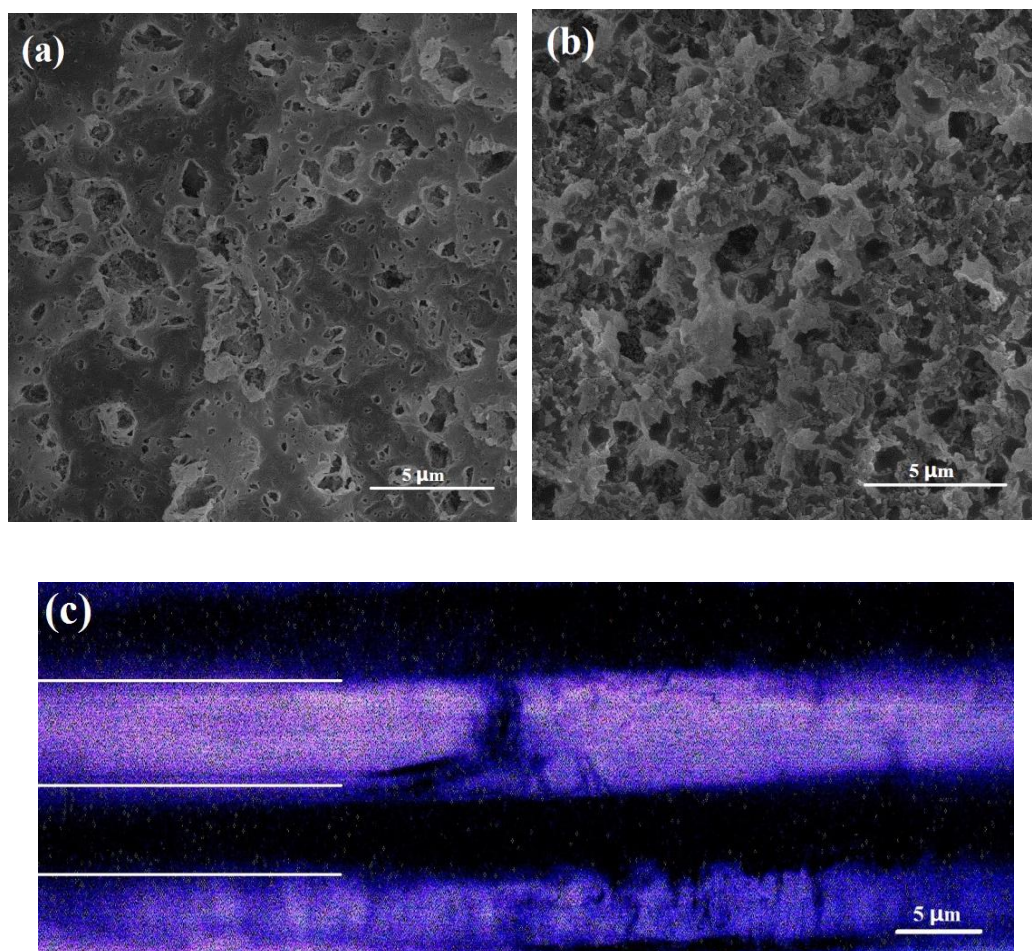


Figure 3.2 (a) SEM image of the surface of the MC-CTM PP/PE. (b) SEM image of the cross-section (fractured in liquid nitrogen) of the MC-CTM PP/PE. (c) Optical microscope image of the MC-CTM PP/PE with multilayer structure (cross-section)

A summary of fundamental physical properties of the MC-CTM PP/PE and the Celgard<sup>®</sup> separator is summarized in Table 3.1. Normally, separators should be relatively thin to provide sufficient place for active materials to increase the battery efficiency and provide lower resistance [209]. The thickness of both separators is around 25  $\mu\text{m}$ , which could meet the requirement of commercial LIBs. Besides, the MC-CTM PP/PE exhibit 46.8% porosity, which is higher than Celgard<sup>®</sup> separator (36.7%). The higher porosity is closely related to the abundant interconnected porous structure in Figure 3.2, which will provide a better reservoir for the liquid electrolyte. The electrolyte uptake of MC-CTM PP/PE is 148% (Table 3.1), which is 30% higher than that of Celgard<sup>®</sup> separator. Moreover, the electrolyte retention of MC-CTM PP/PE is 50% higher than that of Celgard<sup>®</sup> separator. This increment is even higher than the electrolyte uptake, which could be attributed to the unique porous structure. Celgard<sup>®</sup> separator are generated by the uniaxial stretching technology, which has apparent needle-like elliptic pores uniformly distributed along dry-stretching direction, while the relatively lower effective porosity and the pore structure restrict the electrolyte storage capacity [207]. In contrast, the separator prepared in this work possesses abundant three-dimensional interconnected spherical pore structure, which clearly enhanced the electrolyte uptake and retention. The room temperature ionic conductivity (Table 3.1) of both separators is in the same order of magnitude, while the value of MC-CTM PP/PE is 30% higher owing to the improved electrolyte uptake [210]. The mechanical property is another important property for separators. The tensile strength of MC-CTM PP/PE is displayed in Figure 3.3. It can be seen from the stress-strain curve that the tensile strength of the separator is 13 MPa. Although this value is lower than the tensile strength along the stretching direction of commercial Celgard<sup>®</sup> 2325 separators, it is still sufficient as separator membranes for LIBs [211].

Table 3.1 Physical properties of MC-CTM PP/PE and Celgard<sup>®</sup> 2325

Sample	Composition	Thickness [ $\mu\text{m}$ ]	Porosity <sup>a)</sup> [%]	EU <sup>b)</sup> [%]	ER <sup>c)</sup> [%]	$\sigma$ <sup>d)</sup> [ $\text{mS cm}^{-1}$ ]
MC-CTM PP/PE	PP/PE/PP/PE	25	46.8	148	137	1.35
Celgard <sup>®</sup> 2325	PP/PE/PP	25	36.7	114	90	1.04

<sup>a)</sup> Porosity: calculated as the volume of absorbed n-butanol over the volume of the dry membrane; <sup>b)</sup> Electrolyte uptake; <sup>c)</sup> Electrolyte retention after 48 h; <sup>d)</sup> Ionic conductivity at room temperature.

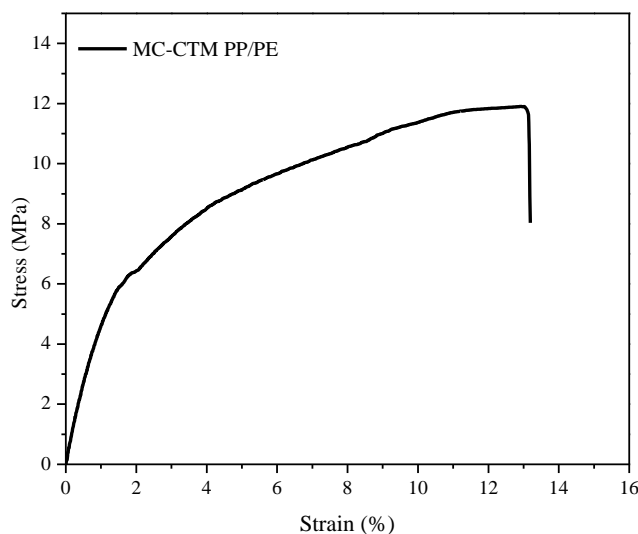


Figure 3.3 Stress-strain curve of MC-CTM PP/PE at room temperature

The temperature dependence of the ionic conductivity of electrolyte-soaked separators was further investigated, as shown in Figure 3.4. The ionic conductive behavior of both separators exhibits typical Arrhenius behavior, i.e., with the elevation of temperature, the ionic conductivity gradually increases, indicating more charge carriers and/or the ionic mobility. This behavior suggests that the mechanism of ionic conduction was the same for these two separators <sup>[212]</sup>. According to Arrhenius equation <sup>[213]</sup>,

$$\sigma = \sigma_0 \exp(-E_a / k_B T) \quad (3-5)$$

where  $\sigma_0$  is pre-exponential factor,  $E_a$  is activation energy,  $k_B$  is Boltzmann constant, and  $T$  is absolute temperature.  $E_a$  can be calculated from the slope of the lines in Figure 3.4. The calculations yielded respective  $E_a$  values of  $6.5 \text{ kJ mol}^{-1}$  and  $7.4 \text{ kJ mol}^{-1}$  for MC-CTM PP/PE and Celgard<sup>®</sup> separator.  $E_a$  value is the indicative of the total movement of anions and cations <sup>[206]</sup>. The results indicate that the transport of ions in electrolyte soaked MC-CTM PP/PE is slightly easier than that in Celgard<sup>®</sup> separator.

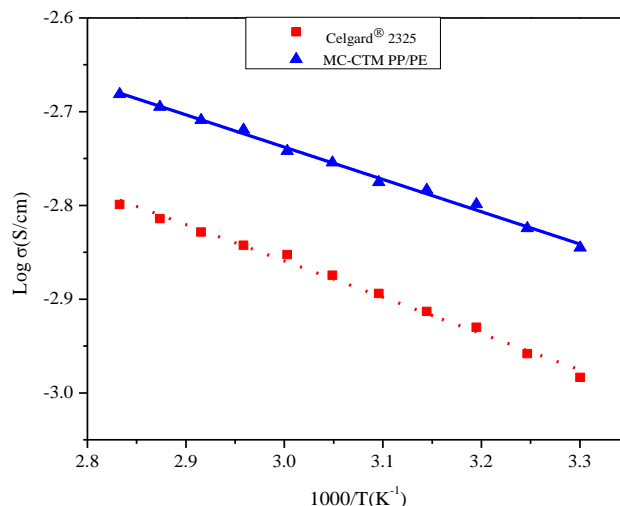


Figure 3.4 Arrhenius plots of ionic conductivity of MC-CTM PP/PE and Celgard® separator at elevated temperatures (from 30 to 80 °C)

The essential function of a separator within a battery is to prevent the direct contact between the positive and negative electrodes while enabling ion to transport between the electrodes. Thus the separators should be mechanically and chemically stable inside the battery at charged and discharged states and at elevated temperatures. Otherwise, the short circuit would generate lots of heat and cause potential thermal runaway, even combustion or explosion. Therefore, the dimensional thermo-stability of the separator, as one of most important factors for the high power batteries <sup>[67]</sup>, was studied by treating the separators at a certain temperature for 0.5 h and then measured the dimensional change before and after heat-treatment, as shown in Figure 3.5. It can be found in Figure 3.5a that Celgard® 2325 is easy to lose the dimensional stability after exposure to high temperature over 100 °C, and exhibits a remarkable dimensional shrinkage of 28% after storing at 170 °C for 0.5 h. As shown in Figure 3.5b, the shrinkage of Celgard® separator mainly happened in the stretching direction and little shrinkage happens in the transverse direction. The large shrinkage can be explained by the shape recovery behavior resulting from the multiple stretching process used to induce adequate porosity during manufacture, which makes them easily to lose the dimensional stability after exposure to high temperature above 100 °C <sup>[212]</sup>. In contrast, during the same test, MC-CTM PP/PE displayed much better thermal stability with no obvious dimensional shrinkage until 160 °C. This improvement in thermo-stability can be attributed to the fabrication method without stretching process <sup>[214]</sup>. Besides, the residual CaCO<sub>3</sub> nanoparticles can act as a rigid skeleton to prevent thermal shrinkage of membranes.

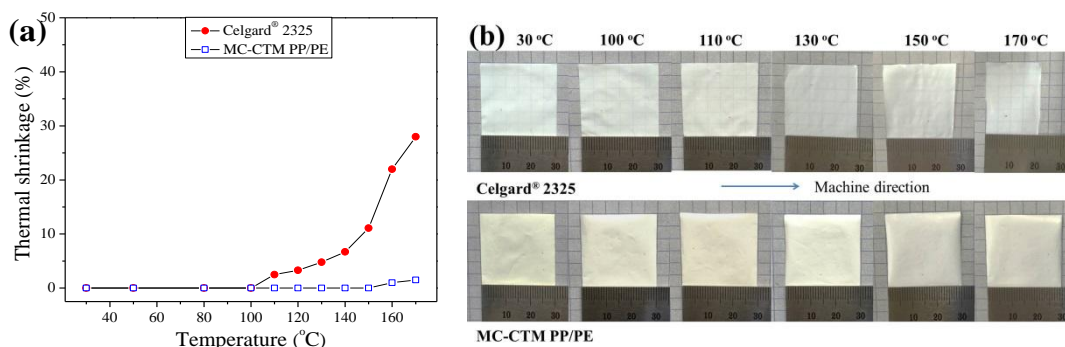


Figure 3.5 (a) Thermal shrinkage of MC-CTM PP/PE and Celgard® 2325 as a function of heat treatment temperature; (b) photographs of MC-CTM PP/PE and Celgard® 2325 after heat treatment at different temperature for 0.5 h

The shutdown and meltdown characteristics of the separators can be determined by measuring the impedance of the sandwich cell of the electrolyte-containing separator at various temperatures. For comparison, three different separators were tested, commercial PE separator (SK Energy), commercial PP/PE/PP separator (Celgard® 2325), and MC-CTM PP/PE prepared by the current work. The variation of the impedance with the temperature was plotted in Figure 3.6a. The dot line corresponds to a cell containing commercial PE separator. The shutdown in this cell occurs at around 130 °C indicated by the sharp rise in impedance at this temperature, which is caused by the melted PE blocking off the pores of the separator. This will substantially slows down the ionic conduction between the electrodes and eventually cuts off the electrode reactions at elevated temperature [194]. After that, the impedance of PE separators exhibit a sudden drop at a temperature about 140 °C which indicates that melted PE shrinks and loses mechanical integrity thus can no longer be served as separator to separate cathode and anode. An electrical short circuiting is unavoidable. The impedance increases by approximately three orders of magnitude than the value in room temperature, which is large enough for complete shutdown, i.e., separators can effectively stop ionic transport between the electrodes, and cells may not continue to be overcharged albeit without external heat sources. Therefore, in this work, 1000 ohm is selected to be a general standard to define the shutdown window. As for the cell containing a commercial PP/PE/PP separator is labeled by the dash line, the shutdown temperature is similar with PE separator, while the meltdown increases to 153 °C due to the existence of PP layers [68]. While the meltdown temperature is lower than the melting point of PP, which is attributed to the severe shrinkage resulting from the residual stresses induced during the stretching process. PP/PE multilayer separators prepared by this work (the solid line) provide a wider temperature window from 127 to 165 °C. In this system, the low melting PE layer can act as a thermal fuse and block the pathway of ions when the temperature is close to its melting temperature [215]. At the same time, the higher melting PP layer retains the dimensional

structure and mechanical strength, and thus prevents short circuiting between two electrodes <sup>[215]</sup>. It could be observed that the temperature window is wider than the commercial PP/PE/PP separators, which could be explained by the following reasons. On the one hand, the dimensional thermo-stability of MC-CTM PP/PE is much better than the commercial separator (Figure 3.5), which leads to a higher rupture temperature. This result indicates that CaCO<sub>3</sub> template method helps prevent the distortion of the separators at high temperature to some extent, compared to the stretching method. On the other hand, the stretching process of commercial separators is beneficial to the crystallization of polymers, and higher crystallinity will increase the melting point and lead to a higher shutdown temperature [C. Shi\_2015]. Figure 3.6b shows DSC thermogram of MC-CTM PP/PE. It could be observed that the separators have two endothermic peaks at 127 °C and 165 °C, respectively, indicating the melting point of plastic PE and PP, which agrees well with the impedance results.

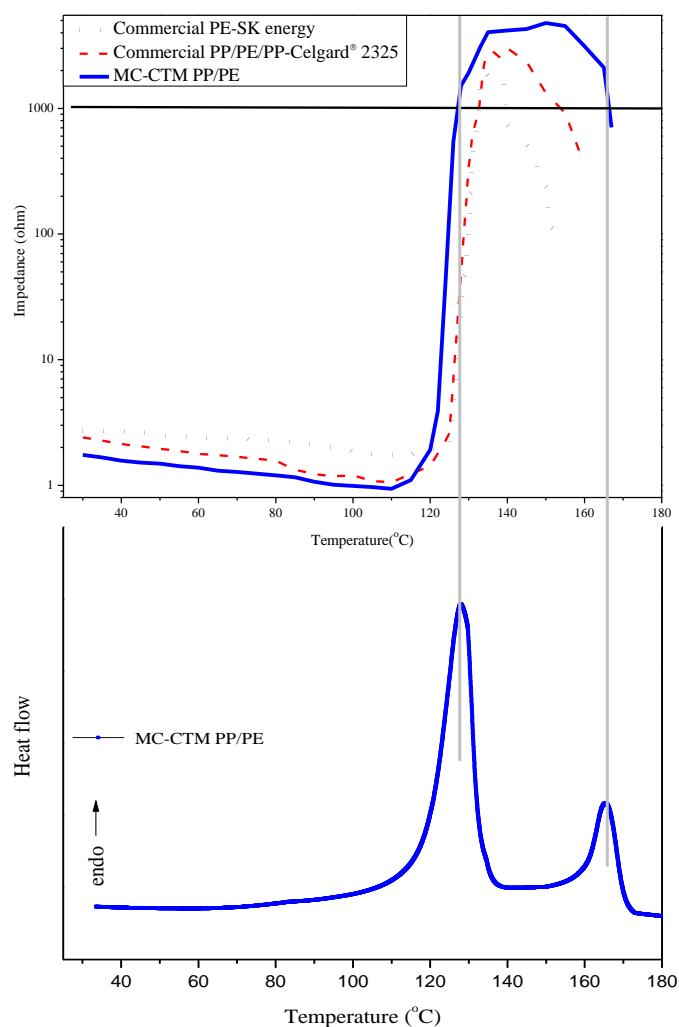


Figure 3.6 (a) Impedance vs. temperature curves for cells containing different separators, commercial PE separator (SK Energy), commercial PP/PE/PP separator (Celgard® 2325), and MC-CTM PP/PE; (b) DSC curve of MC-CTM PP/PE

The transport of lithium cations is essential for battery operation under high current densities. The major drawbacks of dual ion conducting in lithium ion batteries are the low  $\text{Li}^+$  ion transference number and the polarization of the electrodes caused by the moving anions. Moreover, the mobile anions also take part in undesirable side reactions at the electrodes, which can also directly affect the performance of batteries. Therefore it is necessary to improve lithium ion transference to gain good performance for lithium ion batteries. The ionic mobility of  $\text{Li}^+$  ion is estimated by chronoamperometry through comparing the lithium ion transference number ( $t^+$ ), which is obtained by the ratio of the final and initial current values after and before chronoamperometry, as shown in Figure 3.7.  $t^+$  of MC-CTM PP/PE (0.43) is larger than that of Celgard<sup>®</sup> separator (0.28). This indicates larger real ionic conductivity of  $\text{Li}^+$  ions for MC-CTM PP/PE than that of the commercial separator, which is attributed to the larger porosity and the liquid electrolyte retained in the pores [206].

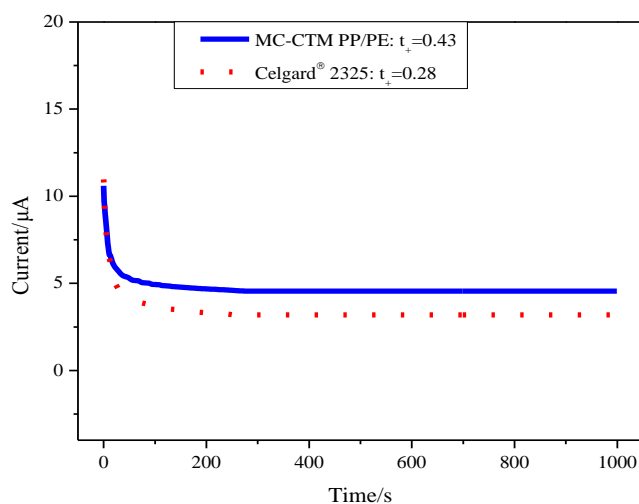


Figure 3.7 Chronoamperometry profiles of Li/electrolyte soaked separator/Li cells assembled with MC-CTM PP/PE and Celgard<sup>®</sup> separator by a step potential of 10 mV

The electrochemical stability of separators is one of the most important features for their application in battery system, a large electrochemical window is an important aspect for high battery performance [216]. Figure 3.8 shows the results of LSV profiles of MC-CTM PP/PE and Celgard<sup>®</sup> 2325 using lithium metal as the counter and reference electrode, stainless steel as the working electrode. The voltage corresponding to the onset of a steady increase in the observed current density indicates the limit for electrochemical stability of the electrolyte-soaked separators, at which oxidative decomposition of an electrolyte-soaked separator happened [67]. According to the results shown in Figure 3.8, the electrolyte-soaked Celgard<sup>®</sup> separator exhibits an anodic stability up to 4.22 V versus  $\text{Li}^+/\text{Li}$ , while the anodic stability for MC-CTM PP/PE increases to 5.1 V. This stability

enhancement may be attributed to the improved electrolyte affinity of MC-CTM PP/PE, since the free solvent molecules in the liquid electrolyte tend to be decomposed on the cathode of lithium ion battery. The excellent electrolyte uptake of separators can reduce the decomposition of solvent molecules on the cathode of lithium ion battery <sup>[216]</sup>. This result demonstrates that MC-CTM PP/PE have a wider electrochemical window than Celgard<sup>®</sup> separators, which indicates better electrochemical stability and safety performance.

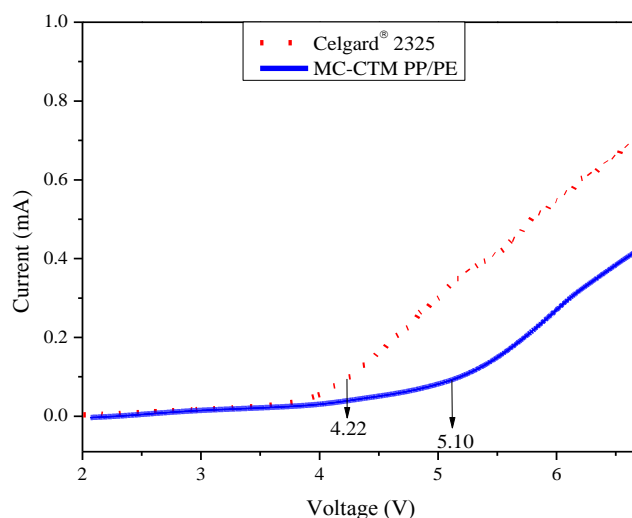


Figure 3.8 Linear sweep voltammetry (LSV) curves of Li/electrolyte soaked separator/SS cells assembled with MC-CTM PP/PE and Celgard<sup>®</sup> separator with a scanning rate of  $5 \text{ mV s}^{-1}$  over voltage range from 2 to 7 V

The electrochemical performances were investigated using cells consisting of the electrolyte-soaked MC-CTM PP/PE or Celgard<sup>®</sup> 2325 sandwiched between two electrodes.  $\text{LiFePO}_4$  served as the working electrode and lithium metal as the counter and reference electrode. The discharge property of lithium-ion batteries mainly depends on the electrode material, electrolyte, and separator, while in this work, the only influence factor is in the separator <sup>[217]</sup>. Figure 3.9a depicts 1<sup>st</sup>, 10<sup>th</sup> and 50<sup>th</sup> discharge profiles of cells assembled with MC-CTM PP/PE and Celgard<sup>®</sup> separator, under a current density of 0.2 C and voltages ranging from 4.2 to 2 V. The discharge curves are similar to what is observed for lithium ion batteries in general, which implies a good contact between the electrodes and the separators. The typical flat-shaped voltage profiles around 3.4 V is consistent with the reported two phase coexistence reaction for  $\text{LiFePO}_4$  cathode <sup>[218]</sup>, which reflects the reversible charge-discharge cycling behavior of  $\text{LiFePO}_4$  cathode material. Furthermore, the specific discharge capacity of MC-CTM PP/PE ( $135 \text{ mAh g}^{-1}$ ) is slightly higher than that ( $131 \text{ mAh g}^{-1}$ ) of Celgard<sup>®</sup> separator, which indicates faster and easier lithium ion transportation between the electrodes and lower interfacial impedance <sup>[219]</sup>.

Cycling performance is used to evaluate the performance of a battery in the long run. Figure 3.9b shows the variation of the capacity retention with cycle numbers (up to 50 cycles) of cells with different separators at a current density of 0.2 C. The cell with MC-CTM PP/PE shows similar cycling behavior as the one with Celgard<sup>®</sup> separator. Both of them are relatively stable throughout 50 cycles with small performance degradation, indicating a stable cycle performance. In addition, compared to a battery with PE membrane, a little higher discharge capacity of a battery with MC-CTM PP/PE during 50 charge-discharge cycles is achieved, and the gap between the two curves becomes larger with increasing cycle number. The difference is probably due to the higher affinity of MC-CTM PP/PE for the liquid electrolyte. Normally, it is the electrode materials that play a major role in both the energy density and capacity retention of the cell<sup>[220]</sup>. However, the electrolyte uptake and ionic conductivities of separators can also influence the capacity of the cell since the separator can directly influence the cell capacity by acting both as the medium of transport of the ions for the electrochemical reaction and a barrier to separate two electrodes. The large liquid electrolyte uptake can wet electrode materials more sufficiently, and achieve high ionic conductivity<sup>[213]</sup>, which would favor intercalation and deintercalation of lithium ions on a cathode. This will result in a higher discharge capacity. Furthermore, the unique spherical pore structure of MC-CTM PP/PE can help seal the electrolyte for longer time, resulting in less capacity loss during the long-term discharge and charge process<sup>[213]</sup>. This result suggests that the cell with MC-CTM PP/PE exhibits a better reversibility.

The rate performance was also of great significance for batteries. Figure 3.9c compares the rate behavior of both separators with C-rates increasing from 0.2 to 2.0 C every five cycles. It is noteworthy that MC-CTM PP/PE presents larger discharge capacities over various discharge current densities from 0.2 to 2 C, reflecting higher cathode utilization and discharge C-rate capabilities. The difference in the discharge capacities between two separators becomes larger at higher current densities where the influence of ionic transport on the ohmic polarization is more significant<sup>[221]</sup>. For both separators, the discharge capacities of cells gradually decrease with increasing discharge current density, which means high energy loss resulting from fast ions motion and higher polarization at higher current densities<sup>[222]</sup>. The main affecting factors of separators on the C-rate capacity of cells include the ion conductivity and Li-ion transfer through the separator/electrode interface<sup>[223]</sup>. As discussed above, the combination of increased conductivity of electrolyte and higher Li-ion transference number of MC-CTM PP/PE can allow faster mobility of Li-ions inside the separator and reduce the polarization caused by the counter anions. Furthermore, the smaller interfacial impedance of MC-CTM PP/PE with the lithium electrode means better contact between

the separator surface and the electrode, facilitating Li-ion diffusion through the separator/electrode interface. These advantageous characteristics contribute to the higher discharge capacity of the cells with PP/PE multilayer separator [200]. Such ideal cycle and rate performances make MC-CTM PP/PE promising for the use in lithium ion batteries with fast and enhanced performances.

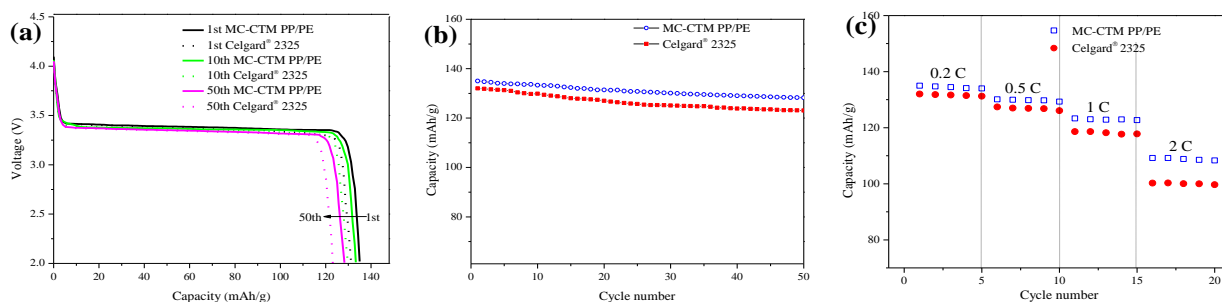


Figure 3.9 Electrochemical performances of MC-CTM PP/PE and Celgard® separator tested in Li/separator/LiFePO<sub>4</sub> configuration, (a) First discharge profiles at 0.2 C-rate, (b) Cycling performance at 0.2 C-rate, (c) C-rate behavior where the current densities are varied from 0.2 C to 2 C

### 3.4 Conclusions

A facile and volume preparation method for porous PP/PE multilayer membranes has been demonstrated via the combination of multilayer coextrusion and CaCO<sub>3</sub> template method. The as-prepared MC-CTM PP/PE separators exhibit abundant and interconnected spherical submicron porous structure, which results in increased liquid electrolyte uptake and retention. Consequently, the ionic conductivity and lithium ion transference number are enhanced, both of which are considered key factors in improving the battery performances. Particularly, the rate behavior and cycling performance of MC-CTM PP/PE outperform those of commercial PP/PE/PP separator (Celgard® 2325). Most importantly, the porous membranes prepared by the template method exhibits higher thermal stability than the commercial separators produced by the stretching method. MC-CTM PP/PE can provide the shutdown function in a temperature range from 127 °C to more than 165 °C, which is wider than Celgard® separator. The multilayer separators can maintain their integrity and low thermal shrinkage at high temperature. Considering the aforementioned attractive features and the easily scale-up preparation process, MC-CTM PP/PE are deemed to have great promise for the application in high safety lithium ion batteries. A notable contribution of this study is providing a new method to fabricate separators for lithium ion batteries, which might be an interesting direction for the next-generation separators. In addition, this easily scale-up preparation process can be extended to fabricate other multilayer separators by choosing various types of polymeric resin matrix and templates.

# Chapter 4 **Preparation of Multilayer Porous Lithium-Ion Battery Separators by Combination of Multilayer Coextrusion and Thermal Induced Phase Separation**

## 4.1 Introduction

Improvements in safety are still urgently required for the wider acceptance of lithium-ion batteries (LIBs) especially in the newly growing application fields such as electric vehicles and aerospace systems <sup>[224]</sup>. The shutdown function of separators is a useful strategy for the safety protection of LIBs by preventing thermal runaway reactions. Compared to the single layer separators, polypropylene (PP)/polyethylene (PE) bilayer or trilayer separators are expected to provide wider shutdown window by combining the lower melting temperature of PE with high melting temperature and high strength of PP <sup>[68]</sup>. The traditional method to prepare such kind of bilayer or trilayer separators is bonding the pre-stretched microporous monolayer membranes into bilayer or trilayer membranes by calendaring, adhesion or welding, and then stretched to obtain the required thickness and porosity <sup>[69]</sup>, which will enhance the mechanical strength but decrease the production efficiency. Moreover, such kind of separators will suffer significant shrinkage at high temperature due to the residual stresses induced during the stretching process, hereby a potential internal shorting of the cell could occur <sup>[197]</sup>. During the past decades, various modifications have been devoted to improve the dimensional thermos-stability of separators including the surface dip-coating of organic polymers or inorganic oxides <sup>[71]</sup>, and chemically surface grafting. However, the coated layers are easy to fall off when the separators are bent or scratched during the battery assembly process <sup>[199]</sup>. Besides, most of the above approaches focused on modifying or reinforcing the existing separators <sup>[73]</sup>, which makes the manufacturing process more complicated and the separators more expensive. Thus it is essential to find new solutions that can optimize the thermal stability, shutdown property, and electrochemical performance without sacrificing the convenient and cost-effective preparation process.

Multilayer coextrusion (MC) represents an advanced polymer processing technique which is capable of economically and continuously producing multilayer materials <sup>[203]</sup>. Thermal induced phase separation (TIPS) is a widely used manufacturing process for commercial LIBs separators <sup>[225]</sup>, which is based on a rule that a polymer is miscible with a diluent at high temperature, but demixes at low temperature. The separators prepared by TIPS process show well-controlled and uniform pore

structure, high porosity, and good modifiability <sup>[225]</sup>. To the best of our knowledge, no studies have been reported on the combination of the above two methods to prepare multilayer porous separators. Thus in the present chapter, a novel strategy is proposed to prepare the multilayer LIBs separators comprising alternated layers of microporous PP and PE layers via the combination of multilayer coextrusion and TIPS method, aim to combine the advantages of both methods. Besides, in this work the TIPS composed of a binary system, including one polymer (PP or PE), one diluent (paraffin) and therefore only one extractant (petroleum ether). Hence, the extractant is recyclable and offers higher reproducibility, which is of critical importance for the cost reduction and environmental protection <sup>[226]</sup>. Another key benefit of this method is that the one-step route provides a more efficient way for large scale fabrication of multilayer separators with high porosity. More significantly, the porous structure is formed without traditional stretching process, which is in favor of the dimensional thermo-stability. The thermal shutdown property and thermal stability of the resultant separators are expected to be improved obviously compared to the commercial bilayer or trilayer separators. The as-prepared separators are also expected to exhibit cellular-like and submicron grade porous structure, sufficient electrolyte uptake, high ionic conductivity, and good battery performance. These advantages make such kind of multilayer membranes a promising alternative to the commercialized bilayer or trilayer LIBs separators at elevated temperatures.

## 4.2 Experimental section

### 4.2.1 Materials

Polypropylene (V30G), polyethylene (Q210), and paraffin wax (66#) were purchased from Sinopec Shanghai Petrochemical Co.. Petroleum ether (AR) was purchased from Sinopharm Chem. Reagent Co.. The commercialized PP/PE/PP trilayer separator (Celgard<sup>®</sup> 2325) and commercialized PE separator (SK Energy) were provided by Shenzhen Yuanchenghui Electronic Co.. Prior to the preparation, PP, PE, and paraffin wax were dried at 50 °C for 24 h in vacuum oven to remove any humidity which may have been adsorbed during storage.

### 4.2.2 Preparation of porous PP/PE multilayer membranes

Prior to the multilayer coextrusion, paraffin wax as diluent and PP (or PE) resin with the mass ratio of 55: 45 were mixed and put into the twin-screw extruder to prepare the PP/paraffin and PE/paraffin masterbatches. The schematic illustration of preparation process through the co-joint of

MC and TIPS is shown in Figure 4.1. The mechanism of the multilayer coextrusion has been reported in our previous work [203]. In this study, the layer number is chosen to be 4. After the multilayer coextrusion, the extruded multilayer membranes were immersed in water immediately at 20 °C to conduct the thermal induced phase separation. The principle of TIPS is that a homogeneous polymer/diluent system would be thermodynamically unstable when rapidly cooling the solution below a bimodal solubility temperature. Firstly the initial phase separated structure were formed through the nucleation and growth process, then the phase separated droplets come together during the spinodal decomposition, proceed to minimizing the interfacial free energy [227]. This coarsening process was induced by a differential interfacial tension between the polymer-lean and polymer-rich phases due to the reduction in surface energy associated with the interfacial area [228]. The two-phase structures formed by the phase separation were the prototype of pore structures. After the multilayer coextrusion and the thermal induced phase separation, the membrane was immersed in petroleum ether (act as extractant) for 6 h to extract the diluent and subsequently dried at 60 °C for 12 h, the obtained PP/PE multilayer separator was referred to as MC-TIPS PP/PE.

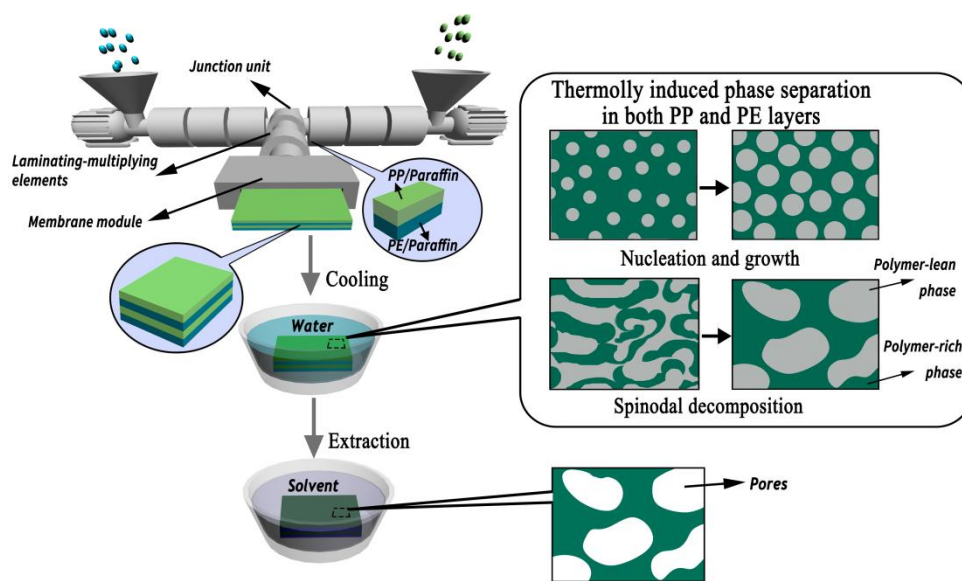


Figure 4.1 Schematic illustration showing the preparation process of MC-TIPS PP/PE via the combination of multilayer coextrusion and thermal induced phase separation

### 4.2.3 Characterization

The surface and the fractured surface of the porous membranes were observed through the field emission scanning electron microscopy (FESEM, QUANTA 250FEG, FEI Co.). The pore size distribution was determined by the randomly measured size of the pores from FESEM images using the dimensional analysis software (Nano Measure V.1.2.5). The multilayer configuration was

observed by the optical microscope (Lake Success, NY). The thickness of the separator was measured using an electronic thickness gauges, test for 8 times to obtain the average values. The tensile strength of the separators was measured on WDT30 universal material testing machine (Kailiqiang Machinery Co.) according to ASTM D882-09, where the stretching rate was 50 mm min<sup>-1</sup>. Differential scanning calorimetry (DSC) was measured on STA 449 F3 Jupiter Netzsch using a heating rate of 5 °C min<sup>-1</sup>. The porosity ( $\varepsilon$ ) of the separators was determined by n-butanol soaking method, the weight of the separators was measured before and after soaking in n-butanol for 2 h at room temperature, and calculated by the following equation,

$$\varepsilon(\%) = \frac{W - W_0}{\rho_L \times V_0} \times 100\% \quad (4-1)$$

where  $W$  and  $W_0$  are the weight of n-butanol soaked and dry separators respectively,  $\rho_L$  is the density of n-butanol, and  $V_0$  is the geometric volume of the separators<sup>[64]</sup>. The electrolyte uptake (EU) was calculated using the following equation,

$$EU(\%) = \frac{W_a - W_b}{W_b} \times 100\% \quad (4-2)$$

where  $W_b$  and  $W_a$  are the weight of separators before and after soaking in the electrolyte, respectively<sup>[64]</sup>. Afterwards the soaked separators were put into an airtight container for 48 h, and the same method was adopted to calculate the electrolyte retention (ER) after 48 h. The porosity, electrolyte uptake and electrolyte retention of the separators were obtained as the average of the values determined in five measurements. The thermal dimensional stability of the separators at enhanced temperature was investigated by treating them at different temperatures for 0.5 h, the thermal shrinkage rate was determined by calculating the dimensional change (area based, 3 cm square) before and after the heat treatment using the following equation,

$$\text{Shrinkage}(\%) = \frac{S_0 - S}{S_0} \times 100\% \quad (4-3)$$

where  $S_0$  and  $S$  are the area of the separators before and after thermal treatment, respectively<sup>[67]</sup>. The electrochemical properties of the separators were determined on CHI 604C electrochemical workstation. The cells (2025-type coin) were assembled by sandwiching the separators between cathode and anode materials in an argon-filled glove box (Lab 2000, Etelux) with water and oxygen content lower than 0.1 ppm. The ionic conductivity ( $\sigma$ ) was measured on the electrochemical impedance spectroscopy (EIS) via sandwiching the separator between two stainless steel electrodes

(SS). Impedance spectra were recorded over a frequency range from 1 Hz to  $10^5$  Hz with AC amplitude of 5 mV.  $\sigma$  was calculated using the following equation,

$$\sigma = \frac{d}{A \cdot R_b} \quad (4-4)$$

where  $d$  is the thickness of the separator,  $A$  is the contact area between the separator and electrodes, and  $R_b$  is the bulk impedance <sup>[205]</sup>. The lithium ion transference number ( $t^+$ ) was calculated from the chronoamperometry profile with the step potential of 10 mV by sandwiching the separators between two lithium metal (LM) electrodes <sup>[205]</sup>. With the aim to measure the electrochemical stability of the separators, a SS/separator/LM coin cell was assembled and measured by the liner sweep voltammetry (LSV) test with the scanning rate of  $5 \text{ mV s}^{-1}$  over voltage range from 2 to 6 V. The battery performance of the separators was measured by assembling the coin cell by sandwiching the separator between a  $\text{LiFePO}_4$  cathode ( $\text{LiFePO}_4/\text{Acetylene black}/\text{PVDF}=80/10/10$ , w/w/t) and a LM anode <sup>[207]</sup>. The tests were carried on a multichannel battery tester (LANHE, LAND 2001A, Wuhan, China) in the voltage window of 2.0-4.2 V. The charge and discharge cycling test was performed for 50 cycles at a current density of 0.2 C, and the C-rate capability measurements were performed at the current rates of 0.2 to 2 C.

### 4.3 Results and discussion

The porous structure is a key characteristic for LIB separators. Figure 4.2 show the surface and cross-sectional morphology of MC-TIPS PP/PE. According to FESEM images, the separator possesses cellular-like pore structure, which is the typical structure formed by the liquid-liquid TIPS process <sup>[206]</sup>. In addition, the separator also exhibits several long pores, which are attributed to the coalescence and deformation of a number of diluent droplets <sup>[229]</sup>. Figure 4.2 also display the pore size distribution of surface and cross-section of MC-TIPS PP/PE. The average size of them is all around 500 nm. The relatively small pore size and uniform pore size distribution are attributed to the fast quenching speed in water bath and the liquid droplets do not have enough time to grow bigger before the solidification of the matrix <sup>[230]</sup>. The pore size has a major impact on preventing the penetration of particles from the cathode/anode through the separator and on the inhibition of lithium dendritic. The submicron grade pore size of MC-TIPS PP/PE is suitable for LIBs, which can balance the ionic conductivity and electrical insulation well. Besides, the uniform pore size distribution can suppress the growth of lithium dendrites on the anode and ensure a uniform current distribution throughout the separator, which can avoid performance losses arising from non-uniform current

densities [64]. The cross-sectional multilayer configurations of MC-TIPS PP/PE can be observed from optical microscope image, as shown in Figure 4.2c. Several types of color masterbatches were mixed with PE layer to facilitate the distinction. It could be observed that alternated layers of PP (brighter slabs) and layers of PE (darker slabs) are clearly visible, all the layers are parallel and continuous along the coextrusion directions.

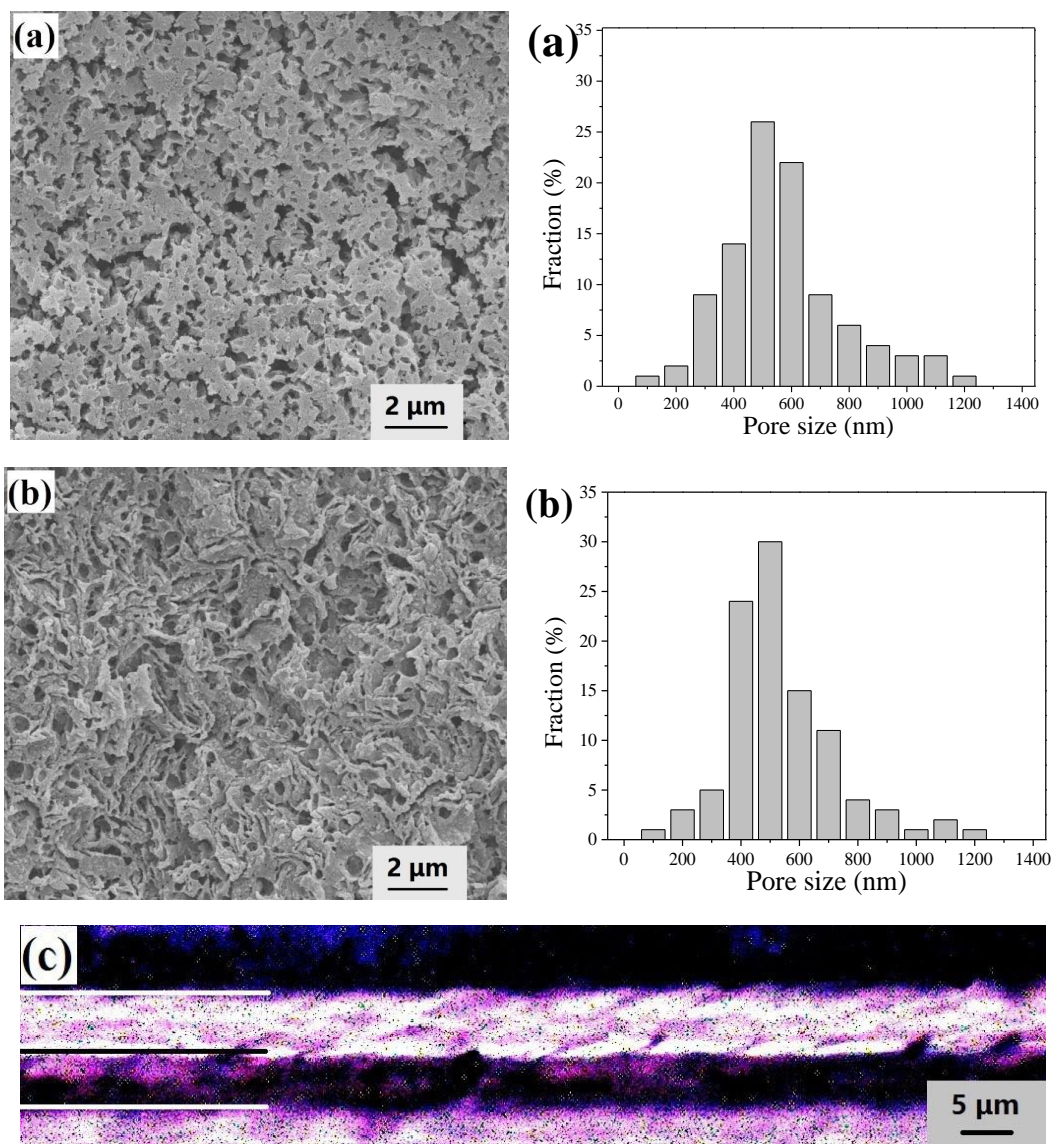


Figure 4.2 (a) FESEM image and pore size distribution of the surface of MC-TIPS PP/PE; (b) FESEM image and pore size distribution of the cross-section of MC-TIPS PP/PE, fractured by liquid nitrogen; (c) Optical microscope image of the cross-sectional multilayer structure of MC-TIPS PP/PE

The fundamental physical properties of MC-TIPS PP/PE and Celgard<sup>®</sup> separator are summarized in Table 4.1. The thickness of both separators is around 25 μm, which could meet the requirement of commercial LIBs. Besides, MC-TIPS PP/PE exhibits higher porosity (54.6%) than Celgard<sup>®</sup> separator (36.7%) due to the abundant cellular-like porous structure, as shown in Figure 4.2, which

will definitely provide a better reservoir for the liquid electrolyte and thus enhance the ionic conductivity <sup>[231]</sup>. As shown in Table 4.1, the electrolyte uptake, electrolyte retention, and the ionic conductivity of MC-TIPS PP/PE at room temperature are all higher than that of Celgard<sup>®</sup> separator. Figure 4.3 shows the stress-strain curve of MC-TIPS PP/PE. It can be seen that the tensile strength is 11.3 MPa, although this value is much lower than the commercial separators, it is still sufficient for LIBs separators <sup>[211]</sup>.

Table 4.1 Physical properties of MC-TIPS PP/PE and Celgard<sup>®</sup> 2325

Sample	Layer configuration	Thickness [μm]	ε <sup>a)</sup> [%]	EU <sup>b)</sup> [%]	ER <sup>c)</sup> [%]	σ <sup>d)</sup> [mS cm <sup>-1</sup> ]
Celgard <sup>®</sup> 2325	PP/PE/PP	25	36.7	115	90	1.05
MC-TIPS PP/PE	PP/PE/PP/PE	25	54.6	157	141	1.46

a) Porosity; b) Electrolyte uptake; c) Electrolyte retention after 48 h; d) Ionic conductivity at room temperature.

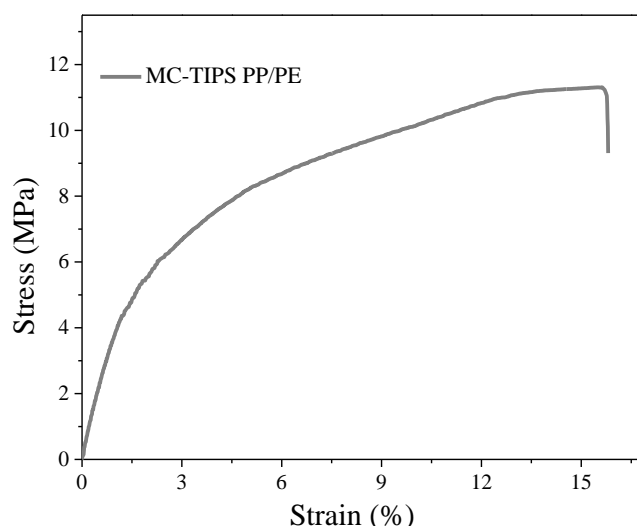


Figure 4.3 Stress-strain curve of MC-TIPS PP/PE at room temperature

The temperature dependence of the ionic conductivity of electrolyte-soaked separators is shown in Figure 4.4. For both MC-TIPS PP/PE and Celgard<sup>®</sup> separator, the ionic conductivity gradually increases with increasing temperature, which exhibits typical Arrhenius behavior. This behavior suggests that the mechanism of ionic conduction is the same for these two separators <sup>[212]</sup>. According to Arrhenius equation,

$$\sigma = \sigma_0 \exp(-E_a / k_B T) \quad (4-5)$$

where  $\sigma_0$  is pre-exponential factor,  $E_a$  is activation energy related to ionic mobility,  $k_B$  is Boltzmann constant, and  $T$  is absolute temperature.  $E_a$  is indicative of the total movement of anions and cations and can be calculated from the slope of the lines in Figure 4.4. It is worth noticing that the  $E_a$  value of MC-TIPS PP/PE ( $6.14 \text{ kJ mol}^{-1}$ ) is lower than that of Celgard<sup>®</sup> separator ( $7.4 \text{ kJ mol}^{-1}$ ). The result confirms that the transport of ions through electrolyte soaked MC-TIPS PP/PE is a little easier than that in Celgard<sup>®</sup> separator<sup>[232]</sup>.

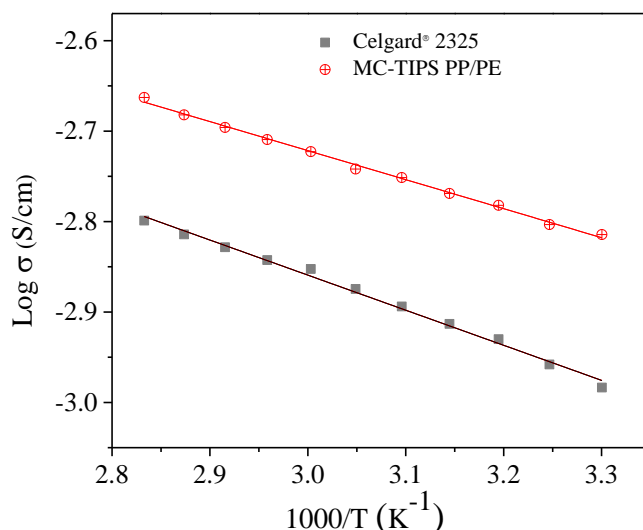


Figure 4.4 Temperature dependence of ionic conductivity of MC-TIPS PP/PE and Celgard<sup>®</sup> separators

Prevent the physical contact of the positive and negative electrode is one of the most important functions of the separators. Thus the separator should be mechanically and chemically stable inside the battery at charged and discharged states and at elevated temperatures. Otherwise, the short circuit would occur and generate lots of heat, cause potential thermal runaway, even combustion or explosion. In order to investigate the thermal-resistant characteristics of the separator, thermal shrinkage behavior is observed by measuring the dimensional change (area-based) after storing the separator at a series of temperature from 30 to 170 °C for 0.5 h, respectively<sup>[195]</sup>. The results are shown in Figure 4.5a. It could be observed that the Celgard<sup>®</sup> 2325 is easy to lose the dimensional stability (mainly in the machine direction) after exposure to high temperatures of over 100 °C due to the shape recovery behavior resulting from the multiple stretching process. Thermal shrinkage of Celgard<sup>®</sup> 2325 at 110 °C, 120 °C, 130 °C, 140 °C, 150 °C, 160 °C and 170 °C was 2.5%, 3.3%, 4.8%, 7.2%, 11%, 23% and 28%, respectively. In contrast, the MC-TIPS PP/PE displayed much better thermal stability with no obvious dimensional shrinkage until 160 °C. Figure 4.5b shows the photographs of MC-TIPS PP/PE and Celgard<sup>®</sup> 2325 after heat treatment of 100 °C, 120 °C, 140 °C, 160 °C for 0.5 h. The photographs clearly show that Celgard<sup>®</sup> 2325 suffers a high degree of dimensional change after exposure to high temperature condition. For comparison, the MC-TIPS

PP/PE has less thermal shrinkage than the commercial separator over a wider range of range of temperatures. This improvement in thermos-stability can be attributed to the fabrication method without stretching processes, the superior thermal stability of MC-TIPS PP/PE would improve the safety characteristic of LIBs at elevated temperature <sup>[221]</sup>.

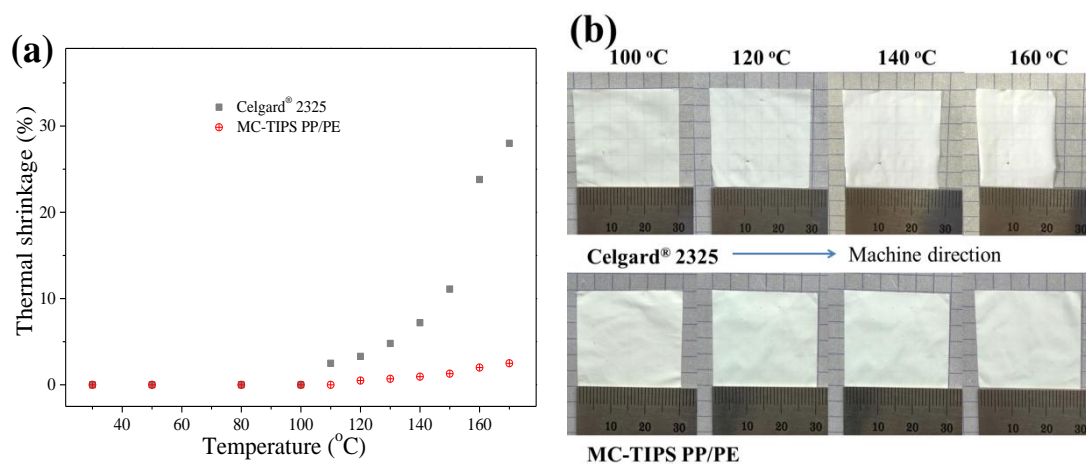


Figure 4.5 (a) Thermal shrinkage rate of MC-TIPS PP/PE and Celgard® 2325 as a function of heat treatment temperature; (b) photographs of MC-TIPS PP/PE and Celgard® 2325 after heat treatment at various temperatures for 0.5 h

The shutdown function of the separator is determined by measuring the electrical resistance of the coin cells with the electrolyte-containing separator at various temperatures. For comparison, three different separators were tested, including commercial PE separator (SK Energy), commercial PP/PE/PP separator (Celgard® 2325), and the MC-TIPS PP/PE, the variation of the impedances with the temperature were plotted in Figure 4.6a. The sharp rise in impedance at around 130 °C is caused by the block off of the pores by the melted PE, therefore slows down the ionic conduction and cuts off the electrode reactions <sup>[194]</sup>. With the increasing of the temperature, the impedance of the separators exhibit rapid decline, which indicates that the separator shrinks or loses mechanical integrity and can no longer separate the electrodes. The impedance increases by approximately three orders of magnitude is large enough for ‘complete’ shutdown. Therefore 1000 ohm is selected to be a general standard to define the efficacious shutdown window herein <sup>[68]</sup>. The wider temperature window of MC-TIPS PP/PE (129 °C-165 °C) than the commercial separators can be explained by the improved dimensional thermo-stability, as is proved in Figure 4.5 This result indicate that compare to the stretching method, separators prepared by this novel method avoid the severe shrinkage and distortion at high temperature. Figure 4.6b shows the DSC thermogram of the MC-TIPS PP/PE, the two endothermic peaks are corresponding to the melting point of PE and PP, which agreed well with the impedance results.

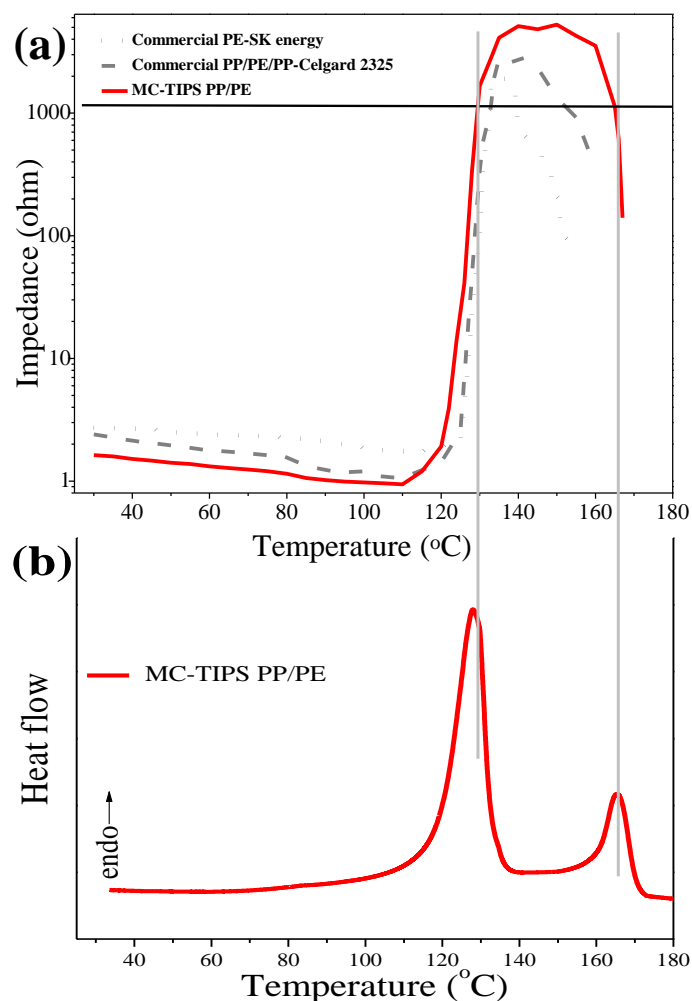


Figure 4.6 (a) Impedance versus temperature curve for cells containing commercial PE separator (SK Energy), commercial PP/PE/PP separator (Celgard<sup>®</sup> 2325), and MC-TIPS PP/PE. (b) The DSC curve of MC-TIPS PP/PE

The ionic mobility of the  $\text{Li}^+$  ion was confirmed by the lithium ion transference number ( $t^+$ ) estimated by chronoamperometry, as is shown in Figure 4.7a. The  $t^+$  was calculated by the ratio of the initial and final current values before and after chronoamperometry. The  $t^+$  of the MC-TIPS PP/PE (0.481) is larger than that of the Celgard<sup>®</sup> separator (0.287), indicates larger effective ionic conductivity of  $\text{Li}^+$  ions for the MC-TIPS PP/PE than that of the commercial separator, which is attributed to the larger porosity and the liquid electrolyte retained in the pores<sup>[205]</sup>. Electrochemical stability of the separators, as one of the most important features for their application in LIBs, was measured by the LSV method. Figure 4.7b shows the results of the LSV profiles of the MC-TIPS PP/PE and Celgard<sup>®</sup> 2325. The electrolyte-soaked Celgard<sup>®</sup> separator exhibits an anodic stability up to 4.13 V. In contrast, the MC-TIPS PP/PE had no typical decomposition peak below 5.21 V vs  $\text{Li}^+/\text{Li}$ . This enhanced electrochemical stability performance is attributed to the improved electrolyte affinity of MC-TIPS PP/PE, which can reduce the decomposition of solvent molecules on the

cathode of lithium ion battery <sup>[216]</sup>. This result demonstrates that the MC-TIPS PP/PE had a wider electrochemical window than Celgard<sup>®</sup> separator, and had the capability to apply as high-voltage LIB separators.

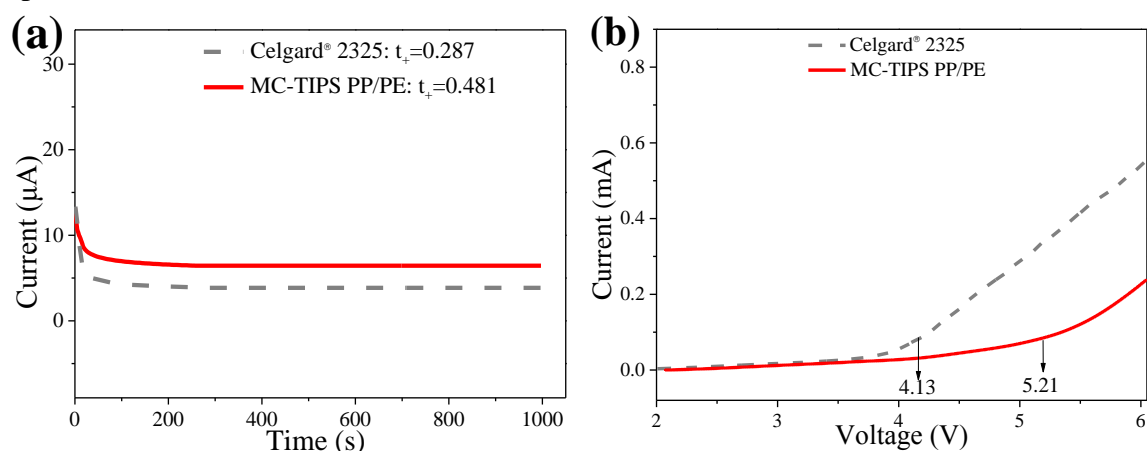


Figure 4.7 (a) Chronoamperometry profiles of LM/electrolyte soaked separator/LM cells assembled with MC-TIPS PP/PE and Celgard<sup>®</sup> separator by a step potential of 10 mV. (b) LSV curves of LM/electrolyte soaked separator/SS cells assembled with MC-TIPS PP/PE and Celgard<sup>®</sup> separator with a scanning rate of 5 mV s<sup>-1</sup> over voltage range from 2 to 6 V

Cycling performance is used to evaluate the performance of a battery in the long run. Figure 4.8a shows the variation of the capacity retention with cycle numbers of cells with MC-TIPS PP/PE and Celgard<sup>®</sup> separator at a current density of 0.2 C. Both of them are relatively stable throughout the first 50 cycles with little performance degradation, indicating a stable cycle performance. While the discharge capacity of the battery with MC-TIPS PP/PE is relatively higher and the gap between two curves becomes larger with the cycle number. The difference can be explained by the higher liquid electrolyte affinity and higher ionic conductivity of the MC-TIPS PP/PE, which can wet the electrode materials more sufficiently <sup>[213]</sup>, accordingly favor intercalation and deintercalation of lithium ions on a cathode, and resulting in higher discharge capacity. Furthermore, the cellular-like and submicron grade pore structure can help seal the electrolyte for longer time, resulting in better reversibility .

The rate performance was also of great significance for LIBs. Figure 4.8b compares the rate behavior of both separators with C-rates increasing from 0.2 to 2.0 C for every five cycles. It could be observed that the cell with MC-TIPS PP/PE presents larger discharge capacities over various discharge current densities, suggesting higher cathode utilization and discharge C-rate capabilities. This improved rate capacity was attributed to the higher porosity and electrolyte uptake, which are in favor of the facile Li<sup>+</sup> transport and good electrolyte retention during cycling. The difference between two separators becomes larger at higher current densities where the influence of ionic transport on

the ohmic polarization is more significant [221]. For both separators, the discharge capacities of cells gradually decrease with the increase of discharge current density, which means high energy loss resulting from fast ions motion and high polarization at higher current densities [222]. When the current densities decreased to 0.2 C, the capacities of both cells with different separators almost recovered to their original values, which meet the requirement of the LIBs. Such ideal cycle and rate performances make MC-TIPS PP/PE a promising candidate for the use in LIBs with stable and enhanced performances.

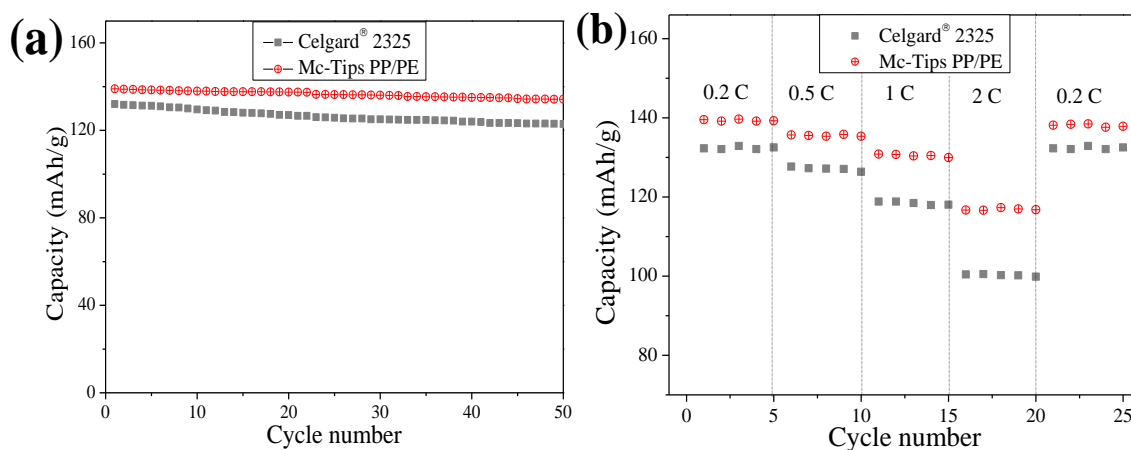


Figure 4.8 Battery performances of MC-TIPS PP/PE and Celgard® separator tested in Li/separator/LiFePO<sub>4</sub> configuration. (a) Cycling performance at 0.2 C-rate and (b) C-rate behavior where the current densities ranging from 0.2 C to 2 C

## 4.4 Conclusions

A facile and continuous preparation method for multilayer PP/PE lithium-ion battery separators has been achieved via the combination of multilayer coextrusion and thermal induced phase separation, which can combine the advantages of both methods. The resultant separator possesses cellular-like and submicron grade pore structure with the porosity of 54.6%. Most impressively, this separator delivers a substantial improvement in the thermal stability compared to the commercial separator, provides wider shutdown temperature window (129-165 °C) and negligible dimensional shrinkage (up to 160 °C). Moreover, the as-prepared separator exhibits higher ionic conductivity, larger lithium ion transference number, and better battery performance. Considering the aforementioned attractive features and the easily scale-up preparation process, this separator is deemed to have great promise for the application in high safety lithium ion batteries.

# Chapter 5 Preparation of Porous Polystyrene Membranes via Multilayer Coextrusion and Adsorption Performance of Polycyclic Aromatic Hydrocarbons

## 5.1 Introduction

As an ubiquitous class of organic compounds consisting of two or more condensed benzene rings and/or pentacyclic molecules, polycyclic aromatic hydrocarbons (PAHs) have been identified in a variety of waters and wastewaters <sup>[233]</sup>. The potential toxic, mutagenic, and carcinogenic properties of PAHs together with their ability to bio-accumulation in aquatic organisms make it urgent to reduce the level of PAHs in aqueous environment <sup>[78]</sup>. A number of effective remediation techniques of the aqueous environment containing PAHs have been investigated, including physical, biological, and phytoremediation processes <sup>[234]</sup>, whereas most of these methods possess disadvantages, such as high upfront investment costs, complicated operating procedures with high maintenance costs, and the release of harmful byproducts, etc <sup>[235]</sup>. Among various methods, the adsorption is found to be a promising technique due to its simplicity of design and operation, high efficiency, low investment and maintenance costs, and no formation of undesirable secondary products. In the past decades, many materials have been reported to be feasible in adsorbing PAHs in aqueous environment including zeolites <sup>[236]</sup>, clays <sup>[76]</sup>, plant residue materials <sup>[237]</sup>, and activated carbon <sup>[238]</sup>, while most of the above materials are less effective for trace PAHs in water. Some micro- or nano-scale adsorbents have been proved to efficiently capture trace water pollutants <sup>[239]</sup>, however, the size of them are too small to separate from water. Thus it is essential to propose new materials that can adsorb trace PAHs and easily to separate from water, moreover, the adsorption method is particularly appealing when the adsorbent is low-priced and could be mass produced <sup>[84]</sup>. According to the similar compatible principle, adsorbents with aromatic ring are comparatively suitable materials for PAHs adsorption. In our previous work, it is found that porous polystyrene (PS) bulk materials via high internal phase emulsion polymerization are good candidates to deal with PAHs contamination in water <sup>[85]</sup>. Among the porous adsorption materials, the porous membranes are preferable over bulk and powder materials since they possess higher contact area with water and are much easier to be separated from wastewaters.

Currently, the porous membranes can be fabricated through numerous methods, including foaming process, phase separation method<sup>[86]</sup>, electrospinning<sup>[87]</sup>, top-down lithographic techniques<sup>[88]</sup>, breath figure method<sup>[89]</sup>, template technique<sup>[240]</sup>, and extrusion spinning process for hollow fiber membranes<sup>[241]</sup>. Among the above methods, the template technique has attracted much attention due to its relatively simple preparation process and tunable pore structure. With the help of the template method, the extrusion-blown molding seems a highly efficient way for the large-scale fabrication of porous membranes. However, the extrusion-blown molding is not suitable for the preparation of brittle PS or particle-embedded polymer membranes. The multilayer coextrusion represents an advanced polymer processing technique, which is capable of economically and efficiently producing films of multilayers with individual layer thickness varying from micron to nanoscale<sup>[61]</sup>.

In the present chapter, a novel strategy is proposed to prepare porous PS membranes with tunable porous structure via multilayer coextrusion combined with the template method, which is a highly efficient pathway for large-scale fabrication of porous PS membranes. In principle, this method is applicable to any melt-processable polymers in addition to PS. The potential application of the porous PS membranes in adsorbing PAHs is explored preliminarily. Pyrene, a representative PAH with medium molecular weight and moderate solubility in water, is selected as the model compound to explore the adsorption performance of the porous PS membranes on PAHs. The related adsorption kinetics and isotherms of the porous PS are also discussed.

## 5.2 Experimental section

### 5.2.1 Materials

PS (GPPS-116, melt index (MI)=7.8, 200 °C/2.16 kg) was purchased from Shanghai SECCO Petrochem. Co.. Low density polyethylene (LDPE) (Q210, MI=9.0, 200 °C/2.16 kg) was purchased from Sinopec Shanghai Petrochem. Co.. CaCO<sub>3</sub> particles (diameter 0.8 μm, electronic grade) were purchased from Aladdin Chem. Co.. Hydrochloric acid (AR grade, 36.0-38.0%) was purchased from Sinopharm Chem. Reagent Co.. Isopropyl dioleic (dioctylphosphate) titanate (TMC 101) was obtained from Tianchang Green Chem. Additive Factory. Cationic dye (turquoise blue X-GB) was purchased from Guangzhou Rongqing Chem. Products Co.. Prior to the processing, PS, LDPE, and CaCO<sub>3</sub> particles were dried separately at 70 °C for 48 h in vacuum oven to remove any humidity which may have been adsorbed during storage.

## 5.2.2 Preparation of PS(CaCO<sub>3</sub>) masterbatches

Prior to the multilayer coextrusion, CaCO<sub>3</sub> particles were pre-dispersed in PS via melt blending, with TMC 101 as the dispersing agent. CaCO<sub>3</sub> particles and PS with the ratio of M: (100-M) were mixed and put into the twin-screw extruder, then the PS(CaCO<sub>3</sub>) masterbatches were obtained, with CaCO<sub>3</sub> content of M wt%.

## 5.2.3 Preparation of PS(CaCO<sub>3</sub>) membranes

As shown in Figure 5.1a, LDPE and PS(CaCO<sub>3</sub>) masterbatches were extruded from extruder A and B respectively. These two melt streams were combined as two parallel layers and then flowed through a series of laminating-multiplying elements (LMEs) and each element doubled the number of layers, as shown in Figure 5.1b. An assembly of n LMEs could produce a tape with 2<sup>(n+1)</sup> layers. In this study, the value of n was taken as 3, 4, and 5, and the total thickness of the multilayer film was fixed at 320 μm. As a result, the single layer thickness of PS(CaCO<sub>3</sub>) membrane is about 20 μm, 10 μm, and 5 μm theoretically.

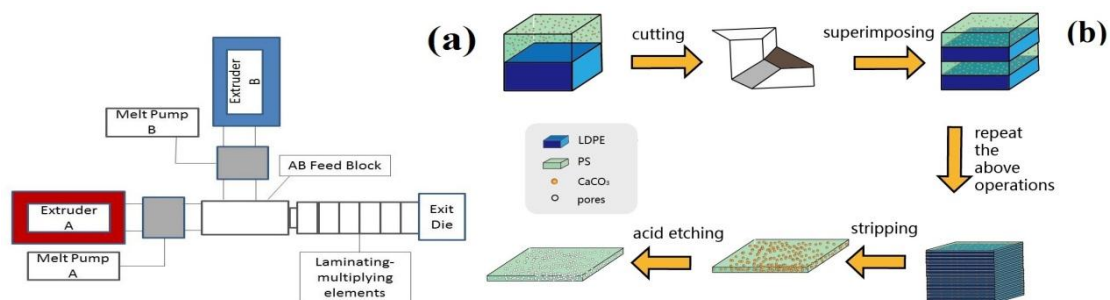


Figure 5.1 (a) Schematic representation of the two-component multilayer coextrusion system, (b) Preparation of porous PS membranes via the combination of multilayer coextrusion and CaCO<sub>3</sub> template method

## 5.2.4 Preparation of porous PS membranes via acid etching method

The single layer PS(CaCO<sub>3</sub>) membranes can be separated from the multilayer structure of LDPE/PS(CaCO<sub>3</sub>) coextrusion films via the mechanical method. Then the PS(CaCO<sub>3</sub>) membranes were soaked into diluted hydrochloric acid solutions (15 wt%) for certain hours (named as i h). Then the membranes were washed to remove the excess acid and dried for 24 h at 60 °C.

## 5.2.5 Characterization

The fractured surface of the porous membranes was observed through the field emission scanning electron microscopy (FESEM, Philips XL30FEG). The optical microscope (Nanjing Kell Instrument Co., KEL-XMT-3100) was used to observe the multilayer configuration of layer-by-layer structure of LDPE/PS(CaCO<sub>3</sub>) coextrusion films and the distribution of CaCO<sub>3</sub> in single layer PS(CaCO<sub>3</sub>) membranes. Thermal gravimetric analysis (TGA) was performed to explore the weight percentage of each material, using a Netzsch STA 449 C thermogravimetric analyzer with a heating rate of 20 °C min<sup>-1</sup> from ambient temperature to 1000 °C under the air flow. Fourier transform infrared spectroscopy (FTIR) (EQUINOX 55, Bruker Co.) was utilized to check whether CaCO<sub>3</sub> templates could be etched by HCl or not. The porosity ( $\varepsilon$ ) of the PS membranes was determined by the n-butanol soaking method, in which the weight of the membrane was measured before and after soaking in n-butanol for 4 h at room temperature, and calculated using the following equation,

$$\varepsilon(\%) = \frac{W - W_0}{\rho_L \times V_0} \times 100\% \quad (5-1)$$

where  $W$  and  $W_0$  are the weight of the membranes with soaked n-butanol and dry membranes respectively;  $\rho_L$  is the density of n-butanol, and  $V_0$  is the geometric volume of the membranes<sup>[64]</sup>.

The adsorption performance tests were carried out by using pyrene as the model compound for PAH. Typically, a large stock of pyrene-contaminated solution (130 ppb) were prepared by phosphate buffer (0.01 M, pH = 7.4). A certain amount of PS membranes were added to the pyrene solution with slight shaking for 20 h. After removal of the solid adsorbent by centrifugation or filtration, the solution was subjected to fluorescent detection on a Thermo Scientific Lumina fluorescence spectrometer (Hitachi F-2700). The  $\lambda_{ex}$  was set at 335 nm and the emission within 350-550 nm was recorded. The residual concentration of pyrene could be determined from the fluorescent intensity-concentration calibration curve.

## 5.3 Results and discussion

### 5.3.1 Preparation of porous PS membranes

PS was selected as the matrix for the porous membranes, CaCO<sub>3</sub> as the template, and LDPE as the split layer. The multilayer configurations of layer-by-layer LDPE/PS(CaCO<sub>3</sub>) coextrusion films with different layer numbers are shown in Figure 5.2a-c. Alternated LDPE (brighter slabs) and PS(CaCO<sub>3</sub>) (darker slabs) layers are clearly visible, and there is no significant interpenetration

between the individual layers. All the layers are parallel and continuous along the coextrusion directions. These results confirm the highly ordered multilayer structure presented in the two basic constituent blocks of LDPE and PS( $\text{CaCO}_3$ ). The clear interface between nearby layers should be attributed to the immiscibility of LDPE and PS.

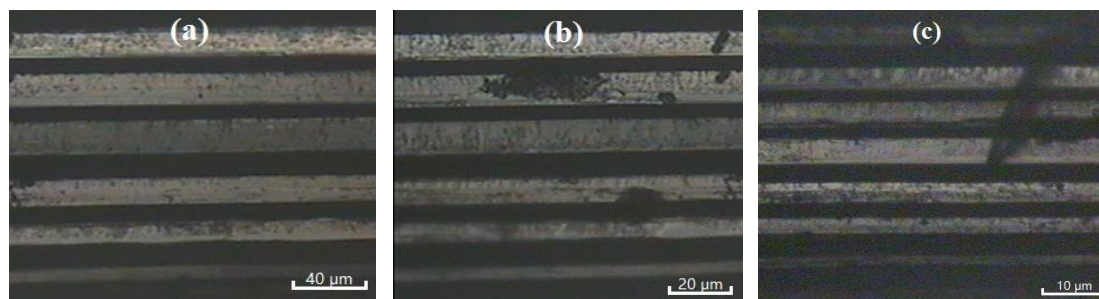


Figure 5.2 Optical microscope images (reflection mode) of the cross-section of LDPE/PS( $\text{CaCO}_3$ ) coextrusion films with multilayer structure, (a) 16 layers, (b) 32 layers, and (c) 64 layers

In order to further verify the influence of the multilayer coextrusion on the distribution of  $\text{CaCO}_3$  particles in PS, optical microscope images of PS( $\text{CaCO}_3$ ) membranes (40 wt%  $\text{CaCO}_3$ ) via traditional method and multilayer coextrusion were compared, as shown in Figure 5.3a and 5.3b. The optical microscope image of the PS( $\text{CaCO}_3$ ) membrane obtained via the twin-screw extruder blending followed by compression molding is shown in Figure 5.3a. It can be observed that there are many opaque and non-uniform white spots, which are caused by the aggregation of  $\text{CaCO}_3$  particles. By contrast, the PS( $\text{CaCO}_3$ ) membrane, prepared via multilayer coextrusion, has achieved better dispersion of  $\text{CaCO}_3$  particles, as shown in Figure 5.3b. The higher shearing during the multilayer coextrusion and the confined space are favorable for the well-dispersion of  $\text{CaCO}_3$  particles in PS membranes.

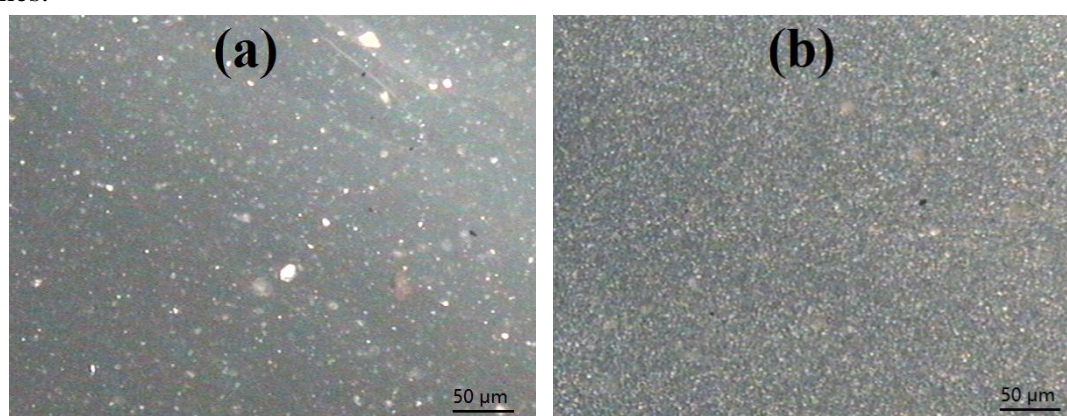


Figure 5.3 Optical microscope images (transmission mode) of PS( $\text{CaCO}_3$ ) membranes (40 wt%  $\text{CaCO}_3$ ), (a) blended by the twin-screw extruder followed by compression molding, (b) prepared via multilayer coextrusion

The PS( $\text{CaCO}_3$ ) membranes prepared via multilayer coextrusion were immersed in dilute hydrochloric acid solution to etch  $\text{CaCO}_3$  particles to obtain the porous PS membranes. The digital

photographs of the single layer of PS( $\text{CaCO}_3$ ) membranes before and after hydrochloric acid etching are shown in Figure 5.4a and 5.4b. The morphological integrity of the membranes was sustained after acid etching and the transparency of the membranes has improved after  $\text{CaCO}_3$  particles were etched by hydrochloric acid due to homogeneous dispersion of  $\text{CaCO}_3$  particles in PS.

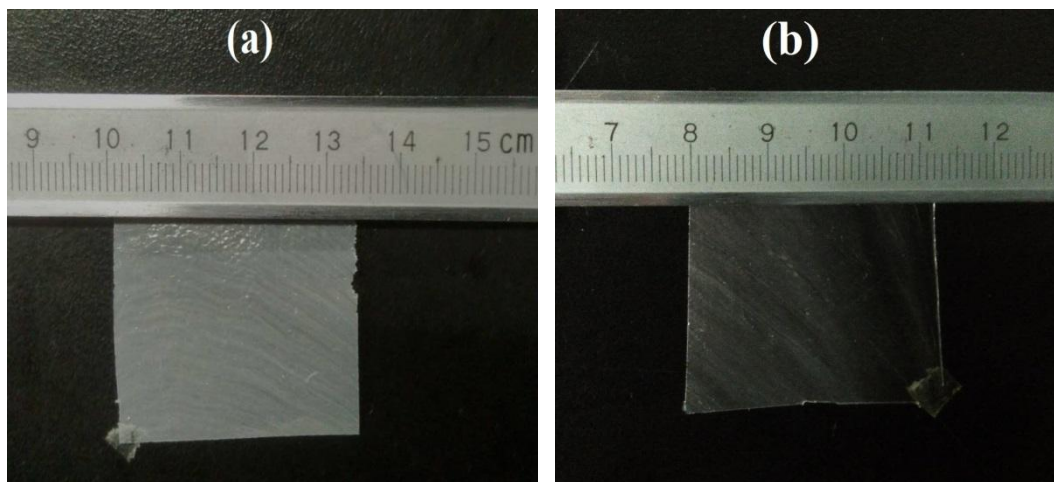


Figure 5.4 Digital photographs of single layer PS( $\text{CaCO}_3$ ) membranes (a) before and (b) after etched in 15 wt% HCl solution for 48 h

### 5.3.2 Regulating and controlling pore structure of PS membranes

To regulate and control the pore structure of PS membranes, three key factors (membrane thickness, etching time, and  $\text{CaCO}_3$  content) were selected as the variable quantities to design a series of control tests. The influence of the membrane thickness on the pore structure was explored with the thickness of 20  $\mu\text{m}$ , 10  $\mu\text{m}$ , and 5  $\mu\text{m}$ , respectively. The SEM images of the fracture surface of the single layer of porous PS membranes with different thickness are shown in Figure 5.5a-5.5c. It can be found that both the quantity and the mean grain diameter of the residual  $\text{CaCO}_3$  particles decrease with decreasing thickness of the membranes. The etched membrane with the thickness of 5  $\mu\text{m}$  (Figure 5.5c) possesses abundant porous structure, and  $\text{CaCO}_3$  particles could rarely be observed. When the membrane thickness is reduced to less than 5  $\mu\text{m}$ , the membrane becomes fragile and easy to be broken, thus the optimal thickness of the membrane is 5  $\mu\text{m}$ . The above results demonstrate the influences of the membrane thickness on the pore structure. With the decrease of the membrane thickness, the ratio of the diameter of  $\text{CaCO}_3$  template to the thickness of the membranes increases. The proportion of the particles near the membrane surface also increases, which is beneficial for the acid etching and also in favor of the acid to penetrate into the internal region of the membranes. However, when the thickness is reduced to less than 5  $\mu\text{m}$ , the mechanical properties of the membrane are deteriorated.

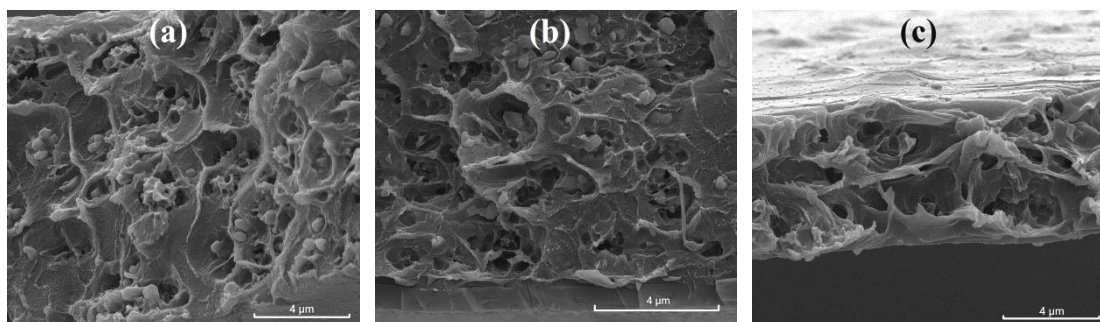


Figure 5.5 SEM images of the frozen brittle fracture surface of porous PS membranes (40 wt%  $\text{CaCO}_3$ , etched for 48 h) with different thickness, (a) 20  $\mu\text{m}$ , (b) 10  $\mu\text{m}$ , (c) 5  $\mu\text{m}$ .

The influence of the etching time on the pore structure has been explored by the comparison of the microscopic morphologies of the PS membranes prepared with different etching time. SEM images are shown in Figure 5.6. The results indicate that the longer the etching time lasts, the more thoroughly  $\text{CaCO}_3$  will be etched. The etching kinetics of  $\text{CaCO}_3$  in the membranes prepared with the  $\text{CaCO}_3$  content of 40 wt% and the thickness of 5  $\mu\text{m}$  are also investigated. The variation of the residual mass percentage of  $\text{CaCO}_3$  versus etching time is plotted in Figure 5.7. During the first 30 h, the mass percentage of residual  $\text{CaCO}_3$  decreases rapidly from 100% to 10%, which is probably due to the etching mainly occurred on the surface and at the near surface region. In the following 30 h, the change is rather slow and the curve becomes more and more flat. This might be due to the remaining particles inside the membranes are relatively difficult for the acid to etch, therefore etching for 30 h is recommended from temporal and economical points of view.

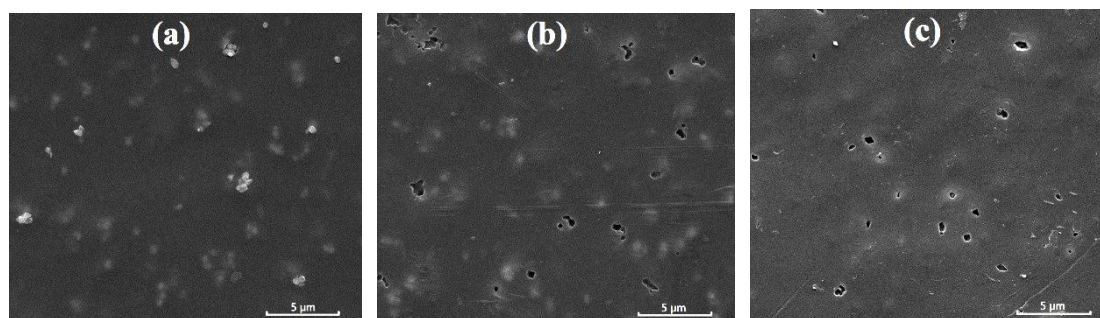


Figure 5.6 SEM images of the surface of polystyrene membranes with different etching time (in 15 wt% HCl solution), (a) before etching, (b) etched for 24 h, (c) etched for 48 h

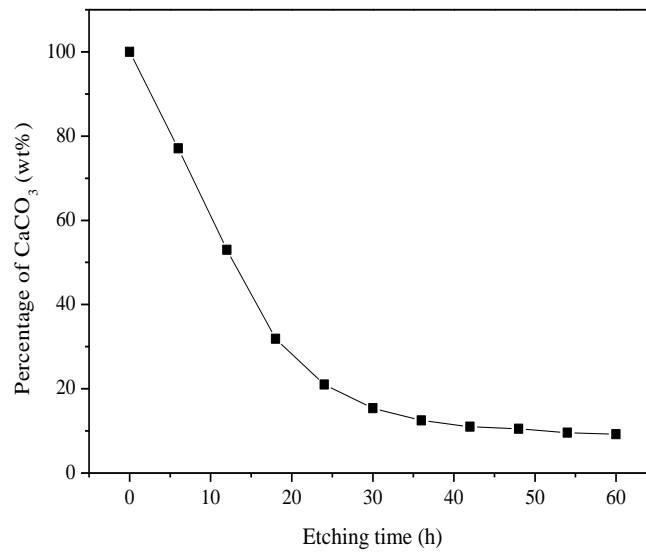


Figure 5.7 Etching (in 15 wt% HCl solution) kinetics of CaCO<sub>3</sub> in the membranes (40 wt% CaCO<sub>3</sub> in the membranes, thickness 5 μm)

The influence of CaCO<sub>3</sub> contents on the pore structure was explored with the CaCO<sub>3</sub> contents of 20 wt%, 40 wt%, and 60 wt%, respectively. The SEM images of the fractured surface of porous PS membranes are shown in Figure 5.8. It can be observed that when CaCO<sub>3</sub> content increases from 20 wt% (Figure 5.8a) to 40 wt% (Figure 5.8b), the membranes possess more abundant pore structure and the grain diameter of the residual CaCO<sub>3</sub> particles become smaller. This is because the CaCO<sub>3</sub> particles are more likely to be in contact with each other at higher CaCO<sub>3</sub> content, which is beneficial for the hydrochloric acid to penetrate into the membrane to conduct the double decomposition reaction with CaCO<sub>3</sub> and form the porous structure. However, when the CaCO<sub>3</sub> content increases to 60 wt%, the CaCO<sub>3</sub> particles tend to agglomerate and act as structure defects in the PS membranes, which will lead to a stress concentration and reduce the mechanical properties such as strength and tenacity.

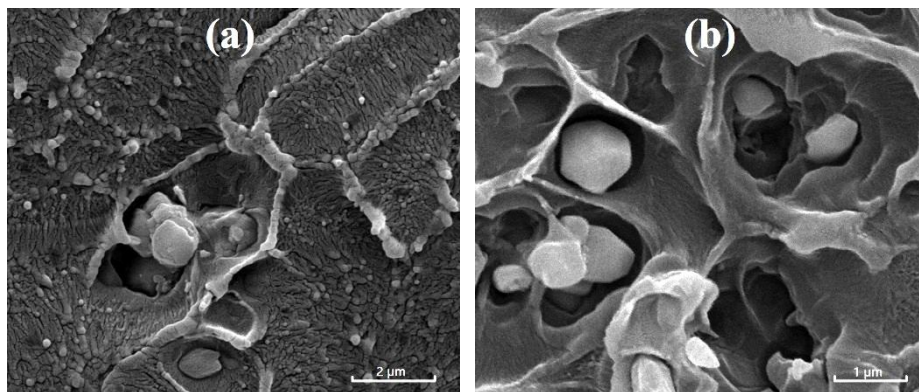


Figure 5.8 SEM images of the frozen brittle fracture surface of PS membranes with different CaCO<sub>3</sub> contents after etched in 15 wt% HCl solution for 48 h, (a) 20 wt% CaCO<sub>3</sub>, (b) 40 wt% CaCO<sub>3</sub>

The porosity P of PS membranes plays an important role on the adsorption properties of PAHs. The porosity of the membranes prepared with different etching time, CaCO<sub>3</sub> content, and membrane thickness was measured, as shown in Table 5.1. It is indicated that the porosity is in positive correlation with the etching time and the initial CaCO<sub>3</sub> content, while in negative correlation with the thickness of the membranes, which are consistent with the analysis of SEM images, through-hole structure test and TGA curves. It can be concluded that the porous membranes, which were prepared with CaCO<sub>3</sub> content of 40 wt%, thickness of 5 μm, and etched for 48 h, possess the optimal through-hole structure.

Table 5.1 Regulation and controlling of the porosity of PS membranes

Sample	1 <sup>#</sup>	2 <sup>#</sup>	3 <sup>#</sup>	4 <sup>#</sup>	5 <sup>#</sup>	6 <sup>#</sup>
Etching time (h)	0	24	48	48	48	48
CaCO <sub>3</sub> content (wt%)	20	20	20	40	40	40
Thickness (μm)	20	20	20	20	10	5
Porosity (%)	0.0	4.3	7.2	10.5	12.1	19.4

### 5.3.3 Adsorption of porous PS membranes on pyrene

By comparing the fluorescence intensity of pyrene solution after and before the adsorption of the porous membranes (6<sup>#</sup>) for 12 h, it can be found that the fluorescence intensity decreases with increasing amount of the membranes, as shown in Figure 5.9a. The adsorption can reach the equilibrium when the amount of porous PS membranes is larger than 0.8 g L<sup>-1</sup>. The residual concentration of pyrene solution after the adsorption can be calculated through the fluorescence intensities according to the standard curve, and the adsorption kinetic curve at the wavelength of 370 nm is plotted in Figure 5.9b. Through the comparison of the concentration of the solution, the minimum residual concentration of pyrene in the aqueous solution is only 9.5 ppb, which is much lower than the initial value (130 ppb). The saturated adsorbing capacity of the porous PS membrane (6<sup>#</sup>) can also be calculated from Figure 5.9b, with a value of 0.584 mg g<sup>-1</sup>, which is really higher than many other adsorption materials. For example, the saturated adsorbing capacity of the dendritic amphiphile mediated porous monolith of pyrene is proved to be 0.2 mg g<sup>-1</sup> [242], which is much lower than the value in the current work.

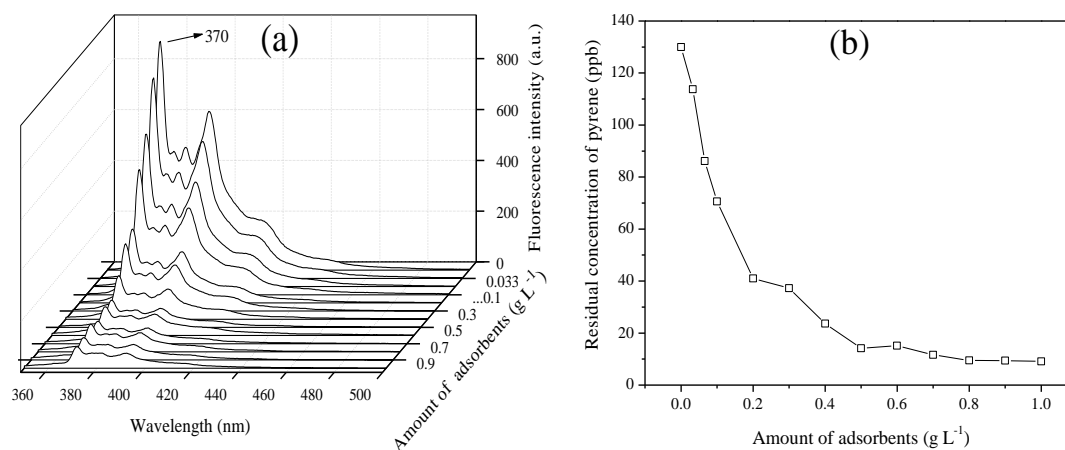
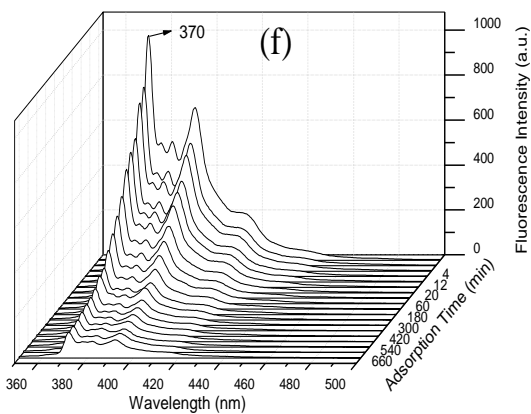
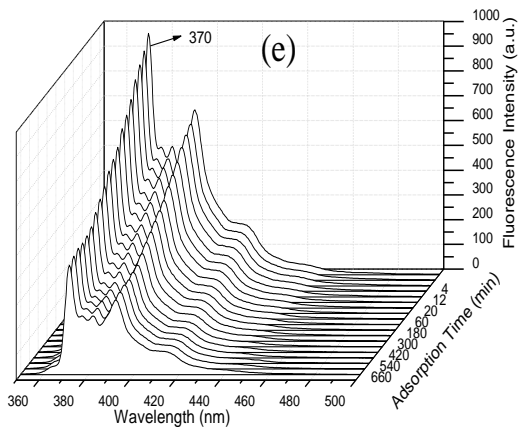
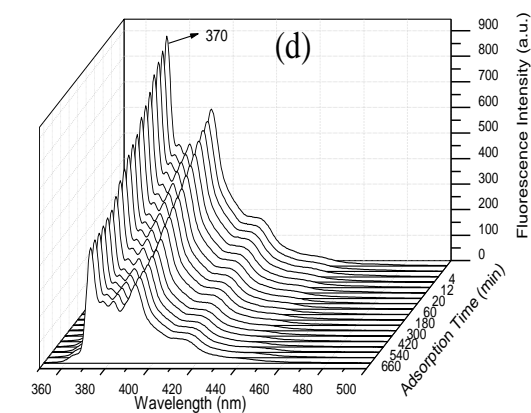
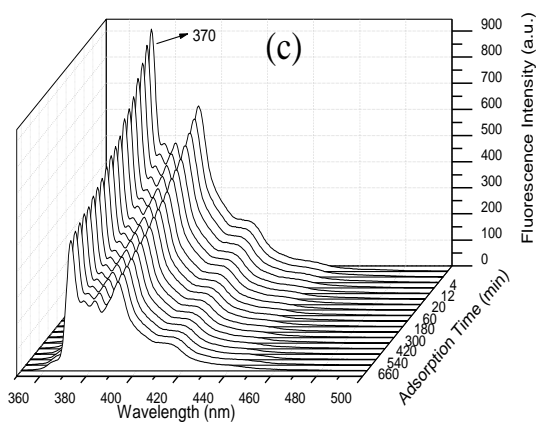
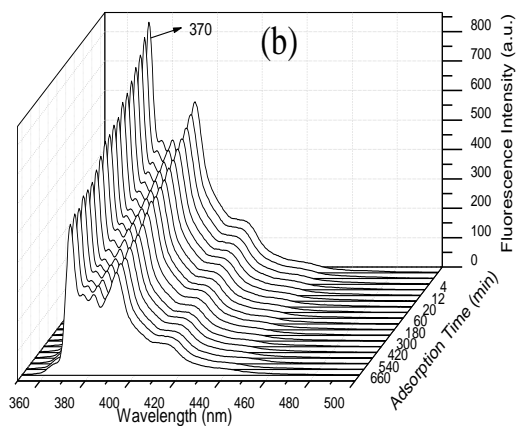
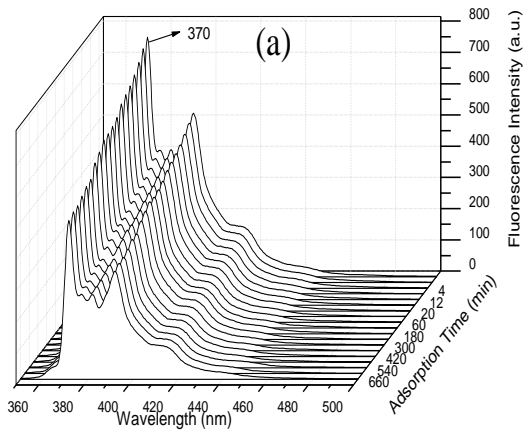


Figure 5.9 (a) Fluorescence spectra of pyrene in aqueous solution after adsorbed by porous PS membranes (6<sup>#</sup>) for 12 h; (b) effects of the amount of porous PS membranes (6<sup>#</sup>) on the residual concentration of pyrene solution, which can be calculated according to the fluorescence intensity of the solution at 370 nm; the initial concentration of pyrene solution is 130 ppb

In the following part, the ratio of the membrane mass to the volume of the aqueous solution was chosen to be  $0.8 \text{ g L}^{-1}$ , and the initial concentration of pyrene is  $0.13 \text{ mg L}^{-1}$  (130 ppb). For comparison, the adsorption properties of the membranes prepared with different membrane thickness, etching time, and  $\text{CaCO}_3$  content (from 1<sup>#</sup> to 6<sup>#</sup>) were all examined. From the declined trend of the fluorescence intensity with increasing time as plotted in Figure 5.10a to Figure 5.10f, it could be clearly observed that the declining rate of 6<sup>#</sup> is the highest, followed by 5<sup>#</sup>, 4<sup>#</sup>, 3<sup>#</sup>, 2<sup>#</sup>, and 1<sup>#</sup>. Based on the above fluorescence curves, the variation of the residual concentration of pyrene versus the adsorption time (at the wavelength of 370 nm) were calculated according to the standard curve and were plotted in Figure 5.10g. It can be observed that the concentration of pyrene adsorbed separately by six groups of membranes descends rapidly during the first hour, while the gap between the curves becomes larger as time increases. The adsorption equilibrium time for the membranes is similar to the value of 8 h, while the final residual concentrations of pyrene are quite different. The sequence of the adsorption performance of the membranes is  $6^{\#} > 5^{\#} > 4^{\#} > 3^{\#} > 2^{\#} > 1^{\#}$ , which is in line with the order of the porosity. This illustrates that the porous membranes have better adsorption capability attributed to the higher porosity. The possible reason is that the abundant pore structure and surface area increase the contact probability between the pyrene molecules and the inner wall of the porous membranes. As a result, more pyrene molecules can be adsorbed by the inner wall of the porous membranes with higher porosity according to the collision mechanism. Besides, according to the similar compatible principle, both pyrene and PS have aromatic ring structures, which is beneficial for the pyrene adsorption of PS membranes. Theoretically, it can be concluded that such kind of porous membranes can also be used to adsorb other PAHs with aromatic ring.



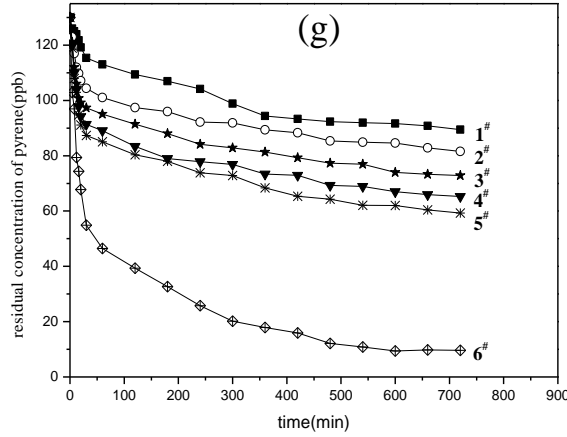


Figure 5.10 Fluorescence spectra of pyrene in aqueous solution after adsorbed for different time by (a) 1<sup>#</sup> membranes, (b) 2<sup>#</sup> membranes, (c) 3<sup>#</sup> membranes, (d) 4<sup>#</sup> membranes, (e) 5<sup>#</sup> membranes, and (f) 6<sup>#</sup> membranes; (g) Adsorption kinetics of pyrene in aqueous solution by membranes from 1<sup>#</sup> to 6<sup>#</sup> with 0.8 g L<sup>-1</sup> membranes in the solution, which can be calculated according to the fluorescence intensity of the solution at 370 nm, the initial concentration of pyrene solution is 130 ppb

To further understand the adsorption process, the adsorption kinetics is investigated according to two models, pseudo-first- and pseudo-second-order equation. In this part, membrane 1<sup>#</sup> represents the solid PS membranes and membrane 6<sup>#</sup> stands for the porous PS membranes. The pseudo-first-order equation can be expressed as,

$$\frac{dQ_t}{dt} = k_1(Q_{eq} - Q_t) \quad (5-2)$$

where  $Q_{eq}$  and  $Q_t$  (mg g<sup>-1</sup>) stand for the amount of pyrene adsorbed at equilibrium state and time  $t$  respectively;  $k_1$  is the pseudo-first-order rate constant [75]. After definite integration, equation (5-2) turns into,

$$\ln(Q_{eq} - Q_t) = \ln Q_{eq} - k_1 t \quad (5-3)$$

Theoretically, there exists a straight line (slope- $k_1$ ) in the plot of  $\ln(Q_{eq}-Q_t)$  versus  $t$ . The correlation coefficients for membrane 1<sup>#</sup> (solid) and 6<sup>#</sup> (porous) are 0.94 and 0.95, respectively, as shown in Figure 5.11a. Although the correlation coefficients are high, the linear fitting degree has not reached the expected results yet. Thus, the pseudo-second-order equation is introduced as below,

$$\frac{dQ_t}{dt} = k_2(Q_{eq} - Q_t)^2 \quad (5-4)$$

Integrating the above equation by applying initial conditions, equation (5-4) becomes,

$$\frac{t}{Q_t} = \frac{1}{k_2 Q_{eq}^2} + \frac{t}{Q_{eq}} \quad (5-5)$$

As shown in Figure 5.11b, the two linear plots of  $t/Q_t$  against  $t$  give higher correlation coefficients, 0.96 and 0.99 for membrane 1<sup>#</sup> (solid) and 6<sup>#</sup> (porous) separately. Especially for porous PS membranes, the linear fit agrees well with the pseudo-second-order model.

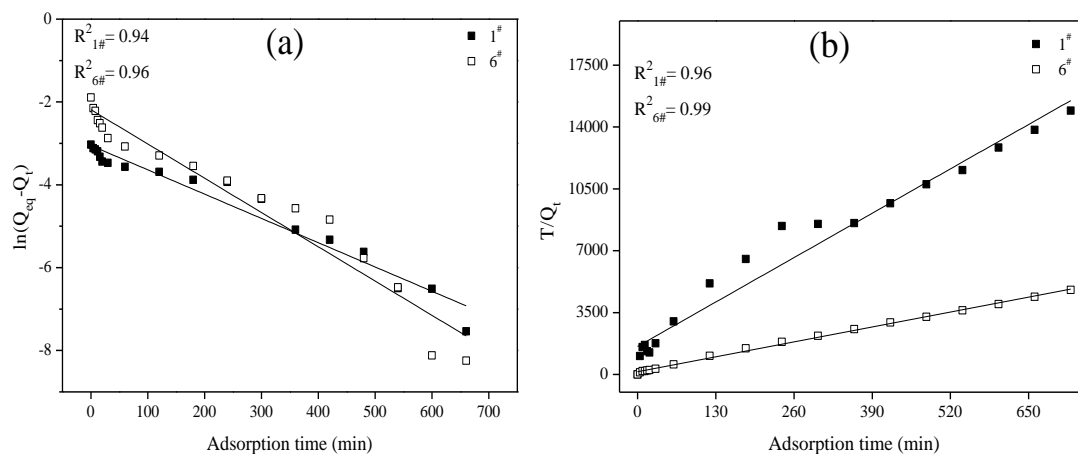


Figure 5.11 (a) First-order rates for the adsorption of pyrene by membrane 1<sup>#</sup> and 6<sup>#</sup>; (b) Second-order rates for the adsorption of pyrene by membrane 1<sup>#</sup> and 6<sup>#</sup> PS membranes; the initial concentration of pyrene is 0.13 mg L<sup>-1</sup>

### 5.3.4 Adsorption isotherms

The way adsorbates interact with adsorbents is generally described by the adsorption isotherm, which is of vital importance to understand the mechanism of adsorption and to design an adsorption system meeting the necessary requirements. Several isotherm models can be found in the literature [243]. This study used Freundlich and Langmuir isotherm models, which have been widely adopted in the adsorption isotherm studies, to fit the experimental data for pyrene adsorbed by porous PS membranes (6<sup>#</sup>). Figure 5.12a shows the adsorption isotherm for pyrene at equilibrium.

The linearized form of Freundlich model can be described as follows [75],

$$\ln Q_{eq} = \ln K_F + b_F \ln C_{eq} \quad (5-6)$$

where  $K_F$  is Freundlich constant;  $C_{eq}$  (mg L<sup>-1</sup>) is the equilibrium concentration of pyrene in the solution;  $b_F$  is a constant depicting the adsorption intensity. The value of  $\ln Q_{eq}$  vs.  $\ln C_{eq}$  is plotted in Figure 5.12b according to the experimental data, and the corresponding correlation coefficient for pyrene adsorption is 0.96, indicating that the adsorption of pyrene by porous PS membranes (6<sup>#</sup>) highly obeys Freundlich model. While, the assumption of Langmuir theory is that the adsorption takes place at the specific homogeneous sites equivalently within adsorbent [75] and no interaction among adsorbate molecules exists. The Langmuir isotherm is expressed as below,

$$\frac{C_{eq}}{Q_{eq}} = \frac{C_{eq}}{Q_{max}} + \frac{1}{Q_{max} K_L} \quad (5-7)$$

where  $Q_{max}$  ( $\text{mg g}^{-1}$ ) is the maximum capacity of the adsorbent and  $K_L$  ( $\text{L mg}^{-1}$ ) is the Langmuir adsorption constant <sup>[75]</sup>. The experimental values of  $C_{eq}/Q_{eq}$  against  $C_{eq}$  are shown in Figure 5.12c. As can be found, the corresponding correlation coefficient for the adsorption of pyrene is 0.79. The lower correlation coefficient indicates the poor agreement of this adsorption cases with Langmuir isotherm model. Thereby, in this case, for the adsorption of pyrene by the porous PS membranes (6<sup>#</sup>), the fitting via Freundlich model is better.

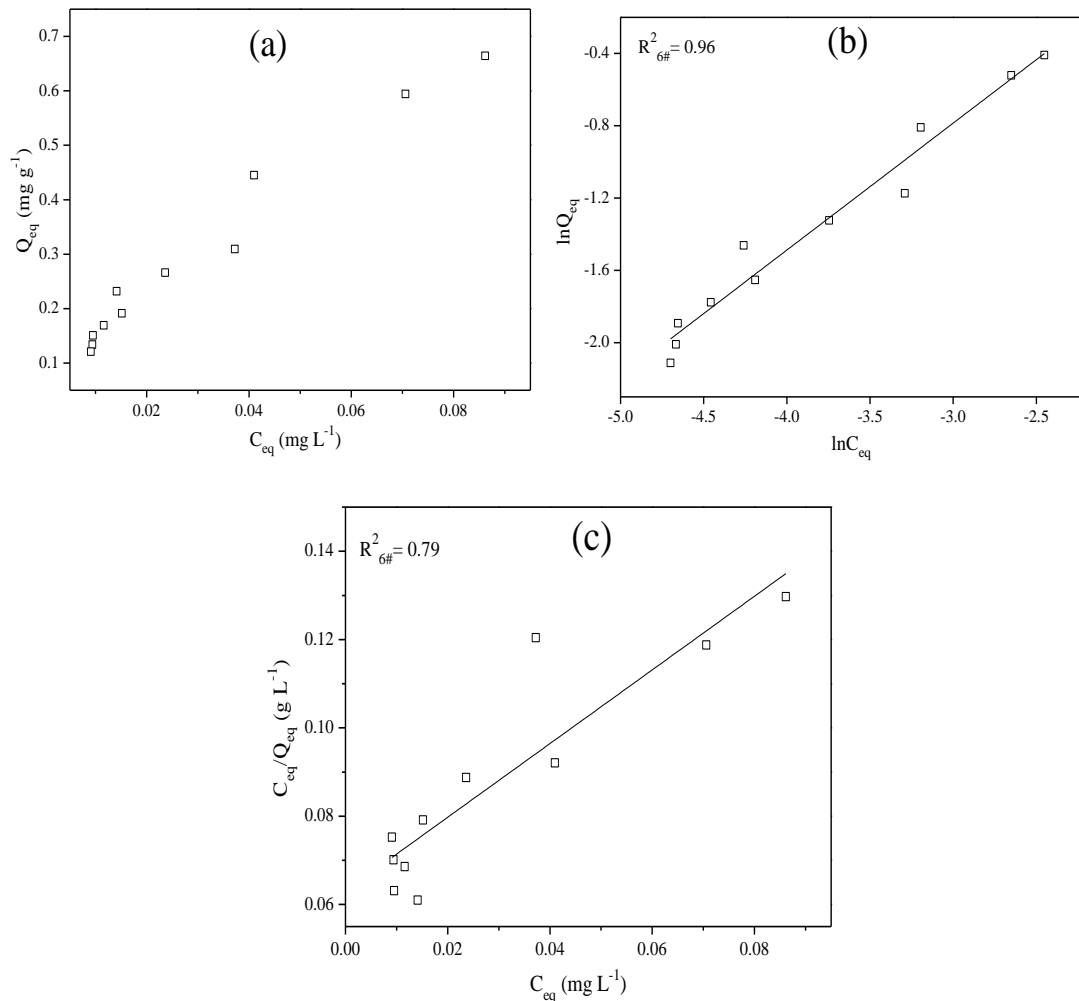


Figure 5.12 Adsorption isotherm for the adsorption of pyrene by porous PS membranes (6<sup>#</sup>); (b) the values of  $\ln Q_{eq}$  against  $\ln C_{eq}$  based on Freundlich isotherm model; (c) the linear dependence of  $C_{eq}/Q_{eq}$  on  $C_{eq}$  based on Langmuir isotherm model

## 5.4 Conclusions

A continuous and convenient preparation method for porous PS membranes has been achieved via the combination of multilayer coextrusion and CaCO<sub>3</sub> template method. The higher shearing during the multilayer coextrusion and the confined space are favorable for the well-dispersion of CaCO<sub>3</sub> particles in PS membranes. A series of controlling tests were designed to explore the key factors which can regulate and control the porous structures. The results indicate that the membranes prepared with the CaCO<sub>3</sub> content of 40 wt%, a thickness of 5 μm, and etched for 48 h possess the optimal open pore structure. In addition, the confined space created by LMEs in multilayer coextrusion plays an important role in the dispersion of CaCO<sub>3</sub> particles, and accordingly is beneficial for the formation of homogeneous porous membranes via acid etching. Pyrene is chosen as the model compound to explore the PAH adsorption performance of the membranes. The results show that the porous PS membranes with higher porosity exhibit much higher adsorption performance on pyrene in dilute aqueous solution, compared with that adsorbed by PS membranes with lower porosity. This is attributed to the abundant pore structure of the membrane and the similar compatible principle between the membrane surface and the adsorbates. The adsorption kinetics and isotherm of porous PS membranes were found to follow pseudo second-order kinetics and Freundlich isotherm model, respectively. Considering the continuous fabrication process and the good adsorption properties of porous PS membranes, it is believed that this fascinating adsorbent can be a promising candidate for the adsorption of PAHs from wastewater and industrial effluents.

## **Part II : Transport of Colloidal Particles in Polymeric Porous Media :**

### **Numerical Modeling**

#### **Chapter 6 Colloidal Particle Deposition in Porous Media Idealized as a Bundle of Capillaries**

##### **6.1 Introduction**

Porous media are of scientific and technological interest because of the wide spectrum of applications they have attained during the past decades <sup>[2]</sup>. Various methods have been used for the design of porous media, such as foaming process, template technique, sol-gel, hydrothermal synthesis, precipitation, chemical etching methods and photolithographic techniques <sup>[244]</sup>. Several types of porous media including porous polymers, organic-inorganic hybrid porous materials, and porous carbon aerogels have been successfully synthesized in our previous works <sup>[245]</sup>. These porous materials are used for many purposes, namely for water filtration and waste water treatment which are the focus of this study.

Moreover, particle transport and deposition processes in porous media are of great technological and industrial interest since they are useful in many engineering applications and fundamentals including contaminant dissemination, filtration, chromatographic separation and remediation processes <sup>[6, 113]</sup>. To characterize these processes, numerical simulations have become increasingly attractive due to growing computer capacity and calculation facilities offering an interesting alternative, especially to complex in situ experiments <sup>[95-97]</sup>. Basically, there are two types of simulation methods, namely macro-scale simulations and micro-scale (pore scale) simulations. Macro-scale simulations describe the overall behavior of the transport and deposition process by solving a set of differential equations that gives spatial and temporal variation of particles concentration in the porous sample without providing any information regarding the nature or mechanism of the retention process <sup>[95]</sup>. Micro-scale (pore scale) numerical simulations directly solve the Navier-Stokes or Stokes equation to compute the flow and model particle diffusion processes by random walk for example <sup>[110]</sup>. Lopez et al. <sup>[17]</sup> carried out micro-scale numerical simulations of colloidal particles deposition onto the surface of a simple pore geometry consisting of two parallel

planar surfaces. Messina et al. <sup>[246]</sup> used micro-scale simulations to estimate the particle attachment efficiency.

The objective of the current work is to simulate the process of particles transport and deposition in porous media at the micro-scale by means of CFD simulations in an easy way in order to get the most relevant quantities by capturing the physics underlying the process. The main idea, here, is to revisit the work of Lopez and co-authors <sup>[17]</sup> by considering a more realistic 3D geometry such as a pipe. Indeed their work was limited to a particular geometry restricted to a slot-like geometry unlikely to be encountered in real porous media.

## 6.2 Methodology and tools

### 6.2.1 Methodology

The present work focuses on three-dimensional numerical modeling of the process of transport of particles in a pipe as porous media are usually represented as a bundle of capillaries. This is done by coupling two available soft wares. First, the velocity field is obtained by means of the popular OpenFOAM<sup>®</sup> (Open Field Operation and Manipulation) shareware and secondly particle's tracking is performed with Python<sup>®</sup> software.

The particle-pore wall interaction is considered purely attractive while particle-particle interaction is purely repulsive. Particles are injected sequentially at a random initial position at the inlet of the pipe and their center of mass is tracked until either they reach the outlet of the domain or are deposited onto the pipe surface. The particles' mean diameter and flow conditions are chosen in a way that the particle's Reynolds number is sufficiently small so that the particles can be treated as a mass point. However, once a particle is deposited, an equivalent volume surrounding the deposition location is set to be solid on the pore surface. Then the new velocity field is recalculated to take into account the influence of the presence of the deposited particle on the flow and a new particle is then injected. The injection process is repeated until particle deposition probability vanishes.

### 6.2.2 Determining the flow field in OpenFOAM shareware

The hydrodynamic model is solved with OpenFOAM<sup>®</sup> package, which is a versatile equations' solver and can be used to solve different kinds of differential equations. The velocity field is obtained by solving the Stokes and continuity equations. No-slip boundary condition is applied on

the pore wall, and the pressure at the inlet and outlet are set to fixed values. It should be noticed that the hydrodynamic model is used to generate input flow data for the particle transport model.

### 6.2.3 Lagrangian particle tracking in Python<sup>®</sup>

Injected particles are tracked using a Lagrangian method. Three situations may occur: (i) the particle is adsorbed onto the solid wall when it approaches it closely if a free surface is available for deposition; (ii) the particle leaves the domain and never comes close to the wall surface; (iii) the particle comes close to the solid surface but the deposition site is occupied by another particle repelling it to the bulk flow. The velocity at every node is the vector summation of the interpolated convection velocity  $\mathbf{V}_{\text{int}}$  (obtained from OpenFOAM) and the Brownian diffusion velocity  $\mathbf{V}_{\text{diff}}$ :

$$\mathbf{V} = \mathbf{V}_{\text{int}} + \mathbf{V}_{\text{diff}} \quad (6-1)$$

where  $\mathbf{V}_{\text{int}}$  is the flow velocity computed at a given position by interpolating the velocity values calculated by the hydrodynamic model for the eight surrounding nodes. The stochastic movement of the particles is realized through the calculation of  $\mathbf{V}_{\text{diff}}$  at every position knowing its diffusivity coefficient,  $D$ , given by

$$D = \frac{k_B T}{6\pi \mu a_p} \quad (6-2)$$

where  $k_B$  is the Boltzmann constant,  $T$  the absolute temperature,  $\mu$  the dynamic viscosity of the suspending fluid and  $a_p$  the particle radius. The diffusion velocity  $\mathbf{V}_{\text{diff}}$  is related to the diffusion coefficient  $D$  through the following relationship:

$$\mathbf{V}_{\text{diff}} = \sqrt{\frac{D}{t_r}} \quad (6-3)$$

where  $t_r$  is the referential time <sup>[17]</sup>,

$$t_r = \zeta / (2 u_{\text{max}}) \quad (6-4)$$

In equation (6-4);  $\zeta$  stands for the characteristic mesh size and  $u_{\text{max}}$  is the maximum of actual velocity along the mean flow axis. New positions of the moving particle are obtained by summing the old position vector and the sum of the diffusion velocity and the convection velocity multiplied by the referential time <sup>[17]</sup>:

$$\mathbf{X}_{\text{new}} = \mathbf{X}_{\text{old}} + \mathbf{V} t_r \quad (6-5)$$

## 6.2.4 Simulation parameters

The parameters used in the simulations are summarized in table 6.1.

Table 6.1 Detailed parameters of the simulation

Parameters	Values
Particle diameter, $a_p$ (m)	$4 \times 10^{-7}$
Pipe length, $L$ (m)	$1.5 \times 10^{-5}$
Pipe radius, $R$ (m)	$4 \times 10^{-6}$
Pressure drop, $\Delta p$ (Pa)	From $10^{-5}$ to 1
Péclet number, $Pe$	From 0.0015 to 150
Boltzmann constant, $k_B$ (J/°K)	$1.38 \times 10^{-23}$
Absolute temperature, $T$ (°K)	293.15
Diffusion coefficient, $D$ (m <sup>2</sup> /s)	$5 \times 10^{-11}$
Dynamic viscosity, $\mu$ (Pa s)	$10^{-3}$

Following a sensitivity analysis, for all simulations a mesh number of  $50 \times 50 \times 40$  is chosen with a mesh refinement in the vicinity of solid walls.

The Péclet number ( $Pe$ ) is a dimensionless number that is relevant for the study of transport phenomena of colloidal dispersions. Here, it is defined to be the ratio of the rate of advection to the rate of particle's diffusion:

$$Pe = \frac{\bar{u} a_p}{D} \quad (6-6)$$

where  $\bar{u}$  is the average convection velocity along the mean flow axis.

## 6.3 Results and discussion

### 6.3.1 Deposition probability

Figure 6.1 shows the variation of the deposition probability versus the number of injected particles for different Péclet numbers ranging from low  $Pe$  where diffusion is dominant to high  $Pe$  where the transport is mainly governed by convection. The probability of deposition is defined as the

ratio of the deposited particles over the injected particles and is calculated over groups of 200 injected particles.

For the diffusion-dominant regime at low Péclet number, the deposition probability is high for a small number of injected particles and decreases slowly as more particles are injected. This is due to the fact that for a lower number of injected particles, the wall surface is free and the injected particles easily find a place to deposit. When the number of adsorbed particles reaches a certain value, the deposition probability drops sharply to reach lower values for higher numbers of injected particles. When this sharp transition is approached, the surface wall is already covered by many adsorbed particles and further injected particles will have much less probability to deposit. For high Péclet numbers, where the transport is dominated by convection, the available surface for adsorption is potentially lower than that for the diffusion dominant regime. Indeed, there is a larger exclusion surface around already deposited particles due to hydrodynamic shadowing effect. This leads to lower values for the deposition probability [17].

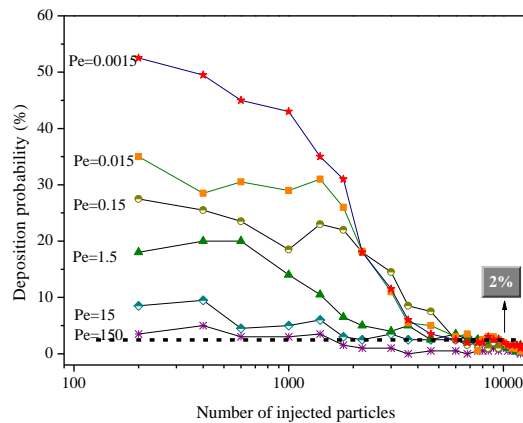


Figure 6.1 Variation of deposition probability versus the number of injected particles for different Péclet numbers

### 6.3.2 Surface coverage

Surface coverage ( $\Gamma$ ) is defined as the ratio of the total projection area of the deposited particles to the pipe surface area. Moreover, it is well known that for pure diffusion regime and a flat surface using the Random Sequential Adsorption (RSA) model, the maximum surface coverage,  $\Gamma_{RSA}$ , is found to be close to 0.546 [17, 247]. The surface coverage  $\Gamma$  is therefore made dimensionless using this value.

The dependency of  $\Gamma/\Gamma_{RSA}$  on the number of injected particles for different Péclet numbers is shown in Figure 6.2. As expected, the surface coverage increases with the number of injected

particles and it decreases with the Péclet number. For the most diffusive case considered here,  $Pe = 0.0015$ , the dimensionless surface coverage reaches values close to  $0.95 \Gamma_{RSA}$ , while for the large Péclet number,  $Pe = 150$ , corresponding to a fully convection-dominant regime,  $\Gamma/\Gamma_{RSA}$  is as low as  $0.22 \Gamma_{RSA}$ . We must recall that the surface coverage is an important parameter because it is linked to the performance of the porous medium when it is used for water filtration for solid particles or micro-organisms removal. For these applications, a high value of surface coverage is therefore aimed.

In Figure 6.3, the geometry and the adsorbed particles are presented after the injection of 3000 particles for the two extreme  $Pe$  numbers ( $Pe=0.0015$  and  $Pe=150$ ). As it can be seen, for higher  $Pe$ , the number of deposited particles is much less than that obtained for lower  $Pe$ , which is a visual illustration of the analysis is made above.

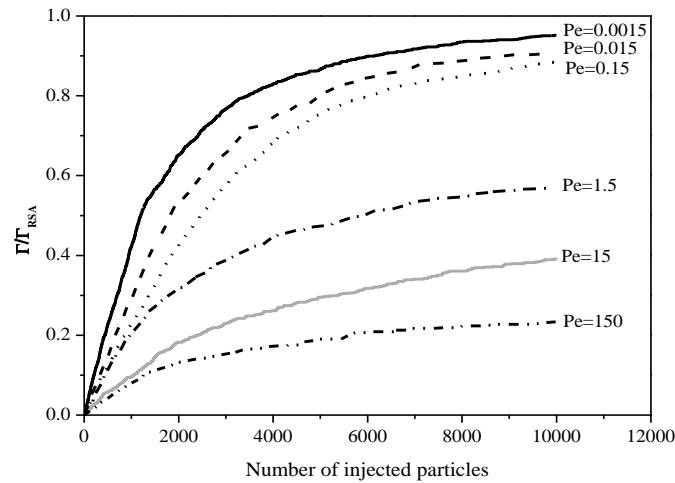


Figure 6.2 Variation of  $\Gamma/\Gamma_{RSA}$  versus the Péclet number

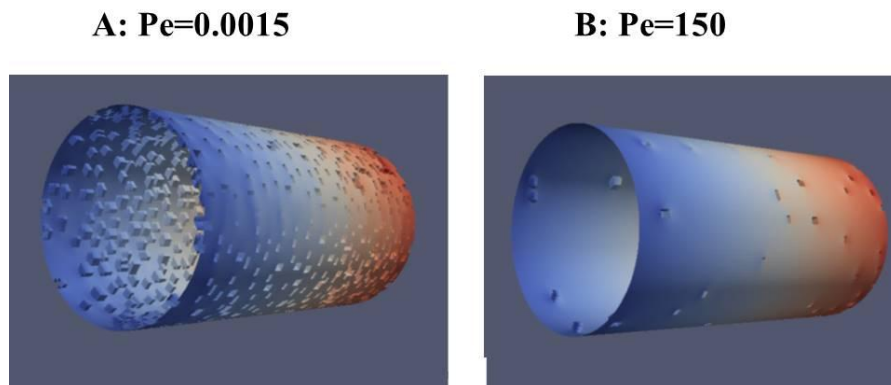


Figure 6.3 Visual illustration of adsorbed particles for two different Péclet numbers after the injection of 3000 particles (A)  $Pe=0.0015$  and (B)  $Pe=150$

### 6.3.3 Porosity and permeability reduction

In processes such as water reinjection in enhanced oil recovery technics, colloids transport and namely particle deposition has an important role in porous media damage and water injectivity decline, since deposited particles influence the petrophysical properties of the reservoir namely the porosity and the permeability. The variations of these properties versus the number of the injected particles are plotted in Figure 6.4 and Figure 6.5.

Here, the porosity is defined as the ratio of the pore volume after deposition and the overall initial pipe volume. As expected, for different Péclet numbers, the porosity decreases with the number of injected particles. The porosity reduction trend is faster for smaller Péclet numbers as a consequence of mechanisms discussed previously and the final porosity decreases with the Péclet number as well.

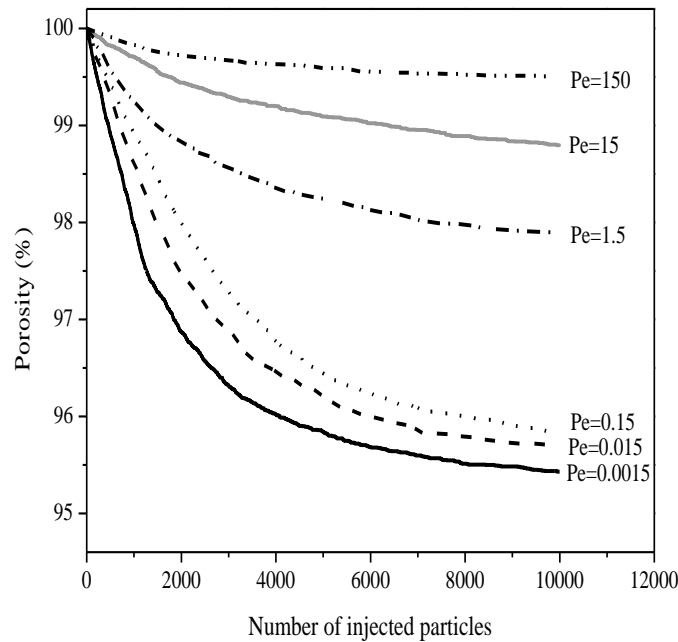


Figure 6.4 Variation of porosity values versus N at different Pe

In this study, the permeability is calculated by:

$$K = \frac{\bar{u} \mu L \varepsilon}{\Delta p} \quad (6-7)$$

where  $\bar{u}$  is the average convection velocity along the mean flow axis,  $\mu$  is the dynamic viscosity of the injected fluid, L is the length of the pipe,  $\varepsilon$  is the porosity of the pipe, and  $\Delta p$  is the pressure

drop between the inlet and the outlet face. The permeability reduction factor,  $R_k$  is defined as the ratio of  $K$  to  $K_r$  where  $K$  and  $K_r$  stand for the permeability before and after deposition.  $K$  is constant for all  $Pe$  and equal to  $1.51 \times 10^{-12} \text{ m}^2$ . The variation of  $R_k$  versus the number of injected particles is plotted in Figure 6.5a for each value of  $Pe$ . The permeability decreases with the number of injected particles, and the trend is more pronounced for diffusion dominant regimes (smaller Péclet numbers). Knowing the  $R_k$  values, one can estimate the hydrodynamic thickness of deposited layer  $\delta$  using Poiseuille's law:

$$\frac{\delta}{R} = 1 - R_k^{-1/4} \quad (6-8)$$

where  $R$  is the initial pore radius. In this study, the ratio  $(\delta/2a_p)$  of the final hydrodynamic thickness to the particle diameter versus  $Pe$  is plotted in Figure 6.5b to compare with the experimental work and the simulation results. For  $Pe < 1$ , the curve shows a relatively stable plateau in our work as well as in the simulation results by Lopez et al. [17] Particularly speaking, for the diffusion-dominant regime ( $Pe=0.0015$ ), the surface coverage is very closed to the RSA limit, and the  $\delta/2a_p$  reaches an upper limit of 0.87, a value quite close to the outcome obtained by S. Buret and co-authors who used a simple modified Poiseuille's law with the average hydrodynamic thickness of the deposition layer equal to 0.9 times the droplet diameter. Remember that a large value of  $\delta/2a_p$  is corresponding to a high number of deposited particles. While for  $Pe > 1$ , the experimental and simulation data show that  $\delta/2a_p$  is a decreasing function of flow strength. The reason for the horizontal shifts among the three groups of data may be explained by the difference in geometries of porous media as well as in the calculation methods for the parameters [17, 248, 249].

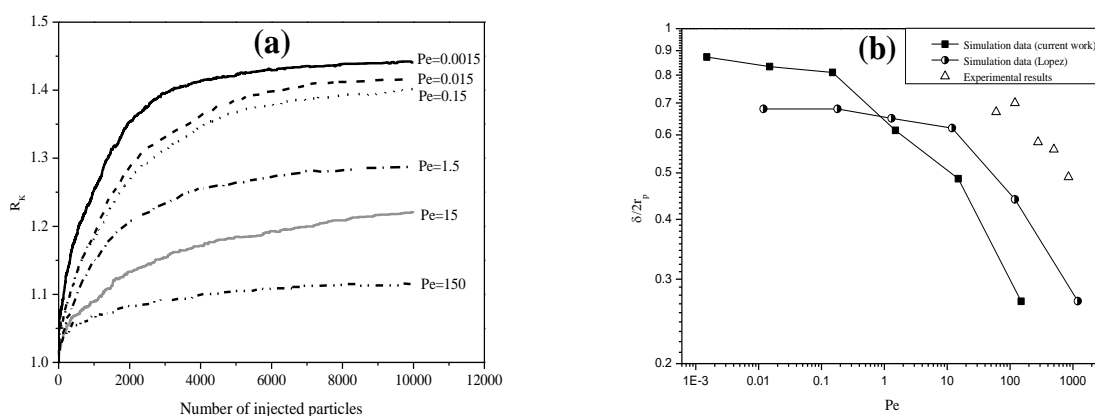


Figure 6.5 Variation of permeability reduction versus  $N$  at various  $Pe$  (A); Hydrodynamic thickness  $\delta/2r_p$  of the deposited layer versus  $Pe$  (B) [17]

## 6.4 Conclusions

Numerical simulations of the deposition of colloidal particles onto porous media of simple geometry under flow have been carried out by coupling two available soft wares: the OpenFOAM<sup>®</sup> shareware is used to obtain the velocity field by solving the Stokes and continuity equations and a software developed in this work using Python<sup>®</sup> programming language and used for the particle tracking process. Important quantities such as deposition probability, surface coverage, porosity and permeability were calculated during the simulations. The variations of these quantities versus the number of injected particles for different Péclet numbers were examined. Preliminary results were analyzed and the some conclusions may be drawn. The deposition probability decreases with the number of the injected particle and with the Péclet number. At low Péclet number values, the surface coverage  $\Gamma$  is shown to closely approach the RSA value and it drops noticeably for high Pe values. Both the porosity and the permeability decrease with the number of deposited particles. At lower Pe numbers, the final hydrodynamic thickness of the deposit layer is lower than the particle diameter showing the formation of a loose monolayer deposit and it decreases for higher Pe. The above results, though they need to be consolidated, are consistent with theoretical predictions, demonstrating that the numerical method used is relevant to describe deposition of colloids in porous media from dilute dispersions. Future developments of this work will include a larger range of the related parameters on the one hand and more realistic pore geometries on the other hand.

# Chapter 7 **Three-Dimensional Microscale Simulation of Colloidal Particle Transport and Deposition in Model Porous Media with Converging/Diverging Geometries**

## 7.1 Introduction

Transport and deposition of colloidal particles in porous media under flow is encountered in a wide range of environmental and industrial applications including aquifer remediation <sup>[250]</sup>, fouling of surfaces <sup>[250]</sup>, fouling of surfaces <sup>[251]</sup>, therapeutic drug delivery <sup>[252]</sup>, catalytic processes carried out through filter beds <sup>[253]</sup> and drinking water treatment <sup>[13]</sup>. It has therefore received considerable attention during the last decades by investigating colloid transport and deposition process in porous media as well as by focusing on a particular mechanism among all those generally involved in such a process <sup>[254][255]</sup>. The most realistic representation of a porous medium is as a collection of solid grains, each being considered as a collector. The process of particle deposition is, therefore, divided into two steps: transport to the collector and deposition due to short-range particle/collector physico-chemical interactions. Such interactions are represented through a potential function usually obtained from the DLVO theory that includes electrostatic, van der Waals, and short range Born repulsion forces <sup>[13]</sup>. If particles and collectors are similarly charged and salt is low, the interaction potential contains two minima and one energy barrier making deposition condition unfavorable. When the salt concentration is very high or when particles and collectors are of opposite charges, the potential is purely attractive, leading to favorable deposition <sup>[117][104][256]</sup>.

To experimentally investigate colloids deposition mechanisms, impinging jet flow or parallel-plate cells are commonly used because of simplicity of flow structure and are coupled to various techniques such as direct observation techniques<sup>[103-105, 257]</sup>. In porous media, column experiments using native or fluorescent polystyrene Latex particles are the most commonly performed owing to their simplicity giving output data in the form of Breakthrough curves (BTC) <sup>[106]</sup>. These are sometimes coupled to other techniques as gamma-ray attenuation <sup>[106, 258, 259]</sup>, magnetic resonance imaging <sup>[260]</sup>, laser scanning cytometry <sup>[261]</sup>, microscopy and image processing <sup>[262, 263]</sup>.

In column experiments, the BTC encompass all involved sorts of particle-particle and particle-collector interactions. To interpret experimental data, an Eulerian approach may be adopted

consisting in solving the advection-dispersion equation containing one or two source terms representing adsorption and desorption isotherms <sup>[107]</sup>.

Risbud and Drazer <sup>[108]</sup> have considered the case of non-Brownian particles moving past a spherical or a cylindrical collector in Stokes regime by focusing on the distribution of particles around the obstacle and the minimum particle-obstacle distance attained during particle motion. They show that very small surface-to-surface separation distances would be common during the motion highlighting that short-range non-hydrodynamic interactions may have a great impact during particle motion.

Unni and Yang <sup>[105]</sup> have experimentally investigated colloid deposition in a parallel-plate flow cell by means of direct videomicroscopic observation. They focused on the influence of the flow's Reynolds number, physico-chemical conditions and particle size on surface coverage. To simulate deposition therein, the Langevin equation, particle-particle and particle-wall hydrodynamic interactions together with the DLVO theory were used. Accordance between experimental and simulation results were observed for flow Reynolds numbers scanned between 20 and 60.

In filtration processes, the porous medium is usually assumed to be composed of unit bed elements each containing a given number of unit cells whose shape is cylindrical with constant or varying cross sections. Chang et al. <sup>[109]</sup> have used Brownian dynamic simulation to investigate deposition of Brownian particles in model parabolic constricted tubes, hyperbolic constricted tubes and sinusoidal constricted tubes. Here again Langevin equation with corrected hydrodynamic particle/wall interactions and DLVO interaction were solved to get particles trajectories. Therefore the single collector efficiency that describes the initial deposition rate was evaluated for each geometry at various Reynolds numbers.

A more realistic porous media geometry for the study of transport and deposition is a bed of packed collectors of a given shape. Boccardo et al <sup>[95]</sup> have numerically investigated deposition of colloidal particles under favorable conditions in 2D porous media composed of grains of regular and irregular shapes. For that purpose they solved Navier-Stokes equations together with the advection-dispersion equation. Then and even if particles trajectories can't be specified, it was possible to determine how neighboring grains mutually influence their collection rates. They show that the Brownian attachment efficiency deviates appreciably from the case of single collector. Similarly Coutelieis et al. <sup>[112]</sup> have considered flow and deposition in a stochastically constructed 3D spherical grain assemblage by focusing on the dependence of capture efficiency at low to moderate Péclet numbers and found that the well-known sphere-in-cell model remains applicable

provided that the right porous medium properties are taken into account. Nevertheless the scanned porosities were too close to unity to be representative of actual porous media. In their work, Lagrangian approaches are used to track particles displacement in 3D packed beds allowing to study microscale transport and deposition of colloidal particles. For that purpose Lattice Boltzmann techniques are used for calculating hydrodynamic and Brownian forces acting on moving particles with local evaluation of physico-chemical interaction potential showing the hydrodynamic retardation to reduce the kinetics of deposition in the secondary minimum under unfavorable conditions <sup>[112]</sup> and particles retention in flow vortices <sup>[264]</sup>.

In most of these simulation approaches the characteristic size of the flow domain is many orders of magnitude greater than the particle size so that the jamming ratio (the ratio of characteristic size of flow domain to the particle size) is high enough to consider that the initial flow domain remains unaffected by particle deposition. For many systems however the jamming ratio may be low and thought straining phenomenon is negligible, colloids deposition should greatly impact the flow structure and strength and therefore the particle deposition process. In the present paper we focus on such impact and will simulate colloids deposition in porous media under favorable deposition condition by adopting the unit bed approach where the unit cell is a constricted tube with two converging-diverging forms, i.e.: tapered pipe and venturi-like tube. To balance the inherent rising of simulation cost, we will restrict this study to dilute colloidal suspensions where hydrodynamic interactions between flowing particles are negligible and will adopt a simple approach that is detailed hereafter and a novel 3D-PTPO (Three-Dimensional Particle Tracking model by Python<sup>®</sup> and OpenFOAM<sup>®</sup>) code developed in our laboratory. We will mainly focuses on deposition probability, the spatial distribution of deposited particles and surface coverage as functions of flow strength through the particle Péclet number.

## 7.2 Numerical simulations

Porous media are often considered as a bundle of capillaries, therefore when particle transport and deposition has been simulated in one capillary, the process in the whole porous media could be predicted with suitable imposed boundary conditions between capillaries <sup>[17]</sup>. The simplest model consist in representing the porous medium as a series of parallel capillaries of circular cross section whose mean radius is given by  $\sqrt{(8k / \varepsilon)}$  where  $k$  and  $\varepsilon$  are the porous medium permeability and porosity respectively. As this is a crude representation of the pore geometry, in the present work, we deal with three-dimensional numerical modeling of the process of transport and deposition of

particles in capillaries with converging/diverging geometries (Figure 7.1) that are believed to be more realistic pore shapes. The two pore geometries considered have a length of 15  $\mu\text{m}$ , a volume of 753  $\mu\text{m}^3$ , and the pore body radius ( $R_B$ ) to pore throat radius ( $R_T$ ) ratio is chosen to be 1.5 [265]. The transported particles have a radius,  $a_p$ , of 0.2  $\mu\text{m}$ .

A sensitivity analysis was undertaken to explore the effect of mesh numbers on the accuracy of our results by varying the number of grid block used for the numerical simulations. The analysis was first based on the flow field for both types of capillary tubes before any particle deposit. Moreover, the deposition probability and distribution of deposited particles are compared for various mesh numbers going from 80000 to 160000. The results indicate that 80000 grid blocks are sufficient for our computations.

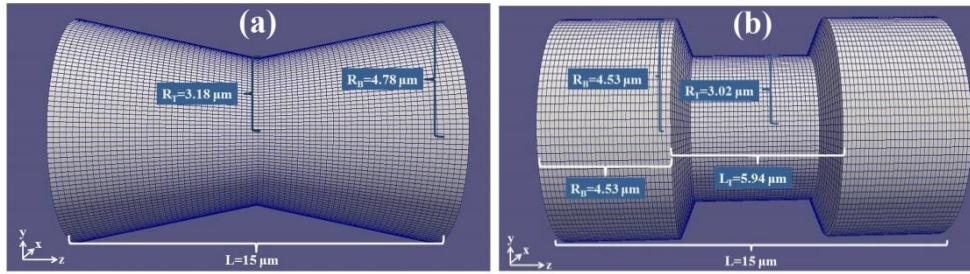


Figure 7.1 Geometry and meshing of the two configurations considered: (a) tapered pipe; (b) venturi tube

### 7.2.1 Hypothesis of this problem

For the numerical simulations in this chapter, the following assumptions are adopted [17, 266]:

1. The fluid is Newtonian and incompressible and the flow is creeping.
2. The particle Reynolds number defined as  $Re = \rho \bar{u} a_p / \mu$  (where  $\rho$  and  $\mu$  are the fluid density and dynamic viscosity,  $a_p$  the particle radius and  $\bar{u}$  the mean velocity at the pore throat under clean bed conditions) is small enough so that the particles can be treated as a mass point during their transport.
3. The particle-pore wall physico-chemical interaction is considered purely attractive and the particle-particle interaction purely repulsive.
4. Deposition is irreversible and both hydrodynamic and physico-chemical removal of deposited particles is prohibited.

## 7.2.2 Governing equations and boundary conditions

The governing equations for the creeping flow of an incompressible Newtonian fluid are the Stokes equations given by <sup>[267]</sup>,

$$\mathbf{0} = -\nabla p + \mu \nabla^2 \mathbf{v} \quad (7-1)$$

$$\nabla \cdot \mathbf{v} = 0 \quad (7-2)$$

where  $p$  is the pressure and  $\mathbf{v}$  stands for the flow velocity.

The no-slip boundary condition is applied on the pore wall and on the interface between the fluid and a deposited particle. At the inlet, the pressure is set to a fixed value, while at the outlet it is set to zero. In order to fulfill the requirement of creeping flow and to investigate a large range of Péclet numbers, the pressure at the inlet will be varied between  $10^{-5}$  and 10 Pa. The Péclet number is defined as:

$$Pe = \frac{\bar{u} a_p}{D} \quad (7-3)$$

where  $D$  is the bulk diffusion coefficient of the particles in the fluid.

## 7.2.3 Methodology and tools

Since the incoming suspension is considered to be dilute, particles are injected individually, randomly and sequentially at the inlet of the geometry and <sup>[17]</sup> a Lagrangian method is used to track the trajectories of the colloidal particles. Once the injected particle is deposited onto the surface wall or leaves the domain, another particle is injected and the whole process will be repeated until the pre-defined cut-off value of deposition probability (2%) is reached. The deposition probability is defined as the ratio of the number of deposited particles over the number of injected particles.

Simulations are carried out by the 3D-PTPO code, coupling OpenFOAM<sup>®</sup> (Open Field Operation and Manipulation) and Python<sup>®</sup>. Firstly, the flow field is computed using OpenFOAM<sup>®</sup> software. Secondly, the injected particles are tracked using a code developed using Python<sup>®</sup>, which is an open source programming language used for both standalone programs and scripting applications in a wide variety of domains.

The detailed steps of the 3D-PTPO code is as following: the calculated flow field (CSV format) is obtained after solving the equation of motion, then a particle is injected at the entrance plane ( $z = 0$ ) with the initial coordinates  $(x,y)$  generated by two independent pseudo-random series <sup>[268]</sup>. Afterwards, a loop is carried out to track the movement of the particle in the flow domain. For that purpose, the particle velocity  $\mathbf{V}$  at every position within the domain is calculated by the vector summation of the advection velocity  $\mathbf{V}_{\text{conv}}$  and the Brownian diffusion velocity  $\mathbf{V}_{\text{diff}}$ .  $\mathbf{V}_{\text{conv}}$  is obtained from OpenFOAM<sup>®</sup> by interpolating the velocity of the nearest eight mesh-nodes surrounding the particle.  $\mathbf{V}_{\text{diff}}$  represents the random velocity of the particle due to Brownian motion at every time-step, given by:

$$\begin{aligned} \mathbf{V}_{\text{diff}} &= \|\mathbf{V}_{\text{diff}}\|(\alpha\mathbf{i} + \beta\mathbf{j} + \gamma\mathbf{k}) \\ \alpha &= \frac{a}{\sqrt{a^2 + b^2 + c^2}}; \quad \beta = \frac{b}{\sqrt{a^2 + b^2 + c^2}}; \quad \gamma = \frac{c}{\sqrt{a^2 + b^2 + c^2}} \\ \|\mathbf{V}_{\text{diff}}\| &= \sqrt{\frac{D}{t_r}} = \sqrt{\frac{kT}{6\pi\mu a_p t_r}} \end{aligned} \quad (7-4)$$

where  $a$ ,  $b$  and  $c$  are random numbers between  $-1$  and  $1$ ;  $\alpha$ ,  $\beta$  and  $\gamma$  are determined by the normalization of the three random numbers, thus giving a unit vector with a random direction  $\alpha\mathbf{i} + \beta\mathbf{j} + \gamma\mathbf{k}$ ,  $k_B$  is the Boltzmann constant and  $T$  is the absolute temperature. The parameters used in the simulation are summarized in Table 7.1. Here we neglect the particles' mobility reduction near the wall that decreases the particle's diffusivity. Indeed, the explicit evaluation of this reduction is of no practical interest in this work since we do not calculate hydrodynamic forces acting on a physical particle moving near the wall albeit one could have advocated a phenomenological correction of the diffusivity coefficient as particles approach the wall. This has not been done in this work where  $D$  is considered constant. In this study, the reference time  $t_r$ , is defined as <sup>[258]</sup>,

$$t_r = \zeta / (2 u_{\text{max}}) \quad (7-5)$$

where  $\zeta$  stands for the characteristic mesh size and  $u_{\text{max}}$  is the maximum value of the advection velocity along the  $z$  axis in the absence of deposited particles. This means that at most the particle can travel through a distance equivalent to one half of a block size during the reference time.

The position of a moving particle is obtained by summing the old position vector  $\mathbf{X}_{\text{old}}$  and the updated velocity multiplied by the reference time  $t_r$ :

$$\mathbf{X}_{\text{new}} = \mathbf{X}_{\text{old}} + \mathbf{V} \times t_r \quad (7-6)$$

Table 7.1 Parameters used for simulations

Parameters	Values
Particle radius, $a_p$ (m)	$2 \times 10^{-7}$
Length of the geometries, L (m)	$1.5 \times 10^{-5}$
Boltzmann constant, $k_B$ (J/K)	$1.38 \times 10^{-23}$
Temperature, T (K)	293.15
Dynamic viscosity, $\mu$ (Pa s)	$10^{-3}$

During the particle tracking process, three situations may occur: (1) the particle leaves the domain without deposition (Figure 7.2a); (2) the center-to-center distance between the moving particle and any other particle already deposited is less than a predefined value, the transported particle will bounce back to the bulk flow, and the tracking process will continue, (Figure 7.2b); (3) the particle approaches the pore wall and will be deposited if enough free surface is available for deposition (Figure 7.2c). In that case, the meshes containing the reconstructed deposited particle are considered as solid to take the particle's volume into account, and the flow field is then recalculated. As soon as the loop for one particle finishes, another particle is injected. The injection process is repeated until the particle deposition probability defined as the ratio of the number of deposited particles over the number of injected particles, reaches a minimum value of 2%.

It must be noted that in order to ensure feasible numerical computations in terms of meshing and therefore computation time, the volume of the deposited particle reconstructed is not spherical but a circle based cylinder.

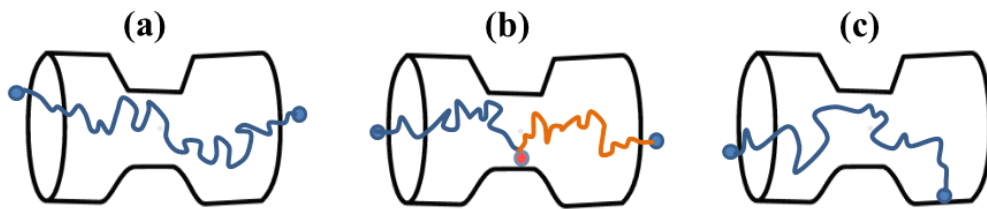


Figure 7.2 Sketches of possible particle trajectories: (a) flow through; (b) approaching a deposited particle (in blue) and bouncing back to the bulk flow (in red); (c) deposited on the wall

### 7.3 Results and discussion

For each pore's geometry, seven simulation runs at different Péclet numbers ranging typically from  $10^{-3}$  to 103 were carried out to investigate the influence of the flow regime on particle's deposition probability, the spatial density distribution of the deposit and the surface coverage. For

low Pe ( $Pe \ll 1$ ), the particle movement is dominated by the diffusion mechanism, while for high Pe ( $Pe \gg 1$ ), the particle's transport is governed by advection.

### 7.3.1 Deposition probability

The deposition probability is defined as the ratio of the number of deposited particles over the number of injected particles and is calculated over groups of 200 particles for each simulation run. This was done for each pore's geometry and since obtained results are almost similar, only those corresponding to the tapered pipe are presented for clarity. The evolution of the deposition probability versus the number of injected particles ( $N$ ) at different Pe is plotted in Figure 7.3 in case of tapered pipe. For the advection-dominant regime corresponding to high Péclet numbers, the value of the deposition probability is relatively small. This is due on the one hand to the low residence time of the particles in the domain, as the advection velocity is high and to the hydrodynamic shadowing effect on the other hand that leads to larger exclusion surfaces compared to the diffusion dominant regime and therefore smaller areas are available for deposition around the already deposited particles. These exclusion zones are more extended downstream of deposited particles and increase both in size and shape complexity as Pe increases. For low Péclet numbers, the deposition probability is relatively high and exhibits a plateau at the early stages of the injection process. This is due to the fact that compared to the high Péclet regime, the exclusion area at low Pe ( $4\pi a_p^2$ , for deposition of non-interacting spheres on a flat surface in purely diffusive regime) is smaller and the pore-wall surface is available to a large extent for the injected particles to deposit on. However and strictly speaking, in evaluating the extent of the exclusion area due to blocking effect one should in general take into account not only steric interaction but also the extra contribution of DLVO origin <sup>[119, 269, 270]</sup>. In this work only steric contribution has been considered. Moreover due to shortness of the pore length and still low residence time of flowing particles in the pore space, the maximum deposition probability is only 44% even for  $Pe=0.0019$ . For a sufficient length of the pipe, the maximum value of the deposition probability is expected to approach unity as Lopez et al. have previously shown using an analogous approach in case of a longer domain for the parallel plate configuration <sup>[17]</sup>. When the number of the deposited particles reaches a critical value, the deposition probability drops sharply to rather low values indicating that any newly injected particles will have much less chance to deposit. This phenomenon is similar to the Random sequential Adsorption (RSA) process where the deposition kinetics becomes slow as the jamming limit is approached <sup>[271]</sup>. Furthermore, it is noteworthy that for all Péclet numbers, the overall deposition probability tends to decrease with  $N$ , and under our conditions, when  $N$  exceeds 15000 all values of the deposition probability are less

than 2% with only minor variations afterwards, indicating that the deposition process is almost over. Therefore, in this work, 2% was selected as the cut-off value for the injection process.

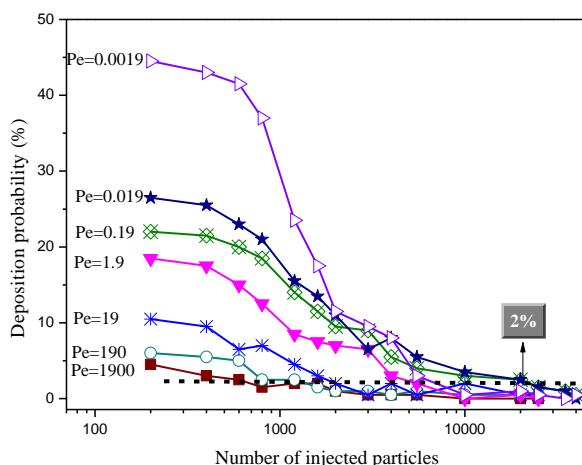


Figure 7.3 Variation of deposition probability versus  $N$  at different  $Pe$  for the tapered pipe

### 7.3.2 Spatial distribution of the density of the deposited particles

Since particles are considered to be volumeless until they adsorb, the density distribution of the deposited particles, expressed as the number of deposited particles per unit area, is obviously isotropic in any  $x$ - $y$  plane perpendicular to the pore symmetry axis. To show the influence of  $Pe$  on the axial ( $z$ -axis) variation of such a density, we will consider successively the tapered pipe geometry and the venturi-like geometry to highlight the difference between them. For the former, two Péclet numbers (0.0019 and 190) that are representative of diffusion dominant and advection dominant regimes were selected. For each  $Pe$ , the pore is divided into 15 slices along the  $z$  axis (the mean flow direction) and the density profile of the deposited particles is plotted for various numbers of injected particles,  $N$  (Figure 7.4a and 7.5a).

For  $Pe$  equal to 0.0019, the deposition process is shown to be nearly piston-like. When  $N$  is small, the deposition distribution exhibits an apparent plateau near the inlet of the pipe, while the density remains small near the exit (Figure 7.4b). By further increasing  $N$ , the density increase is more remarkable near the exit, where a large surface is still available for deposition, while it undergoes only a moderate change at the inlet zone. At later stages of deposition, a uniform deposit along the pipe is expected. Similar behavior was reported in the literature for column experiments when Polystyrene latex colloidal particles were injected into a synthetic consolidated porous medium and where deposition density was determined through local measurement of the attenuation of an incident gamma ray due to particles deposition<sup>[259, 272]</sup>. Indeed, for low  $Pe$  the particle movement is

mainly dominated by diffusion so that the velocity in the x-y plane may be higher than the velocity component in the mean flow direction. As a consequence, particles approach the surface wall and deposit first close to the inlet of the pipe. For high number of injected particles (over 2000) deposition at the inlet is almost over and the plateau value increases only slightly there approaching the jamming limit. Then, any further increase of injected particles mainly contributes to increase density in the rear part of the tube where free surface is still available for particles deposition leading to a uniform and dense deposit at the process end (Figure 7.4a and 7.4c). This piston-like deposition was experimentally observed in column experiments [272] and the covering front displacement would be similar if the simulation domain was longer.

For  $Pe=190$ , particle transport is dominated by advection, the spatial density distribution curves are nearly uniform along the pipe whatever the number of injected particles (Figure 7.5a, 7.5b and 7.5c) leading to a scanty final deposit. This is a consequence of the high value of  $V_{conv}$  that greatly modify the excluded zone both in magnitude and shape. In this advection dominant regime, the restricted area in the rear of deposited particles is increased as flow velocity (or particle velocity here) increases resulting in a great impact of the hydrodynamic shadowing effect on pore surface covering. This phenomenon that is sometimes expressed in terms of the blocking factor was already experimentally evidenced [133, 259, 273, 274] and was modelled [133, 274] and numerically assessed [17, 104]. Figure 7.6a and 7.6b offer a clear view for  $Pe=1.9$  on how flow streamlines are modified in the vicinity of the wall due to particle deposition. It is then clearly seen that the original streamlines that were straight and parallel to the wall become highly deformed and peeled from the wall. Moreover and as the jamming ratio (ratio of characteristic size of the pore to that of the particle) is not too large, the streamlines become also squeezed decreasing the local Péclet number. Consequently, the capture efficiency decreases in a manner similar to that of an isolated spherical collector for which the capture efficiency of Brownian particles is predicted to vary as  $Pe^{-2/3}$  [275].

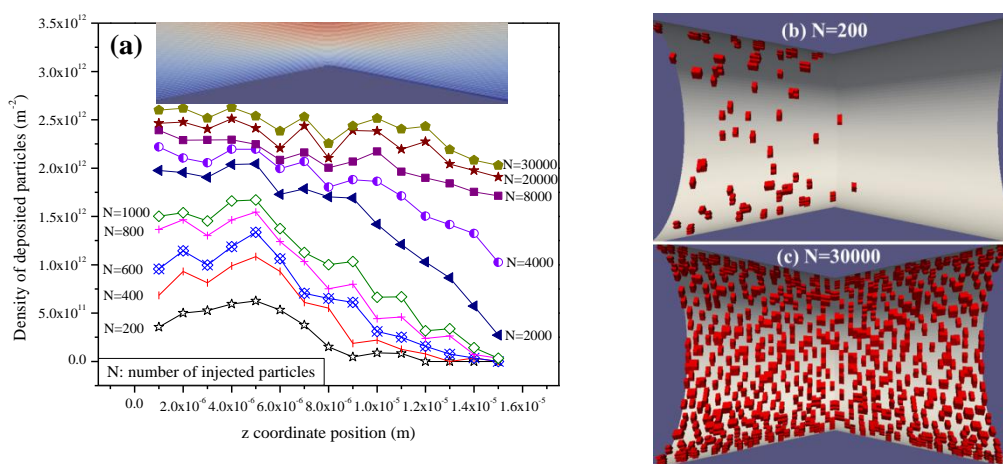


Figure 7.4 (a) Spatial distribution of the density of deposited particles along the z coordinate at different N for Pe=0.0019; (b) 3D sectional view of the tapered pipe at N=200; (c) 3D sectional view of the tapered pipe at N=30000 (the flow occurs from left to right)

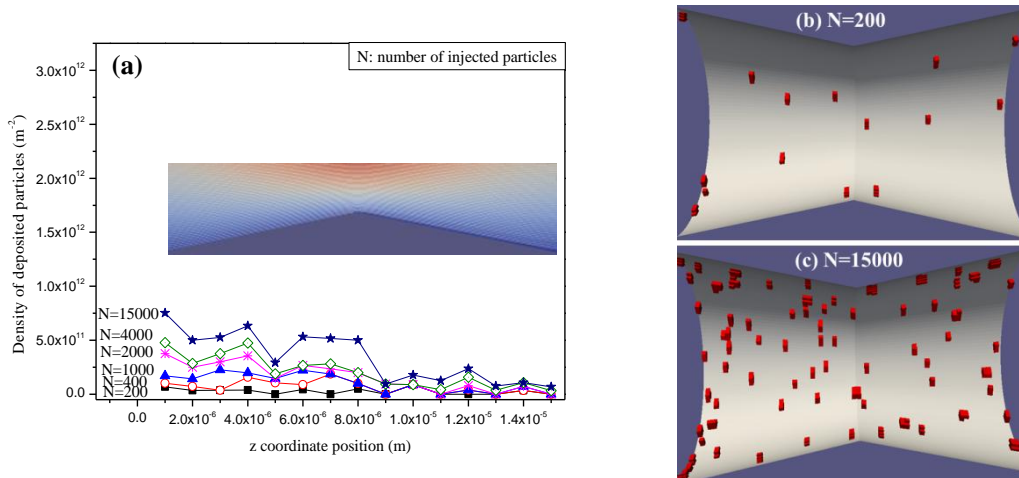


Figure 7.5 (a) Spatial distribution of the density of deposited particles along the z coordinate at different N for Pe=190; (b) 3D sectional view of the tapered pipe at N=200; (c) 3D sectional view of the tapered pipe at N=15000 (Pe=190, the flow occurred from left to right)

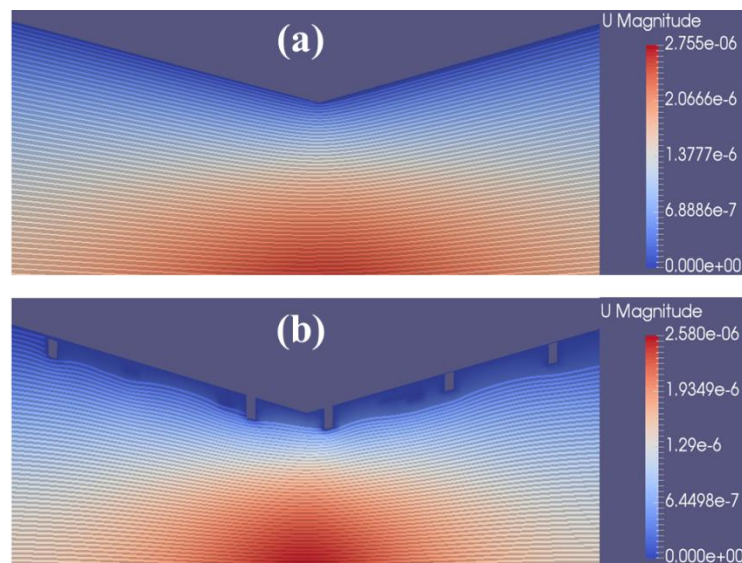


Figure 7.6 Streamline profiles in the tapered pipe without (a) and with (b) deposited particles (Pe=1.9)

Similarly, in case of venturi geometry, we studied the variation of the spatial distribution of deposit density with the number of injected particles along the pore axis and for a Pe interval that covers diffusion-dominant and advection-dominant regimes. In overall the observed behavior is similar to that observed for trapped pipe with the same features. However the existence of corners in this geometry may be seen to locally impact the density distribution. This is obvious in Figure 7.7, corresponding to Pe=0.0014, that shows a more or less deep minimum at each corner location corresponding to lower deposition.

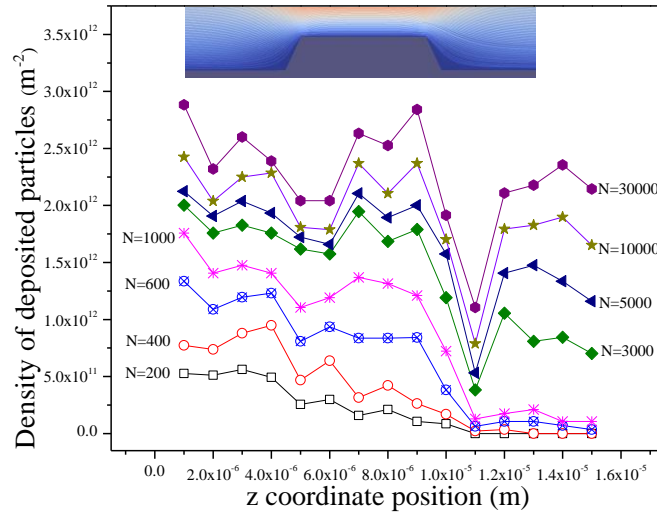


Figure 7.7 Spatial distribution of the density of deposited particles along the z coordinate at different N for  $Pe=0.0014$

An explanation of such behavior may come from the flow structure in these zones since flow streamlines behave differently in this geometry. On Figure 7.8 an enlarged view of flow at corners is displayed showing a net detachment of the streamlines at the corners that impede the particle deposition as locally flowing particles will tediously cross the critical distance for deposition. Moreover, such a detachment is more marked at corners D and C evidencing the higher energy loss for the diverging part of the pore where deposition is less likely to occur and the minimum there is consistently deeper than the first one corresponding to corners A & B (Figure 7.8). Analogous behavior was observed at various Pe numbers even if the evaluation of the density of deposited particles is rather difficult at high Pe values due to less deposition as we emphasized before. However, one can expect additional hydrodynamic retention of Brownian particles in these zones when the Reynolds number is high due to flow recirculation. Such a retention mechanism was proven to be important in real porous media at grain-grain edges <sup>[112, 262]</sup> and in cracks for rough pore surfaces <sup>[113]</sup>.

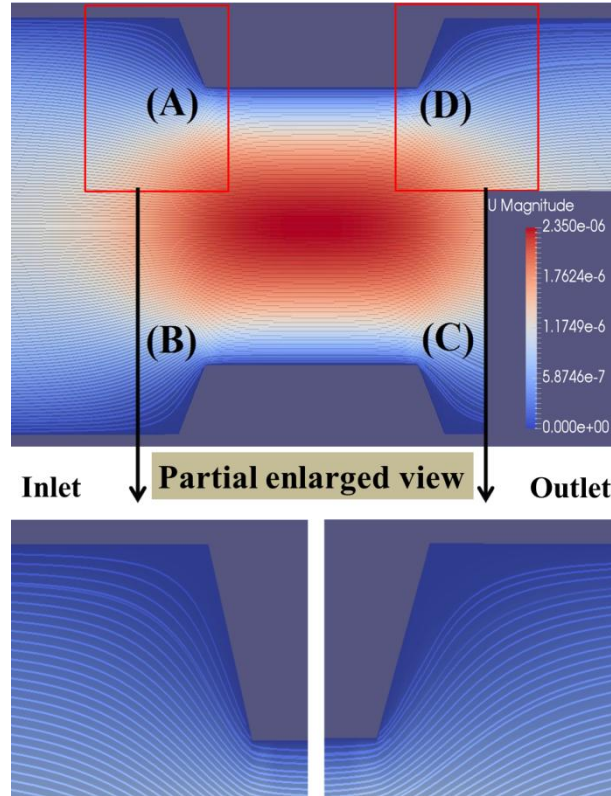


Figure 7.8 Initial streamlines distribution in the venturi pipe at  $Pe=1.4$  and  $Re=0.48 \times 10^{-4}$

### 7.3.3 Variation of the dimensionless surface coverage

Surface coverage ( $\Gamma$ ) is defined as the ratio of the total projection area of deposited particles to the total initial surface area of the pore surface before deposition. In this work, results are presented in terms of the dimensionless surface coverage  $\Gamma/\Gamma_{RSA}$ , where  $\Gamma_{RSA}$  was taken to be 0.546<sup>[271]</sup> which corresponds to the value for pure diffusion regime and a flat surface using the RSA model. The use of such a value is justified since the ratio of particle radius to pore surface curvature is low enough. The variation of  $\Gamma/\Gamma_{RSA}$  versus the number of injected particles ( $N$ ) at Péclet numbers spanning from very low to very high values is plotted in Figure 7.9 for the tapered pipe. It can be seen that, for all  $Pe$  values,  $\Gamma/\Gamma_{RSA}$  increases sharply with  $N$  in the early deposition stages and tends to a plateau value,  $\Gamma_{final}/\Gamma_{RSA}$ , that is of course reached for a smaller value of  $N$  for higher  $Pe$ . In the diffusion-dominant regime (for example, at  $Pe = 0.0019$ ),  $\Gamma_{final}/\Gamma_{RSA}$  is found to be close to that obtained in the same conditions for a straight capillary tube<sup>[276]</sup> and in parallel plates as well<sup>[17]</sup>. For  $Pe = 1900$  where particle transport is mostly due to advection,  $\Gamma_{final}/\Gamma_{RSA}$  is significantly reduced and is of only 0.08. It should be noted here that even at that extreme  $Pe$  values, the flow Reynolds number is low enough ( $<0.1$ ) and the flow may still be considered as creeping. Similar behavior was also observed in the case of the venturi geometry despite the existence of the corners with reduced deposition density

therein affecting only slightly the value of  $\Gamma_{\text{final}}/\Gamma_{\text{RSA}}$  (data not shown). On Figure 7.10,  $\Gamma_{\text{final}}/\Gamma_{\text{RSA}}$  is plotted as a function of Pe for the two considered geometries, for the tube geometry already investigated under the same conditions in a previous work <sup>[276]</sup>, as well as the data obtained by Lopez and co-workers <sup>[17]</sup> from simulations performed in parallel plates geometry under comparable conditions. As we can see, as long as diffusion dominates ( $\text{Pe} \ll 1$ ), the surface coverage is close to  $\Gamma_{\text{RSA}}$  and is almost constant due to the high deposition probability in this regime and the precise form of the pore has a weak impact on the attained value of  $\Gamma_{\text{final}}$ . It is obvious that the upper limit of this regime varies from one geometry to another due to the values of  $\bar{u}$  used for Pe calculation. Furthermore, for the advection-dominant regime ( $\text{Pe} \gg 1$ ),  $\Gamma_{\text{final}}/\Gamma_{\text{RSA}}$  decreases significantly with Pe. This is because the hydrodynamic shadowing effect comes to play and as mentioned before, particles are transported by the fluid over a distance increasing with the advection velocity until they may deposit downstream away from an already deposited particle, resulting hence in a lower surface coverage <sup>[17, 133, 259, 273, 274]</sup>. This finding is in qualitative agreement with experimental data that were already obtained by Veerapen and co-workers when sub-micrometric latex particles are injected through a non-consolidated silicon carbide porous medium <sup>[274]</sup>. Salehi <sup>[277]</sup> has developed a simple model that describes deposition of colloidal particles in advection-dominant regime and predicts the surface coverage for a flat surface to follow a power law as  $\Gamma_{\text{final}} \cong \text{Pe}^{-1/3}$ , which was shown to fit well the experimental data of Veerapen et al. <sup>[274]</sup>. This power law is also drawn on Figure 7.10 showing that despite the fact that the surface coverage in the venturi pipe leads to a satisfactory fit with such a trend, the agreement is less obvious when the other geometries are considered and more *in-silico* experiments at higher Péclet numbers are needed to draw any definite conclusion. Unni and Yang <sup>[257]</sup> have investigated colloids deposition in parallel channel by means of Brownian dynamic simulation by focusing on the variation of surface coverage with flow strength. They showed that  $\Gamma$  is a decreasing function of flow Reynolds number in a much more pronounced way but the considered range, from 20 to 60, was many orders of magnitude greater than in the present work.

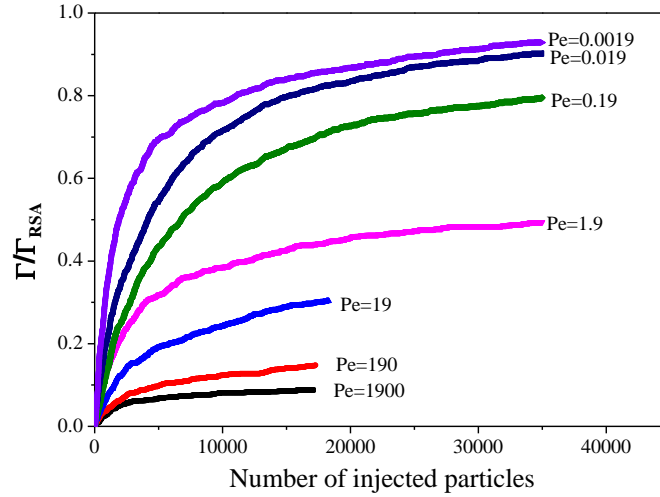


Figure 7.9 Variation of dimensionless surface coverage  $\Gamma/\Gamma_{RSA}$  versus  $N$  at different  $Pe$

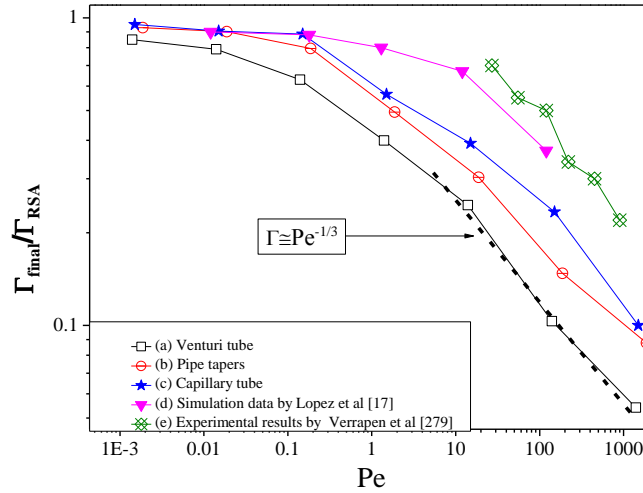


Figure 7.10 Variation of  $\Gamma_{final}/\Gamma_{RSA}$  versus Péclet number: (a) venturi tube; (b) tapered pipe; (c) capillary tube; (d) parallel planes of Lopez *et al* [17]; (e) experimental results of Verrapen *et al* [274]

## 7.4 Conclusions

The present study proposes the 3D-PTPO code (Three-Dimensional Particle Tracking model by Python<sup>®</sup> and OpenFOAM<sup>®</sup>) using a Lagrangian method to carry out microscale simulations of colloidal particle transport and deposition in converging/diverging capillaries (tapered pipe and venturi tube). The idea is to approach the behavior in porous media idealized as a bundle of capillaries with variable cross sections. The main originality of the tool is to take into account the modification of the pore-space and therefore the flow field as particles are deposited on the pore-wall. The variations of the key parameters including the deposition probability and the dimensionless surface coverage  $\Gamma/\Gamma_{RSA}$ , as well as the detailed spatial distribution of the density of the deposited particles were investigated. The main conclusions drawn from this work are as follows:

(i) The probability for a particle to be deposited on the pore-wall surface is much higher when the transport is dominated by diffusion for the two geometries considered in this work. In this regime, at the early stages of injection, the deposit probability is high and nearly constant and decreases sharply close to the jamming limit as the pore-wall is covered by particles. For advection-dominant regime, the probability of deposition is rather low at all stages of injection due to the high advection velocity vs diffusion (high Pe) and to the hydrodynamic shadowing effect which is predominant in this case.

(ii) The deposited particle distribution along the pipes is piston-like for the diffusion-dominant regime, while the distribution is more uniform for the advection-dominant regime. Especially, for the venturi tube with steep corners, the density of deposited particles is relatively low in the vicinity of the pore throat entrance and exit due to streamlines modification.

(iii) For all values of the Péclet number considered in this work ranging between 0.0019 and 1900, the dimensionless surface coverage  $\Gamma/\Gamma_{RSA}$  as a function of the number of injected particles (N) features a sharp increase in the early deposition stages and tends to a plateau value for higher N. The final surface coverage is reached for much lower N values for higher values of Pe. The behavior of the final plateau corresponding to the maximum surface coverage  $\Gamma_{final}/\Gamma_{RSA}$  as a function of Pe has been analyzed. For low Pe, a plateau could be observed for both geometries, the plateau value and the deposition kinetics are consistent with the random sequential adsorption (RSA) theory. For high Pe, the declining trends for  $\Gamma_{final}/\Gamma_{RSA}$  versus Pe are in good agreement with experimental and simulation results found in the literature. The matching of the trend with the power law  $Pe^{-1/3}$  observed in some studies in the literature is not general and needs further investigation.

(iv) The introduction of divergence/convergence (tapered pipe) or cross section constriction (venture pipe) can lead to a modification of the deposition phenomenon. However, the small angle chosen for the divergence or convergence of the tapered pipe in this work leads to very weak differences in comparison with the capillary tube of constant cross section studied in a previous work [276]. A thorough study of the influence of the convergence divergence angle is beyond the scope of this paper, but could be of interest. For the venturi pipe, there is an obvious decrease of the density of deposited particles at the entrance and exit of the pore-throat especially for the diffusion-dominant regime. Moreover the decrease at the exit is much more pronounced and corresponds to a zone where particles are less likely to reach the wall. In the same manner, it can be noticed that  $\Gamma_{final}/\Gamma_{RSA}$  versus Pe for the tapered pipe is rather close to that of the straight tube, while the dependence on Pe for the venturi tube is rather different. This may be partly attributed to the particular geometry in this case,

although as mentioned before the definition of the Péclet number based on the average pore-throat velocity can also be considered as a possible explanation for this shift.

Finally, the above results demonstrate that the numerical method used seems able to capture the physics of transport and deposition of colloidal particles in pores of simple geometry and could be used as a basis for further developments namely transport in more complex geometries (unit cell of a sphere packing), multi-layer particle deposition, chemically patterned surfaces, etc.

# Chapter 8 **Three-Dimensional Microscale Simulation of Colloidal Particle Transport and Deposition in Chemically Heterogeneous Porous Media**

## 8.1 Introduction

Colloidal particle transport and deposition (irreversible adsorption) processes in porous media are of great environmental and industrial interest since they are critical to numerous applications ranging from drug delivery to drinking water treatment <sup>[250, 252]</sup>. Accordingly, particle deposition on homogeneous porous media has been extensively studied both experimentally and theoretically. For example, Buret et al. <sup>[146]</sup> carried out a laboratory study of oil-in-water emulsion flow in porous media to investigate the mechanisms of oil-droplet retention and its effect on permeability. The results demonstrate that, the induced permeability loss is significant even at high pore-size/droplet size ratio. Experimental investigations can help to understand the particle transport and deposition kinetics to a large extent. To further characterize the colloidal particle transport and deposition in porous media at the microscale level, one can carry out numerical simulations by idealizing the porous medium as a bundle of capillaries with various kinds of geometries. For instance, Lopez et al. <sup>[17]</sup> carried out micro-scale numerical simulations of colloidal particles deposition onto the surface of a simple pore geometry consisting of two parallel planar surfaces, and investigated the deposition kinetics of stable colloidal spheres from dilute dispersions. The results show that both the surface coverage  $\Gamma$  and the equivalent hydrodynamic thickness of the deposit,  $\delta_h$ , possess a definite plateau at small Pe, and both are decreasing functions of flow strength at high Pe. Li et al. <sup>[276]</sup> simulated the transport and deposition of colloidal particles at the pore scale in a porous medium idealized as a bundle of 3D capillaries. The results indicate that the adsorption probability and the surface coverage are decreasing functions of the particles' Péclet number.

The above investigations provided valuable insight on the understanding of particle transport and deposition process in smooth and homogeneous pore surfaces, which simplify the simulation process obviously. However, from a practical point of view, the problem of particle deposition in porous media featuring heterogeneity at the pore scale is more relevant since most natural or artificial porous media are physically and/or chemically heterogeneous <sup>[188]</sup>. When particles under flow approach such heterogeneously patterned surfaces, they exhibit various deposition behaviors

depending on the nature, magnitude and form of such heterogeneities <sup>[159, 162]</sup>. Thus, particle transport and deposition in heterogeneous porous media have been an area of investigation, and significant amount of relevant researches has been performed <sup>[170, 179]</sup>. For example, in the presence of surface roughness and particle/pore physicochemical attractive interaction, the simulation of solid colloidal particle transport in porous media at the pore scale was carried out by Sefrioui et al. <sup>[113]</sup>. They found that the existence of surface roughness is a necessary but not sufficient condition for particles retention. In this current work, instead of physical heterogeneity, the impact of chemical heterogeneity is investigated. During the past two decades, particle deposition in chemically heterogeneous surfaces has been extensively investigated <sup>[161, 167]</sup>. Chatterjee et al. <sup>[171]</sup> analyze particle deposition on Janus and patchy collectors. The results indicate that particles tend to deposit at the edges of the favorable strips. Besides, this preferential accumulation varies along the tangential position, this is due to the nonuniform nature of the collector. Recently, Pham et al. <sup>[176]</sup> investigated the effect of spatial distribution of the porous matrix surface heterogeneity on particle deposition. They found that the attachment rate constant is affected by heterogeneity pattern, the particle size, and the fraction of surface that is favorable to deposition. Adamczyk et al. <sup>[103, 278, 279]</sup> investigated the irreversible adsorption of colloid particles and globular proteins at heterogeneous surfaces theoretically and experimentally. It was revealed that the initial attachment flux increased significantly with the  $\Gamma/\Gamma_{RSA}$  and the  $\lambda_r$  parameter, here,  $\Gamma/\Gamma_{RSA}$  is the site coverage dimensionless coverage,  $\lambda_r$  is the particle size ratio (the averaged size of the latex versus the size of the particle). This behavior was quantitatively interpreted in terms of the scaled particle theory. It also was demonstrated that particle adsorption kinetics and the jamming coverage increased significantly, at fixed site coverage, when the  $\lambda_r$  parameter increased. Rizwan et al. <sup>[161]</sup> experimentally created charge-heterogeneous surfaces by employing soft lithographic techniques, and presented a simple mathematical description of particle deposition on the created rectangular surface features. The results demonstrate that particles tend to preferentially deposit at the edges of the favorable strips, while the extent of this bias can be controlled by the proximity of consecutive favorable strips and the ratio of particle size to the strip width. Liu et al. <sup>[178]</sup> studied the role of collector surface charge heterogeneity on transport of oocyst and carboxylate microsphere in 2D micromodels. The results show that under higher pH, particles tend to deposit on the patch. Among the various geometries of porous media, the transport of particles in capillaries/microchannels is central to numerous microfluidic and nanofluidic systems <sup>[182]</sup>. Moreover, the porous media are usually considered as a bundle of capillaries/microchannels and when particle transport and deposition has been simulated in one capillary/microchannel, the process in the whole porous media could be predicted with suitable imposed boundary between capillaries/microchannel <sup>[17]</sup>. To the best of our knowledge, Chatterjee et

al. <sup>[188]</sup> have investigated the particle transport in patchy heterogeneous cylindrical microchannels. The surface heterogeneity is modeled as alternate bands of attractive and repulsive regions on the channel wall to facilitate systematic continuum type evaluation. This study provides a comprehensive theoretical analysis of how the transport of such suspended particles is affected in these microchannels due to the heterogeneities on the microchannel walls. Hence, 3D simulations must be performed once again to develop a complete picture of particle transport in a capillary. This is one of the most significant objectives of the present work.

Moreover, it is important to investigate the coupled effect of hydrodynamics and chemical heterogeneity on particle deposition. Nazemifad et al. <sup>[121]</sup> used particle trajectory analysis to investigate the effect of microscopic surface charge heterogeneity on particle trajectories and deposition efficiency near a two-dimensional patterned charged substrate. They demonstrated that as a result of the coupled effects of hydrodynamics and colloidal forces, there exists a zone at the leading edge of each favorable strip that is inaccessible for particle deposition and acts as an unfavorable region from the deposition point of view. This observation also suggests that deliberately micropatterning alternating charge heterogeneous strips on a substrate can significantly modify the particle deposition behavior in presence of tangential flow. There is so far few reported works where attention is paid to the combined effects of surface heterogeneity and hydrodynamics on colloidal particle deposition in three-dimensional capillaries/microchannels, which is also one of the objective in the present work.

In this chapter, 3D-PTPO (Three-dimensional particle tracking model by Python<sup>®</sup> and OpenFOAM<sup>®</sup>) code developed in I2M laboratory was used to investigate the influence of the surface heterogeneities and hydrodynamics on particle deposition. The three-dimensional axisymmetric capillary with periodically repeating chemical heterogeneous surface (crosswise strips patterned and chess board patterned) of positive and negative surface charges (or alternate attractive and repulsive regions) is employed for the heterogeneity model. Finally, the dependence of the deposition probability, dimensionless surface coverage on the frequency of the pitches,  $Pe$  and the favorable surface coverage, as well as the spatial density distribution of deposited particles are all investigated.

## 8.2 Numerical simulations

The present work focuses on three-dimensional numerical modeling of the process of transport and deposition of particles in a pore throat of a porous medium idealized as a capillary with

periodically repeating heterogeneous surface pattern (crosswise strips patterned and chess board patterned) with Poiseuille flow profile, as is depicted in Figure 8.1. The frequency of the pitches ( $\lambda$ ) is calculated by the ratio of  $L$  to  $p$ , where  $L$  is the length of the capillary and  $p$  is the pitch length (summation of one negative and one positive band (patch) widths). The favorable area fraction is denoted as  $\theta=A_f/A_t$ , where  $A_f$  is the area of the surface wall favoring deposition and  $A_t$  is the total surface area of the capillary wall. The geometries considered have a length of  $15\ \mu\text{m}$  and a radius of  $4\ \mu\text{m}$ . The transported particles have a radius,  $a_p$ , of  $0.2\ \mu\text{m}$ . A sensitivity analysis was undertaken to explore the effect of mesh numbers on the accuracy of our results by varying the number of grid block used for the numerical simulations. The analysis was based on the flow field for various mesh numbers going from 125 to 200000. The results indicate that 120000 grid blocks are sufficient for our computations.

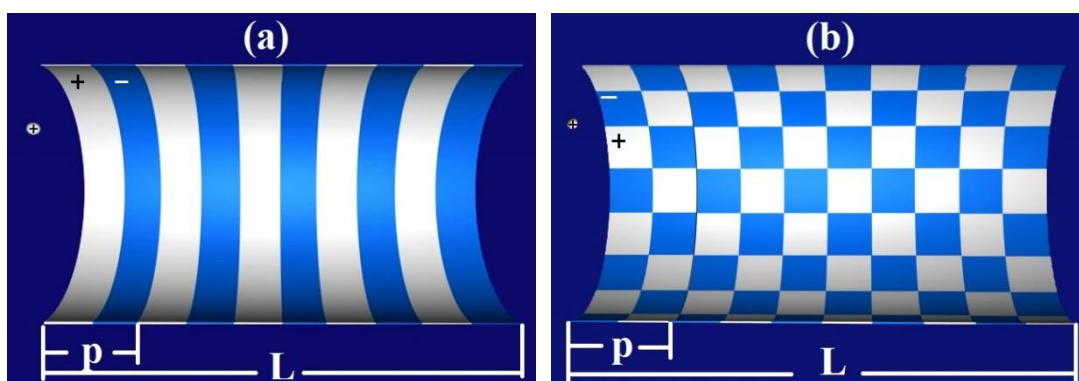


Figure 8.1 Surface heterogeneity is modeled as alternate bands (patches) of attractive and repulsive regions on the capillary wall to facilitate systematic continuum type evaluation: (a): Crosswise strips patterned; (b): Chess board patterned. Bright bands (patches) represent positively charged regions, blue bands (patches) represent negatively charged regions, and the particles are positively charged

### 8.2.1 Hypothesis of this problem

In the present work the following assumptions are adopted <sup>[17, 266]</sup>:

1. The fluid is Newtonian and incompressible and the flow is creeping.
2. The particle Reynolds number defined as  $Re = \rho \bar{u} a_p / \mu$  (where  $\rho$  and  $\mu$  are the fluid density and dynamic viscosity,  $a_p$  the particle radius and  $\bar{u}$  the mean velocity at the pore throat under clean bed conditions) is small enough so that the particles can be treated as a mass point during their transport.
3. The particle-particle interaction is purely repulsive, therefore particle deposition is monolayer.

4. Deposition is irreversible and both hydrodynamic and physico-chemical removal of deposited particles is prohibited.

## 8.2.2 Governing equations and boundary conditions

The governing equations for the creeping flow of an incompressible Newtonian fluid are the Stokes equations given by <sup>[267]</sup>:

$$0 = -\nabla p + \mu \nabla^2 \mathbf{v} \quad (8-1)$$

$$\nabla \cdot \mathbf{v} = 0 \quad (8-2)$$

where  $p$  is the pressure and  $\mathbf{v}$  stands for the flow velocity.

The no-slip boundary condition is applied on the pore wall and on the interface between the fluid and a deposited particle. At the inlet, the pressure is set to a fixed value, while at the outlet it is set to zero. In order to fulfill the requirement of creeping flow and to investigate a large range of Péclet numbers, the pressure at the inlet will be varied between  $10^{-5}$  and 10 Pa. The Péclet number is defined as:

$$Pe = \frac{\bar{u} a_p}{D} \quad (8-3)$$

where  $D$  is the bulk diffusion coefficient of the particles in the fluid,  $\bar{u}$  is the average velocity along the mean flow axis.

## 8.2.3 Methodology and tools

Since the incoming suspension is considered to be dilute, particles are injected individually, randomly and sequentially at the inlet of the geometry [23]. A Lagrangian method is used to track the trajectories of the colloidal particles. Once the injected particle is deposited onto the surface wall or leaves the domain, another particle is injected and the whole process will be repeated until the pre-defined cut-off value of deposition probability (2%) is reached. The deposition probability is defined as the ratio of the number of deposited particles over the number of injected particles. Simulations are carried out by the 3D-PTPO code. The detailed steps of the 3D-PTPO code could be found in Chapter 6 and Chapter 7. The parameters used for the simulation are summarized in Table 8.1.

Table 8.1 Parameters used for simulations

Parameters	Values
Particle radius, $a_p$ (m)	$2 \times 10^{-7}$
Length of the geometries, $L$ (m)	$1.5 \times 10^{-5}$
Boltzmann constant, $k_B$ (J/K)	$1.38 \times 10^{-23}$
Temperature, $T$ (K)	293.15
Dynamic viscosity, $\mu$ (Pa s)	$10^{-3}$

During the particle tracking process, four situations may occur: (1) the particle leaves the domain without deposition (Figure 8.2a); (2) the center-to-center distance between the moving particle and any other particle already deposited is less than a predefined value, the transported particle will bounce back to the bulk flow, and the tracking process will continue (Figure 8.2b); (3) the distance between the particle center and the pore wall is less than a certain value ( $0.5 a_p$ ), while the local surface wall is repulsive (positively charged), the transported particle will also bounce back to the bulk flow, and the tracking process will continue (Figure 8.2c); (4) the distance from the particle center to the pore wall is less than a certain value ( $0.5 a_p$ ), and the local surface wall is attractive (negatively charged), the particle will be deposited if enough free surface is available for deposition (Figure 8.2d). In that case, the meshes containing the reconstructed deposited particle are considered as solid to take the particle's volume into account, and the flow field is then recalculated. As soon as the loop for one particle finishes, another particle is injected. The injection process is repeated until the particle deposition probability defined as the ratio of the number of deposited particles over the number of injected particles, reaches a minimum value of 2%.

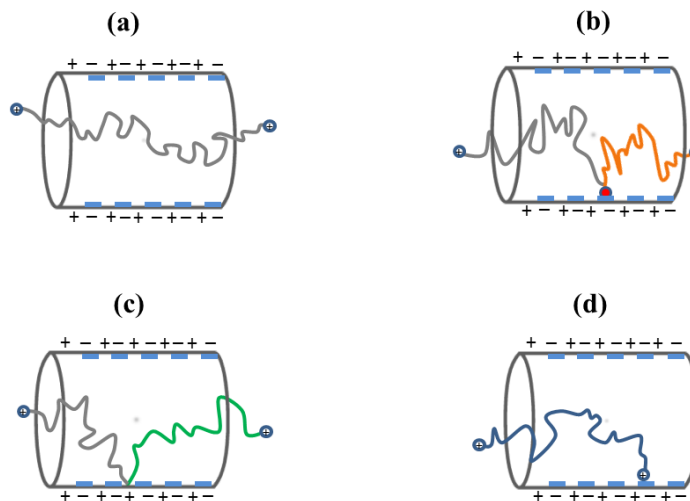


Figure 8.2 Sketches of possible particle trajectories: (a) flowing through the capillary; (b) approaching a deposited particle (in grey line) and bouncing back to the bulk flow (in orange line); (c) approaching repulsive regions (positively charged) on the capillary wall (in grey line) and bouncing back to the bulk flow (in green line); (d) approaching attractive regions (negatively charged) and depositing on the wall

## 8.3 Results and discussion

### 8.3.1 Transport and deposition of colloidal particles in the crosswise strips patterned capillary

#### 8.3.1.1 Local deposition behavior

For the chemically heterogeneous capillary, it is important to firstly investigate the local deposition behavior of colloidal particles along the length of the geometry. Since gravity is ignored in this work, spatial distribution of the deposited particles in all cross sections is uniform. This distribution is expressed in terms of a spatial density which is the number of deposited particles per unit area. For that purpose, the geometry is divided into 15 segments along the Z axis (the mean flow direction). The density profile of the deposited particles is plotted for various numbers of injected particles,  $N$  (Figure 8.3a). For comparison, the density profile of the deposited particles in a homogeneous capillary was also plotted in Figure 8.3a. The solid boxes represents the concentration profile for the heterogeneous (in this part, we take the case with  $\lambda=5$  and  $\theta=0.5$  for example) capillary, while the hollow stars represents the concentration profile for the homogeneous capillary. For both cases,  $N$  is 2000 and  $Pe$  is 0.0015. Three major features could be observed from Figure 8.3a. Firstly, the concentration profile of the heterogeneous capillary follows the oscillatory surface potential profile along the channel length<sup>[188]</sup>. The spatial distribution of deposition closely emulates the periodic nature of the heterogeneous pattern. Secondly, the concentration peaks tend to form at the leading and trailing edges of the favorable strips. These results are similar to those found in the literature<sup>[257]</sup>. This could be explained by the coupled effects of hydrodynamic and colloidal interactions<sup>[188]</sup>. Figure 8.3b schematically depicts the above effects on the particle behavior near the boundaries between the favorable and unfavorable strips. When the particles are relatively far from the collector surface, they tend to accumulate over the unfavorable strips since they cannot get closer to the surface due to the energy barrier (left case)<sup>[280]</sup>. Consequently, with the presence of the convection and diffusion, the particles can be transferred toward the nearest favorable strips, causing an enhanced concentration at the leading edges (right case). Similarly, the sharp concentration peaks

at the trailing edges could be explained by the combined action of the attraction by the favorable strip, the repulsive colloidal interactions of the next unfavorable strip and the transverse Brownian diffusion velocity <sup>[121]</sup>. Thirdly, the deposition is much more uniform along the length of a patterned capillary wall (favorable regions) compared to the homogeneous one in which all the particles will deposit within a very short distance from the inlet, which means that particles tend to travel further along the heterogeneous capillary compared to homogeneous capillary, similar behavior has also been reported by Chatterjee et al. <sup>[188]</sup> and Nazemifard et al. <sup>[121]</sup> To be more intuitive, the above results could be clearly observed in the corresponding 3D sectional views (obtained in this work by numerical simulations) of the heterogeneous and homogeneous capillary with deposited particles, as depicted in Figure 8.3c and Figure 8.3d.

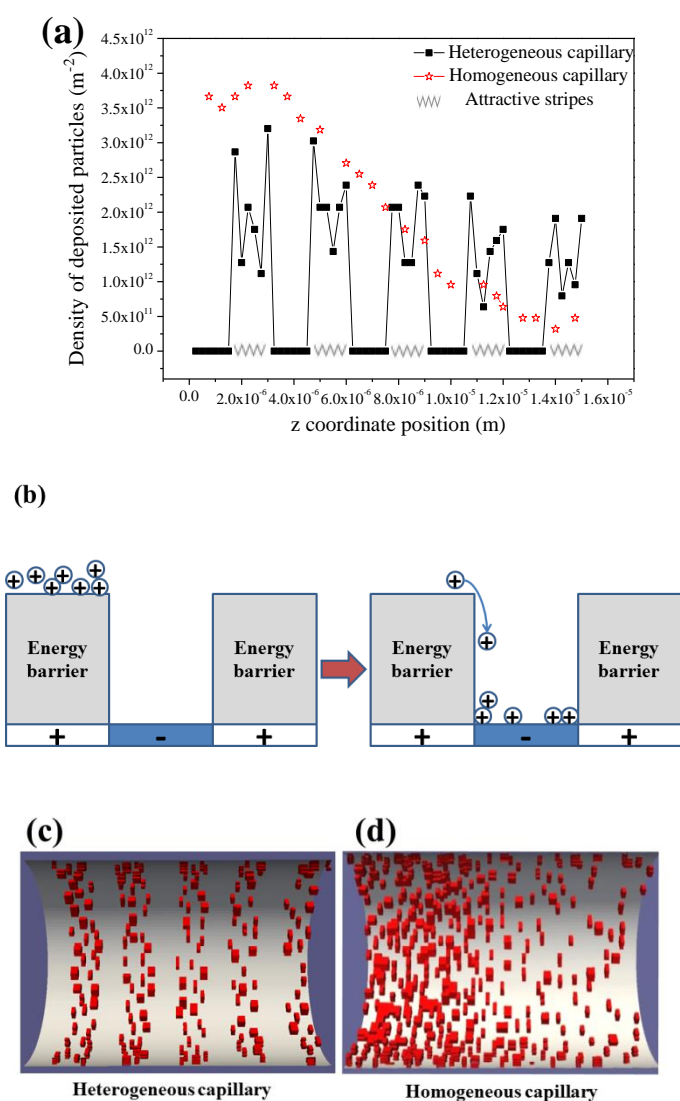


Figure 8.3 (a) Spatial density distribution of the deposited particles versus the z coordinate at N=2000, Pe=0.0015 for both heterogeneous ( $\lambda=5$  and  $\theta=0.5$ ) and homogeneous capillary; (b) schematic representation of particle behavior near the boundaries between the favorable and unfavorable strips <sup>[280]</sup>. 3D sectional view of the

heterogeneous (c) and homogeneous (d) capillary (the red small geometries represent the deposited particles; the flow occurred from left to right)

### 8.3.1.2 Dependence of deposition behavior on the frequency of the pitches and Péclet number

The probability of deposition is defined as the ratio of the number of deposited particles over the number of injected particles and is calculated over groups of 200 particles for each simulation <sup>[276]</sup>. The evolution of the deposition probability versus the number of injected particles (N) with different  $\lambda$  is plotted in Figure 8.4. For comparison, the variation of deposition probability in a homogeneous capillary is also plotted in Figure 8.4. The Péclet number for both heterogeneous and homogeneous capillary is 0.0015, and in this part  $\theta$  was chosen to be 0.5 for the heterogeneous cases.

exhibits a plateau at the early stage of the injection process, which is due to the fact that the exclusion area at low Pe is small and the pore-wall surface is available to a large extent for the injected particles to deposit on. When the number of the deposited particles reaches a critical value, the deposition probability drops sharply to rather low values, indicating that any newly injected particles will have much less chance to deposit <sup>[17]</sup>. This phenomenon is similar to the RSA process where the deposition kinetics becomes slow as the jamming limit is approached <sup>[247]</sup>. Furthermore, for all  $\lambda$ , the overall deposition probability tends to decrease with N, and when N exceeds 10000, all values of the deposition probability are less than 2% with only minor variations afterwards, which suggests that the deposition process is almost over. Therefore, 2% was selected as the cut-off value for the injection process in this work.

More importantly, an obvious observation from Figure 8.4 is that the deposition probability tends to increase with  $\lambda$ . In this work, larger  $\lambda$  means higher frequency of the pitches, which indicates smaller pitch width and therefore larger number of favorable strips with the given length of the capillary. This result demonstrates that although the fraction of the surface area favorable for deposition is the same ( $\theta=0.5$ ), higher frequency of the pitches is conducive to the deposition as a particle can access a larger number of favorable sections along a given length of the capillary. As a limiting case, the capillary with  $\lambda=1$  is half favorable and half unfavorable along the entire pipe length. In such a situation, only one half of the capillary allows particle to deposit on the walls and there is a greater probability that a particle might be transported over the favorable section without depositing. In contrast, if the frequency of the pitches is higher, there is a greater possibility of the particle being captured anywhere (on any one of the favorable strips) along the length of the capillary <sup>[188]</sup>. Consequently, the deposition probability is dependent on the frequency of the pitches, and therefore on the distribution of the surface charge.

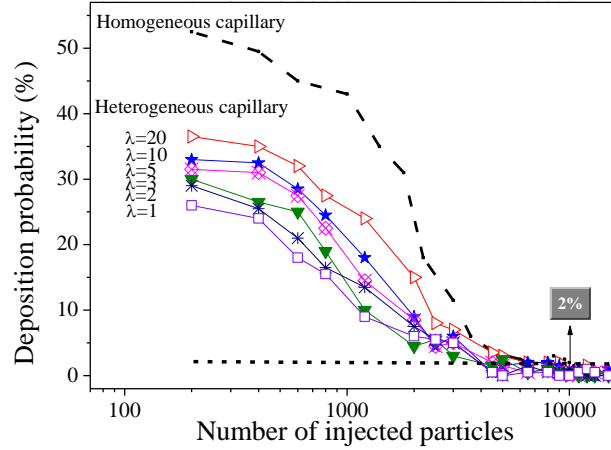


Figure 8.4 Variation of deposition probability versus the number of injected particles (N) for heterogeneous (with different  $\lambda$ ) and homogeneous capillaries. (Pe=0.0015)

Generally, for the homogeneous capillary, the surface coverage ( $\Gamma$ ) is usually defined as the ratio of the total projection area of deposited particles to the total initial surface area of the pore before deposition. And normally the dimensionless surface coverage of  $\Gamma/\Gamma_{RSA}$  is used, where  $\Gamma_{RSA}$  was taken to be 0.546<sup>[247]</sup> which corresponds to the value for pure diffusion regime and a flat surface using the Random Sequential Adsorption (RSA) model. Therefore for the chemically heterogeneous capillary, the dimensionless surface coverage needs to be defined in a specific manner. Here, we define two methods, as is depicted in Figure 8.5a, to calculate the  $\Gamma/\Gamma_{RSA}$  by taking the case of  $\lambda=5$  and  $\theta=0.5$  as an example, and compare with the case of homogeneous capillary, with the same Péclet number of 0.0015. For Method 1, the  $\Gamma/\Gamma_{RSA}$  is calculated by:

$$\frac{\Gamma}{\Gamma_{RSA}} = \frac{n \times s_{particle} / s_{attractive}}{0.546} = \frac{(n \times s_{particle \& \text{ blue}})}{(0.5 \times s_{capillary(\text{green})})} \quad (8-4)$$

Where  $n$  is the number of deposited particles,  $s_{particle}$  is the projection area of one deposited particle (colored by blue in Figure 8.5a) and  $s_{attractive}$  is the total surface area of the attractive regions (colored by dark green in Figure 8.5a), for  $\theta=0.5$  the  $s_{attractive}$  is equal to half of the total surface area of the capillary.

In addition, deposited particles are counted by the z-axis coordinates of the center of the particles, and the average density of deposited particles at the leading and ending edge of the strips is relatively higher, leading to the “extended zones” around the attractive regions (colored by light green in Figure 8.5a). Following these considerations, Method 2 was proposed, where  $\Gamma/\Gamma_{RSA}$  is calculated by:

$$\frac{\Gamma}{\Gamma_{RSA}} = \frac{n \times s_{particle} / (s_{attractive} + s_{extended})}{0.546} = \frac{n \times s_{particle} / (0.5 \times s_{capillary} + 2\pi R \times 2a_p \times \lambda)}{0.546} \quad (8-5)$$

where  $s_{extended}$  is the extended surface areas of every attractive region, the length of the extended band is equal to the radius of the particle. The  $\Gamma/\Gamma_{RSA}$  versus  $N$  calculated by Method 1 and 2 are plotted in Figure 8.5a, and the result of homogeneous capillary is also plotted as the dotted line in Figure 8.5a. It could be observed that the curve calculated by Method 1 is close to the homogeneous one, which indicates that this calculation way is much more suitable, hence the dimensionless surface coverage is calculated by Method 1 in the following part of this chapter.

In order to explore the influence of  $\lambda$  on the dimensionless surface coverage, the variation of  $\Gamma/\Gamma_{RSA}$  versus the number of injected particles ( $N$ ) at different  $\lambda$  is plotted in Figure 8.5b. It can be seen that  $\Gamma/\Gamma_{RSA}$  increases with  $N$  and  $\lambda$ . The overall particle deposition probability versus  $\lambda$  with  $N=5000$ . ( $Pe=0.0015$ ) is plotted in the inset of Figure 8.5b.

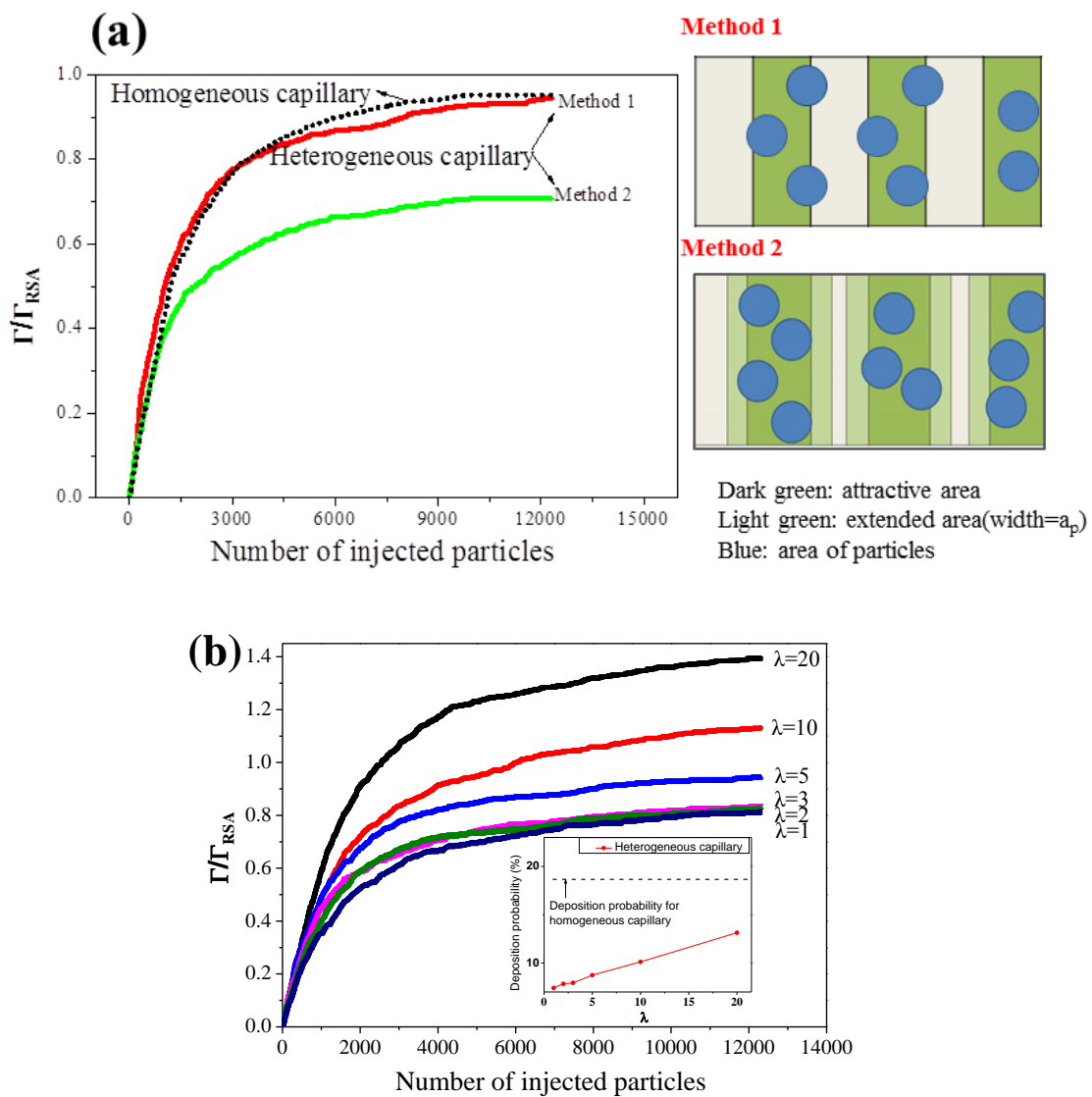


Figure 8.5 (a) Determination of the calculation method of the dimensionless surface coverage for heterogeneous capillary, the dotted line stands for the homogeneous capillary. ( $Pe=0.0015$ ); (b) Variation of the dimensionless

surface coverage versus  $N$  for heterogeneous capillary with different  $\lambda$ . The inset plot represents the overall particle deposition probability versus  $\lambda$  with  $N=5000$  ( $Pe=0.0015$ )

Furthermore, the dependence of  $\Gamma/\Gamma_{RSA}$  on  $Pe$  is significant to understand the influence of flow field on the particle deposition behavior in the heterogeneous capillary. For this purpose, seven simulations with different  $Pe$  (ranging from 0.0015 to 1500) were carried out to investigate the influence of  $Pe$  on the surface coverage. For lower  $Pe$  ( $Pe \ll 1$ ), the particle movement is mainly dominated by the diffusion mechanism, while for higher  $Pe$  ( $Pe \gg 1$ ), the particle transport is mainly governed by convection. In this part,  $\lambda=5$  and  $\theta=0.5$ , the variation of  $\Gamma/\Gamma_{RSA}$  versus  $N$  at various  $Pe$  is plotted in Figure 8.6a. It can be seen that,  $\Gamma/\Gamma_{RSA}$  increases with  $N$ , while it decreases with  $Pe$ . At  $Pe = 0.0015$  (in a diffusion-dominant regime),  $\Gamma/\Gamma_{RSA}$  reaches a value close to 0.92; while at  $Pe = 1500$  (in a convection-dominant regime),  $\Gamma/\Gamma_{RSA}$  approaches to a value of 0.09. This trend also coincides with the result obtained for the homogeneous case [276]. On the other hand,  $\Gamma_{final}/\Gamma_{RSA}$  decreases with  $Pe$  in a more pronounced way for high  $Pe$ . This behavior is more obvious in Figure 8.6b where  $\Gamma_{final}/\Gamma_{RSA}$  is plotted as a function of  $Pe$ . Both the heterogeneous capillary (solid boxes) and the homogeneous capillary (hollow stars) possess similar characteristics. For the diffusion-dominant regime ( $Pe < 1$ ), the surface coverage is close to  $\Gamma_{RSA}$  and is almost constant due to the high deposition probability in this regime. For the convection-dominant regime ( $Pe > 1$ ),  $\Gamma_{final}/\Gamma_{RSA}$  decreases significantly with  $Pe$ , since the hydrodynamic shadowing effect is more obvious for higher  $Pe$ . Indeed, as already mentioned, particles are transported by the fluid over a distance increasing with the convection velocity and are deposited downstream further away from an already deposited particle, resulting in a lower surface coverage [274]. In addition, the derived power law dependence of surface coverage versus Péclet number  $\Gamma_{final}/\Gamma_{RSA} \cong Pe^{-1/3}$  obtained for the convection dominant regime is depicted in Figure 8.6b showing a good agreement with our simulation data. [17, 274]

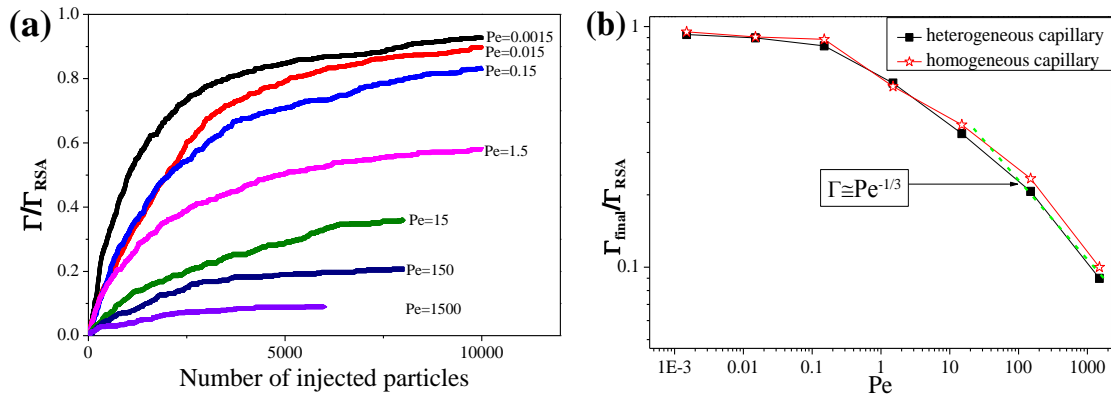


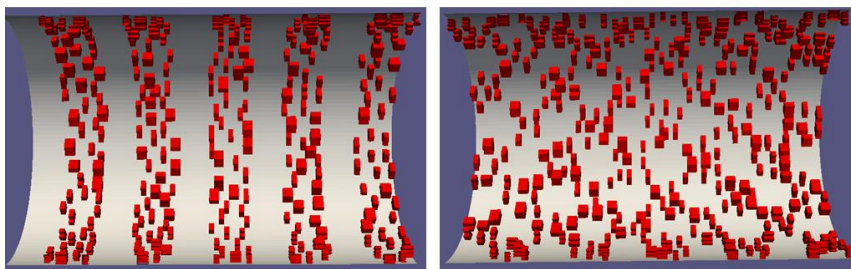
Figure 8.6 Variation of dimensionless surface coverage  $\Gamma/\Gamma_{RSA}$ . (a)  $\Gamma/\Gamma_{RSA}$  versus  $N$  at different  $Pe$ ; (b)  $\Gamma_{Max}/\Gamma_{RSA}$  as a function of  $Pe$ . ( $\lambda=5$  and  $\theta=0.5$  for the heterogeneous capillary)

### 8.3.2 Transport and deposition of colloidal particles in chess board patterned capillary

### 8.3.2.1 Dependence of the dimensionless surface coverage on periodic surface pattern shape

As mentioned earlier, the surface heterogeneity is modeled as alternate bands (patches) of attractive and repulsive regions on the capillary wall to facilitate two systematic continuum type evaluations: crosswise strips patterned and chess board patterned surface heterogeneities. Here, we compared the above two kinds of surface heterogeneous patterns and investigated the influence of periodic surface pattern shape on the dimensionless surface coverage. For both patterns,  $\theta=0.5$  and  $Pe=0.0015$  were selected, and the pitch length is  $3\ \mu\text{m}$ . The schematic diagram of the heterogeneous capillary are plotted in Figure 8.1, and the 3D sectional view of the heterogeneous capillary with deposited particles obtained from our simulations are shown in Figure 8.7a. The obtained figure is coincide with the schematic diagram, demonstrate that the above two kinds of surface heterogeneous pattern were successfully realized. Subsequently, the variation of  $\Gamma/\Gamma_{\text{RSA}}$  versus  $N$  were calculated and plotted in Figure 8.7b. It could be clearly observed that the  $\Gamma/\Gamma_{\text{RSA}}$  of the chess board patterned capillary is always higher than the crosswise strips patterned one. As discussed in section 8.3.1, the average density of deposited particles at the leading and ending edge of the favorable region are relatively higher. Thereby the number of deposited particles is increased with the length of the edges of the favorable region, or to say the “extended zones” around the attractive regions. Under the same simulation conditions, the chess board patterned capillary possesses larger edge length thus larger area of “extended zones”, which leads to a larger number of deposited particles although the additional edges are parallel to the flow direction. Moreover, Pham et al. <sup>[176]</sup> also observed a similar phenomenon by investigating packed beds with four different patterns of surface charge heterogeneity, on which favorable surfaces for particle attachment are placed at different locations. The results indicated that the attachment coefficient of random pattern is higher than the strips pattern. This is because for the chess board patterned capillary with more uniform distributed active surface area, the particles have more time and higher opportunity to move towards and collide with the active collector surface as they propagate through the porous domain.

(a)



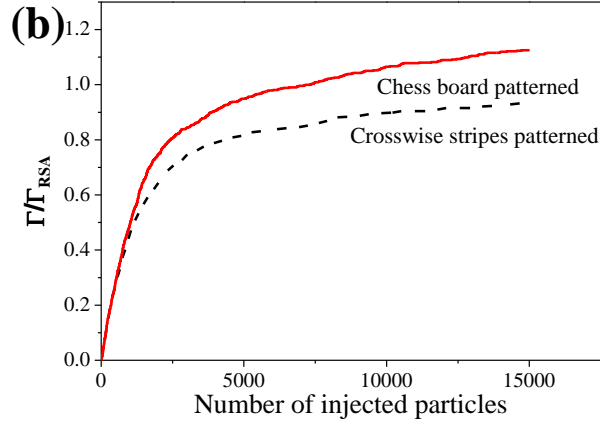


Figure 8.7 (a). 3D sectional view (left: crosswise strips patterned), (right: chess board patterned) of the heterogeneous capillary with deposited particles ; (b) variation of dimensionless surface coverage  $\Gamma/\Gamma_{RSA}$  versus  $N$  for crosswise strips patterned and chess board patterned capillaries. For both cases,  $\theta=0.5$ , pitch length= $3 \mu\text{m}$  and  $Pe=0.0015$

### 8.3.2.2 Dependence of deposition behavior on the favorable surface coverage

In order to investigate the influence of favorable surface ratio,  $\theta$ , on the particle deposition, nine groups of numerical simulation with  $\theta$  ranging from 20% to 100% were carried out, and the 3D sectional view of the heterogeneous capillary with deposited particles are provided in Figure 8.8a. According to the simulation results, the number of deposited particles ( $n$ ) versus  $N$  with different  $\theta$  were recorded and plotted into nine curves, as is illustrated in Figure 8.8b. It could be clearly observed that  $n$  is increasing with  $N$  and  $\theta$ . This result is in line with the patchwise heterogeneity model, which provides the overall deposition efficiency as a linear combination of favorable and unfavorable deposition efficiencies. For a chemically heterogeneous porous media containing a random distribution of favorable and unfavorable regions, the two-site patch model simply gives the effective collector efficiency as <sup>[121, 160]</sup>:

$$\frac{\eta_{\text{effective}}}{\eta_f} = (1-\theta) \frac{\eta_u}{\eta_f} + \theta \quad (8-6)$$

where  $\eta_{\text{effective}}$  is the overall deposition efficiency,  $\eta_f$  and  $\eta_u$  are the deposition efficiencies for favorable and unfavorable regions, respectively. Since the particle can only adsorb if the projection of its center lies within the favorable bands, and no particles can deposit on unfavorable bands ( $\eta_u = 0$ ), equation (8-6) simplifies to <sup>[121]</sup>:

$$\frac{\eta_{\text{effective}}}{\eta_f} = \theta \quad (8-7)$$

For comparison, the value of  $\eta_{\text{effective}}/\eta_f$  predicted by the patch model (the dashed diagonal line), and those obtained from our simulations (the solid boxes) are plotted in Figure 8.8c.  $\eta_{\text{effective}}$  is calculated by the overall deposition efficiency for  $N=10000$ , and  $\eta_f$  is the deposition efficiencies for a completely favorable surface [121, 188]. The patch model provides a remarkably accurate prediction of the deposition efficiency for surfaces with macroscopic charge heterogeneity [120, 146]. In order to characterize the correlation degree between the simulation results and the patch model, the simulation data were fitted into a straight line, as is shown in the red line in Figure 8.8c, the correlation coefficient of the data points is up to 0.997, which is highly corresponding to the dashed diagonal line calculated by the patchwise heterogeneity model. Overall, the overall collector deposition efficiency is in good agreement with the results predicted by the patch model, even when the heterogeneous bands are comparable to the particle dimensions.

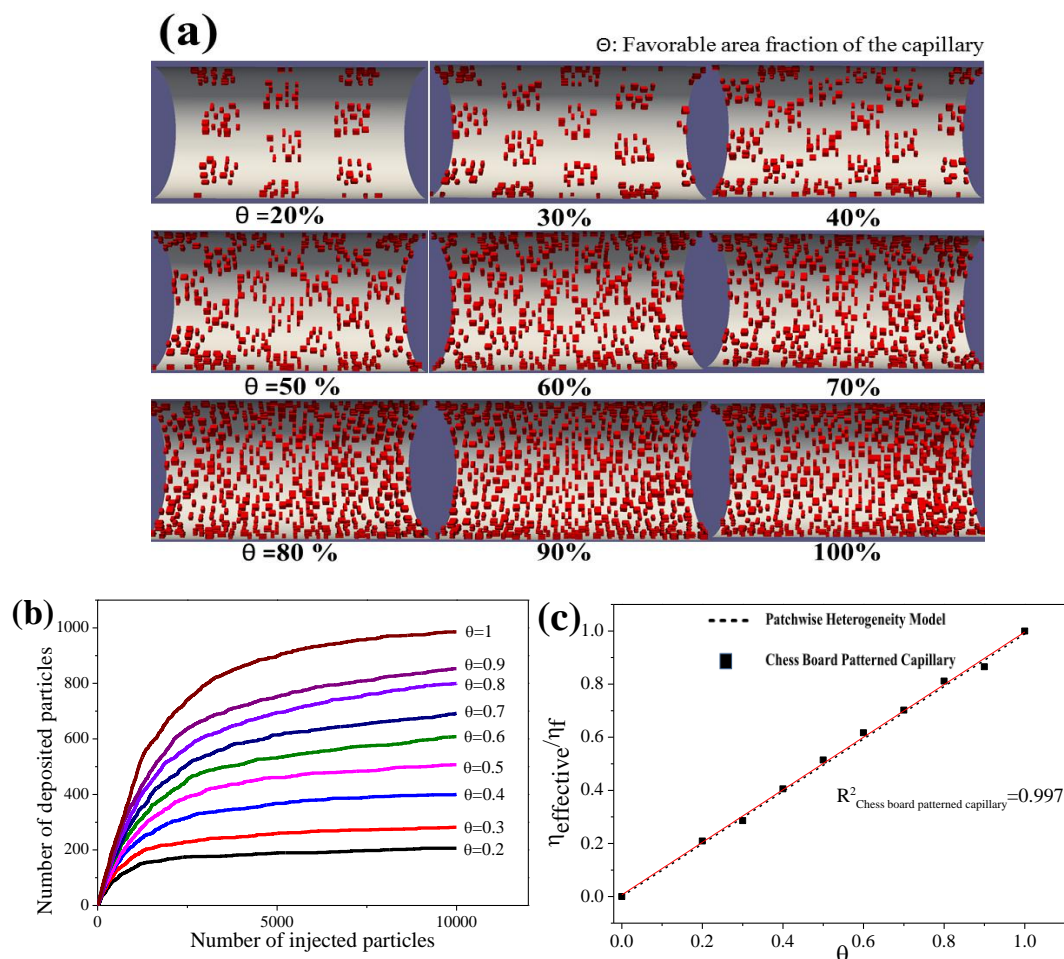


Figure 8.8 (a) 3D sectional view of the heterogeneous capillary with deposited particles,  $\lambda=5$ ,  $Pe=0.0015$ ,  $\theta$  is ranging from 20% to 100%; (b) variation of the number of deposited particles ( $n$ ) versus the number of injected particles ( $N$ ) with different  $\theta$ ; (c) the dependence of the effective collector efficiency ( $\eta_{\text{effective}}/\eta_f$ ) on  $\theta$ . ( $\lambda=5$ ,  $Pe=0.0015$ ,  $N=10000$ )

## 8.4 Conclusions

In this work, the proposed 3D-PTPO code is shown to be a useful and flexible tool for the microscale simulation of colloidal particle transport and deposition in a 3D chemically heterogeneous capillary. The main conclusions can be drawn as follows: Firstly, the coupled effect of the charge heterogeneity and the three-dimensional velocity field can bring out a complex concentration distribution of deposited particles on the wall, leading to a higher density of deposited particles at the leading and trailing edges of each favorable strip, and the deposition is more uniform along the patterned capillary compared to the homogeneous one. Secondly, the deposition probability is in line with the frequency of the pitches. Under the same favorable surface ratio,  $\theta$ , smaller pitch length will result in higher deposition probability and accordingly higher dimensionless surface coverage. Moreover, for the diffusion-dominant regime at lower  $Pe$ , the surface coverage is close to the  $\Gamma_{RSA}$  and features a relatively stable plateau. For the convection-dominant regime at high  $Pe$ , the declining trend of  $\Gamma/\Gamma_{RSA}$  versus  $Pe$  is in good agreement with the derived power law dependence of surface coverage versus  $Pe$ . Finally, the overall deposition probability is increasing with the favorable area fraction. The correlation coefficient of the data points is up to 0.997, which is in good agreement with the patchwise heterogeneity model. This study provides insight in designing artificially heterogeneous porous media for particle capture in various engineering and biomedical applications including targeted drug therapy. Furthermore, the model can be further improved by incorporating more realistic fluid flow profiles and more random heterogeneous patterns.

## Chapter 9 Conclusions and Perspectives

Polymeric porous media with an original porous structure, high porosity, low density, and good chemical stability are proved to be promising materials in a wide range of application fields. Despite significant progress made on preparation of polymeric porous media, no particular method is better than others, and each method has its' advantages and limitations. Currently, the main problem is that the production processes of these methods are relatively cumbersome and clearly decrease the production efficiency and increase the cost. Thus a long-term goal for the preparation of porous polymer materials is still the development of simple and scalable procedures. It is, therefore, essential to find new methods that can optimize the porous structure without sacrificing the low-cost. This is one of the main objectives of this thesis. The multilayer coextrusion represents an advanced polymer processing technique, that is capable of economically and efficiently producing films of multilayers. Thus in this thesis, a novel strategy is proposed to prepare polymeric porous media with a tunable porous structure via multilayer coextrusion combined with the template method/TIPS, which is a highly efficient pathway for large-scale fabrication of porous polymer materials. This approach combines the advantages of the multilayer coextrusion (continuous process, economic pathway for large-scale fabrication, and tunable layer structures) and the template method/phase separation method (simple preparation process and tunable pore structure). Afterwards, applications of the polymeric porous media in PAHs adsorption and lithium-ion battery separator have been investigated. The obtained results indicate that the multilayer PP/PE separators prepared by this new combination exhibit higher porosity, higher electrolyte uptake and retention than commercial separators. This will definitely increase the ionic conductivity, and consequently improve the battery performances. More importantly, the PP/PE multilayer separator shows effective thermal shutdown function and a thermal stability up to 160 °C, that is wider than commercial separators. The porous polystyrene obtained via this new combination possesses abundant and uniform porous structure which exhibits much higher adsorption performance of traces of pyrene than the solid medium. The adsorption kinetics and isotherm of porous PS membranes can be well fitted by pseudo second-order kinetics and Freundlich isotherm model. In principle, this novel method is applicable to any melt-processable polymer in addition to PP, PE and PS. Thus in the future, investigations could be carried out on the preparation and application of other kinds of polymeric porous media such as porous polyvinylidene fluoride, polyethylene oxide, polymethyl methacrylate and so on.

More importantly, the basic mechanism of the above application processes (PAHs adsorption or Li-ion transport through separator) is based on particles transport and deposition in porous media.

Besides, transport and deposition of colloidal particles in porous media is a frequently encountered phenomenon in a wide range of applications in addition to the above cases, including aquifer remediation, fouling of surfaces, and therapeutic drug delivery. Thus it is essential to have a thorough understanding of such processes as well as the dominant mechanisms. Therefore, in the second part of the thesis, the microscale simulation of particle transport and deposition in porous media was carried out by a novel colloidal particle tracking model, called 3D-PTPO (Three-Dimensional Particle Tracking model by Python<sup>®</sup> and OpenFOAM<sup>®</sup>) code.

Firstly, particle deposition is investigated on a homogeneous capillary in order to revisit the work of Lopez and co-authors [17] by considering a more realistic 3D geometry, as well as to validate theoretical basic laws of transport and deposition of particles using the simulation method developed here. Preliminary results were analyzed and some conclusions may be drawn:

- The deposition probability decreases with the number of injected particles and with the Péclet number.
- At low Péclet number values, the ultimate surface coverage  $\Gamma$  is shown to closely approach the RSA value and drops noticeably for high Pe values.
- Both porosity and permeability decrease with the number of deposited particles.
- At low Pe numbers, the equivalent hydrodynamic thickness of the deposit layer is lower than the particle diameter showing the formation of a loose monolayer deposit before decreasing for higher Pe.

The above results demonstrate that the numerical method used is relevant to describe deposition of colloids in porous media from dilute dispersions.

Secondly, the three-dimensional numerical modeling of the process of particle transport and deposition in a porous media with more complex geometry is carried out by representing the elementary pore structure as a capillary tube with converging/diverging geometries (tapered pipe and venturi tube). The main conclusions can be drawn as follows:

- The probability for a particle to be deposited on the pore-wall surface is much higher for the diffusion-dominant regime, and the deposited particle distribution along the pipes is piston-like as for the simple tube model.

- The distribution is more uniform for the advection-dominant regime. In particular, for the venturi tube, the density of deposited particles is relatively low in the vicinity of the pore throat entrance and exit due to the particular flow structure therein.
- The behavior of the dimensionless final plateau of the maximum surface coverage  $\Gamma_{\text{final}}/\Gamma_{\text{RSA}}$  as a function of Pe has been analyzed. For low Pe, a plateau could be observed for both geometries and the plateau value and the deposition kinetics are consistent with the RSA theory. For high Pe, the declining trends for  $\Gamma_{\text{final}}/\Gamma_{\text{RSA}}$  versus Pe are in good agreement with experimental and simulation results found in the literature.

Thirdly, the coupled effect of surface chemical heterogeneity and hydrodynamics on particle transport and deposition in a pore-throat idealized as a three-dimensional capillary with periodically repeating chemically heterogeneous surface (crosswise strips patterned and chess board patterned) was investigated. The main conclusions can be drawn as follows: the coupled effect of heterogeneity and the velocity field can bring out a complex concentration distribution of deposited particles on the wall. For example, higher density of deposited particles are observed at the leading and trailing edges of each favorable strip. Besides, the deposition probability is in line with the frequency of the pitches. In addition, the surface coverage is still close to the  $\Gamma_{\text{RSA}}$  and features a relatively stable plateau at lower Pe. The declining trend of  $\Gamma_{\text{final}}/\Gamma_{\text{RSA}}$  versus Pe is again in good agreement with the derived power law dependence of surface coverage versus Pe at higher Pe. Moreover, the overall deposition probability is increasing with the favorable area fraction.

The above results are consistent with theoretical predictions, demonstrating that the numerical method used is relevant to describe deposition of colloids in porous media from dilute dispersions. Future developments of this work will include a larger range of the related parameters on the one hand and more realistic pore geometries on the other hand.

## Acknowledgement

How time flies! It has been almost five years since the first enrollment in the spring of 2013, and every details flashback vividly in my mind. I would like to extend my sincerely thanks to Prof. Hongting Pu, who is my Chinese supervisor. Prof. Pu is a talented, frankly, and upright professor, his merits have had a profound impact on me. He is also diligent and rigorous in teaching, he teaches me how to select topic, how to do research, how to write an article, and how to submission. It has been one of my greatest pleasures to work with him during the past years.

I would like to express my heartfelt gratitude to my French supervisor Prof. Azita Ahmadi for her international vision, innovative thinking, and meticulous academic style. I miss and appreciate the inspiring seminars, her motivating words and sincere suggestions so much. She is the goddess in my heart, how I wish I can become an elegant and successful lady like her in the future! I would like to give my special thanks to Prof. Aziz Omari, who has brought me a broader view of my research subject. He is intelligent, knowledgeable and warm-hearted. I am also impressed by his cheerful personality, open minded, hard-working and sense of humor. He provided so much helpful advices and corrected almost every mistake for me carefully. His guidance has been instrumental in making my PhD experience a fruitful one. Although I only study in France for only 18 months, Prof. Ahmadi and Prof. Omari still invested so many efforts in helping me with my work. They are always by my side when I encountered troubles, and encouraged me to move on and be a better researcher. I feel so grateful for all the things they have done for me.

I will also give my thanks to Otar and yibiao, who helped me a lot during the simulation. Many thanks to the teachers and students in I2M and ENSAM, they are quite nice, funny and easygoing. Many thanks to Cyril, Anne, Ali, Valerie, Muriel, Henri, Florence, Tingting, Yingying, and Jeremy, the experience and memory here will be the most precious thing in my life and I will treasure them forever. Thanks to all the teachers of the FPI at Tongji University for helping and caring during my studies, they are Prof. Wan, Prof. Du, Prof. Jin, Prof. Chang, and Prof. Pan. Thanks to my classmates and dear friends, they are Feng, Haicun, Junfeng, Min, Danyun, Zhu, Hong, Yue, Yonglian, Daobin, and Haicheng.

Finally yet importantly, I sincerely thank my parents for your full support and understanding, family is my strongest backing. I hope that one day I could be as perfect as you are.

December, 2017

## References

- [1] Bear J, Bachmat Y. Introduction to modeling of transport phenomena in porous media [M]. Springer science & business media, 2012, Vol.4.
- [2] Coutelieis F A, Delgado J M P Q. Transport processes in porous media [M]. Advanced structured materials, 2012, Vol.20.
- [3] Qiu G, Xiao J, Zhu J. Research history, classification and applications of metal porous material [J]. *Metalurgia international*, 2016, Vol.18(5): 1-11.
- [4] Yang H, Jiang P. Large-scale colloidal self-assembly by doctor blade coating [J]. *Langmuir : the ACS journal of surfaces and colloids*, 2010, Vol.26(16): 13173-13182.
- [5] Wu D, Xu F, Sun B, et al. Design and preparation of porous polymers [J]. *Chemical reviews*, 2012, Vol.112(7): 3959-4015.
- [6] Scozzari A, El Mansouri B. Water security in the Mediterranean region: an international evaluation of management, control, and governance approaches [M]. Springer science & business media, 2011.
- [7] Corapcioglu M Y, Jiang S. Colloid-facilitated groundwater contaminant transport [J]. *Water resources research*, 1993, Vol.29(7): 2215-2226.
- [8] Herzig J P, Leclerc D M, Goff P L. Flow of suspensions through porous media-application to deep filtration [J]. *Industrial & engineering chemistry*, 1970, Vol.62(5): 8-35.
- [9] Stevik T K, Aa K, Ausland G, et al. Retention and removal of pathogenic bacteria in wastewater percolating through porous media: a review [J]. *Water research*, 2004, Vol.38(6): 1355-1367.
- [10] Behnke J J. Clogging in surface spreading operations for artificial ground-water recharge [J]. *Water resources research*, 1969, Vol.5(4): 870-876.
- [11] Kanov K, Burns R. Particle tracking in open simulation laboratories [C]. High performance computing, networking, storage and analysis, 2015 SC-International Conference for. IEEE, 2015: 1-11.
- [12] Scott C F. Particle tracking simulation of pollutant discharges [J]. *Journal of environmental engineering*, 1997, Vol.123(9): 919-927.
- [13] Yao K M, Habibian M T, O'Melia C R. Water and waste water filtration. Concepts and applications [J]. *Environmental science & technology*, 1971, Vol.5(11): 1105-1112.
- [14] Rajagopalan R, Tien, C. Trajectory analysis of deep-bed filtration with the sphere-in-cell porous media model [J]. *AIChE Journal*, 1976, Vol.22(3): 523-533.
- [15] Salama A, Negara A, El Amin M, et al. Numerical investigation of nanoparticles transport in anisotropic porous media [J]. *Journal of contaminant hydrology*, 2015, Vol.181:114-130.
- [16] Bianco C, Tosco T, Sethi R A. 3-dimensional micro- and nanoparticle transport and filtration model (MNM3D) applied to the migration of carbon-based nanomaterials in porous media [J]. *Journal of contaminant hydrology*, 2016, Vol.193:10-20.
- [17] Lopez P, Omari A, Chauveteau G. Simulation of surface deposition of colloidal spheres under flow [J]. *Colloids and surfaces A: physicochemical and engineering aspects*, 2004, Vol.240(1-3): 1-8.
- [18] Ishizaki K, Komarneni S, Nanko M. Porous materials process technology and applications [M]. Springer science & business media, 2013, Vol.4.

- [19] Doonan C J, Tranchemontagne D J, Glover T G, et al. Exceptional ammonia uptake by a covalent organic framework [J]. *Nature chemistry*, 2010, Vol.2(3): 235-238.
- [20] Rzyayev J, Hillmyer, M. A. Nanochannel array plastics with tailored surface chemistry [J]. *Journal of the American chemical society*, 2005, Vol.127(38): 13373-13379.
- [21] Schaefer D W. Engineered porous materials [J]. *MRS Bulletin*, 1994, Vol.19(4): 14-19.
- [22] Ishizu K, Kobayakawa N, Uchida S. Ordered microporous surface films formed by core-shell-type nanospheres [J]. *Macromolecular rapid communications*, 2006, Vol.27(12): 961-965.
- [23] Sun Q, Dai Z, Meng X, et al. Porous polymer catalysts with hierarchical structures [J]. *Chem Soc Rev*, 2015, Vol.44(17): 6018-6034.
- [24] El-Kaderi H M, Hunt J R, Mendoza-Cortés J L, et al. Designed synthesis of 3D covalent organic frameworks [J]. *Science*, 2007, Vol.316(5822): 268-272.
- [25] Kim J K, Yang S Y, Lee Y, et al. Functional nanomaterials based on block copolymer self-assembly [J]. *Progress in polymer science*, 2010, Vol.35(11): 1325-1349.
- [26] Jiang J X, Trewin A, Su F, et al. Microporous poly(tri(4-ethynylphenyl)amine) networks: synthesis, properties, and atomistic simulation [J]. *Macromolecules*, 2009, Vol.42(7): 2658-2666.
- [27] Cote A P, Benin A I, Ockwig N W, et al. Porous, crystalline, covalent organic frameworks [J]. *Science*, 2005, Vol.310(5751): 1166-1170.
- [28] Kaur P, Hupp J T, Nguyen S T. Porous organic polymers in catalysis: opportunities and challenges [J]. *ACS Catalysis*, 2011, Vol.1(7): 819-835.
- [29] Cooper A I, DeSimone J M. Polymer synthesis and characterization in liquid/supercritical carbon dioxide [J]. *Current opinion in solid state and materials science*, 1996, Vol.1(6): 761-768.
- [30] Sa-nguanrukxa J, Rujiravanit R, Supaphol P, et al. Porous polyethylene membranes by template-leaching technique: preparation and characterization [J]. *Polymer testing*, 2004, Vol.23(1): 91-99.
- [31] Johnson S A, Ollivier P J, Mallouk T E. Ordered mesoporous polymers of tunable pore size from colloidal silica templates [J]. *Science*, 1999, Vol.283(5404): 963-965.
- [32] Jiang P, Hwang K S, Mittleman D M, et al. Template-directed preparation of macroporous polymers with oriented and crystalline arrays of voids [J]. *Journal of the American chemical society*, 1999, Vol.121(50): 11630-11637.
- [33] Chakraborty S, Colón Y J, Snurr R Q, et al. Hierarchically porous organic polymers: highly enhanced gas uptake and transport through templated synthesis [J]. *Chemical science*, 2015, Vol.6(1): 384-389.
- [34] Wang D, Caruso F. Fabrication of polyaniline inverse opals via templating ordered colloidal assemblies [J]. *Advanced materials*, 2001, Vol.13(5): 350-354.
- [35] Pavia F C, La Carrubba V, Brucato V. Morphology and thermal properties of foams prepared via thermally induced phase separation based on polylactic acid blends [J]. *Journal of cellular plastics*, 2012, Vol.48(5): 399-407.
- [36] Aram E, Mehdipour-Ataei S. A review on the micro- and nanoporous polymeric foams: Preparation and properties [J]. *International journal of polymeric materials and polymeric biomaterials*, 2015, Vol.65(7): 358-375.
- [37] Zhao J, Luo G, Wu J, et al. Preparation of microporous silicone rubber membrane with tunable pore size via solvent evaporation-induced phase separation [J]. *ACS appl mater interfaces*, 2013, Vol.5(6) 2040-2046.

- [38] Strathmann H. Production of microporous media by phase inversion processes [M]. 1985, Vol.269:165-195.
- [39] Yave W, Quijada R, Ulbricht M, et al. Syndiotactic polypropylene as potential material for the preparation of porous membranes via thermally induced phase separation (TIPS) process [J]. *Polymer*, 2005, Vol.46(25): 11582-11590.
- [40] Stropnik Č, Musil V, Brumen M. Polymeric membrane formation by wet-phase separation; turbidity and shrinkage phenomena as evidence for the elementary processes [J]. *Polymer*, 2000, Vol.41(26): 9227-9237.
- [41] Bikel M, Punt I G, Lammertink R G, et al. Micropatterned polymer films by vapor-induced phase separation using permeable molds [J]. *ACS applied materials & interfaces*, 2009, Vol.1(12): 2856-2861.
- [42] Kim J K, Taki K, Ohshima M. Preparation of a unique microporous structure via two step phase separation in the course of drying a ternary polymer solution [J]. *Langmuir*, 2007, Vol.23(24): 12397-12405.
- [43] Lloyd D R, Kinzer K E, Tseng H S. Microporous membrane formation via thermally induced phase separation. I. Solid-liquid phase separation [J]. *Journal of membrane science*, 1990, Vol.52(3): 239-261.
- [44] Ramaswamy S, Greenberg A R, Krantz W B. Fabrication of poly (ECTFE) membranes via thermally induced phase separation [J]. *Journal of membrane science*, 2002, Vol.210(1): 175-180.
- [45] Matsuyama H, Yuasa M, Kitamura Y, et al. Structure control of anisotropic and asymmetric polypropylene membrane prepared by thermally induced phase separation [J]. *Journal of membrane science*, 2000, Vol.179(1): 91-100.
- [46] Martínez-Pérez C A, Olivás-Armendariz I, Castro-Carmona J S, et al. Scaffolds for tissue engineering via thermally induced phase separation [M]. *Advances in regenerative medicine InTech*, 2011.
- [47] Vandeweerdt P, Berghmans H, Tervoort Y. Temperature-concentration behavior of solutions of polydisperse, atactic poly (methyl methacrylate) and its influence on the formation of amorphous, microporous membranes [J]. *Macromolecules*, 1991, Vol.24(12): 3547-3552.
- [48] Zhang M, Zhang C F, Yao Z K, et al. Preparation of high density polyethylene / polyethylene - block - poly (ethylene glycol) copolymer blend porous membranes via thermally induced phase separation process and their properties [J]. *Chinese journal of polymer science*, 2010, Vol.28(3): 337-346.
- [49] Yang Z, Li P, Xie L, et al. Preparation of iPP hollow-fiber microporous membranes via thermally induced phase separation with co-solvents of DBP and DOP [J]. *Desalination*, 2006, Vol.192(1-3): 168-181.
- [50] Matsuyama H, Ohga K, Maki T, et al. Porous cellulose acetate membrane prepared by thermally induced phase separation [J]. *Journal of applied polymer science*, 2003, Vol.89(14): 3951-3955.
- [51] Cha B J, Yang J M. Preparation of poly(vinylidene fluoride) hollow fiber membranes for microfiltration using modified TIPS process [J]. *Journal of membrane science*, 2007, Vol.291(1-2): 191-198.
- [52] Fu X, Maruyama T, Sotani T, et al. Effect of surface morphology on membrane fouling by humic acid with the use of cellulose acetate butyrate hollow fiber membranes [J]. *Journal of membrane science*, 2008, Vol.320(1-2): 483-491.

- [53]Jang H, Song D H, Lee H J, et al. Preparation of dual-layer acetylated methyl cellulose hollow fiber membranes via co-extrusion using thermally induced phase separation and non-solvent induced phase separation methods [J]. *Journal of applied polymer science*, 2015, Vol.132(43): 42715.
- [54]Cheng Q, Cui Z, Li J, et al. Preparation and performance of polymer electrolyte based on poly(vinylidene fluoride)/polysulfone blend membrane via thermally induced phase separation process for lithium ion battery [J]. *Journal of power sources*, 2014, Vol.266:401-413.
- [55]Fu X Y, Sotani T, Matsuyama H. Effect of membrane preparation method on the outer surface roughness of cellulose acetate butyrate hollow fiber membrane [J]. *Desalination*, 2008, Vol.233(1-3): 10-18.
- [56]Cui Z, Xu Y, Zhu L, et al. Preparation of PVDF/PEO-PPO-PEO blend microporous membranes for lithium ion batteries via thermally induced phase separation process [J]. *Journal of membrane science*, 2008, Vol.325(2): 957-963.
- [57]Zhou N, Bates F S, Lodge T P. Mesoporous membrane templated by a polymeric bicontinuous microemulsion [J]. *Nano letters*, 2006, Vol.6(10): 2354-2357.
- [58]Barrow M S, Jones R L, Park J O, et al. Physical characterisation of microporous and nanoporous polymer films by atomic force microscopy, scanning electron microscopy and high speed video microphotography [J]. *Spectroscopy*, 2004, Vol.18(4): 577-585.
- [59]Park J S, Lee S H, Han T H, et al. Hierarchically ordered polymer films by templated organization of aqueous droplets [J]. *Advanced functional materials*, 2007, Vol.17(14): 2315-2320.
- [60]Pitois O, Francois B. Crystallization of condensation droplets on a liquid surface [J]. *Colloid & polymer science*, 1999, Vol.277(6): 574-578.
- [61]Armstrong S R, Du J, Baer E. Co-extruded multilayer shape memory materials: Nano-scale phenomena [J]. *Polymer*, 2014, Vol.55(2): 626-631.
- [62]Arora P, Zhang Z. Battery separators [J]. *Chemical Reviews*, 2004, Vol.104(10): 4419-4462.
- [63]Lu W, Yuan Z, Zhao Y, et al. Porous membranes in secondary battery technologies [J]. *Chemical Society reviews*, 2017, Vol.46(8): 2199-2236.
- [64]Ye W, Zhu J, Liao X, et al. Hierarchical three-dimensional micro/nano-architecture of polyaniline nanowires wrapped-on polyimide nanofibers for high performance lithium-ion battery separators [J]. *Journal of power sources*, 2015, Vol.299:417-424.
- [65]Chen W, Liu Y, Ma Y, et al. Improved performance of PVdF-HFP/PI nanofiber membrane for lithium ion battery separator prepared by a bicomponent cross-electrospinning method [J]. *Materials letters*, 2014, Vol.133:67-70.
- [66]Chen H L, Jiao X N, Zhou J T. The research progress of Li-ion battery separators with inorganic oxide nanoparticles by electrospinning: A mini review [J]. *Functional materials letters*, 2016, Vol.09(05):1630003.
- [67]Li D, Shi D, Feng K, et al. Poly (ether ether ketone) (PEEK) porous membranes with super high thermal stability and high rate capability for lithium-ion batteries [J]. *Journal of membrane science*, 2017, Vol.530:125-131.
- [68]Venugopal G, Moore J, Howard J, et al. Characterization of microporous separators for lithium-ion batteries [J]. *Journal of power sources*, 1999, Vol.77(1): 34-41.
- [69]Deimede V, Elmasides C. Separators for lithium-ion batteries: A review on the production processes and recent developments [J]. *Energy technology*, 2015, Vol.3(5): 453-468.
- [70]Baginska M, Blaiszik B J, Merriman R J, et al. Autonomic shutdown of lithium-ion batteries using thermoresponsive microspheres [J]. *Advanced energy materials*, 2012, Vol.2(5): 583-590.

- [71] Jeong H S, Lee S Y. Closely packed SiO<sub>2</sub> nanoparticles/poly(vinylidene fluoride - hexafluoropropylene) layers-coated polyethylene separators for lithium-ion batteries [J]. *Journal of power sources*, 2011, Vol.196(16): 6716-6722.
- [72] Lee J Y, Lee Y M, Bhattacharya B, et al. Separator grafted with siloxane by electron beam irradiation for lithium secondary batteries [J]. *Electrochimica acta*, 2009, Vol.54(18):4312-4315.
- [73] Zhang C, Xia Y, Zuo K, et al. The Effect of Silica Addition on the Microstructure and Properties of Polyethylene Separators Prepared by Thermally Induced Phase Separation [J]. *Journal of applied polymer science*, 2014, Vol.131(17):40724-40729.
- [74] Armstrong S R, Offord G T, Paul D R, et al. Co-extruded polymeric films for gas separation membranes [J]. *Journal of applied polymer science*, 2013, Vol.131(2):218-224.
- [75] Zhou L, Gao C, Xu W. Magnetic dendritic materials for highly efficient adsorption of dyes and drugs [J]. *ACS applied materials & interfaces*, 2010, Vol.2(5): 1483-1491.
- [76] Osagie E I, Owabor C N. Adsorption of naphthalene on clay and sandy soil from aqueous solution [J]. *Advances in chemical engineering and science*, 2015, Vol.05(03): 345-351.
- [77] Wang S, Wang K, Pang Y, et al. Open-cell polypropylene/polyolefin elastomer blend foams fabricated for reusable oil-sorption materials [J]. *Journal of applied polymer science*, 2016, Vol.133(33): 43812.
- [78] Awoyemi A. Understanding the adsorption of polycyclic aromatic hydrocarbons from aqueous phase onto activated carbon [D]. Doctoral dissertation University of Toronto, 2011.
- [79] Hu Y, He Y, Wang X, et al. Efficient adsorption of phenanthrene by simply synthesized hydrophobic MCM-41 molecular sieves [J]. *Applied surface science*, 2014, Vol.311:825-830.
- [80] Zhang J, Séquaris J M, Narres H D, et al. Pyrene and phenanthrene sorption to model and natural geosorbents in single-and binary-solute systems [J]. *Environmental science & technology*, 2010, Vol.44(21): 8102-8107.
- [81] An C, Huang G. Stepwise adsorption of phenanthrene at the fly ash-water interface as affected by solution chemistry: experimental and modeling studies [J]. *Environmental science & technology*, 2012, Vol.46(22): 12742-12750.
- [82] Tang X, Zhou Y, Xu Y, et al. Sorption of polycyclic aromatic hydrocarbons from aqueous solution by hexadecyltrimethylammonium bromide modified fibric peat [J]. *Journal of chemical technology & biotechnology*, 2010, Vol.85(8): 1084-1091.
- [83] Hall S, Tang R, Baeyens J, et al. Removing polycyclic aromatic hydrocarbons from water by adsorption on silicagel [J]. *Polycyclic aromatic compounds*, 2009, Vol.29(3): 160-183.
- [84] Pu H T, Li Y J. A porous styrenic material for the adsorption of polycyclic aromatic hydrocarbons [P]. Chinese patent 2015108125669, 2016.
- [85] Simkevitz S L, Naguib H E. Fabrication and analysis of porous shape memory polymer and nanocomposites [J]. *High performance polymers*, 2009, Vol.22(2): 159-183.
- [86] Luo Y S, Cheng K C, Huang N D, et al. Preparation of porous crosslinked polymers with different surface morphologies via chemically induced phase separation [J]. *Journal of polymer science part B: polymer physics*, 2011, Vol.49(14): 1022-1030.
- [87] Li Y, Yang F, Yu J, et al. Hydrophobic fibrous membranes with tunable porous structure for equilibrium of breathable and waterproof performance [J]. *Advanced materials interfaces*, 2016, Vol.3(19): 1600516.
- [88] Singamaneni S, Bertoldi K, Chang S, et al. Instabilities and pattern transformation in periodic, porous elastoplastic solid coatings [J]. *ACS applied materials & interfaces*, 2009, Vol.1(1): 42-47.

- [89] Srinivasarao M, Collings D, Philips A, et al. Three-dimensionally ordered array of air bubbles in a polymer film [J]. *Science*, 2001, Vol.292(5514): 79-83.
- [90] Bonyadi S, Chung T S. Highly porous and macrovoid-free PVDF hollow fiber membranes for membrane distillation by a solvent-dope solution co-extrusion approach [J]. *Journal of membrane science*, 2009, Vol.331(1-2): 66-74.
- [91] Jin C, Ren C L, Emelko M B. Concurrent modeling of hydrodynamics and interaction forces improves particle deposition predictions [J]. *Environmental science & technology*, 2016, Vol.50(8): 4401-4412.
- [92] Kretzschmar R, Barmettler K, Grolimund D, et al. Experimental determination of colloid deposition rates and collision efficiencies in natural porous media [J]. *Water resources research*, 1997, Vol.33(5): 1129-1137.
- [93] Weroński P, Walz J Y, Elimelech M. Effect of depletion interactions on transport of colloidal particles in porous media [J]. *Journal of colloid and interface science*, 2003, Vol.262(2): 372-383.
- [94] Yoon J S, Germaine J T, Culligan P J. Visualization of particle behavior within a porous medium: Mechanisms for particle filtration and retardation during downward transport [J]. *Water resources research*, 2006, Vol.42(6): 1-16.
- [95] Boccardo G, Marchisio D L, Sethi R. Microscale simulation of particle deposition in porous media [J]. *Journal of colloid and interface science*, 2014, Vol.417: 227-237.
- [96] Long W, Huang H, Serlemitsos J, et al. Pore-scale study of the collector efficiency of nanoparticles in packings of nonspherical collectors [J]. *Colloids and surfaces A: physicochemical and engineering aspects*, 2010, Vol.358(1-3): 163-171.
- [97] Long W, Hilpert M. A Correlation for the collector efficiency of brownian particles in clean-bed filtration in sphere packings by a Lattice-Boltzmann method [J]. *Environmental science & technology*, 2009, Vol.43(12): 4419-4424.
- [98] Zamani A, Maini B. Flow of dispersed particles through porous media-Deep bed filtration [J]. *Journal of petroleum science and engineering*, 2009, Vol.69(1-2): 71-88.
- [99] Elimelech M, Gregory J, Jia X, et al. Particle deposition and aggregation. measurement, modelling and simulation [M]. Butterworth-Heinemann, 1995.
- [100] Ghidaglia J M, Saut J C. Nonexistence of travelling wave solutions to nonelliptic nonlinear schrödinger equations [J]. *Journal of Nonlinear Science*, 1996, Vol.6(2): 139-145.
- [101] Wan J, Tokunaga T K, Tsang C F, et al. Improved glass micromodel methods for studies of flow and transport in fractured porous media [J]. *Water resources research*, 1996, Vol.32(7): 1955-1964.
- [102] Lanning L M, Ford R M. Glass micromodel study of bacterial dispersion in spatially periodic porous networks [J]. *Biotechnology and bioengineering*, 2002, Vol.78(5): 556-566.
- [103] Adamczyk Z, Siwek B, Jaszczółt K, et al. Deposition of latex particles at heterogeneous surfaces [J]. *Colloids and surfaces A: physicochemical and engineering aspects*, 2004, Vol.249(1-3): 95-98.
- [104] Areepitak T, Ren J. Model simulations of particle aggregation effect on colloid exchange between streams and streambeds [J]. *Environmental science & technology*, 2011, Vol.45(13): 5614-5621.
- [105] Unni H N, Yang C. Brownian dynamics simulation and experimental study of colloidal particle deposition in a microchannel flow [J]. *Journal of colloid and interface science*, 2005, Vol.291(1): 28-36.

- [106] Canseco V, Djehiche A, Bertin H, et al. Deposition and re-entrainment of model colloids in saturated consolidated porous media: Experimental study [J]. *Colloids and surfaces A: physicochemical and engineering aspects*, 2009, Vol.352(1-3): 5-11.
- [107] Sasidharan S, Torkzaban S, Bradford S A, et al. Coupled effects of hydrodynamic and solution chemistry on long-term nanoparticle transport and deposition in saturated porous media [J]. *Colloids and surfaces A: physicochemical and engineering aspects*, 2014, Vol.457:169-179.
- [108] Risbud S R, Drazer G. Trajectory and distribution of suspended non-Brownian particles moving past a fixed spherical or cylindrical obstacle [J]. *Journal of fluid mechanics*, 2013, Vol.714:213-237.
- [109] Chang Y I, Chen S C, Lee E. Prediction of Brownian particle deposition in porous media using the constricted tube model [J]. *Journal of colloid and interface science*, 2003, Vol.266(1): 48-59.
- [110] Xiao F. Pore-scale simulation frameworks for flow and transport in complex porous media [D]. Colorado school of Mines, 2013
- [111] Meakin P, Tartakovsky A M. Modeling and simulation of pore-scale multiphase fluid flow and reactive transport in fractured and porous media [J]. *Reviews of Geophysics*, 2009, Vol.47(3):1-47.
- [112] Coutelieiris F A, Kainourgiakis M E, Stubos A K. Low Peclet mass transport in assemblages of spherical particles for two different adsorption mechanisms [J]. *Journal of colloid and interface science*, 2003, Vol.264(1): 20-29.
- [113] Sefrioui N, Ahmadi A, Omari A, et al. Numerical simulation of retention and release of colloids in porous media at the pore scale [J]. *Colloids and surfaces A: physicochemical and engineering aspects*, 2013, Vol.427:33-40.
- [114] Sirivithayapakorn S, Keller A. Transport of colloids in saturated porous media: A pore-scale observation of the size exclusion effect and colloid acceleration [J]. *Water resources research*, 2003, Vol.39(4): 1109.
- [115] Bradford S A, Torkzaban S. Determining parameters and mechanisms of colloid retention and release in porous media [J]. *Langmuir : the ACS journal of surfaces and colloids*, 2015, Vol.31(44): 12096-12105.
- [116] Reeshav C. Transport and deposition of particles onto homogeneous and chemically heterogeneous porous media geometries [D]. Thesis, University of Alberta, 2011.
- [117] Elimelech M, O'Melia C R. Kinetics of deposition of colloidal particles in porous media [J]. *Environmental science & technology*, 1990, Vol.24(10): 1528-1536.
- [118] Tan J. Numerical simulation of Nanoparticle delivery in microcirculation [D]. Lehigh University, 2012.
- [119] Johnson P R, Elimelech M. Dynamics of colloid deposition in porous media: Blocking based on random sequential adsorption [J]. *Langmuir : the ACS journal of surfaces and colloids*, 1995, Vol.11(3): 801-812.
- [120] Kemps J A, Bhattacharjee S. Particle tracking model for colloid transport near planar surfaces covered with spherical asperities [J]. *Langmuir : the ACS journal of surfaces and colloids*, 2009, Vol.25(12): 6887-6897.
- [121] Nazemifard N, Masliyah J H, Bhattacharjee S. Particle deposition onto micropatterned charge heterogeneous substrates: trajectory analysis [J]. *Journal of colloid and interface science*, 2006, Vol.293(1): 1-15.

- [122] Yeh I C, Hummer G. System-size dependence of diffusion coefficients and viscosities from molecular dynamics simulations with periodic boundary conditions [J]. *The journal of physical chemistry B*, 2004, Vol.108(40): 15873-15879.
- [123] Probstein R F. *Physicochemical hydrodynamics: An introduction* [M]. John Wiley & Sons, 2005.
- [124] Liu P C. *Experimental and numerical investigations into fundamental mechanisms controlling particle transport in saturated porous media* [D]. Doctoral dissertation of Columbia University, 2016.
- [125] Levich V G. *Physicochemical hydrodynamics*[M]. Prentice hall, 1962.
- [126] Tang H, Cao T, Liang X, et al. Influence of silicone surface roughness and hydrophobicity on adhesion and colonization of *Staphylococcus epidermidis* [J]. *Journal of biomedical materials research Part A*, 2009, Vol.88(2): 454-463.
- [127] Happel J. Viscous flow in multiparticle systems slow motion of fluids relative to beds of spherica [J]. *AIChE Journal*, 1958, Vol.4(2): 197-201.
- [128] Nelson K E, Ginn T R. Colloid filtration theory and the Happel sphere-in-cell model revisited with direct numerical simulation of colloids [J]. *Langmuir*, 2005, Vol.21(6): 2173-2184.
- [129] Cushing R S, Lawler D F. Depth filtration: fundamental investigation through three-dimensional trajectory analysis[J]. *Environmental science & technology*, 1998, Vol.32(23): 3793-3801..
- [130] Elimelech M, O'Melia C R. Effect of particle size on collision efficiency in the deposition of Brownian particles with electrostatic energy barriers [J]. *Langmuir : the ACS journal of surfaces and colloids*, 1990, Vol.6(6): 1153-1163.
- [131] Tan Y, Gannon J T, Baveye P, et al. Transport of bacteria in an aquifer sand: experiments and model simulations [J]. *Water resources research*, 1994, Vol.30(12): 3243-3252.
- [132] McDowell-Boyer L M, Hunt J R, Sitar N. Particle transport through porous media [J]. *Water resources research*, 1986, Vol.22(13): 1901-1921.
- [133] van Loenhout M T J, Kooij E S, Wormeester H, et al. Hydrodynamic flow induced anisotropy in colloid adsorption [J]. *Colloids and surfaces A: physicochemical and engineering aspects*, 2009, Vol.342(1-3): 46-52.
- [134] Happel J. Viscous flow in multiparticle systems: slow motion of fluids relative to beds of spherical particles[J]. *AIChE Journal*, 1958, Vol.4(2): 197-201.
- [135] Khan H, Mirabolghasemi M, Yang H, et al. Comparative study of Formation damage due to straining and surface deposition in porous media [C]. *SPE international conference and exhibition on formation damage control*. Society of petroleum engineers, 2016.
- [136] Johnson W P, Li X, Yal G. Colloid retention in porous media: mechanistic confirmation of wedging and retention in zones of flow stagnation [J]. *Environmental science & technology*, 2007, Vol.41(4): 1279-1287.
- [137] Civan F. Modified formulations of particle deposition and removal kinetics in saturated porous media [J]. *Transport in porous media*, 2015, Vol.111(2): 381-410.
- [138] Zhang T, Murphy M, Yu H, et al. Mechanistic model for nanoparticle retention in porous media [J]. *Transport in porous media*, 2016, Vol.115(2): 387-406.
- [139] Ahfir N D, Hammadi A, Alem A, et al. Porous media grain size distribution and hydrodynamic forces effects on transport and deposition of suspended particles [J]. *Journal of environmental sciences*, 2017, Vol. 53: 161-172.

- [140] Lin Y J, He P, Tavakkoli M, et al. Examining asphaltene solubility on deposition in model porous media [J]. *Langmuir : the ACS journal of surfaces and colloids*, 2016, Vol.32(34): 8729-8734.
- [141] Koullapis P G, Kassinos S C, Bivolarova M P, et al. Particle deposition in a realistic geometry of the human conducting airways: Effects of inlet velocity profile, inhalation flowrate and electrostatic charge [J]. *Journal of biomechanics*, 2016, Vol.49(11): 2201-2212.
- [142] Becker M D, Wang Y, Paulsen J L, et al. In situ measurement and simulation of nano-magnetite mobility in porous media subject to transient salinity [J]. *Nanoscale*, 2015, Vol.7(3): 1047-1057.
- [143] Park C M, Chu K H, Heo J, et al. Environmental behavior of engineered nanomaterials in porous media: a review [J]. *Journal of hazardous materials*, 2016, Vol.309:133-150.
- [144] Wang M, Gao B, Tang D. Review of key factors controlling engineered nanoparticle transport in porous media [J]. *Journal of hazardous materials*, 2016, Vol.318:233-246.
- [145] Li X, Lin C L, Miller J D, et al. Pore-scale observation of microsphere deposition at grain-to-grain contacts over assemblage-scale porous media domains using X-ray microtomography [J]. *Environmental science & technology*, 2006, Vol.40(12): 3762-3768.
- [146] Buret S, Nabzar L, Jada A. Water quality and well injectivity do residual oil-in-water emulsions matter [J]. *SPE Journal*, 2010, Vol.15(02): 557-568.
- [147] Li X, Lin C L, Miller J D, et al. Role of grain-to-grain contacts on profiles of retained colloids in porous media in the presence of an energy barrier to deposition [J]. *Environmental science & technology*, 2006, Vol.40(12): 3769-3774.
- [148] Ahmadi-S énichault A, Canseco V, Sefrioui-Chaibainou N, et al. Displacement of colloidal dispersions in Porous Media experimental & numerical approaches [C]. *Diffusion foundations*. Trans Tech Publications, 2016, Vol.7: 53-68.
- [149] Taghavy A, Pennell K D, Abriola L M. Modeling coupled nanoparticle aggregation and transport in porous media: a Lagrangian approach [J]. *Journal of contaminant hydrology*, 2015, Vol.172:48-60.
- [150] Tosco T, Sethi R. MNM1D: a numerical code for colloid transport in porous media: implementation and validation [J]. *American journal of environmental sciences*, 2009, Vol.5(4): 516-524.
- [151] Katzourakis V E, Chrysikopoulos C V. Mathematical modeling of colloid and virus cotransport in porous media: Application to experimental data [J]. *Advances in water resources*, 2014, Vol.68:62-73.
- [152] Syngouna V I, Chrysikopoulos C V. Cotransport of clay colloids and viruses in water saturated porous media [J]. *Colloids and surfaces A: Physicochemical and engineering aspects*, 2013, Vol.416:56-65.
- [153] Hoepfner M P, Limsakoune V, Chuenmeechao V, et al. A fundamental study of asphaltene deposition [J]. *Energy & fuels*, 2013, Vol.27(2): 725-735.
- [154] Su J, Gu Z, Xu X Y. Discrete element simulation of particle flow in arbitrarily complex geometries [J]. *Chemical engineering science*, 2011, Vol.66(23): 6069-6088.
- [155] Brand Á, HÄUßINGER K, Meyer T, et al. Intrapulmonary distribution of deposited particles [J]. *Journal of aerosol medicine*, 1999, Vol.12(4): 275-284.
- [156] Kusaka Y, Duval J F L, Adachi Y. Morphology and breaking of latex particle deposits at a cylindrical collector in a microfluidic chamber [J]. *Environmental science & technology*, 2010, Vol.44(24): 9413-9418.

- [157] Li Q, Dai C S, Jiao W J. Fine particle dispersion and deposition in three different square pore flow structures [J]. *Applied mechanics and materials*, 2011, Vol.84-85: 91-95.
- [158] Duffadar R, Kalasin S, Davis J M, et al. The impact of nanoscale chemical features on micron-scale adhesion: crossover from heterogeneity-dominated to mean-field behavior [J]. *Journal of colloid and interface science*, 2009, Vol.337(2): 396-407.
- [159] Bendersky M, Santore M M, Davis J M. Statistically-based DLVO approach to the dynamic interaction of colloidal microparticles with topographically and chemically heterogeneous collectors [J]. *Journal of colloid and interface science*, 2015, Vol.449:443-451.
- [160] Chen J Y, Ko C H, Bhattacharjee S, Elimelech, M. Role of spatial distribution of porous medium surface charge heterogeneity in colloid transport [J]. *Colloids and surfaces A: physicochemical and engineering aspects*, 2001, Vol.191(1): 3-15.
- [161] Rizwan T, Bhattacharjee S. Particle deposition onto charge-heterogeneous substrates [J]. *Langmuir : the ACS journal of surfaces and colloids*, 2009, Vol.25(9): 4907-4918.
- [162] Duffadar R D, Davis J M. Interaction of micrometer-scale particles with nanotextured surfaces in shear flow [J]. *Journal of colloid and interface science*, 2007, Vol.308(1): 20-29.
- [163] Suresh L, Walz J Y. Effect of surface roughness on the interaction energy between a colloidal sphere and a flat plate [J]. *Journal of colloid and interface science*, 1996, Vol.183(1): 199-213.
- [164] Zhao K, Mason T G. Suppressing and enhancing depletion attractions between surfaces roughened by asperities [J]. *Physical review letters*, 2008, Vol.101(14): 148301.
- [165] Wang X L, Lu Z Y, Li Z S, et al. Molecular dynamics simulation study on controlling the adsorption behavior of polyethylene by fine tuning the surface nanodecoration of graphite. [J]. *Langmuir : the ACS journal of surfaces and colloids*, 2007, Vol.23(2): 802-808.
- [166] Phenrat T, Cihan A, Kim H J, et al. Transport and deposition of polymer-modified FeO nanoparticles in 2-D heterogeneous porous media: Effects of particle concentration, FeO content, and coatings [J]. *Environmental science & technology*, 2010, Vol.44(23): 9086-9093.
- [167] Bendersky M, Davis J M. DLVO interaction of colloidal particles with topographically and chemically heterogeneous surfaces [J]. *Journal of colloid and interface science*, 2011, Vol.353(1): 87-97.
- [168] Elimelech M, Chen J Y, Kuznar Z A. Particle deposition onto solid surfaces with micropatterned charge heterogeneity: The “hydrodynamic bump” effect [J]. *Langmuir : the ACS journal of surfaces and colloids*, 2003, Vol.19(17): 6594-6597.
- [169] Bradford S A, Torkzaban S. Colloid interaction energies for physically and chemically heterogeneous porous media [J]. *Langmuir: the ACS journal of surfaces and colloids*, 2013, Vol.29(11): 3668-3676.
- [170] Duffadar R D, Davis J M. Dynamic adhesion behavior of micrometer-scale particles flowing over patchy surfaces with nanoscale electrostatic heterogeneity [J]. *Journal of colloid and interface science*, 2008, Vol.326(1): 18-27.
- [171] Chatterjee R, Mitra S K, Bhattacharjee S. Particle deposition onto Janus and Patchy spherical collectors [J]. *Langmuir : the ACS journal of surfaces and colloids*, 2011, Vol.27(14): 8787-8797.
- [172] Zhang M, Bradford S A, Simunek J, et al. Do goethite surfaces really control the transport and retention of multi-walled carbon nanotubes in chemically heterogeneous porous media? [J]. *Environmental science & technology*, 2016, Vol.50(23): 12713-12721.

- [173] Lin S, Cheng Y, Bobcombe Y, et al. Deposition of silver nanoparticles in geochemically heterogeneous porous media: predicting affinity from surface composition analysis [J]. *Environmental science & technology*, 2011, Vol.45(12): 5209-5215.
- [174] Johnson P R, Ning S, Elimelech M. Colloid transport in geochemically heterogeneous porous media: Modeling and measurements [J]. *Environmental science & technology*, 1996, Vol.30(11): 3284-3293.
- [175] Pham N H, Papavassiliou D V. Nanoparticle transport in heterogeneous porous media with particle tracking numerical methods [J]. *Computational particle mechanics*, 2016, Vol.4(1): 87-100.
- [176] Pham N H, Papavassiliou D V. Effect of spatial distribution of porous matrix surface charge heterogeneity on nanoparticle attachment in a packed bed [J]. *Physics of fluids*, 2017, Vol.29(8): 082007.
- [177] Erickson D, Li D. Three-dimensional structure of electroosmotic flow over heterogeneous surfaces [J]. *The journal of physical chemistry B*, 2003, Vol.107(44): 12212-12220.
- [178] Liu Y, Zhang C, Hu D, et al. Role of collector alternating charged patches on transport of *Cryptosporidium parvum* oocysts in a patchwise charged heterogeneous micromodel [J]. *Environmental science & technology*, 2013, Vol.47(6): 2670-2678.
- [179] Bradford S A, Torkzaban S. Colloid adhesive parameters for chemically heterogeneous porous media [J]. *Langmuir : the ACS journal of surfaces and colloids*, 2012, Vol.28(38): 13643-13651.
- [180] Shen C, Lazouskaya V, Zhang H, et al. Influence of surface chemical heterogeneity on attachment and detachment of microparticles [J]. *Colloids and surfaces A: physicochemical and engineering aspects*, 2013, Vol.433:14-29.
- [181] Adamczyk Z, Van De Ven T G M. Deposition of particles under external forces in Laminar flow through parallel-plate and cylindrical channels [J]. *Journal of colloid and interface science*, 1981, Vol.80(2): 340-356.
- [182] Waghmare P R, Mitra S K. Finite reservoir effect on capillary flow of microbead suspension in rectangular microchannels [J]. *Journal of colloid and interface science*, 2010, Vol.351(2): 561-569.
- [183] Fridjonsson E O, Seymour J D, Cokelet G R, et al. Dynamic NMR microscopy measurement of the dynamics and flow partitioning of colloidal particles in a bifurcation [J]. *Experiments in fluids*, 2010, Vol.50(5): 1335-1347.
- [184] Waghmare P R, Mitra S K. Mechanism of cell transport in a microchannel with binding between cell surface and immobilized biomolecules [C]. *ASME 2009 International mechanical engineering congress and exposition. American society of mechanical engineers*, 2009: 779-784.
- [185] Saadatmand M, Ishikawa T, Matsuki N, et al. Fluid particle diffusion through high-hematocrit blood flow within a capillary tube [J]. *Journal of biomechanics*, 2011, Vol.44(1): 170-175.
- [186] Chein R, Dutta P. Effect of charged membrane on the particle motion through a nanopore [J]. *Colloids and surfaces A: Physicochemical and engineering aspects*, 2009, Vol.341(1-3): 1-12.
- [187] Gudipaty T, Stamm M T, Cheung L S L, et al. Cluster formation and growth in microchannel flow of dilute particle suspensions [J]. *Microfluidics and nanofluidics*, 2010, Vol.10(3): 661-669.
- [188] Chatterjee R, Bhattacharjee S, Mitra S K. Particle transport in patterned cylindrical microchannels [J]. *Microfluidics and nanofluidics*, 2012, Vol.12(1-4): 41-51.
- [189] Tarascon J M, Armand M. Issues and challenges facing rechargeable lithium batteries [J]. *Nature*, 2001, Vol.414(6861): 359-367.

- [190] Etacheri V, Marom R, Elazari R, et al. Challenges in the development of advanced Li-ion batteries: a review [J]. *Energy & environmental science*, 2011, Vol.4(9): 3243.
- [191] Joho F, Novák P, Spahr M E. Safety aspects of graphite negative electrode materials for lithium-ion batteries [J]. *Journal of the electrochemical society*, 2002, Vol.149(8): A1020.
- [192] Wang Q, Ping P, Zhao X, et al. Thermal runaway caused fire and explosion of lithium ion battery [J]. *Journal of power sources*, 2012, Vol.208:210-224.
- [193] Baginska M, Blaiszik B J, Rajh T, et al. Enhanced autonomic shutdown of Li-ion batteries by polydopamine coated polyethylene microspheres [J]. *Journal of power sources*, 2014, Vol.269:735-739.
- [194] Ji W, Jiang B, Ai F, et al. Temperature-responsive microspheres-coated separator for thermal shutdown protection of lithium ion batteries [J]. *RSC Adv*, 2015, Vol.5(1): 172-176.
- [195] Shi C, Zhang P, Huang S, et al. Functional separator consisted of polyimide nonwoven fabrics and polyethylene coating layer for lithium-ion batteries [J]. *Journal of power sources*, 2015, Vol.298:158-165.
- [196] Tabatabaei S H, Carreau P J, Ajji A. Microporous membranes obtained from PP/HDPE multilayer films by stretching [J]. *Journal of membrane science*, 2009, Vol.345(1-2): 148-159.
- [197] Zhang S S. A review on the separators of liquid electrolyte Li-ion batteries [J]. *Journal of power sources*, 2007, Vol.164(1): 351-364.
- [198] Park J H, Park W, Kim J H, et al. Close-packed poly(methyl methacrylate) nanoparticle arrays-coated polyethylene separators for high-power lithium-ion polymer batteries [J]. *Journal of power sources*, 2011, Vol.196(16): 7035-7038.
- [199] Huang X, Hitt J. Lithium ion battery separators: Development and performance characterization of a composite membrane [J]. *Journal of membrane science*, 2013, Vol.425-426:163-168.
- [200] Zhang J, Liu Z, Kong Q, et al. Renewable and superior thermal-resistant cellulose-based composite nonwoven as lithium-ion battery separator [J]. *ACS applied materials & interfaces*, 2013, Vol.5(1): 128-134.
- [201] Shi J, Xia Y, Yuan Z, et al. Porous membrane with high curvature, three-dimensional heat-resistance skeleton: a new and practical separator candidate for high safety lithium ion battery [J]. *Scientific reports*, 2015, Vol.5(0):82521.
- [202] Wang Q, Jian Z, Song W L, et al. Facile fabrication of safe and robust polyimide fibrous membrane based on triethylene glycol diacetate-2-propenoic acid butyl ester gel electrolytes for lithium-ion batteries [J]. *Electrochimica acta*, 2014, Vol.149:176-185.
- [203] Cheng J, Pu H, Du J. A processing method with high efficiency for low density polyethylene nanofibers reinforced by aligned carbon nanotubes via nanolayer coextrusion [J]. *Polymer*, 2017, Vol.111:222-228.
- [204] Obata K, Tamesue S, Hashimoto K, et al. Preparation of porous poly(pyrrole) utilizing agar particles as soft template and evaluation of its actuation property [J]. *Macromolecular materials and engineering*, 2015, Vol.300(8): 766-771.
- [205] Zhu Y, Xiao S, Shi Y, et al. A trilayer poly(vinylidene fluoride)/polyborate/poly(vinylidene fluoride) gel polymer electrolyte with good performance for lithium ion batteries [J]. *Journal of materials chemistry A*, 2013, Vol.1(26): 7790-7797.

- [206] Liao H, Zhang H, Hong H, et al. Novel cellulose aerogel coated on polypropylene separators as gel polymer electrolyte with high ionic conductivity for lithium-ion batteries [J]. *Journal of membrane science*, 2016, Vol.514:332-339.
- [207] Liu Q, Xia M, Chen J, et al. High performance hybrid Al<sub>2</sub>O<sub>3</sub>/poly(vinyl alcohol-co-ethylene) nanofibrous membrane for lithium-ion battery separator [J]. *Electrochimica acta*, 2015, Vol.176:949-955.
- [208] Wen H, Zhang J, Chai J, et al. Sustainable and superior heat-resistant alginate nonwoven separator of LiNi<sub>0.5</sub>Mn<sub>1.5</sub>O<sub>4</sub>/Li batteries operated at 55 degrees C [J]. *ACS applied materials & interfaces*, 2017, Vol.9(4): 3694-3701.
- [209] Prasanna K, Lee C W. Physical, thermal, and electrochemical characterization of stretched polyethylene separators for application in lithium-ion batteries [J]. *Journal of solid state electrochemistry*, 2013, Vol.17(5): 1377-1382.
- [210] An M Y, Kim H T, Chang D R. Multilayered separator based on porous polyethylene layer, Al<sub>2</sub>O<sub>3</sub> layer, and electro-spun PVdF nanofiber layer for lithium batteries [J]. *Journal of solid state electrochemistry*, 2014, Vol.18(7): 1807-1814.
- [211] Li M X, Wang X W, Yang Y Q, et al. A dense cellulose-based membrane as a renewable host for gel polymer electrolyte of lithium ion batteries [J]. *Journal of membrane science*, 2015, Vol.476:112-118.
- [212] Blake A J, Kohlmeyer R R, Hardin J O, et al. 3D printable ceramic-polymer electrolytes for flexible high-performance li-ion batteries with enhanced thermal stability [J]. *Advanced energy materials*, 2017, Vol.7(14): 1602920.
- [213] Zhang J, Chen S, Xie X, et al. Porous poly(vinylidene fluoride-co-hexafluoropropylene) polymer membrane with sandwich-like architecture for highly safe lithium ion batteries [J]. *Journal of membrane science*, 2014, Vol.472:133-140.
- [214] Zheng W, Zhu Y, Na B, et al. Hybrid silica membranes with a polymer nanofiber skeleton and their application as lithium-ion battery separators [J]. *Composites science and technology*, 2017, Vol.144:178-184.
- [215] Zhang H, Zhou M Y, Lin C E, et al. Progress in polymeric separators for lithium ion batteries [J]. *RSC Advances*, 2015, Vol.5(109): 89848-89860.
- [216] Fu K K, Gong Y, Dai J, et al. Flexible, solid-state, ion-conducting membrane with 3D garnet nanofiber networks for lithium batteries [J]. *Proceedings of the national academy of sciences of the united states of America*, 2016, Vol.113(26): 7094-7099.
- [217] Tang X, Cao Q, Wang X, et al. Study of the effect of a novel high-performance gel polymer electrolyte based on thermoplastic polyurethane/poly(vinylidene fluoride)/polystyrene and formed using an electrospinning technique [J]. *RSC Advances*, 2015, Vol.5(72): 58655-58662.
- [218] Yamada A, Koizumi H, Nishimura S, et al. Room-temperature miscibility gap in Li<sub>x</sub>FePO<sub>4</sub> [J]. *Nature materials*, 2006, Vol.5(5): 357-360.
- [219] Nunes-Pereira J, Kundu M, Gören A, et al. Optimization of filler type within poly(vinylidene fluoride-co-trifluoroethylene) composite separator membranes for improved lithium-ion battery performance [J]. *Composites part B: Engineering*, 2016, Vol.96:94-102.
- [220] Agubra V A, De la Garza D, Gallegos L, et al. ForceSpinning of polyacrylonitrile formassproduction of lithiumionbattery separators [J]. *Journal of applied polymer science*, 2015, Vol.131(1): 42847-42854.

- [221] Jeong H S, Kim J H, Lee S Y. A novel poly(vinylidene fluoride-hexafluoropropylene) / poly(ethylene terephthalate) composite nonwoven separator with phase inversion-controlled microporous structure for a lithium-ion battery [J]. *Journal of materials chemistry*, 2010, Vol.20(41): 9180-9186.
- [222] Chi M, Shi L, Wang Z, et al. Excellent rate capability and cycle life of Li metal batteries with ZrO<sub>2</sub>/POSS multilayer-assembled PE separators [J]. *Nano energy*, 2016, Vol.28:1-11.
- [223] Wang Z, Guo F, Chen C, et al. Self-assembly of PEI/SiO<sub>2</sub> on polyethylene separators for Li-ion batteries with enhanced rate capability [J]. *ACS applied materials & interfaces*, 2015, Vol.7(5): 3314-3322.
- [224] Liu M, Zhang P, Gou L, et al. Enhancement on the thermostability and wettability of lithium-ion batteries separator via surface chemical modification [J]. *Materials letters*, 2017, Vol.208:98-101.
- [225] Shi J, Li H, Fang L, et al. Improving the properties of HDPE based separators for lithium ion batteries by blending block with copolymer PE-b-PEG[J]. *Chinese journal of polymer science*, 2013, Vol.31(2): 309-317
- [226] Kim J F, Jung J T, Wang H H, et al. Microporous PVDF membranes via thermally induced phase separation (TIPS) and stretching methods [J]. *Journal of membrane science*, 2016, Vol.509:94-104.
- [227] Akbarzadeh R, Yousefi A M. Effects of processing parameters in thermally induced phase separation technique on porous architecture of scaffolds for bone tissue engineering [J]. *Journal of biomedical materials research Part B, Applied biomaterials*, 2014, Vol.102(6): 1304-1315.
- [228] Barroca N, Daniel-da-Silva A L, Vilarinho P M, et al. Tailoring the morphology of high molecular weight PLLA scaffolds through bioglass addition [J]. *Acta biomaterialia*, 2010, Vol.6(9):3611-3620.
- [229] Laxminarayan A, McGuire K S, Kim S S, et al. Effect of initial composition, phase separation temperature and polymer crystallization on the formation of microcellular structures via thermally induced phase separation [J]. *Polymer*, 1994, Vol.35(14): 3060-3068.
- [230] Ji G L, Zhu B K, Cui Z Y, et al. PVDF porous matrix with controlled microstructure prepared by TIPS process as polymer electrolyte for lithium ion battery [J]. *Polymer*, 2007, Vol.48(21): 6415-6425.
- [231] Wu Q Y, Liang H Q, Gu L, et al. PVDF/PAN blend separators via thermally induced phase separation for lithium ion batteries [J]. *Polymer*, 2016, Vol.107: 54-60.
- [232] Chai J, Zhang J, Hu P, et al. A high-voltage poly(methylethyl a-cyanoacrylate) composite polymer electrolyte for 5 V lithium batteries [J]. *Journal of materials chemistry A*, 2016, Vol.4(14): 5191-5197.
- [233] Rubio-Clemente A, Torres-Palma R A, Penuela G A. Removal of polycyclic aromatic hydrocarbons in aqueous environment by chemical treatments: a review [J]. *The science of the total environment*, 2014, Vol.478: 201-225.
- [234] Peng R H, Fu X Y, Zhao W, et al. Phytoremediation of phenanthrene by transgenic plants transformed with a naphthalene dioxygenase system from *Pseudomonas* [J]. *Environmental science & technology*, 2014, Vol.48(21): 12824-12832.
- [235] Shih K L, Lederberg J. Chloramine mutagenesis in *Bacillus subtilis* [J]. *Science*, 1976, Vol.192(4244): 1141-1143.

- [236] Lemić J, Tomašević-Čanović M, Adamović M, et al. Competitive adsorption of polycyclic aromatic hydrocarbons on organo-zeolites [J]. *Microporous and mesoporous materials*, 2007, Vol.105(3): 317-323.
- [237] Xi Z, Chen B. Removal of polycyclic aromatic hydrocarbons from aqueous solution by raw and modified plant residue materials as biosorbents [J]. *Journal of environmental sciences*, 2014, Vol.26(4): 737-748.
- [238] Ge X, Tian F, Wu Z, et al. Adsorption of naphthalene from aqueous solution on coal-based activated carbon modified by microwave induction: Microwave power effects [J]. *Chemical engineering and processing: Process intensification*, 2015, Vol.91:67-77.
- [239] Wan D, Wang G, Pu H, et al. Can nonspecific host-guest interaction lead to highly specific encapsulation by a supramolecular nanocapsule? [J]. *Macromolecules*, 2009, Vol.42(17): 6448-6456.
- [240] Zhou Y, Wang L, Ye Z, et al. Mango core inner shell membrane template-directed synthesis of porous ZnO films and their application for enzymatic glucose biosensor [J]. *Applied surface science*, 2013, Vol.285: 344-349.
- [241] Zhao L, Wu C, Liu Z, et al. Highly porous PVDF hollow fiber membranes for VMD application by applying a simultaneous co-extrusion spinning process [J]. *Journal of membrane science*, 2016, Vol.505:82-91.
- [242] Ye Y, Wan D, Du J, et al. Dendritic amphiphile mediated porous monolith for eliminating organic micropollutants from water [J]. *Journal of materials chemistry A*, 2015, Vol.3(12): 6297-6300.
- [243] Srinivasan A, Viraraghavan T. Decolorization of dye wastewaters by biosorbents: a review [J]. *Journal of environmental management*, 2010, Vol.91(10): 1915-1929.
- [244] Zawadzki M, Wrzyszczyński J. Hydrothermal synthesis of nanoporous zinc aluminate with high surface area [J]. *Materials research bulletin*, 2000, Vol.35(1): 109-114.
- [245] Li Y J, Ni X Y, Shen J, et al. Nitric acid activated carbon aerogels for supercapacitors [J]. *Applied mechanics and materials*, 2013, Vol.302:158-164.
- [246] Messina F, Icardi M, Marchisio D, et al. Microscale simulation of nanoparticles transport in porous media for groundwater remediation [C]. *The COMSOL conference in Milan*, 2012.
- [247] Talbot J, Tarjus G, Van Tassel P R, et al. From car parking to protein adsorption an overview of sequential adsorption processes [J]. *Colloids and surfaces A: Physicochemical and engineering aspects*, 2000, Vol.165(1): 287-324.
- [248] Chauveteau G, Nabzar L, Coste J P. Physics and modeling of permeability damage induced by particle deposition [C]. *SPE formation damage control conference*. Society of petroleum engineers, 1998. Vol.SPE 39463:409-419.
- [249] Nabzar L, Chauveteau G, Roque C. A new model for formation damage by particle retention [C]. *SPE formation damage control symposium society of petroleum engineers*, 1996.
- [250] Tosco T, Bosch J, Meckenstock R U, et al. Transport of ferrihydrite nanoparticles in saturated porous media: role of ionic strength and flow rate [J]. *Environmental science & technology*, 2012, Vol.46(7): 4008-4015.
- [251] Ngene I S, Lammertink R G H, Wessling M, et al. A microfluidic membrane chip for in situ fouling characterization [J]. *Journal of membrane science*, 2010, Vol.346(1): 202-207.
- [252] Asgharian B, Price O T, Hofmann W. Prediction of particle deposition in the human lung using realistic models of lung ventilation [J]. *Journal of aerosol science*, 2006, Vol.37(10): 1209-1221.

- [253] Bensaid S, Marchisio D L, Fino D. Numerical simulation of soot filtration and combustion within diesel particulate filters [J]. *Chemical engineering science*, 2010, Vol.65(1): 357-363.
- [254] Bradford S A, Simunek J, Bettahar M, et al. Modeling colloid attachment, straining, and exclusion in saturated porous media [J]. *Environmental science & technology*, 2003, Vol.37(10): 2242-2250.
- [255] Chatterjee R. Transport and deposition of particles onto homogeneous and chemically heterogeneous porous media geometries [D]. University of Alberta, 2011.
- [256] Feder J. Random sequential adsorption [J]. *Journal of theoretical biology*, 1980, Vol.87(2): 237-254.
- [257] Adamczyk Z, Nattich M, Barbasz J. Deposition of colloid particles at heterogeneous and patterned surfaces [J]. *Advances in colloid and interface science*, 2009, Vol.147-148(2-17).
- [258] Djehiche A, Gafsi M, Canseco V, et al. Effet de la force ionique et hydrodynamique sur le dépôt de particules colloïdales dans un milieu poreux consolidé [J]. *The Canadian journal of chemical engineering*, 2015, Vol.93(4): 781-787.
- [259] Gharbi D, Bertin H, Omari A. Use of a gamma ray attenuation technique to study colloid deposition in porous media [J]. *Experiments in Fluids*, 2004, Vol.37(5): 665-672.
- [260] Baumann T, Werth C J. Visualization of colloid transport through heterogeneous porous media using magnetic resonance imaging [J]. *Colloids and surfaces A: Physicochemical and engineering aspects*, 2005, Vol.265(1-3): 2-10.
- [261] May R, Li Y. The effects of particle size on the deposition of fluorescent nanoparticles in porous media: Direct observation using laser scanning cytometry [J]. *Colloids and surfaces A: Physicochemical and engineering aspects*, 2013, Vol.418:84-91.
- [262] Klauth P, Bauer R, Ralfs C, et al. Fluorescence macrophotography as a tool to visualise and quantify spatial distribution of deposited colloid tracers in porous media [J]. *Colloids and surfaces A: Physicochemical and engineering aspects*, 2007, Vol.306(1-3): 118-125.
- [263] Johnson W P, Pazmino E, Ma H. Direct observations of colloid retention in granular media in the presence of energy barriers, and implications for inferred mechanisms from indirect observations [J]. *Water research*, 2010, Vol.44(4): 1158-1169.
- [264] Gao H, Qiu C Q, Fan D, et al. Three-dimensional microscale flow simulation and colloid transport modeling in saturated soil porous media [J]. *Computers & mathematics with applications*, 2010, Vol.59(7): 2271-2289.
- [265] Malvault G, Omari A, Ahmadi A. Numerical simulation of yield stress fluids flow in capillaries bundle: Influence of the form and the axial variation of the cross-section [J]. *Journal of colloid and interface science*, 2016.
- [266] Díaz J J D C, Nieto P J G, Castro-Fresno D, et al. Steady state numerical simulation of the particle collection efficiency of a new urban sustainable gravity settler using design of experiments by FVM [J]. *Applied mathematics and computation*, 2011, Vol.217(21): 8166-8178.
- [267] Wirner F. Flow and transport of colloidal suspensions in porous media [D]. Physikalisches Institut der Universi at Stuttgart, 2015.
- [268] Dieter U. Pseudo-random numbers: The exact distribution of Pairs [J]. *Mathematics of computation*, 1971, Vol.25(116): 855-883.
- [269] Adamczyk Z, Siwek B, Szyk L. Flow-induced surface blocking effects in adsorption of colloid particles [J]. *Journal of colloid and interface science*, 1995, Vol.174(1): 130-141.

- [270] Ko C H, Bhattacharjee S, Elimelech M. Coupled influence of colloidal and hydrodynamic Interactions on the RSA dynamic blocking function for particle deposition onto packed spherical collectors [J]. *Journal of colloid and interface science*, 2000, Vol.229(2): 554-567.
- [271] Talbot J, Tarjus G, Van Tassel P R, et al. From car parking to protein adsorption an overview of sequential adsorption processes [J]. *Colloids and surfaces A: Physicochemical and engineering aspects*, 2000, Vol.165(1): 287-324.
- [272] Djehiche A, Canseco V, Omari A, et al. Étude expérimentale du dépôt de particules colloïdales en milieu poreux : Influence de l'hydrodynamique et de la salinité [J]. *Comptes rendus mécanique*, 2009, Vol.337(9-10): 682-692.
- [273] Ko C H, Elimelech M. The “shadow effect” in colloid transport and deposition dynamics in granular porous media-Measurements and mechanisms [J]. *Environmental science & technology*, 2000, Vol.34(17): 3681-3689.
- [274] Veerapen J P, Nicot B, Chauveteau G A. In-depth permeability damage by particle deposition at high flow rates [J]. *Society of petroleum engineers*, 2001, Vol. SPE 68962.
- [275] V.Levich. *Physicochemical hydrodynamics* [M]. Prentice-Hall, Englewood Cliffs, New Jersey, 1962.
- [276] Li Y J, Sarishvili O, Omari A, et al. Colloidal particle deposition in porous media under flow: A numerical approach [J]. *International journal of modeling and optimization*, 2017, Vol.7(1): 43-47
- [277] Salehi N. *Mecanismes de retention hydrodynamique de suspension colloïdales en milieux poreux modeles* [D]. Doctoral dissertation, UNIVERSITÉ PARIS, 1996,
- [278] Adamczyk Z, Weroński P, Musiał E. Irreversible adsorption of hard spheres at random site (heterogeneous) surfaces [J]. *The journal of chemical physics*, 2002, Vol.116(11): 4665-4672.
- [279] Adamczyk Z, Weroński P, Musiał E. Colloid particle adsorption at random site (heterogeneous) surfaces. *Journal of colloid and interface science* [J]. *Journal of colloid and interface science*, 2002, Vol.248(1): 67-75.
- [280] Nazemifard N, Masliyah J H, Bhattacharjee S. Particle deposition onto charge heterogeneous surfaces: convection-diffusion-migration model [J]. *Langmuir: the ACS journal of surfaces and colloids*, 2006, Vol.22(24): 9879-9893.

## Nomenclature

Abbreviation	Definition	Units
3D-PTPO	three-dimensional particle tracking model by Python <sup>®</sup> and OpenFOAM <sup>®</sup> code	
Pe	Péclet number	
PP	polypropylene	
PE	polyethylene	
LIB	lithium-ion battery	
MC	multilayer coextrusion	
CTM	CaCO <sub>3</sub> template method	
TIPS	thermal induced phase separation	
MC-CTM PP/PE	PP/PE separators prepared by multilayer coextrusion and CaCO <sub>3</sub> template method	
MC-TIPS PP/PE	PP/PE separators prepared by multilayer coextrusion and thermal induced phase separation	
PS	polystyrene	
RSA	random sequential adsorption	
$\Gamma/\Gamma_{\text{RSA}}$	dimensionless surface coverage	
$\lambda$	the frequency of the pitches	
$\theta$	the reactive area fraction	%
CFD	computational fluid dynamics	
IUPAC	the International Union of Pure and Applied Chemistry	
NIPS	nonsolvent-induced phase separation	
VIPS	vapor induced phase separation	
EIPS	solvent evaporation-induced phase separation	
PVDF	poly(vinylidene fluoride)	
CA	cellulose acetate	
CAB	cellulose acetate butyrate	
PAN	polyacrylonitrile	
HIPE	high internal phase emulsion	
BCP	block copolymer	

BFs	breath figures method	
PAHs	polycyclic aromatic hydrocarbons	
WHO	World Health Organization	
EEA	European Environmental Agency	
BTC	breakthrough curves	
$\eta$	collection efficiency	
$D$	diffusion coefficient	$\text{m}^2 \text{s}^{-1}$
$k_B$	Boltzmann constant	$\text{J K}^{-1}$
$T$	absolute temperature	$\text{K}$
$a_p$	particle radius	$\text{m}$
$\mu$	dynamic viscosity	$\text{Pa s}$
VDW	van der Waals attraction	
EDL	electrical double-layer interaction	
ADS	advection dispersion-sorption	
$\xi$	the surface-to-surface separation	
$\mathbf{d}$	the unit vector in the radial direction	
$I$	the overall rate at which particles strike the collector	
$a_c$	the radius of the collector	
$U$	the approach velocity of the fluid	
$C_0$	the number concentration of particles in the fluid approaching the collector	
$A_s$	Happel's flow parameter	
$s$	adsorbed mass per unit mass of the solid phase	
$c$	free particle mass concentration	
$v_D$	Darcy velocity	$\text{m s}^{-1}$
$\varepsilon$	porosity	$\%$
$\rho_b$	dry bulk density of the porous medium	$\text{kg m}^{-3}$
$R_w$	the decay or inactivation rates for particles in the liquid phase	
$R_s$	the decay or inactivation rates for particles in the solid phase	
$k_a$	the first order kinetic attachment rates	
$k_d$	the first order kinetic detachment rates	
$L_s$	the hydrodynamic shadowing length	
CFT	classical filtration theory	
GSD	grain size distribution	

ENP	engineered nano particles	
PM	porous media	
HELP-1D	one-dimensional hybrid Eulerian-Lagrangian particle	
MNM1D	micro-and nanoparticle transport model in porous media	
MNM3D	micro and nanoparticle transport model in 3D geometries	
RIGID	spherical particle and geometry interaction detection	
LBM	lattice boltzmann method	
REV	representative elementary volume	
GB	glass beads	
IS	ionic strength	
E	Young's modulus	
REA	representative elementary area	
$T_A$	resisting torque	
$S_f^*$	colloid immobilization	
$P_+$	the amount of chemical heterogeneity	
MWCNTs	multi-walled carbon nano tubes	
QS	quartz sand	
GQS	goethite coated quartz sand	
NP	nano particles	
GSI	grid surface integration	
PDFs	probability density functions	
LOC	Lab-On-Chip	
FAA	Federal Aviation Administration	
TGA	thermal gravimetric analysis	
FESEM	field emission scanning electron microscopy	
DSC	differential scanning calorimetry	
FTIR	Fourier Transform infrared spectroscopy	
EU	electrolyte uptake	%
ER	electrolyte retention	%
W	the weight of n-butanol soaked membrane	g
$W_0$	the weight of dry membrane	g
$W_b$	the weight of membranes before soaking in the electrolyte	g
$W_a$	the weight of membranes after soaking in the electrolyte	g

$\rho_L$	density of n-butanol	$\text{g cm}^{-3}$
$V_0$	the geometric volume of the membranes	$\text{cm}^3$
$S_0$	area of the membrane before thermal treatment	$\text{cm}^2$
$S$	area of the membrane after thermal treatment	$\text{cm}^2$
EIS	electrochemical impedance spectroscopy	
SS	stainless steel electrodes	
$\sigma$	ionic conductivity	$\text{mS cm}^{-1}$
$R_b$	bulk impedance	ohm
$D$	thickness of separators	cm
$A$	the contact area between the separator and electrodes	$\text{cm}^2$
LSV	liner sweep voltammetry	
$\sigma_0$	pre-exponential factor	
$E_a$	activation energy	$\text{kJ mol}^{-1}$
$t^+$	lithium ion transference number	
LM	lithium metal	
LDPE	low density polyethylene	
LME	laminating-multiplying elements	
$Q_{eq}$	the amount of pyrene adsorbed at equilibrium state	$\text{mg g}^{-1}$
$Q_t$	the amount of pyrene adsorbed at time $t$	$\text{mg g}^{-1}$
$k_1$	pseudo-first-order rate constant	
$K_F$	Freundlich constant	
$C_{eq}$	the equilibrium concentration of pyrene in the solution	$\text{mg L}^{-1}$
$b_F$	constant depicting the adsorption intensity	
$Q_{max}$	the maximum capacity of the adsorbent	$\text{mg g}^{-1}$
$K_L$	the Langmuir adsorption constant	$\text{L mg}^{-1}$
$\lambda_r$	the particle size ratio (the averaged size of the latex versus the size of the particle)	
$V_{int}$	the interpolated convection velocity	$\text{m s}^{-1}$
$V_{diff}$	the Brownian diffusion velocity	$\text{m s}^{-1}$
$t_r$	referential time	s
$Z$	characteristic mesh size	m
$u_{max}$	the maximum of actual velocity along the mean flow axis	$\text{m s}^{-1}$
$a_p$	particle diameter	m

L	pipe length	m
R	pipe radius	m
$\Delta p$	pressure drop	Pa
$\bar{u}$	the average convection velocity along the mean flow axis	$\text{m s}^{-1}$
$\Gamma$	surface coverage	$\text{m}^2$
$R_k$	the ratio of the permeability before and after deposition	
K	permeability before deposition	$\text{m}^2$
$K_\Gamma$	permeability after deposition	$\text{m}^2$
$\delta$	the hydrodynamic thickness of deposited layer	m
$R_B$	the pore body radius	m
$R_T$	the pore throat radius	m
Re	Reynolds number	
$\rho$	the fluid density	$\text{kg m}^{-3}$
p	pressure	Pa
v	flow velocity	$\text{m s}^{-1}$
OpenFOAM <sup>®</sup>	Open Field Operation and Manipulation	
a, b and c	random numbers between -1 and 1	
$\alpha, \beta$ and $\gamma$	the normalization of three random numbers	
N	the number of injected particles	
$A_f$	the area of the surface wall favoring deposition	$\text{m}^2$
$A_t$	the total surface area of the capillary wall	$\text{m}^2$
n	the number of deposited particles	
$S_{\text{particle}}$	the projection area of one deposited particle	$\text{m}^2$
$S_{\text{attractive}}$	the total surface area of the attractive regions	$\text{m}^2$
$S_{\text{extend}}$	the extended surface areas of every attractive region	$\text{m}^2$
$\eta_{\text{effective}}$	the overall deposition efficiency	%
$\eta_f$	the deposition efficiencies for completely favorable regions	%
$\eta_u$	the deposition efficiencies for completely unfavorable regions	%

## Résumé

Le polymère poreux (PM) associe les avantages des matériaux poreux et des polymères, ayant une structure unique de pore, de grande porosité et de densité faible, ce qui lui confère un potentiel d'application important dans les domaines de l'adsorption, les supports de catalyseur, le séparateur de batterie, la filtration, etc. Actuellement, il existe plusieurs façons de préparer le PM, comme la méthode de gabarit, la méthode de séparation de phase, la méthode d'imagerie respiratoire, etc. Chacune des méthodes ci-dessus a ses propres avantages, mais la préparation à grande échelle de PM à structure de pore contrôlable et aux fonctions spécifiques est toujours un objectif à long terme sur le domaine et constitue l'un des principaux objectifs de ce mémoire. La co-extrusion de microcouches est une méthode pour produire de façon efficace et répétable des polymères avec des structures de couches alternées, ayant les avantages de haute efficacité et faible coût. Par conséquent, vues les exigences structurelles de PM de l'application spécifique dans cette étude, le PM est conçu avec une structure spécifique et une co-extrusion de microcouches de manière novatrice combinée avec la méthode traditionnelle de préparation de PM (méthode de gabarit, méthode de séparation de phase). En combinant les avantages des deux méthodes, les PM avec une structure de pore idéale peuvent être préparés en grande quantité et l'on peut également explorer son application dans les séparateurs de batteries lithium-ion et l'adsorption d'hydrocarbures aromatiques polycycliques.

Dans la deuxième partie de ce mémoire on s'intéresse à la simulation numérique pour étudier le transport et le dépôt de micro-particules dans des milieux poreux pour explorer le mécanisme des matériaux poreux dans les domaines de l'adsorption et du séparateur de batterie. Le code de 3D-PTPO (un modèle tridimensionnel de suivi des particules combinant Python<sup>®</sup> et OpenFOAM<sup>®</sup>) est utilisé pour étudier le transport et le dépôt de particules colloïdales dans des milieux poreux. Trois modèles de pores (colonne, venturi et tube conique) pour représenter différentes formes de matériaux poreux ont été considérés. Les particules sont considérées comme des points matériels pendant le transport, le volume des particules sera reconstitué dès que la particule est déposée à la surface du matériau poreux, la caractéristique principale de ce code est de considérer l'influence du volume des particules déposées sur la structure des pores, les lignes d'écoulement et le processus du dépôt des autres particules. Les simulations numériques sont d'abord conduites dans des capillaires simples, le

travail de Lopez et al. (2004) est réexaminé en établissant un modèle géométrique tridimensionnel plus réaliste et il explore les mécanismes gouvernant le transport et le dépôt. Par la suite, des simulations numériques sont effectuées dans des capillaires convergents-divergents pour étudier la structure des pores et l'effet de nombre Peclet sur le dépôt de particules. Enfin, l'on étudie l'effet double de l'hétérogénéité de surface et de l'hydrodynamique sur le comportement de dépôt de particules.

Le travail de recherche principal de cette thèse est le suivant :

- 1) Par la méthode de co-extrusion de microcouche, (MC) combinée à la méthode du modèle (CTM), on prépare efficacement et en continu la couche mince (MC-CTM PP) de polypropylène (PP) / polyéthylène (PE) avec une structure multicouche, pour son application dans le séparateur de batterie lithium-ion. Le résultat nous montre que le séparateur a une structure poreuse submicronique sphérique riche. Comparé au diaphragme multicouche commercial Celgard<sup>®</sup> 2325, le MC-CTM PP / PE présente une porosité, une absorption et une rétention de liquide plus élevées, ce qui améliore la conductivité ionique et les performances de la batterie. De plus, cette membrane possède une performance thermique efficace avec une fenêtre de sécurité allant de 127 °C à 165 °C, plus large qu'un diaphragme commercial. Il maintient toujours l'intégrité de la membrane lorsque la température est élevée à 160 °C, ce qui surmonte les inconvénients d'un retrait thermique grave causé par l'étirement de la membrane commerciale pendant le processus de production et présente une excellente stabilité thermique et une performance de sécurité supérieure.
- 2) Par la méthode de MC combinée à une séparation de phase induite thermiquement (TIPS), le séparateur multicouche de batterie au lithium-ion PP / PE (MC-TIPS PP / PE) avec une structure de pores submicroniques de type cellulaire est fabriqué de manière efficace et en continu. Le résultat montre que cette membrane possède non seulement une fonction de limitation thermique efficace et une fenêtre de sécurité plus large, mais aussi une stabilité thermique supérieure à celle des membranes commerciales. À mesure que la température s'élève à 160 °C, le retrait

dimensionnel reste encore négligeable. De plus, MC-TIPS PP / PE possède une porosité (54.6%) et une absorption de liquide (157%) plus élevées, ce qui favorise l'amélioration de la conductivité ionique ( $1.46 \text{ mS cm}^{-1}$ ) et des performances de la batterie.

- 3) Par la méthode de combinaison de MC et de CTM, nous réalisons des couches minces de polystyrène poreux (PS) et étudions l'influence du type d'empreinte (gravure), de la teneur en  $\text{CaCO}_3$  et de l'épaisseur de membrane sur l'effet de gravure. En prenant comme exemple le pyrène représentatif des hydrocarbures aromatiques polycycliques, on recherche la performance d'adsorption de pyrène des membranes de PS poreux. Le résultat montre que les membranes de PS poreux d'une porosité supérieure ont une capacité d'adsorption de pyrène plus élevée que ceux de PS d'une porosité inférieure, ce qui est due à la compatibilité entre la structure poreuse riche en membrane et l'adsorption interstitielle des adsorbants. On apprend également que la cinétique d'adsorption et de l'isotherme sorption-désorption sont en accord avec l'équation cinétique d'ordre 2 et le modèle isotherme de Freundlich respectivement.
- 4) Le procédé de suivi Lagrangien des particules est adopté et le code 3D-PTPO utilisé pour simuler le transport et le dépôt de particules colloïdales dans des milieux poreux simples (capillaires à section transversale circulaire). En résolvant l'équation de Stokes et l'équation de continuité, l'on obtient la vitesse d'écoulement des particules à laquelle est ajouté la vitesse de diffusion des particules. Les particules se déposent lorsqu'elles s'approchent de la paroi des pores. Le résultat indique que la probabilité de dépôt et le taux de couverture de surface,  $\theta$ , diminuent avec l'augmentation du nombre de Péclet,  $Pe$ . Lorsque  $Pe$  est bas, le champ d'écoulement est dominé par la diffusion et la couverture de surface est proche de la valeur limite,  $\theta_{RSA}$  (RSA : Random Sequential Adsorption), alors que pour  $Pe$  élevé le champ d'écoulement est dominé par la convection et la couverture de surface diminue fortement.
- 5) Ensuite on s'est intéressé à la simulation numérique du transport et du dépôt de particules colloïdales dans des milieux poreux convergents-divergents (tubes venturi et tubes coniques) avec le code 3D-PTPO amélioré et étudié l'effet du nombre de  $Pe$  des particules et la structure

des pores sur le dépôt des particules. Le résultat montre que dans la zone dominée par la convection, la probabilité de dépôt et le taux de couverture de surface présentent un plateau faible et la distribution des particules déposées est uniforme. Dans la zone dominée par la diffusion, la probabilité de dépôt et le taux de couverture sont fonctions du nombre de Pe, et la distribution des particules sédimentaires montre une forme de piston à très bas Pe. De plus, pour les tubes de venturi, la densité des particules de dépôt à proximité de l'entrée et de la sortie de la gorge est inférieure en raison du changement de lignes de courant. Lorsque Pe est élevé, le taux de couverture de surface anormalisé maximal  $\Gamma_{\text{final}}/\Gamma_{\text{RSA}}$  est en accord avec les résultats numériques et expérimentaux de la littérature avec la tendance à la baisse en  $Pe^{-1/3}$ .

- 6) On simule dans cette partie le transport et le dépôt de particules colloïdales dans des milieux poreux de surface hétérogène avec le code 3D-PTPO amélioré et étudie l'effet conjoint de l'hétérogénéité de surface et de l'hydrodynamique sur le transport et le dépôt des particules. Les milieux poreux sont représentés par des capillaires tridimensionnels à hétérogénéité structurale périodique (en forme de raie et damier). On explore la relation entre la probabilité de dépôt,  $\Gamma/\Gamma_{\text{RSA}}$  et la période des hétérogénéités ( $\lambda$ ), Pe et le rapport de la zone attractive par rapport à la surface totale ( $\theta$ ). Le résultat montre que les particules colloïdales ont tendance à se déposer aux extrémités de la bande attractive, et que la distribution de dépôt des particules est plus uniforme que la situation de l'homogénéité de surface. De plus, dans le cas du même  $\theta$ , la probabilité de dépôt est positivement corrélée avec  $\lambda$ . La probabilité totale de dépôt augmente avec  $\theta$ , ce qui est cohérent avec la règle du mode d'hétérogénéité en « patch ».

L'introduction détaillée et le travail de recherche sont les suivants :

## **Chapitre 1 & Chapitre 2** Introduction générale et revue de la littérature

Les matériaux peuvent être divisés en matériaux denses et en matériaux poreux en fonction de leur densité. L'étude des matériaux poreux est une branche importante de la science des matériaux,

qui joue un rôle important dans notre recherche scientifique et notre production industrielle. Chaque milieu poreux est typiquement composé d'un squelette solide et d'un espace vide, généralement rempli d'au moins un type de fluide (liquide ou gazeux). Il existe de nombreux exemples de matériaux naturels (bambou creux, nid d'abeilles et alvéoles dans les poumons) et poreux artificiels (polymère macroporeux, aluminium poreux et silice poreuse). Le milieu poreux polymérique est l'un des composants les plus importants des matériaux poreux organiques, ce qui est l'objet principal de cette thèse. Le milieu poreux polymérique (polymère poreux) présente les avantages combinés des matériaux poreux et des matériaux polymères. Il possède une porosité élevée, une structure microporeuse abondante et une faible densité. Les diverses méthodes de préparation, la structure des pores contrôlable et les propriétés de surface facilement modifiées font du support poreux polymérique des matériaux prometteurs dans un large éventail de domaines d'application : adsorption, séparateur de batterie, filtre, stockage d'énergie, catalyseur et science biomédicale. Par conséquent, il est très intéressant d'étudier la nouvelle fonction des milieux poreux polymères et de développer une nouvelle méthode de préparation pour ce matériau largement utilisé.

Avant la préparation et la réalisation, les fonctions et les structures des milieux poreux polymériques doivent être conçues. L'aspect le plus important à considérer est les principales fonctions que nous aimerions réaliser dans les milieux, qui conduisent à des propriétés d'application spécifiques. Deuxièmement, nous devons déterminer les facteurs clés qui sont directement liés à la fonction désirée, tels que la géométrie des pores, la taille des pores et la porosité de la matrice des matériaux. Troisièmement, sur la base des considérations ci-dessus, le schéma expérimental doit être conçu pour préparer les milieux poreux polymères. Bien que diverses méthodes de préparation existent, telles que la technique de gabarit, la méthode d'émulsion, la méthode de séparation de phase, le procédé de moussage, l'électrofilage, les techniques lithographiques descendantes, la méthode de respiration, etc., la préparation à grande échelle de milieux poreux polymériques à fonctions spécifiées est toujours un objectif à long terme dans ce domaine, qui est l'un des objectifs fondamentaux de cette thèse. Une nouvelle approche, la coextrusion multicouche à assemblage forcé a été utilisée pour produire économiquement et efficacement des polymères de multicouches avec une épaisseur de couche individuelle variant d'un micron au nanomètre. Cette technique de traitement de polymère avancée présente de nombreux avantages, y compris un procédé continu, une

voie économique pour la fabrication à grande échelle, la flexibilité des espèces de polymères et la capacité à produire des structures de couches compatibles. Par conséquent, dans la partie I de cette thèse, les milieux poreux polymères sont conçus sur la base des exigences d'application spécifiques et préparés par la combinaison de la coextrusion multicouche et des méthodes de préparation traditionnelles (technique de gabarit, méthode de séparation de phase). Cette approche combine les avantages de la coextrusion multicouche et de la méthode de séparation modèle / phase (procédé de préparation simple et structure de pore compatible). Ensuite, les applications des milieux poreux polymériques dans l'adsorption des PAH et le séparateur de batteries au lithium-ion ont été étudiées.

Plus important encore, le mécanisme de base des procédés d'application ci-dessus (procédé d'adsorption de PAH ou transport de lithium-ion à travers un séparateur) est basé sur le transport et le dépôt de particules dans des milieux poreux. Il est donc essentiel de bien comprendre les processus de transport et de dépôt des particules dans les milieux poreux ainsi que les mécanismes dominants impliqués. En outre, le transport et le dépôt de particules colloïdales dans des milieux poreux sont d'une grande importance pour d'autres applications techniques et industrielles, comme le transport de contaminants facilités par les particules, la purification de l'eau, le traitement des eaux usées ou la recharge artificielle des aquifères. Afin de comprendre les mécanismes de transport de particules colloïdales dans des milieux poreux, des simulations numériques de dynamique des fluides (CFD pour Computational Fluid Dynamics) ont été réalisées pour visualiser et analyser le champ d'écoulement. Prenant la filtration de l'eau à titre d'exemple, des techniques numériques pourraient être utilisées pour modéliser le transport et la dispersion des contaminants dans un fluide. Fondamentalement, il existe deux bases théoriques fondamentales pour étudier le transport de particules colloïdales dans des milieux poreux, classifiées comme méthodes eulériennes et lagrangiennes. La méthode eulérienne décrit ce qui se passe à un point fixe dans l'espace, tandis que la méthode lagrangienne implique un système de coordonnées se déplaçant avec le flux. Les géométries de pores sont souvent simplifiées en une ou deux dimensions pour réduire le temps des simulations numériques. Cependant, cette simplification limite le mouvement possible des particules et réduit la précision des résultats. Par conséquent, il est nécessaire d'améliorer le modèle de simulation pour permettre des simulations tridimensionnelles dans des géométries plus réalistes. De plus, le transport et le dépôt de particules dans des milieux poreux hétérogènes ont récemment fait

l'objet d'intenses recherches. Jusqu'à présent, il existe peu de travaux sur les effets combinés de l'hydrodynamique et de l'hétérogénéité de surface sur les dépôts de particules colloïdales dans les milieux poreux. Il est donc nécessaire de mieux comprendre les mécanismes responsables de ces phénomènes, ce qui est l'un des objectifs du présent travail.

L'objectif de la partie II de cette thèse est la simulation tridimensionnelle à l'échelle microscopique du transport et du dépôt de particules colloïdales dans des milieux poreux homogènes et hétérogènes au moyen d'outils CFD utilisant la méthode lagrangienne afin d'obtenir les quantités les plus pertinentes en capturant la physique sous-jacente au processus. Afin de réaliser la simulation, un nouveau modèle de suivi des particules colloïdales, à savoir le modèle 3D-PTPO (modèle de suivi des particules tridimensionnel par Python<sup>®</sup> et OpenFOAM<sup>®</sup>) utilisant la méthode lagrangienne, est développé dans la présente étude. Le contenu majeur de la partie II de cette thèse pourrait être résumé comme suit : premièrement, le comportement de dépôt de particules est étudié sur un capillaire homogène afin de revisiter le travail précédent de Lopez et al. (2004) en considérant une géométrie 3D plus réaliste. En effet, leur travail était limité à une géométrie particulière restreinte à une géométrie en forme de fente peu susceptible d'être rencontrée dans des milieux poreux réels. En outre, il est nécessaire de valider les propriétés de transport fondamentales pendant la simulation, car la partie validation initiale du développement du modèle (impliquant un dépôt sur des collecteurs homogènes) était importante pour les simulations suivantes de transport et de dépôt de particules dans les géométries de pores plus complexes. Deuxièmement, la modélisation numérique tridimensionnelle du processus de transport et de dépôt de particules dans une géométrie de pore plus complexe (tube de tube venturi) d'une section transversale circulaire est réalisé pour explorer l'influence de la géométrie des pores sur le champ d'écoulement comme sur les propriétés de transport et de dépôt des particules. Troisièmement, le modèle 3D-PTPO est amélioré en incorporant l'hétérogénéité chimique de surface. Les effets combinés de l'hétérogénéité de surface et de l'hydrodynamique sur le comportement de dépôt de particules sont étudiés.

**Chapitre 3** Préparations des séparateurs de batterie au lithium-ion polyéthylène / polyéthylène poreux multicouches par combinaison d'une méthode de coextrusion multicouche et d'une matrice

Les batteries au lithium-ion (LIB) ont été principalement utilisées dans l'électronique grand public portable en raison de leur densité d'énergie spécifique élevée, de leur longue durée de vie et de l'absence d'effet mémoire. De plus, les LIB sont également considérées comme l'une des sources d'énergie les plus prometteuses pour les véhicules électriques et les systèmes aérospatiaux. Cependant, des améliorations en matière de sécurité sont encore nécessaires de toute urgence pour l'acceptation complète des LIB dans ces nouveaux domaines d'application. La présence de l'électrolyte combustible ainsi que l'oxydant rendent les LIB sensibles aux incendies et aux explosions. Une fois que les LIB sont soumises à des conditions extrêmes telles qu'un court-circuit, une surcharge et un impact thermique à haute température, des réactions chimiques exothermiques sont déclenchées entre les électrodes et l'électrolyte, ce qui augmente la pression interne et la température de la batterie. L'augmentation de la température accélère ces réactions et libère de la chaleur rapidement grâce au dangereux mécanisme de réaction positive qui conduira à un emballement thermique, une fissuration des cellules, un incendie ou même une explosion. Pour prévenir les défaillances thermiques catastrophiques dans les LIB, de nombreuses stratégies comprenant des matériaux d'électrode thermosensibles, des électrodes à coefficient de température positif et une électrode d'arrêt thermique ont été proposées comme mécanisme de protection auto-activant pour empêcher les LIBs de s'échapper. Alors que les procédés ci-dessus impliquent souvent soit une synthèse de matériau difficile, soit un traitement d'électrode compliqué, ce qui les rend peu pratiques pour l'application de la batterie. En outre, les épaisseurs de revêtement des électrodes diminueraient la densité d'énergie des batteries et gêneraient leur utilisation pratique dans les batteries. Du point de vue de l'application industrielle, le séparateur à arrêt thermique est donc le moyen le plus attrayant pour la protection de sécurité des LIB car il peut surmonter les défauts ci-dessus.

Les séparateurs d'arrêt reposent sur un mécanisme de changement de phase pour limiter le transport ionique par la formation d'une couche imperméable aux ions entre les électrodes. Les séparateurs d'arrêt sont généralement constitués d'une bicouche polypropylène (PP) / polyéthylène (PE) ou d'une structure tricouche PP / PE / PP. Dans ce type de séparateurs stratifiés, le PE ayant le point de fusion le plus bas sert d'agent d'arrêt tandis que le PP ayant le point de fusion le plus élevé sert de support mécanique. Une fois que la température interne atteint le point de fusion du PE, la

couche de PE est ramollie et fondue pour fermer les pores internes et ainsi empêcher la conduction ionique et terminer la réaction électrochimique. La majorité des séparateurs bicouches ou tricouches commerciaux sont fabriqués en stratifiant différentes couches fonctionnelles ensemble par calandrage, adhérence ou soudage. Le procédé traditionnel de fabrication de tels séparateurs à deux ou trois couches comprend la procédure de fabrication de la couche de renforcement microporeuse et de la couche d'arrêt par le procédé d'airage, en reliant alternativement les couches microporeuses ci-dessus dans les membranes bicouches ou tricouches. Ensuite, les membranes à deux couches ou à trois couches ont été airées au séparateur de batterie à deux couches ou à trois couches avec l'épaisseur et la porosité requises. Le procédé ci-dessus peut produire des séparateurs multicouches avec une fonction d'arrêt thermique, et la plupart incluent le processus d'airage et améliorent évidemment la résistance mécanique des séparateurs. Néanmoins, le processus de production plutôt encombrant diminue nettement l'efficacité de la production. Plus important encore, ces séparateurs subiront un rétrécissement important à partir d'une gamme de température plutôt limitée, avec un début de rétrécissement autour de 100 °C en raison des contraintes résiduelles induites pendant le processus d'airage. Par conséquent, il est essentiel de trouver de nouvelles méthodes qui peuvent optimiser la stabilité thermique, la propriété d'arrêt et la performance électrochimique des séparateurs de polyoléfine sans sacrifier leur excellente structure microporeuse et à faible coût.

Dans ce chapitre, une nouvelle stratégie est proposée pour préparer des séparateurs LIB multicouches comprenant des couches alternées de couche de PP microporeuse et de couche de PE par coextrusion multicouche combinée avec la méthode du modèle  $\text{CaCO}_3$ . Cette approche combine les avantages de la coextrusion multicouche (processus continu, voie économique pour la fabrication à grande échelle et structures de couche accordables) et la méthode du gabarit (processus de préparation simple et structure de pore ajustable). Une amélioration clé de cette approche est que la structure poreuse est formée par la méthode du gabarit au lieu du processus d'airage, ce qui est bénéfique pour la stabilité thermique. Comparé aux séparateurs bicouches ou tricouches commerciaux, le retrait dimensionnel de ces membranes multicouches peut être réduit. Les séparateurs multicouches peuvent conserver leur intégrité et leur faible retrait thermique à haute température. Les séparateurs multicouches PP / PE présentent non seulement une fonction d'arrêt thermique efficace, mais présentent également des avantages significatifs d'une stabilité thermique

élevé jusqu'à 160 °C. La fonction d'arrêt thermique des membranes multicouches PP / PE peut être largement ajustée dans la plage de température de 127 °C à 165 °C, plus large que celle des séparateurs commerciaux (Celgard® 2325). Plus important encore, cette approche est très pratique et efficace, évite les processus bicouches traditionnels ou tricouches lourds au cours du processus de production. De plus, cette méthode est applicable à tout polymère pouvant être traité à l'état fondu en plus du PP et du PE.

**Chapitre 4** Préparation de séparateurs de batterie au lithium-ion poreux multicouches par combinaison d'une coextrusion multicouche et d'une séparation de phases induite thermiquement

La coextrusion multicouche (MC) représente une technique de traitement de polymère avancée capable de produire de façon économique et continue des matériaux multicouches. La séparation de phase induite thermiquement (TIPS) est un procédé de fabrication largement utilisé pour les séparateurs LIB commerciaux, qui repose sur la règle selon laquelle un polymère est miscible avec un diluant à haute température, mais démiscible à basse température. Les séparateurs préparés par le procédé TIPS montrent une structure de pores bien contrôlée et uniforme, une porosité élevée et une bonne «modifiabilité». À notre connaissance, aucune étude n'a été rapportée sur la combinaison des deux méthodes ci-dessus pour préparer des séparateurs poreux multicouches. Ainsi, dans le présent chapitre, une nouvelle stratégie est proposée pour préparer les séparateurs multicouches LIBs comprenant des couches alternées de couches PP et PE microporeuses via la combinaison de la coextrusion multicouche et de la méthode TIPS, visant à combiner les avantages des deux méthodes. En outre, dans ce chapitre, les TIPS se composent d'un système binaire, comprenant un polymère (PP ou PE), un diluant (paraffine) et donc un seul agent d'extraction (éther de pétrole). Par conséquent, l'agent d'extraction est recyclable et offre une reproductibilité plus élevée, ce qui est d'une importance critique pour la réduction des coûts et la protection de l'environnement. Un autre avantage clé de cette méthode est que la voie en une étape fournit un moyen plus efficace pour la fabrication à grande échelle de séparateurs multicouches à porosité élevée. Plus significativement, la structure poreuse est formée sans processus d'étalement traditionnel, ce qui favorise la thermostabilité dimensionnelle. Le séparateur résultant possède une structure poreuse de qualité cellulaire et

submicronique avec une porosité de 54,6%. Le plus important est que ce séparateur offre une amélioration substantielle de la stabilité thermique par rapport au séparateur commercial, fournit une fenêtre de température d'arrêt plus large (129-165 °C) et un rétrécissement dimensionnel négligeable (jusqu'à 160 °C). De plus, le séparateur tel que préparé présente une conductivité ionique plus élevée, un plus grand nombre de transferts d'ions lithium et une meilleure performance de la batterie. Compte tenu des caractéristiques attrayantes mentionnées ci-dessus et du processus de préparation à grande échelle, ce séparateur est considéré comme très prometteur pour l'application dans des batteries lithium-ion à haute sécurité.

## **Chapitre 5** Préparation de membranes de polystyrène poreux par coextrusion multicouche et performance d'adsorption d'hydrocarbures aromatiques polycycliques

En tant que classe omniprésente de composés organiques constitués de deux ou plusieurs cycles benzéniques condensés et / ou de molécules pentacycliques, des hydrocarbures aromatiques polycycliques (PAH) ont été identifiés dans diverses eaux et eaux usées. Les propriétés toxiques, mutagènes et cancérigènes potentielles des PAH ainsi que leur capacité à s'accumuler dans les organismes aquatiques rendent urgente la réduction du taux de dans l'environnement aqueux. Un certain nombre de techniques d'assainissement efficaces de l'environnement aqueux contenant des PAH ont été étudiées, y compris des processus physiques, biologiques et de phytoremédiation, alors que la plupart de ces méthodes présentent des inconvénients tels que des coûts d'investissement initiaux élevés et des coûts d'entretien élevés. Parmi les diverses méthodes, l'adsorption s'avère être une technique prometteuse en raison de sa simplicité de conception et de fonctionnement, de son rendement élevé de ses faibles coûts d'investissement et de maintenance et de la non-formation de produits secondaires indésirables. Au cours des dernières décennies, de nombreux matériaux ont été rapportés pour adsorber les PAH dans l'environnement aqueux, y compris les zéolites, les argiles, les résidus végétaux et le charbon actif, alors que la plupart des matériaux ci-dessus sont moins efficaces pour détecter les PAH dans l'eau. Certains adsorbants à l'échelle micro ou nanométrique se sont avérés efficaces pour capturer les traces d'eau polluantes, mais leur taille est trop petite pour être séparée de l'eau. Il est donc essentiel de proposer de nouveaux matériaux capables d'adsorber les

traces de PAH et de les séparer facilement de l'eau. De plus, la méthode d'adsorption est particulièrement intéressante lorsque l'adsorbant est bon marché et peut être produit en masse. Selon le principe similaire compatible, les adsorbants à cycle aromatique sont des matériaux comparativement appropriés pour l'adsorption des PAH. On trouve dans la littérature que les matériaux en vrac poreux en polystyrène (PS) par polymérisation en émulsion à phase interne développée sont de bons candidats pour traiter la contamination des PAH dans l'eau. Parmi les matériaux d'adsorption poreux, les membranes poreuses sont préférables aux matériaux en vrac et en poudre puisqu'ils possèdent une surface de contact plus élevée avec l'eau et sont beaucoup plus faciles à séparer des eaux usées. Dans ce chapitre, une nouvelle stratégie est proposée pour préparer des membranes PS poreuses avec une structure poreuse accordable par coextrusion multicouche combinée à la méthode du gabarit, qui est une voie très efficace pour la fabrication à grande échelle de membranes PS poreuses. Pyrène, un PAH représentatif avec un poids moléculaire moyen et une solubilité modérée dans l'eau, est choisi comme composé modèle pour explorer les performances d'adsorption des membranes PS poreuses sur les PAH. La cinétique d'adsorption associée et les isothermes du PS poreux sont également discutés. Une série de tests de contrôle ont été conçus pour explorer les facteurs clés qui peuvent réguler et contrôler les structures poreuses. Les résultats indiquent que les membranes préparées avec la teneur en  $\text{CaCO}_3$  de 40% en poids, une épaisseur de 5  $\mu\text{m}$ , et gravées pendant 48 h possèdent la structure optimale des pores ouverts. En outre, l'espace confiné créé par les LME dans la coextrusion multicouche joue un rôle important dans la dispersion des particules de  $\text{CaCO}_3$  et, par conséquent, est bénéfique pour la formation de membranes poreuses homogènes par attaque acide. Les membranes PS poreuses avec une porosité plus élevée présentent des performances d'adsorption beaucoup plus élevées sur le pyrène dans une solution aqueuse diluée, par rapport à celle adsorbée par des membranes PS avec une porosité inférieure. Ceci est attribué à la structure abondante des pores de la membrane et au principe similaire compatible entre la surface de la membrane et les adsorbats. La cinétique d'adsorption et l'isotherme des membranes PS poreuses se sont révélés suivre une cinétique de pseudo-deuxième ordre et un modèle isotherme de Freundlich, respectivement.

## Chapitre 6 Le dépôt de particules colloïdales dans un milieu poreux idéalisé comme un faisceau de capillaires

Les processus de transport et de dépôt de particules dans des milieux poreux présentent un grand intérêt technologique et industriel, car ils sont utiles dans de nombreuses applications d'ingénierie, notamment la dissémination des contaminants, la filtration, la séparation chromatographique et les processus de remédiation. Pour caractériser ces processus, les simulations numériques sont devenues de plus en plus attrayantes en raison de la croissance de la capacité informatique et des moyens de calcul offrant une alternative intéressante, notamment aux expériences complexes in situ. Fondamentalement, il existe deux types de méthodes de simulation, à savoir les simulations à l'échelle macro et les simulations à l'échelle microscopique (à l'échelle des pores). Les simulations à l'échelle macro décrivent le comportement global du processus de transport et de dépôt en résolvant un ensemble d'équations différentielles qui donne une variation spatiale et temporelle de la concentration des particules dans l'échantillon poreux sans fournir d'informations sur la nature ou le mécanisme du processus de rétention. Des simulations numériques à l'échelle de pore résolvent directement l'équation de Navier-Stokes ou de Stokes pour calculer le flux et les processus de diffusion de particules par un modèle de marche aléatoire par exemple (Lopez et al. (2004) ont réalisé des simulations numériques à micro-échelle de dépôt de particules colloïdales sur la surface d'une géométrie de pore simple constitué de deux surfaces planes parallèles. Messina et al. (2012) ont utilisé des simulations à micro-échelle pour estimer l'efficacité de l'attachement des particules.

L'objectif de ce travail est de simuler le processus de transport et de dépôt de particules dans des milieux poreux à l'échelle microscopique au moyen de simulations CFD afin d'obtenir les quantités les plus pertinentes en capturant la physique sous-jacente au processus. Une fois qu'une particule est adsorbée, le champ de vitesse d'écoulement est mis à jour avant l'injection d'une nouvelle particule. L'idée principale, ici, est de revisiter le travail de Lopez et al. (2004) en considérant une géométrie 3D plus réaliste telle qu'un tube capillaire. En effet, leur travail était limité à une géométrie particulière restreinte à une géométrie en forme de fente peu susceptible d'être rencontrée dans des milieux poreux réels.

Dans ce chapitre, des simulations numériques du dépôt de particules colloïdales sur des pores de géométrie simple ont été réalisées en couplant deux logiciels disponibles : OpenFOAM® permet

d'obtenir le champ de vitesse en résolvant les équations de Stokes et de continuité et un logiciel développé dans ce travail utilisant le langage de programmation Python<sup>®</sup> et utilisé pour le processus de suivi des particules. Des quantités importantes telles que la probabilité de dépôt, le taux de couverture de surface, la porosité et la perméabilité ont été calculées pendant les simulations. Les variations de ces quantités par rapport au nombre de particules injectées pour différents nombres de Péclet ont été examinées. Les résultats préliminaires ont été analysés et les conclusions suivantes peuvent être tirées. La probabilité de dépôt diminue avec le nombre de particules injectées et avec le nombre de Péclet. Pour les valeurs de nombre de Péclet faibles, le taux de couverture finale de surface  $\Gamma$  est proche de la valeur RSA,  $\Gamma_{RSA}$ , et diminue sensiblement pour les valeurs  $Pe$  élevées. La porosité et la perméabilité diminuent toutes deux avec le nombre de particules déposées. À des nombres de  $Pe$  inférieurs, l'épaisseur hydrodynamique finale de la couche de dépôt est inférieure au diamètre de particule montrant la formation d'un dépôt monocouche lâche et elle diminue pour  $Pe$  supérieur. Les résultats ci-dessus, bien qu'ils doivent être consolidés, sont en accord avec les prédictions théoriques, démontrant que la méthode numérique utilisée est pertinente pour décrire le dépôt de colloïdes dans des milieux poreux à partir de dispersions diluées. Les développements futurs de ce travail comprendront d'une part une plus grande gamme de paramètres associés et d'autre part des géométries de pores plus réalistes.

## **Chapitre 7** Simulation micro-échelle tridimensionnelle du transport et du dépôt de particules colloïdales dans des milieux poreux modélisés avec des géométries convergentes / divergentes

La représentation la plus réaliste d'un milieu poreux est une collection de grains solides, chacun étant considéré comme un collecteur. Le processus de dépôt de particules est donc divisé en deux étapes : le transport vers le collecteur et le dépôt dû aux interactions physico-chimiques particules / collecteurs à courte distance. De telles interactions sont représentées par une fonction potentielle généralement obtenue à partir de la théorie DLVO qui comprend les forces de répulsion électrostatique, de van der Waals et de courte portée. Si des particules et des collecteurs sont identiquement chargés et que la concentration en sel est faible, le potentiel d'interaction contient deux minima et une barrière d'énergie rendant la condition de dépôt défavorable. Lorsque la

concentration en sel est très élevée ou lorsque les particules et les collecteurs sont de charges opposées, le potentiel est purement attractif, conduisant à un dépôt favorable.

Dans les procédés de filtration, on suppose habituellement que le milieu poreux est composé d'éléments unitaires contenant chacun un nombre donné de cellules unitaires dont la forme est cylindrique avec des sections transversales constantes ou variables. Chang et al. (2003) ont utilisé la simulation dynamique brownienne pour étudier le dépôt de particules browniennes dans des modèles de tubes avec des constriction paraboliques, hyperboliques et sinusoïdaux. Là encore, l'équation de Langevin avec des interactions hydrodynamiques particules/parois corrigées et l'interaction DLVO ont été résolues pour obtenir des trajectoires de particules. Par conséquent, l'efficacité du collecteur unique qui décrit le taux de dépôt initial a été évaluée pour chaque géométrie à divers nombres de Reynolds. Une géométrie de milieux poreux plus réaliste pour l'étude du transport et du dépôt est un lit de collecteurs tassés d'une forme donnée. Boccardo et al. (2014) ont étudié numériquement le dépôt de particules colloïdales dans des conditions favorables dans des milieux poreux 2D composés de grains de formes régulières et irrégulières. À cette fin, ils ont résolu les équations de Navier-Stokes avec l'équation d'advection-dispersion. Ensuite, et même si les trajectoires de particules ne peuvent être spécifiées, il a été possible de déterminer comment les grains voisins influencent mutuellement leurs taux de collecte. Ils montrent que l'efficacité de l'attachement brownien s'écarte sensiblement du cas du collecteur simple. De même Coutelie et al. (2003) ont étudié le flux et le dépôt dans un assemblage de grains sphériques 3D construit stochastiquement en se concentrant sur la dépendance de l'efficacité de capture aux nombres de Péclet faibles à modérés et ont trouvé que le modèle bien connu de sphère-cellule reste applicable à condition que les bonnes propriétés du milieu poreux soient prises en compte. Néanmoins, les porosités scannées étaient trop proches de l'unité pour être représentatives des milieux poreux réels. Dans leur travail, les approches lagrangiennes sont utilisées pour suivre le déplacement des particules dans des couches compactées en 3D, ce qui permet d'étudier le transport à l'échelle microscopique et le dépôt de particules colloïdales. Les techniques de Lattice Boltzmann sont utilisées pour calculer les forces hydrodynamiques et browniennes agissant sur des particules mobiles avec évaluation locale du potentiel d'interaction physico-chimique montrant le retard hydrodynamique pour réduire la

cinétique de dépôt au minimum secondaire dans des conditions défavorables et la rétention des particules dans les tourbillons .

Dans la plupart de ces approches de simulation, la taille caractéristique du domaine d'écoulement est de plusieurs ordres de grandeur supérieure à la taille des particules, de sorte que le seuil de blocage (rapport entre la taille caractéristique du domaine d'écoulement et la taille des particules) est suffisamment élevé pour que le domaine d'écoulement reste non affecté par le dépôt de particules. Pour de nombreux systèmes, cependant, le seuil de blocage peut être faible et le dépôt de colloïdes devrait avoir un impact important sur la structure et la force du flux et donc sur le processus de dépôt des particules. Dans ce chapitre, nous nous concentrerons sur un tel impact et simulerons le dépôt de colloïdes dans des milieux poreux dans des conditions de dépôt favorables en adoptant l'approche par éléments unitaires où la cellule unitaire est un tube avec deux formes convergentes-divergentes : tube conique et tube venturi. Pour équilibrer la hausse inhérente du coût de la simulation, nous restreindrons cette étude à des cas de suspensions colloïdales diluées où les interactions hydrodynamiques entre particules transportées sont négligeables et adopterons une approche simple détaillée ci-après et un nouveau code 3D-PTPO développé dans notre laboratoire. L'idée est d'approcher le comportement dans des milieux poreux idéalisés comme un faisceau de capillaires avec des sections transversales variables. L'originalité principale de l'outil est de prendre en compte la modification de l'espace interstitiel et donc le champ d'écoulement lorsque les particules sont déposées sur la paroi des pores. Les variations des paramètres clés, y compris la probabilité de dépôt et le taux de couverture de surface adimensionnel  $\Gamma/\Gamma_{RSA}$ , ainsi que la distribution spatiale détaillée de la densité des particules déposées ont été étudiées. Les principales conclusions tirées de ce chapitre sont les suivantes :

La probabilité qu'une particule se dépose sur la surface de la paroi des pores est beaucoup plus élevée lorsque le transport est dominé par la diffusion pour les deux géométries considérées dans ce travail. La distribution des particules déposées le long des tuyaux est semblable à celle d'un piston pour le régime où la diffusion domine, tandis que la distribution est plus uniforme pour le régime dominant par advection. De plus, pour toutes les valeurs du nombre de Péclet considérées dans ce travail comprises entre 0,0019 et 1900, le taux de couverture de surface normalisé  $\Gamma/\Gamma_{RSA}$  en fonction du nombre de particules injectées (N) présente une forte augmentation aux stades précoces de dépôt

et tend à une valeur de plateau pour des valeurs de  $N$  élevées. Le comportement du plateau final correspondant au taux de couverture de surface normalisé maximal  $\Gamma_{\text{final}}/\Gamma_{\text{RSA}}$  en fonction de  $Pe$  a été analysé. Pour un  $Pe$  bas, un plateau peut être observé pour les deux géométries, la valeur du plateau et la cinétique de dépôt sont en accord avec la théorie de l'adsorption séquentielle aléatoire (RSA). Tandis qu'à  $Pe$  élevé, les tendances de variation de  $\Gamma_{\text{final}}/\Gamma_{\text{RSA}}$  en fonction de  $Pe$  sont en bon accord avec les résultats expérimentaux et numériques obtenus par d'autres études. Enfin, les résultats ci-dessus démontrent que le modèle numérique pourrait capturer la physique du transport et du dépôt de particules colloïdales dans des pores de géométrie simple et pourrait être utilisé dans des développements ultérieurs à savoir le transport dans des géométries plus complexes (cellule unitaire de couche de dépôt de particules, surfaces à motifs chimiques, etc).

## **Chapitre 8** Simulation micro-échelle tridimensionnelle du transport et du dépôt de particules colloïdales dans des milieux poreux chimiquement hétérogènes

Les processus de transport et de dépôt de particules colloïdales (adsorption irréversible) dans des milieux poreux présentent un grand intérêt environnemental et industriel, car ils sont essentiels à de nombreuses applications allant de l'administration de médicaments au traitement de l'eau potable. Par conséquent, le dépôt de particules sur des milieux poreux homogènes a fait l'objet de nombreuses études expérimentales et théoriques. Cependant, d'un point de vue pratique, le problème du dépôt de particules dans des milieux poreux présentant une hétérogénéité à l'échelle des pores est plus pertinent puisque la plupart des milieux poreux naturels ou artificiels sont physiquement et/ou chimiquement hétérogènes. Lorsque les particules en écoulement approchent de telles surfaces à motifs hétérogènes, elles présentent divers comportements de dépôt en fonction de la nature, de l'ampleur et de la forme de ces hétérogénéités. Ainsi, le transport et le dépôt de particules dans des milieux poreux hétérogènes ont fait l'objet d'études et une quantité significative de recherches pertinentes ont été effectuées. Parmi les différentes géométries de milieux poreux, le transport de particules dans les capillaires/microcanaux est au cœur de nombreux systèmes microfluidiques et nanofluidiques. De plus, les milieux poreux sont généralement considérés comme un faisceau de capillaires/microcanaux et lorsque le transport et le dépôt de particules ont été simulés dans un

capillaire/microcanal, le processus dans le milieu poreux entier peut être prédit en imposant des conditions aux limites appropriées entre capillaires/microcanaux. À notre connaissance, Chatterjee et al. (2011, 2012) ont étudié le transport de particules dans des microcanaux cylindriques hétérogènes. L'hétérogénéité de surface est modélisée comme des bandes alternées de régions attractives et répulsives sur la paroi du canal pour faciliter l'évaluation systématique de type continuum. Cette étude fournit une analyse théorique complète de la façon dont le transport de ces particules en suspension est affecté dans ces microcanaux en raison des hétérogénéités sur leurs parois. Cependant, cette simulation était bidimensionnelle et pouvait donc difficilement refléter les vrais milieux poreux. Par conséquent, des simulations 3D doivent être effectuées à nouveau pour développer une image complète du transport de particules dans un capillaire. De plus, il est important d'étudier l'effet couplé de l'hydrodynamique et de l'hétérogénéité chimique sur le dépôt de particules. Par ailleurs, il y a peu de travaux rapportés où l'on s'intéresse aux effets combinés de l'hétérogénéité de surface et de l'hydrodynamique sur les dépôts de particules colloïdales dans les capillaires/microcanaux tridimensionnels, ce qui est également l'un des objectifs de ce chapitre. Le code 3D-PTPO a été utilisé pour étudier l'influence des hétérogénéités de surface et de l'hydrodynamique sur le dépôt de particules. Le capillaire axisymétrique tridimensionnel avec une surface avec des hétérogénéités chimiques à répétition périodique (à motifs de type bandes transversales et échiquier) de charges de surface positives et négatives (autrement dit régions attractives et répulsives) est utilisé pour le modèle d'hétérogénéité. Les principales conclusions peuvent être tirées comme suit : Premièrement, l'effet couplé de l'hétérogénéité de charge et du champ de vitesse tridimensionnel peut faire ressortir une distribution de concentration complexe de particules déposées sur la paroi, conduisant à une densité plus élevée de particules déposées sur les parois des pores aux bords de chaque bande favorable, et le dépôt est plus uniforme le long du capillaire à motifs par rapport à capillaire homogène. Deuxièmement, la probabilité de dépôt est en ligne avec la période des hétérogénéités. Avec le même rapport de surface favorable,  $\theta$ , une longueur de période d'hétérogénéité plus petite se traduira par une probabilité de dépôt plus élevée et par conséquent un taux de couverture de surface normalisé supérieur. De plus, pour le régime où la diffusion domine à  $Pe$  faible, le taux de couverture de surface est proche de  $\Gamma_{RSA}$  et présente un plateau relativement stable. Pour le régime à convection dominante à  $Pe$  élevée la décroissance de  $\Gamma/\Gamma_{RSA}$  par rapport à  $Pe$  a une tendance qui est

en bon accord avec la dépendance en loi de puissance observée par ailleurs. Enfin, la probabilité globale de dépôt augmente avec la fraction de surface favorable. Cette étude donne un aperçu de la conception de milieux poreux artificiellement hétérogènes pour la capture de particules dans diverses applications d'ingénierie et biomédicales, y compris la pharmacothérapie ciblée. De plus, le modèle peut être encore amélioré en incorporant des profils d'écoulement de fluide plus réalistes et des motifs hétérogènes plus aléatoires.

## **Chapitre 9** Conclusions et perspectives

Les milieux poreux polymériques avec une structure poreuse originale, une porosité élevée, une faible densité et une bonne stabilité chimique sont des matériaux prometteurs dans une large gamme de domaines d'application. Malgré des progrès significatifs réalisés dans la préparation des milieux poreux polymériques, aucune méthode particulière n'est meilleure que d'autres et chaque méthode a ses avantages et ses limites. Actuellement, le principal problème est que les procédés de production de ces méthodes sont relativement encombrants et diminuent nettement l'efficacité de la production et augmentent le coût. Ainsi, un objectif à long terme pour la préparation de matériaux polymères poreux est toujours le développement de procédures simples et évolutives. Il est donc essentiel de trouver de nouvelles méthodes permettant d'optimiser la structure poreuse sans sacrifier le faible coût. C'est l'un des principaux objectifs de cette thèse. La coextrusion multicouche représente une technique de traitement de polymère avancée, qui est capable de produire économiquement et efficacement des films de multicouches. Ainsi, dans cette thèse, une nouvelle stratégie est proposée pour préparer des milieux poreux polymères avec une structure poreuse accordable par coextrusion multicouche combinée avec la méthode de modèle/TIPS, qui est une voie hautement efficace pour la fabrication à grande échelle de matériaux polymères poreux. Cette approche combine les avantages de la coextrusion multicouche (processus continu, voie économique pour la fabrication à grande échelle et structures de couche accordables) et la méthode modèle / méthode de séparation de phase (processus de préparation simple et structure de pore accordable). Par la suite, des applications des milieux poreux polymères dans l'adsorption des PAH et le séparateur de batteries au lithium-ion ont été étudiées. Les résultats obtenus indiquent que les séparateurs PP/PE multicouches préparés par

cette nouvelle combinaison présentent une porosité plus élevée, une absorption et une rétention d'électrolyte plus élevées que les séparateurs commerciaux. Cela va certainement augmenter la conductivité ionique, et par conséquent améliorer les performances de la batterie. Plus important encore, le séparateur multicouche PP/PE présente une fonction d'arrêt thermique efficace et une stabilité thermique jusqu'à 160 °C, plus large que les séparateurs commerciaux. Le polystyrène poreux obtenu par cette nouvelle combinaison possède une structure poreuse abondante et uniforme qui présente des performances d'adsorption beaucoup plus élevées de traces de pyrène que le milieu solide. La cinétique d'adsorption et l'isotherme des membranes PS poreuses peuvent être bien ajustés par une cinétique de pseudo-deuxième ordre et un modèle isotherme de Freundlich. En principe, cette nouvelle méthode est applicable à tout polymère pouvant être traité à l'état fondu en plus de PP, PE et PS. Ainsi, à l'avenir, des recherches pourraient être menées sur la préparation et l'application d'autres types de milieux poreux polymères tels que le polyfluorure de vinylidène poreux, l'oxyde de polyéthylène, le polyméthacrylate de méthyle, etc.

Plus important encore, le mécanisme de base des procédés d'application ci-dessus (adsorption de PAH ou transport de Li-ion à travers un séparateur) est basé sur le transport et le dépôt de particules dans des milieux poreux. En outre, le transport et le dépôt de particules colloïdales dans des milieux poreux est un phénomène fréquemment rencontré dans un large éventail d'applications en plus des cas ci-dessus, y compris l'assainissement des aquifères, l'encrassement des surfaces et l'administration de médicaments. Il est donc essentiel de bien comprendre ces processus ainsi que les mécanismes dominants. Par conséquent, dans la seconde partie de la thèse, la simulation microscopique du transport et du dépôt de particules en milieux poreux a été réalisée par un nouveau modèle de suivi des particules colloïdales, appelé 3D-PTPO (Modèle tridimensionnel de suivi des particules par Python<sup>®</sup> et OpenFOAM<sup>®</sup>).

Tout d'abord, le dépôt de particules est étudié sur un capillaire homogène afin de revisiter le travail de Lopez et ses co-auteurs (*Lopez et al., 2004*) en considérant une géométrie 3D plus réaliste, ainsi que de valider les lois de base théoriques du transport et du dépôt de particules utilisées dans la méthode développée ici. Les résultats préliminaires ont été analysés et quelques conclusions peuvent être tirées : La probabilité de dépôt diminue avec le nombre de particules injectées et avec le nombre

de Peclet. Pour les valeurs de nombre de Peclet faibles, le taux de couverture ultime de la surface  $\Gamma$  est proche de la valeur RSA et diminue sensiblement pour les valeurs de Peclet élevées. La porosité et la perméabilité diminuent avec le nombre de particules déposées. À de faibles nombres de Peclet, l'épaisseur hydrodynamique équivalente de la couche de dépôt est inférieure au diamètre de particule montrant la formation d'un dépôt monocouche lâche avant de diminuer pour des valeurs plus élevées de Peclet. Les résultats ci-dessus démontrent que la méthode numérique utilisée est pertinente pour décrire le dépôt de colloïdes dans des milieux poreux à partir de dispersions diluées.

D'autre part, la modélisation numérique tridimensionnelle du procédé de transport de particules et le dépôt sur un support poreux avec une géométrie plus complexe est réalisé en représentant la structure élémentaire de pores sous forme de tube capillaire avec convergente/divergente ou rétrécissement/élargissement de section (tube conique et le tube venturi). Les principales conclusions peuvent être tirées de la manière suivante: La probabilité pour une particule à être déposée sur la surface de la paroi des pores est beaucoup plus élevée pour le régime de diffusion dominante, et la distribution des particules déposées le long des tubes est en forme de piston uniquement pour le modèle simple de capillaire à section constante. La distribution est plus uniforme pour le régime dominé par advection. En particulier, pour le tube de venturi, la densité des particules déposées est relativement faible au voisinage de l'entrée et de la sortie de la gorge du pore en raison de la structure particulière de l'écoulement à l'intérieur des tubes. Le comportement du plateau final du taux de couverture de surface normalisé maximal  $\Gamma_{\text{final}}/\Gamma_{\text{RSA}}$  en fonction de Peclet a été analysé. Pour un Peclet bas, un plateau peut être observé pour les deux géométries considérées et la valeur du plateau et la cinétique de dépôt est cohérente avec la théorie RSA. Pour un Peclet élevé les tendances de la variation de  $\Gamma_{\text{final}}/\Gamma_{\text{RSA}}$  versus Peclet sont en bon accord avec les résultats expérimentaux et ceux de simulations trouvés dans la littérature.

Troisièmement, l'effet couplé de l'hétérogénéité chimique de surface et de l'hydrodynamique sur le transport et le dépôt de particules dans un seuil de pore idéalisé en tant que capillaire tridimensionnel avec une surface chimiquement hétérogène à répétition périodique (bandes transversales et échiquier) a été étudié. Les principales conclusions peuvent être tirées comme suit : l'effet couplé de l'hétérogénéité et du champ de vitesse peut faire ressortir une distribution de

concentration complexe des particules déposées sur la paroi. Par exemple, une densité plus élevée de particules déposées est observée aux bords avant et arrière de chaque bande favorable. De plus, la probabilité de dépôt est en ligne avec la période des hétérogénéités. En outre, le taux de couverture de surface est toujours proche de la  $\Gamma_{RSA}$  et présente un plateau relativement stable à  $Pe$  inférieur. La tendance à la baisse de  $\Gamma_{final} / \Gamma_{RSA}$  par rapport à  $Pe$  est de nouveau en bon accord avec la dépendance en loi de puissance obtenue à des valeurs de  $Pe$  forte. De plus, la probabilité globale de dépôt augmente avec la fraction de surface favorable.

Les résultats ci-dessus sont en accord avec les prédictions théoriques, démontrant que la méthode numérique utilisée est pertinente pour décrire le dépôt de colloïdes dans des milieux poreux à partir de dispersions diluées. Les développements futurs de ce travail comprendront d'une part une plus grande gamme de paramètres associés et d'autre part des géométries de pores plus réalistes.

## Conception, Fabrication et Application de Milieux Poreux Polymériques

**RESUME :** La co-extrusion de microcouche est une méthode pour produire de façon efficace et successive des polymères avec des structures de couches alternées, ayant les avantages de haute efficacité et faible coût. Par conséquent, sur les exigences structurelles de PM de l'application spécifique, ce mémoire a conçu le PM avec une structure spécifique et une co-extrusion de microcouche de manière créative combinée avec la méthode traditionnelle de préparation de PM (méthode de gabarit, méthode de séparation de phase), en combinant les avantages des deux méthodes, les PM avec une structure de pore idéale peuvent être préparés en grande quantité et l'on peut également explorer son application dans les séparateurs de batteries au lithium-ion et l'adsorption d'hydrocarbures aromatiques polycycliques.

Le plus important, dans la deuxième partie de cet essai, se trouve que la simulation micro-numérique est utilisée pour étudier le transport et le dépôt de particules dans des milieux poreux pour explorer le mécanisme des matériaux poreux dans les domaines de l'adsorption et du séparateur de batterie. Le code de 3D-PTPO (un modèle tridimensionnel de suivi des particules combinant Python<sup>®</sup> et OpenFOAM<sup>®</sup>) est utilisé pour étudier le transport et le dépôt de particules colloïdales dans des milieux poreux, l'on adopte trois modèles (colonne, venturi et tube conique) pour représenter différentes formes de matériaux poreux. Les particules sont considérées comme des points matériels pendant le transport, le volume des particules sera reconstitué et déposé comme partie de la surface du matériau poreux pendant le dépôt, la caractéristique principale de ce code est de considérer l'influence du volume des particules déposées sur la structure des pores, les lignes d'écoulement et le processus du dépôt des autres particules. Les simulations numériques sont d'abord conduites dans des capillaires simples. Par la suite, des simulations numériques sont effectuées dans des capillaires convergents-divergents pour étudier la structure des pores et l'effet de nombre Peclet sur le dépôt de particules. Enfin, l'on étudie l'effet double de l'hétérogénéité de surface et de l'hydrodynamique sur le comportement de dépôt de particules.

**Mots clés :** milieux poreux polymériques, coextrusion multicouche, séparateur de batterie au lithium-ion, l'adsorption de PAH, simulation à l'échelle microscopique, 3D-PTPO (modèle tridimensionnel de suivi de particules par Python<sup>®</sup> et OpenFOAM<sup>®</sup>), transport et dépôt de particule

## Design, Fabrication and Application of Polymeric Porous Media

**ABSTRACT :** In the first part of the thesis, polymeric porous media are firstly designed based on the specific application requirements. Then the designed polymeric porous media are prepared by the combination of multilayer coextrusion and traditional preparation methods (template technique, phase separation method). This combined preparation method has integrated the advantages of the multilayer coextrusion and the template/phase separation method. Afterwards, the applications of the polymeric porous media in polycyclic aromatic hydrocarbons adsorption and lithium-ion battery separator have been investigated.

More importantly, in the second part of the thesis, numerical simulations of particle transport and deposition in porous media are carried out to explore the mechanisms that form the theoretical basis for the above applications (adsorption, separation, etc.). In this part, the microscale simulations of colloidal particle transport and deposition in porous media are achieved by a novel colloidal particle tracking model, called 3D-PTPO (Three-Dimensional Particle Tracking model by Python<sup>®</sup> and OpenFOAM<sup>®</sup>) code. Numerical simulations were firstly carried out in a capillary tube considered as an element of an idealized porous medium composed of capillaries of circular cross sections. Then microscale simulation is approached by representing the elementary pore structure as a capillary tube with converging/diverging geometries (tapered pipe and venturi tube) to explore the influence of the pore geometry and the particle Péclet number (Pe) on particle deposition. Finally, the coupled effects of surface chemical heterogeneity and hydrodynamics on particle deposition in porous media were investigated in a three-dimensional capillary with periodically repeating chemically heterogeneous surfaces.

**Keywords :** polymeric porous media, multilayer coextrusion, lithium-ion battery separator, PAH adsorption, microscale simulation, 3D-PTPO (three-dimensional particle tracking model by Python<sup>®</sup> and OpenFOAM<sup>®</sup>), particle transport and deposition